

**Single and Double Doping of Nanostructured Titanium Dioxide with Silver and
Copper: Structural, Optical and Gas-Sensing Properties**

by

NUBI OLATUNBOSUN OWOLABI

THESIS

Submitted in fulfilment of the requirements for the degree of

DOCTOR OF PHILOSOPHY

in

PHYSICS

in the

FACULTY OF SCIENCE & AGRICULTURE

(School of Physical and Mineral Sciences)

at the

UNIVERSITY OF LIMPOPO

PROMOTER: Prof. K.E. Rammutla

CO-PROMOTER: Dr. T.E. Mosuang

2016

Dedications

This one is for you, my late parents. A little too late perhaps, but I got there in the end:

Baba, Mama: Bawo ni iba ti dun mo mi ninu to kani e wa laye. Mo dupe pupo lowo yin nitoriwipe e ko fi mi sile. E duro timi titi e fi fi aiye sile. Nitori eyi ni mo fi da lokan wipe mo ma yonju eleyi, yala ohun to o ma gba. E sun re o.

Declaration

I declare that **SINGLE AND DOUBLE-DOPING OF TITANIUM DIOXIDE NANOPARTICLES WITH SILVER AND COPPER: STRUCTURAL, OPTICAL AND GAS-SENSING APPLICATIONS** hereby submitted to the University of Limpopo, for the degree of Doctor of Philosophy (Physics) has not previously been submitted by me for a degree at this or any other university; that it is my work in design and in execution, and that all material contained herein has been duly acknowledged..

.....
NUBI OO (Mr)

.....
Date

Acknowledgements

The synthesis of the nanostructured titanium dioxide samples studied in this research was primarily carried out in the laboratories of the University of Limpopo. Other experimental facilities, particularly those involving sample characterisation, were made available through collaboration with other research centres.

For financial and equipment support we acknowledge:

- University of Limpopo (UL)
- National Research Foundation (NRF)
- Centre for Scientific and Industrial Research (CSIR)
- Department of Science and Technology (DST)
- India-Brazil-South Africa (IBSA)

Academic/research support, supervision and guidance:

- Prof Erasmus Rammutla (RIP God-sent)
- Dr Thuto Mosuang
- Dr Bonex Nwakikunga

Gratitude Statement:

- God made. Papa moulded. Mama nurtured. Wife persevered. Children endured. Uncle insisted. Friends supported. Existence is priceless! I am really very grateful.

Abstract

Single and double doped nanometric powders of titanium dioxide (TiO_2) were synthesised by the sol-gel process using titanium isopropoxide (TTIP) as the precursor. For comparison, an undoped sample was also prepared. The metal dopants, Ag and Cu, were used at doping levels of 5% molar weight. The samples were dried at 100°C in air and post annealing was done at 300°C , 600°C , 900°C and 1100°C .

Structural characterisation of the samples was carried out by X-ray Diffraction (XRD), Raman Spectroscopy, Scanning Electron Microscopy (SEM) and Energy dispersive X-ray Spectrometry (EDS) techniques. Most samples annealed at the 300°C temperature (and lower) revealed the predominantly-anatase phase, while those annealed at 900°C and above were rutile-only. The double-doped powder that was annealed at 300°C was found to be constituted by anatase and brookite phases (with the dopants incorporated into the TiO_2 matrix), and the one annealed at 600°C was a mixture of brookite and rutile. The results suggest that multiple doping of titania may favour a two-phase structure at lower temperatures than singly-doped powders. The co-existence of brookite with anatase is believed to be responsible for the enhancement of anatase to rutile transformation in the double-doped sample.

UV-visible (UV-vis) and Photoluminescence (PL) measurements were also carried out to study the optical properties of the TiO_2 nanoparticles. This revealed the active PL band at around 440 nm. By narrowing the band gap, the double-doped powders that exhibited the brookite phase, again showed improved visible light photo absorption over the other samples, with a significant shift of the absorption edge to shorter wavelengths. Further, PL spectra revealed a change in PL intensity with phase change, as well as the presence of exciton energy levels at the base of the conduction band.

The changes in the electrical conductivities of representative anatase and rutile TiO_2 nanopowders upon exposure to water-vapour, ammonia (NH_3) and hydrogen (H_2) were also investigated. Sensing measurements for water-vapour was done at room temperature for various humidity levels ranging from 5.4% RH to 88.4% RH. The detection of NH_3 and H_2 gases were carried out at temperatures extending from room temperature to 350°C and over concentration ranges of 25 sccm to 500 sccm and 15

sccm to 200 sccm respectively. The gas-sensing results show that the sol-gel fabricated TiO₂ nanoparticles (particularly in anatase form), has excellent fast and stable dynamic responses to humidity, NH₃ and H₂. They feature good sensitivities, even at a low operating temperatures. However, acceptor behaviour, for which there was a conductivity switch from *n*-type to *p*-type, was recorded for the Ag-doped rutile powders at operating temperatures of 300°C and 350°C. Overall, the double-doped sample annealed at 300°C was deemed the most promising candidate for gas-sensing.

Ni Soki...

TiO₂ bintin je atikun ti o se pataki ni orisirisi ona, papa julo ti a ba fi silifa ati kopa die-die kun lapapo.

Table of Contents

Dedications.....	i
Declaration	ii
Acknowledgements	iii
Abstract	iv
List of Tables	xi
List of Figures	xiii
1. BACKGROUND	1
1.1 INTRODUCTION.....	2
1.1.1 Resent Research	2
1.1.2 Key concepts	4
1.2 RESEARCH PROBLEM.....	4
1.2.1 Source and Background of the Problem	4
1.2.2 Statement of the Research Problem	5
1.3 LITERATURE REVIEW	5
1.4 PURPOSE OF THE STUDY.....	6
1.4.1 Research Aim	6
1.4.2 Hypothesis	6
1.4.3 Specific Objectives.....	6
1.5 RESEARCH METHODOLOGY	7
1.6 SIGNIFICANCE OF PROPOSED RESEARCH.....	7
1.7 SCOPE, LIMITATIONS AND DELIMITATIONS OF THE STUDY	8
1.8 DISSERTATION OUTLINE	9
2. FUNDAMENTALS & LITERATURE REVIEW	10
2.1 INTRODUCTION.....	11
2.2 RESEARCH IN NANOTECHNOLOGY.....	12
2.3 SCIENTIFIC REVIEWS ON NANOSTRUCTURED TITANIUM DIOXIDE ...	14

2.4	NANOPARTICLES AND NANOPOWDERS.....	14
2.5	PROPERTIES OF NANOSTRUCTURED TITANIA.....	17
2.5.1	Structural Properties of Nanosized Titania.....	17
2.5.2	Thermodynamic Properties of Nanosized Titania	20
2.5.3	X-ray Diffraction Properties of Nanosized Titania	22
2.5.4	Raman Vibration Properties of Nanosized Titania	25
2.5.5	Electronic Properties of Nanosized Titania	26
2.5.6	Optical Properties of Nanosized Titania.....	30
2.5.7	Photon-Induced Electron & Hole Properties of Nanosized Titania	33
2.5.8	Gas Sensing Properties of Nanosized Titania.....	34
2.6	SYNTHESIS OF TITANIA NANOSTRUCTURES.....	45
2.6.1	The Sol-Gel Method.....	45
2.6.2	Non-Hydrolytic Sol Method	49
2.6.3	Micelle and Inverse Micelle Methods	52
2.6.4	Hydrothermal Method	54
2.6.5	Solvothermal Method	57
2.6.6	Direct Oxidation Method	58
2.6.7	Physical Vapour Deposition	60
2.6.8	Electrodeposition	60
2.6.9	Sonochemical Method	61
2.6.10	Microwave Method.....	61
2.6.11	Mesoporous/Nanoporous Titania Materials	62
2.6.12	Titania Aerogels.....	64
2.6.13	Opal and Photonic Titania Materials.....	64
2.6.14	Preparation of Titania Nanosheets	66
2.7	MODIFICATIONS OF TITANIA NANOMATERIALS.....	67
2.7.1	Doping (Bulk Chemical Modification)	67

2.7.2	Surface Chemical Modifications.....	71
2.8	APPLICATIONS OF TITANIA NANOMATERIALS	73
2.8.1	Photocatalytic Applications	74
2.8.2	Photovoltaic Applications	76
2.8.3	Photocatalytic Water Splitting	80
2.8.4	Electrochromic Devices	82
2.8.5	Hydrogen Storage.....	84
2.8.6	Gas Sensing Applications	85
2.9	CHARACTERISATION TECHNIQUES	88
3.	RESEARCH METHODOLOGY	90
3.1	INTRODUCTION.....	91
3.2	POWDER SAMPLE SYNTHESIS.....	91
3.2.1	Materials	92
3.2.2	Quantities.....	92
3.2.3	Procedure	93
3.2.4	Sample Species	94
3.3	SAMPLE CHARACTERISATION (EXPERIMENTAL)	94
3.3.1	X-Ray Diffraction (XRD).....	95
3.3.2	Raman Spectroscopy.....	100
3.3.3	Scanning Electron Microscopy (SEM).....	105
3.3.4	Energy-Dispersive X-ray Spectroscopy (EDS, EDX, or XEDS).....	107
3.3.5	Ultraviolet–Visible spectroscopy (UV-Vis or UV/Vis).....	110
3.3.6	Photoluminescence (PL).....	115
3.3.7	Gas-Sensing	118
4.	RESULTS & DISCUSSION I: STRUCTURAL PROPERTIES	126
4.1	INTRODUCTION.....	127
4.2	PHASE INDEXING	128

4.2.1	XRD Data.....	128
4.2.2	Anatase and Rutile Phases.....	132
4.2.3	Extraneous Phases.....	134
4.3	CRYSTALLINITY.....	138
4.4	CRYSTALLITE SIZE	139
4.5	LATTICE SIZE.....	141
4.6	POLYMORPHISM	142
4.6.1	Phase Transition	142
4.6.2	Phase Mixing	145
4.6.3	Phase Content	147
4.7	SURFACE MICROSCOPY	149
4.7.1	Raman Microspectroscopy	149
4.7.2	SEM Surface Morphology	150
4.8	ELEMENTAL ANALYSIS.....	155
4.8.1	Energy Dispersive Spectroscopy (EDS)	155
4.9	DISCUSSION.....	157
5.	RESULTS & DISCUSSION II: OPTICAL PROPERTIES.....	158
5.1	INTRODUCTION.....	159
5.2	UV-VIS LIGHT ABSORPTION	159
5.3	PHOTOLUMINESCENCE	163
6.	RESULTS & DISCUSSION III: GAS-SENSING PROPERTIES.....	167
6.1	INTRODUCTION.....	168
6.2	HUMIDITY	172
6.2.1	Response of Anatase TiO ₂ to Humidity.....	172
6.2.2	Response of Rutile TiO ₂ to Humidity.....	176
6.2.3	Performance of Anatase versus Rutile TiO ₂ under Humidity.....	180
6.3	AMMONIA GAS (NH ₃).....	180

6.3.1	Response of Anatase TiO ₂ to NH ₃	181
6.3.2	Response of Rutile TiO ₂ to NH ₃	185
6.3.3	Performance of Anatase versus Rutile TiO ₂ under NH ₃	189
6.4	HYDROGEN GAS (H ₂)	190
6.4.1	Response of Anatase TiO ₂ to H ₂	190
6.4.2	Response of Rutile TiO ₂ to H ₂	194
6.4.3	Performance of Anatase versus Rutile TiO ₂ under NH ₃	198
6.5	DISCUSSION	198
7.	SUMMARY, RECOMMENDATIONS, CONCLUSION	202
7.1	INTRODUCTION	203
7.2	RESEARCH DESIGN AND METHOD	203
7.3	LIMITATIONS OF THE STUDY	203
7.4	OVERVIEW OF RESEARCH FINDINGS	204
7.4.1	Structural Properties	204
7.4.2	Optical Properties	204
7.4.3	Electrical Properties	204
7.5	CONCLUSIONS	205
7.6	RECOMMENDATIONS/FUTURE WORK	206
7.7	CONTRIBUTIONS OF THE STUDY	207
	REFERENCES	208
	Appendix A: List of Publications & Presentations	243
	Appendix B: List of Abbreviations	245
	Appendix C: Specification Sheets	246
	Appendix D: Sigma-Aldrich Data Specification Sheets	255
	Appendix E: Dopant Quantity Calculator	258
	Appendix F: Gas-Sensing Data Sheets	260

List of Tables

Table 1: Characteristic anatase, brookite and rutile XRD peak positions (2θ), featuring their relative intensities and miller indices. The values are from Cu-target diffractometers with a wavelength $\lambda = 1.540598 \text{ \AA}$. Corresponding d-spacing are also displayed, alongside the cell parameter and space group values.....	24
Table 2: Fundamental photon-induced electron and hole processes [110].	33
Table 3: A comparison of advantages and disadvantages of gas sensing materials and techniques [118].	38
Table 4: Classification of the various characterisation techniques that are most widely used in characterising nanostructured materials.	89
Table 5: Quantities of precursors used in the preparation of doped and undoped TiO_2 powder species. Ignoring losses, the calculations were estimated to yield about 100 g of each final sample species.....	93
Table 6: List of the five titania species, dried at 100°C and further annealed at 300°C , 600°C , 900°C and 1100°C – four of which titania is a host to Ag and/or Cu.	94
Table 7: The scheme for the TiO_2 samples available for gas testing measurements.	125
Table 8: A list of the phases found in the TiO_2 powder samples and their COD entry codes. Their major XRD peaks are included in the last column.....	131
Table 9: Quantities (in %) of the phases (anatase TiO_2 , brookite TiO_2 , rutile TiO_2 , Ag (silver), CuO (tenorite) and AgCl (chlorargyrite)) as determined by the Match! 2 program for the TiO_2 powder samples.	131
Table 10: Crystallite sizes (in nm) of the major TiO_2 phases of anatase and rutile in the TiO_2 powder samples – as estimated with the aid of the Origin® program and Scherrer equation.	140
Table 11: The unit cell parameters of all the tetragonal anatase and rutile titania structures. The last column compares their cell volumes with expected values (anatase: 135.74, rutile: 62.15).....	142
Table 12: Anatase, brookite and rutile contents in the TiO_2 samples as calculated from the integrated intensities of the respective peaks of anatase (101), brookite (121) and rutile (110) [47].	148
Table 13: Crystallite sizes (obtained from XRD data) and grain sizes (obtained from SEM micrographs) of the dominant phases in the TiO_2 powder samples.	154

Table 14: Calculated Band gaps of the sample species at various phase structures.	162
Table 15: Performance indices of the anatase TiO ₂ samples that were exposed to various levels of humidity at room temperature.	175
Table 16: Performance indices of the rutile TiO ₂ samples that were exposed to various levels of humidity at room temperature.	179
Table 17: Performance data of the anatase TiO ₂ samples that were exposed to various concentrations of NH ₃ at different operating temperatures.	183
Table 18: Performance data of the rutile TiO ₂ samples that were exposed to various concentrations of NH ₃ at different temperatures.	187
Table 19: Performance data of the anatase TiO ₂ samples that were exposed to various concentrations of H ₂ at different operating temperatures.	192
Table 20: Performance data of the rutile TiO ₂ samples that were exposed to various concentrations of H ₂ at different temperatures.	196
Table 21: A ranking of the overall performances of the TiO ₂ sensor materials tested in the presence of humidity, NH ₃ and H ₂ at various operating temperatures.	201

List of Figures

Figure 1. Primitive tetragonal unit cell of (a) anatase TiO ₂ and (b) rutile TiO ₂ . Oxygen and titanium atoms are coloured red and grey respectively. Anatase (101) and rutile (110) surface planes are shaded. The x, y and z axes correspond to the [100], [010] and [001] directions respectively. Lattice constants are indicated in Å.	17
Figure 2: Predicted morphology for anatase and rutile TiO ₂ under different pH conditions from acid to basic [62].	20
Figure 3: Typical XRD pattern of anatase TiO ₂ nanoparticles.	23
Figure 4: Typical Raman spectra for anatase TiO ₂ nanoparticles, featuring peaks at 144 cm ⁻¹ (corresponding to the E _{g(1)} mode), 197 cm ⁻¹ (corresponding to the E _{g(2)} mode) and 639 cm ⁻¹ (corresponding to the E _{g(3)} mode).	26
Figure 5: Self-consistent band structure of the anatase TiO ₂ structure. The top of the valence band is taken as the zero of energy [93].	27
Figure 6: Total and projected densities of states (DOS) of the anatase TiO ₂ structure. The vertical solid line represents the top of the valence band (the zero of energy). The vertical dashed line indicates the conduction-band minimum [93].	27
Figure 7: Molecular-orbital bonding for the anatase TiO ₂ structure: (a) atomic levels, (b) crystal-field split levels, and (c) final interaction states. The thin-solid and dashed lines represent large and small contributions, respectively [93].	28
Figure 8: Schematic diagram of the energy levels of the lowest unoccupied MO's of a [TiO ₆] ⁸⁻ cluster with O _h , D _{2h} (rutile), and D _{2d} (anatase) symmetry [94].	29
Figure 9: Experimental curves for (a) rutile and (b) anatase TiO ₂ . The left panel is the Ti K-edge XANES spectra, while O K-edge ELNES spectra is on the right [94].	29
Figure 10: Classification of gas sensing methods [118].	36
Figure 11: Typical scheme of a semiconductor gas sensing device [124].	39
Figure 12: A representation of porous semiconducting oxide grains and the space charge region around the surface of each grain and at intergrain contacts. The band model for the corresponding grain model is also shown. X _g refers to grain size and λ _D refers to the Debye length [128].	43
Figure 13: Schematic representation of the structure (A) and operating principles (B) of the DSSC (or dye-sensitised nanocrystalline solar cell).	77
Figure 14: Schematic of the x-ray diffractometer setup. The spectrograph consists of a high voltage power supply (50KV or 100KV), a broad band X-ray tube, usually with	

a tungsten anode and a beryllium window, a specimen holder, an analysing crystal , a goniometer, and an X-ray detector device [261].	95
Figure 15: Typical x-ray diffraction patterns (for anatase, rutile and mixed-phase TiO ₂) featuring the miller indices corresponding to the prominent peaks of the samples [263].	96
Figure 16: Scheme of the x-ray diffraction geometry [262].	97
Figure 23: The XRD instrumentation – PANalytical X'Pert PRO diffractometer – made available by the CSIR.	99
Figure 17: Energy-level scheme of the states involved in the Raman signal. The relative strength of the signal for the different transitions is roughly proportional to the thickness of the lines.	102
Figure 24: The Raman spectrometry instrumentation – Jobin Yvon LabRAM HR 800 UV-VIS-NIR – made available by the CSIR.	104
Figure 25: The SEM instrumentation – Auriga Cobra FIB FESEM – made available by the CSIR.	107
Figure 18: A schematic representation of the EDS principle [274].	108
Figure 26: The EDS instrumentation – JEOL JSM-7500F FESEM / ThermoScientific UltraDry EDS – made available by the CSIR.	110
Figure 19: A typical Tauc's plot of the variation of $\alpha h\nu^2$ with excitation energy $h\nu$ for a TiO ₂ film, in order to identify direct transitions [283]. The straight line extrapolation of the linear region of the plot, yields the band gap energy E_g at the intersection with the $h\nu$ axis.	113
Figure 27: The UV-vis instrumentation – Perkin-Elmer LAMBDA 750S – made available by the CSIR.	114
Figure 20: Typical experimental setup for PL measurements [289].	117
Figure 28: The UV-vis instrumentation – Perkin-Elmer LS 55 Fluorescence Spectrometer – made available by the CSIR.	118
Figure 21: Electrode configurations [121].	119
Figure 22: Typical response-curve of a gas sensor [124].	123
Figure 29: Gas sensor testing system by Kenosistec [291].	123
Figure 30: The XRD diffractograms of the various TiO ₂ species, namely, (a) Pure (undoped) –TiO ₂ , (b) Ag\TiO ₂ , (c) Cu\TiO ₂ and (d) Ag+Cu\TiO ₂ . In the pattern for	

each species, and the samples annealed at 1100°C, 900°C, 600°C, 300°C, 100°C (drying), are arranged from top to bottom respectively. 130

Figure 31: Phase identification results for the undoped -TiO_2 annealed at 600°C, as carried out on the Match! 2 program. The vertical lines represent the COD #96-901-5930 anatase titania 2θ peak positions and their relative intensities (given by the height of the lines). The Miller indices for each peak are displayed near the top of each line. 132

Figure 32: Phase identification results for the undoped -TiO_2 annealed at 900°C, as carried out on the Match! 2 program. The vertical lines represent the COD 96-900-7532 rutile titania 2θ peak positions and their relative intensities (given by the height of the lines). The Miller indices for each peak is displayed near the top of each line. 133

Figure 33: The extraneous peaks of silver (COD #96-900-8460) at 38.11° (111), 44.30° (200), 64.44° (202), 77.4° (311), 81.54° (222) identified in the XRD patterns of Ag/TiO_2 samples annealed at (a) 900°C and (b) 1100°C. Other peaks belong to the rutile TiO_2 135

Figure 34: The XRD diffractogram of the Cu/TiO_2 sample annealed at 900°C containing the peaks belonging to rutile TiO_2 . The unmarked extraneous peaks at 35.41° (002), 35.50° (111), 38.69° (111), 38.89° (200), 48.66° (202) and 61.46° (113) are identified with CuO (tenorite) – COD entry #96-900-6327..... 136

Figure 35: (a) The AgCl peaks in the Ag+Cu/TiO_2 for the powder dried at 100°C, are found at 2θ and Miller indices of 27.84° (111), 32.25° (200), 46.26° (202), 54.85° (311), 57.52° (222) and 76.79° (402), using COD reference of #96-901-1667. (b) XRD patterns for the Ag+Cu/TiO_2 powder at temperatures 1100°C, 900°C, 600°C 300°C, 100°C (top to bottom) showing the relative amounts of AgCl as it decreases with increasing annealing temperature. AgCl is no longer present at 1100°C. 137

Figure 36: XRD diffractograms of the undoped -TiO_2 species dried at 100°C (bottom), heated at 300°C (middle) and at 600°C (top). The anatase TiO_2 patterns show improved resolution of the peaks as temperature increases. 138

Figure 37: Anatase TiO_2 XRD diffractograms of all the titania species (a) dried at 100°C and (b) heated at 300°C. The patterns for Ag+Cu/TiO_2 , Cu/TiO_2 , Ag/TiO_2 , and -TiO_2 , are arranged from top to bottom respectively. The sharp peaks in the Ag+Cu/TiO_2 (top-most) pattern are due to the presence of AgCl..... 139

Figure 38: The variation of the crystallite size with annealing temperature for the various TiO ₂ species (–TiO ₂ , Ag\TiO ₂ , Cu\TiO ₂ and Ag+Cu\TiO ₂) fitted with 4 th order polynomials.....	141
Figure 39: XRD diffractograms for the undoped –TiO ₂ species samples showing the occurrence of the anatase-to-rutile phase transition between the calcination temperatures of 600°C and 900°C.....	143
Figure 40: XRD diffractograms for the single-doped Cu\TiO ₂ species indicating the commencement of the anatase-to-rutile phase transition between the calcination temperatures of 300°C and 600°C.....	144
Figure 41: XRD diffractograms for the double-doped Ag+Cu\TiO ₂ species indicating the nearly completed anatase-to-rutile phase transition at the calcination temperatures of 600°C.....	144
Figure 42: A depiction of the anatase-to-rutile (blue-to-green or bottom-to-top) phase transition at various calcination temperatures, for the different TiO ₂ species.	145
Figure 43: Brookite peaks in the XRD diffractogram of the ½Ag+Cu\TiO ₂ species..	146
Figure 44: The anatase (A), brookite (B), rutile (R), CuO and AgCl phases present in the XRD diffractogram of the ½Ag+Cu\TiO ₂ species annealed at 600°C.	147
Figure 45: Raman spectra of all sample species at the annealing temperature of (a) 300°C and (b) 900°C. (c) Typical vibrational modes for the anatase and rutile phases. Shown are the Raman spectra for the undoped TiO ₂ at 300°C (anatase) and at 900°C (rutile). (d) Blue-shift for all the sample species annealed at 300°C.	150
Figure 46: Typical SEM micrographs for the microstructural evolution of the titania nanoparticle species as the annealing temperature increased from 100°C to 1100°C.	153
Figure 47: EDS spectra of (a) undoped –TiO ₂ calcined at 300°C (b) Ag\TiO ₂ calcined at 300°C (c) Cu\TiO ₂ calcined at 900°C (d) Ag+Cu\TiO ₂ calcined at 600°C	156
Figure 48: Optical absorption spectra of the TiO ₂ samples annealed at various temperatures (from 100°C to 1100°C) for each of the species (a) undoped –TiO ₂ , (b) Ag\TiO ₂ , (c) Cu\TiO ₂ and (d) Ag+Cu\TiO ₂	160
Figure 49: Plots used in the determination of the band gap for the different electronic transitions in the undoped –TiO ₂ that was annealed at 600°C. Extrapolation of the linear portion of the r = 2 (allowed-indirect transitions) curve is shown.....	162
Figure 50: Optical emission (PL) spectra of the TiO ₂ species (a) –TiO ₂ , (b) Ag\TiO ₂ , (c) Cu\TiO ₂ and (d) Ag+Cu\TiO ₂ , at the various annealing temperatures.	163

Figure 51: Optical emission (PL) spectra of the TiO₂ species: Respectively, (a) and (b) are anatase samples annealed at 100°C and 300°C, (b) samples annealed at 600°C, while (d) and (e) are rutile samples annealed at 900°C and 1100°C 165

Figure 52: Schematic diagram depicting the exciton energy levels between the conduction band and valence band [290]. 166

Figure 53: Baseline shift in the initial and final “gas-out” resistances R_f and R_i. The difference may result in a Fractional Baseline Shift value that is (a) positive, (b) negative or (c) zero. 170

Figure 54: Dynamic response chart for anatase samples exposed to NH₃ gas at room temperature. It features the gas concentration profile plotted on the secondary vertical axis. 171

Figure 55: Sensor characteristics plotted for the double-doped anatase sample. It features Sensitivity on the primary vertical axis, while the Response Time and Recovery Time are on the secondary axis. 171

Figure 56: Dynamic response of prepared gas sensors based on undoped -\TiO₂ nanopowders annealed at 300°C, when exposed to various room-temperature humidity levels (5.4% RH – 86.1% RH). 173

Figure 57: The response-recovery profiles for anatase TiO₂ nanopowders (-\TiO₂, Ag\TiO₂, Cu\TiO₂ and Ag+Cu\TiO₂) annealed at 300°C and exposed to room-temperature humidity of 16.7% RH. 173

Figure 58: Sensor characteristics of the prepared gas sensors based on (a) the undoped -\TiO₂, (b) Ag\TiO₂, (c) Cu\TiO₂ and (d) Ag+Cu\TiO₂. The anatase nanopowders (annealed at 300°C) were exposed to various humidity levels (5.4% RH – 86.1% RH) and measured at room temperature. 174

Figure 59: Dynamic response of prepared gas sensors based on rutile -\TiO₂ nanopowders (annealed at 900°C), when exposed to various room-temperature humidity levels (5.4% RH – 86.1% RH). (a) Undoped -\TiO₂, (b) Ag\TiO₂, (c) Cu\TiO₂ and (d) Ag+Cu\TiO₂. 176

Figure 60: The response-recovery profiles for rutile TiO₂ nanopowders (-\TiO₂, Ag\TiO₂, Cu\TiO₂ and Ag+Cu\TiO₂) annealed at 900°C and exposed to room-temperature humidity of 16.7% RH. 177

Figure 61: Sensor characteristics of the prepared gas sensors based on (a) the undoped -\TiO₂, (b) Ag\TiO₂, (c) Cu\TiO₂ and (d) Ag+Cu\TiO₂. The anatase

nanopowders (annealed at 300°C) were exposed to various humidity levels (5.4% RH – 86.1% RH) and measured at room temperature.....	178
Figure 62: The dynamic responses of prepared gas sensors based on anatase TiO ₂ nanopowders (annealed at 300°C), when exposed to various NH ₃ concentrations at different operating temperatures. (a) Room temperature, (b) 250°C, (c) 300°C and (d) Not available. The programmed gas concentration profile is displayed as steps in continuous lines.....	181
Figure 63: Dynamic response of prepared gas sensors based on anatase TiO ₂ nanopowders (annealed at 300°C), when exposed to various concentrations of NH ₃ at room temperature, 250°C and 300°C. (a) Undoped -\TiO ₂ , (b) Ag\TiO ₂ , (c) Cu\TiO ₂ and (d) Ag+Cu\TiO ₂	182
Figure 64: The dynamic responses of prepared gas sensors based on rutile TiO ₂ nanopowders (annealed at 900°C), when exposed to various NH ₃ concentrations at different room temperatures. (a) Room temperature, (b) 250°C, (c) 300°C and (d) 350°C.....	185
Figure 65: The dynamic response of prepared gas sensors based on rutile TiO ₂ nanopowders (annealed at 900°C), when exposed to various concentrations of NH ₃ at room temperature, 250°C, 300°C and 350°C. (a) Undoped -\TiO ₂ , (b) Ag\TiO ₂ , (c) Cu\TiO ₂ and (d) Ag+Cu\TiO ₂	186
Figure 66: The dynamic responses of prepared gas sensors based on anatase TiO ₂ nanopowders (annealed at 300°C), when exposed to various H ₂ concentrations at different operating temperatures. (a) Room temperature, (b) 250°C, (c) 300°C and (d) Not available.....	191
Figure 67: Dynamic response of prepared gas sensors based on anatase TiO ₂ nanopowders (annealed at 300°C), when exposed to various concentrations of H ₂ at room temperature, 250°C and 300°C. (a) Undoped -\TiO ₂ , (b) Ag\TiO ₂ , (c) Cu\TiO ₂ and (d) Ag+Cu\TiO ₂	191
Figure 68: The dynamic responses of prepared gas sensors based on rutile TiO ₂ nanopowders (annealed at 900°C), when exposed to various H ₂ concentrations at different room temperatures. (a) Room temperature, (b) 250°C, (c) 300°C and (d) 350°C.....	194
Figure 69: The dynamic response of prepared gas sensors based on rutile TiO ₂ nanopowders (annealed at 900°C), when exposed to various concentrations of H ₂ at	

room temperature, 250°C, 300°C and 350°C. (a) Undoped TiO_2 , (b) AgTiO_2 , (c) CuTiO_2 and (d) $\text{Ag}+\text{Cu}\text{TiO}_2$ 195

Figure 70: Acceptor behaviour recorded for Ag-doped samples (AgTiO_2) when exposed to intervening gases (a) NH_3 at 300°C, (b) NH_3 at 350°C, (c) H_2 at 300°C and (c) H_2 at 350°C..... 201

BACKGROUND

1.1 INTRODUCTION

1.1.1 Resent Research

Nanomaterials are receiving a wide attention currently because of their unique physical and chemical properties. Titanium dioxide (TiO_2 or titania) nanomaterials in particular, are of special interest in scientific research and technological applications. Thus, extensive studies of the electric, magnetic, catalytic and electrochemical properties of TiO_2 have been conducted [1] – [2]. Its high surface area contributes to its optical properties and is a key factor in its photocatalytic capability [3].

TiO_2 is known to exist in three major natural crystalline polymorphs or phases namely, rutile, anatase and brookite, of which anatase and brookite are metastable phases at lower temperatures that transform to rutile upon heat treatment. Brookite is rarely studied as it is difficult to synthesise [3]. Other polymorphs, such as orthorhombic TiO_2 II or srilankite, cubic fluorite-type, pyrite-type, monoclinic baddeleyite-type, cotunnite-type, are high-pressure phases that are of little significance in current research and technological applications, have been reported in literature [4].

In general, the various methods used in synthesising crystalline TiO_2 primarily yield the anatase phase [5]. The structure of the resulting nanoparticles is closely related to the preparation method. The sol-gel technique, being simple and of simple equipment requirement, is often used to synthesise an amorphous oxide of titanium which is subsequently transformed into crystalline anatase by heat treatment [6].

Titanium dioxide was first commercial produced in the early 20th century. It has since been found useful in several applications ranging from pigments [7] and sunscreens [8], [9], to paints [10], ointments and toothpaste [11]. From the time the phenomenon of photocatalytic splitting of water on a TiO_2 electrode under ultraviolet (UV) light was discovered (by Fujishima and Honda in 1972) [12], numerous efforts have been devoted to the research of TiO_2 . This has resulted in its applications extending to areas such as photovoltaics, photocatalysis, photochromics, electrochromics and sensors [13] – [14]. Many of these applications, which can be broadly categorised

into “energy” and “environmental”, are not only influenced by the intrinsic properties of the TiO₂ material itself, but also by modifications of the TiO₂ host.

The performance of devices based on TiO₂ largely depends on the size and geometry of the material. Recent research activities in nanotechnology continue to reveal remarkable physical and chemical properties of materials at the nanometre scale. This is because the specific surface area and surface-to-volume ratio increase dramatically as the size of a material decreases [15], [16]. Thus enhancing the interaction between devices and their environment.

With breakthroughs in the preparation, modification, and applications of TiO₂, the material is expected to play a vital role in solving many serious environmental and pollution challenges, as well as in easing the energy crisis through efficient utilisation of solar energy – based on photovoltaic and water-splitting devices [17], [18]. The focus of this research is therefore towards improving the properties of titania nanomaterials in order to further tackle the environmental and energy challenges the world is currently faced with. Here, nanostructured TiO₂ is modified through the incorporation of silver (Ag) and copper (Cu) so as to enhance its performance when used in devices.

One of the major activities in industrial and commercial sectors is the monitoring and control of the environment. Invariably, the quest for successful monitoring and control frequently leads to innovations in the fields of comfort, security, health, environment, and energy savings. Precise real time monitoring and control is required in increasing productivity, maintaining health and safety, and limiting environmental pollution. The major challenge that inhibits significant advances in industrial and environmental monitoring has proved to be the sensor, which is positioned at the interface between the system and the environment being monitored. Since sensors have to be exposed directly to the environment for interaction with the target species, the possibility of corrosion and contamination can seriously interfere with sensor operations involving sensitivity, selectivity and stability. Several research-based efforts are being carried out in order to overcome this obstacle. These include introducing novel sensing materials, using catalysts and promoters, surface modification of the sensing material, special fabrication techniques, optimisation of sensor performance and the use of nanotechnology.

Other approaches involve multi-sensor array systems and data processing methods (FFT and wavelet transform, pattern recognition).

Therefore, based on the critical review of literature, which is presented in Chapter 2, this research will also concentrate on the gas sensing abilities of nanosized TiO₂ that has been modified by doping with Ag and Cu.

1.1.2 Key concepts

Nanotechnology, Nanoparticles, Metal oxide semiconductors, Polymorphs, Chemical synthesis, Doping, Structural and optical characterisation, Gas sensing.

1.2 RESEARCH PROBLEM

1.2.1 Source and Background of the Problem

It is of potential economic importance to understand the conditions that affect the transition from one phase of TiO₂ to another; particularly for high-temperature applications, in which phase transformation may influence the properties and performance of devices. The efficiency of nanosized TiO₂ in applications is greatly influenced by electronic modification techniques such as doping [19]. Several studies [20], [19] – [21] have recently investigated the effect of introducing metal impurities into TiO₂ – via chemical synthesis – on strain, grain size evolution and phase transformation and their consequences on sensing devices. However, no systematic research work was found on the simultaneous doping of titania with the two metals, Ag and Cu. Therefore, this study seeks to improve the current understanding of phase transitions in TiO₂ as well as contribute towards maximising the efficiency of TiO₂-based devices. It provides useful data for technological improvement of sensor devices as well as for the scientific understanding of the role of the dopant materials in all these mechanisms.

1.2.2 Statement of the Research Problem

TiO₂ is the most promising material for applications involving photocatalysis and gas sensing. However, the efficiency of TiO₂ as a photocatalyst is severely limited by its large intrinsic band gap (>3 eV) which restricts its absorption of the solar spectrum to the ultra violet (UV) region only [22], [23]. Attempts at improving the light absorption efficiency include doping of the TiO₂ lattice with transition metal cations, such as V, Cr, Mn, Fe, and Ni [24], [25] – [26] and anionic species, such as N, C, S, and B [27].

The structural differences of the TiO₂ polymorphs (brookite, anatase and rutile phases) also introduce differences in the gas sensing properties of TiO₂-based devices. Optimising the basic parameters that characterise gas sensor performance (sensitivity, selectivity and response time) requires adding suitably chosen type and level of impurities to TiO₂.

Several studies have investigated the effect of electronically modifying TiO₂ by doping it with metal impurities. Actually, Choi *et al.* [24] reported that the absorption edge of metal doped TiO₂ shifted to the visible region of the light spectrum. This was also observed for TiO₂ doped with several transition metals via ion implantation, by Anpo *et al.* [28], [29]. It has also been noted that the simultaneous introduction of two or more atoms into TiO₂ structures can improve photocatalytic activity and other important characteristics [30], [31], as compared with single element doping. However, a thorough understanding of combinational doping with more than one metal element is not well established.

1.3 LITERATURE REVIEW

A large number of studies have been carried out by a variety of researchers in the field of nanotechnology in general, and titania nanomaterials in particular. In this report, a comprehensive literature review is presented in Chapter 2.

1.4 PURPOSE OF THE STUDY

1.4.1 Research Aim

The main aim of this study is to investigate how the structural, optical and gas-sensing properties of TiO₂ nanopowders are affected when Ag and Cu – two metal impurities that are known to enhance the performance of TiO₂-based devices individually – are combined as a dopant for the TiO₂ host.

1.4.2 Hypothesis

Several studies [24] have revealed that the properties of titania nanoparticles can be significantly influenced by the incorporation of metal ion impurities. It is anticipated that the simultaneous introduction of two metal impurities into titania nanostructures will result in improved performance over single-element doping.

1.4.3 Specific Objectives

The specific objectives of the study will be to:

1. Synthesise titania nanoparticles doped with two metals.
2. Understand the parameters that inhibit or promote phase formation in TiO₂.
3. Examine the phase composition through structural characterisation procedures.
4. Investigate the optical properties of double-doped titania nanoparticles.
5. Study the performance of nanosized TiO₂ in gas sensing applications.

1.5 RESEARCH METHODOLOGY

The research paradigm for this study is comprised of three categories:

- i. Synthesis, which involves the preparation of doped and undoped samples,
- ii. Characterisation, in which the synthesised samples are subjected to a variety of analytical techniques, and
- iii. Application. Here the samples are tested for their suitability in gas sensing applications.

A detailed methodology of this research is presented in Chapter 3.

1.6 SIGNIFICANCE OF PROPOSED RESEARCH

Increasing energy demand and environmental concerns have brought about a pressing need for solutions to sustainable and clean energy. TiO_2 offers much hope in helping to solve the challenges faced by our world through efficient and effective applications in energy (photovoltaics, photochromics, electrochromics, water-splitting and hydrogen storage) and in environment (photocatalysis and sensing).

As titania nanomaterials continue to play an important part in the protection of the environment and in the pursuit of clean and renewable energy technologies, the present study will illustrate the fundamentals and the working principles of nanosized TiO_2 -based devices, so as to enable the understanding and further development of current and practical titania nanotechnology.

An advanced understanding of the parameters that determine phase formation is crucial for the successful technological application of nanomaterials. With this work, insights will be gained into phase formation mechanisms. This will further enhance the understanding of the structural, thermal, electronic, and optical properties of titania nanomaterials and promote on-going interest in TiO_2 -based research and technological applications.

1.7 SCOPE, LIMITATIONS AND DELIMITATIONS OF THE STUDY

The scope of this study is mainly limited by available resources which include equipment, funds and greatest of all, time. This research focuses on the comparative study of the properties of titania nanoparticles that have been doped with Ag and Cu singly in relation to combinational doping of the material with the two dopants simultaneously. The preparation route is via the sol-gel synthesis and the purity of precursor materials is limited to what is commercially available. Other synthetic methods are not expected to lead to any substantially different conclusions. However, dopant levels are restricted to 5 % wt. As such, other dopant concentrations are not considered here, even though the possibility of a different outcome at other dopant levels may not be ruled out. Combining other metal impurities (aside from Ag and Cu), that have also been found to independently improve the properties of titania, will be the subject of future investigations.

Calcination temperatures are chosen so as to indicate ranges at which the phase transformation of TiO_2 occurred. Clearly, exact phase transformation temperatures are not desired here. Thus the titania data reported in the current research represents more of a qualitative comparative study, rather than quantitative. The main attention is given to establishing whether double-doping of titania with metal impurities has improved properties and performance over single doping. The preliminary findings in this investigation suggested that the standard characterisation techniques employed are sufficient for studying the structural and optical properties. Exotic characterisation techniques are therefore deemed unnecessary at this stage.

The suitability of the titania species in gas sensing applications is also looked into. The focus again is on identifying whether the efficiency of double-doped TiO_2 will prevail over the single-doped nanomaterials in this respect. The performance of triple-doped (more than two dopant impurities) TiO_2 nanoparticles will be the subject of another study.

1.8 DISSERTATION OUTLINE

This section (Chapter 1), which attempts to present a background to the current study, is followed by an extensive review of the fundamental working principles and the “state-of-the-art” of titania as a novel nanomaterial. With this (Chapter 2), an understanding of the current and practical TiO₂ nanotechnology may be facilitated.

Chapter 3 describes the experimental and analytical procedures that were used in this research. The two chapters that follow (Chapters 4 and 5) discuss the structural, thermal, electronic, and optical properties of single-doped nanosized TiO₂ in relation to the double-doped species. Chapter 6 is essentially concerned with the gas-sensing properties of the modified titania nanopowders.

Concluding remarks can be found in Chapter 7 while supplemental information pertaining to the study is featured as appendices at the end of the dissertation.

FUNDAMENTALS
&
LITERATURE REVIEW

2.1 INTRODUCTION

The commercial production of titania began in the early twentieth century. Being inert, of low cost and chemically stable under irradiation, the material has since found a variety of uses in many areas [12]. These include sunscreens (as UV absorbers) [32], paints (as whiteners) [33], ointments, toothpaste [11], and even additives in food. TiO_2 has also been utilised in the photodegradation of pesticides [34] and carcinogenic dyes [35], as well as sterilisation against bacteria [36]. In synthesis, aside from its use in oxidising alcohols to their corresponding carbonyl derivatives, low yields of dihydropyrazines, piperazines, and quinoxalines have been manufactured [12].

The remarkable efforts put into nanostructured TiO_2 materials over the past decades, has led to a wealth of information regarding their synthesis, properties, modifications, and applications. Advances in the synthesis and modifications of titania nanomaterials brings about novel properties and fresh applications with improved efficiency. The breakthroughs include new findings in the synthesis of titania nanotubes, nanorods, nanowires, as well as photonic and mesoporous structures. Aside from the well-recognised quantum-confinement effect, the new nanomaterials reveal the dependence of size, shape and structure on the optical, electronic, thermal and structural properties of TiO_2 [12].

In addition to photocatalytic and photovoltaic applications, titania nanomaterials have also found extensive use in new applications such as electrochromics, sensing, and hydrogen storage. This steady development will continue to play an important part in the search for clean and renewable energy technologies as well as in the protection of the environment [12].

TiO_2 is known to exist in three common phases, namely anatase, brookite and rutile. As a bulk material, rutile is the stable phase; however, solution-phase preparation methods for TiO_2 , such as sol-gel, generally favour the anatase structure [37] – [38]. Coronado *et al.* [39] reported on the synthesis of phase-pure titania nanoparticles in anatase, rutile and brookite structures, using amorphous TiO_2 as a common starting material. They proposed that anatase formation is dominated by surface energy effects, and that rutile and brookite formation follows a dissolution-precipitation mechanism that depended on the reactant chemistry [12].

Transformation from one TiO₂ phase to another has been studied from the point of view of both scientific interest and technological applications [1], [3] – [5], [40], [39] – [41]. Many attempts have been made in order to understand and control anatase-rutile transitions, since this is one of the most critical factors in determining the properties of the material [42].

Hu *et al.* [42] ascribed the enhancement of anatase-rutile transformation in the powders with low synthesised pH value to the presence of the brookite phase. Bakardjieva *et al.* [43] studied the TiO₂ powders with varying compositions of brookite, anatase and rutile obtained by carefully controlling the treatment temperature of brookite powder. They reported that in a three phase mixture of TiO₂ brookite transforms to rutile via anatase. The transformation sequence among the three TiO₂ polymorphs is found to be dependent on grain size by Zhang and Banfield [41]. Their results highlighted extremely important size-dependent behaviour that may be expected in other nanocrystalline systems where multiple polymorphs are possible, thus providing a basis for understanding such phenomena.

2.2 RESEARCH IN NANOTECHNOLOGY

“Nano” (Greek word for dwarf) refers to a reduction in size or time by a factor of 10⁻⁹. Nanotechnology is generally concerned with the design, fabrication and application of materials and systems on the nanometre scale. These structures and components exhibit unique and significantly improved physical, chemical and biological properties, phenomena and processes over their bulk counterparts. Research in nanotechnology aims at exploiting the properties at the nanoscale by acquiring an understanding of structures and devices at atomic and molecular levels, as well as learning how to efficiently manufacture and use these devices.

Before the emergence of nanotechnology, studies in the nanometre scale have been going on for a long time. These include biological systems and the engineering of many materials such as colloidal dispersions, metallic quantum dots, and catalysts. Miniaturisation of systems, such as integrated circuits (ICs), fibre optics, micro-optics, and microelectromechanical systems (MEMS), has brought about advances

in electronic, optical, and mechanical technologies. Devices are becoming smaller and more cost-effective.

Nanotechnology research has been further fuelled by the discovery of synthetic materials such as carbon fullerenes [44], carbon nanotubes [45], and ordered mesoporous materials [46]. Recent developments in the characterisation and control techniques of nanostructured materials have also stepped up the advancement of nanotechnology and have made it a compelling undertaking from the standpoint of science, industry, business and even politics.

Nanotechnology facilitates the creation of functional materials, devices and systems by manipulating matter at the atomic and molecular scales and to exploit novel properties and phenomena [47]. In particular, it offers a unique advantage to the sensor industry by controlling materials at the molecular level, where sensing events occur. In literature, numerous nanostructured materials have been reported to be functional as highly sensitive sensors for chemical and biological species [48]. The higher percentage of active surface atoms in nanostructured materials enables the detection of molecular events more effectively and maximises sensor output signal in comparison with polycrystalline material based thin film devices [47]. The larger surface area offered by these materials greatly increases the number of binding sites for the detection of a specific analyte. Further, each crystallite of a semiconducting metal oxide has an electron depleted surface layer of the depth of the Debye length (λ_D) which is modulated by the reactions with the gas species. Generally, the whole crystallite is depleted of electrons if the diameter of the crystallite is comparable to twice λ_D , thus resulting in high sensitivity towards gas species [49]. Nanotechnology thus offer devices with greater sensitivity and reliability than conventional semiconductor, electro-chemical and optical sensors [50]. However, there are challenges encountered by sensor manufacturers in exploiting the advantages of nanomaterials. These include the difficulties in manufacturing nanostructures, controlling their behaviour from the nano to the macro scale, reading reliable responses and compensating for small signal drifts [47].

2.3 SCIENTIFIC REVIEWS ON NANOSTRUCTURED TITANIUM DIOXIDE

A number of scientific reviews [4], [12], [40], [51], [52] have provided general overviews of the present state in the field of titania nanomaterials. These articles expose the various aspects of synthesis, properties, modifications and applications of TiO₂. Various preparation methods of doped-TiO₂ with metallic and non-metallic species, including various types of dopants and doping methods currently available were examined [51]. The mechanism of heterogeneous photocatalysis in the presence of TiO₂ was also discussed. In their review of anatase to rutile phase transformation, Hanaor and Sorrell [4] discussed its thermodynamics and further provided a comprehensive analysis of the reported effects of dopants on the transformation, as well as the mechanisms by which these effects are brought about. Nie *et al.* [40] compiled recent investigations on the effect of doping on the optical properties of titania polymorphs by comparing the undoped polymorphs of TiO₂. The results were also tabulated and discussed in the context of doping by elements of the same chemical group. The authors interpreted the effects of doping on the photocatalytic activity and band gap reduction with reference to a simple qualitative picture of the electronic structure of titania, which is supported with first-principles calculations. A number of synthesis methods, as well as a discussion on the applications of nano-TiO₂ in medical, environmental, sensor and photocatalytic fields have been reviewed [52].

2.4 NANOPARTICLES AND NANOPOWDERS

Nanosized materials (materials whose dimensions lie between those of the atom, or molecule, and those of their bulk materials) are receiving growing attention for various applications and in research. With regards to size, these materials have at least one dimension between 1 nm and 100 nm, and can be classified as zero dimensional (quantum dots), one-dimensional (nanowires, nanobelts) and two dimensional (films). Of these, the main focus of intensive research for nanoscale device applications are one dimensional (1-D) nanostructures such as wires, rods, belts, tubes, and fibres [50]. A critical aspect of nanotechnology is the synthesis of materials with the desired size, morphology, crystal structure and orientation, and

chemical composition. Nanosized materials are essentially a bridge between bulk materials and atomic (or molecular) structures. For bulk materials (sized larger than one micron) the proportion of atoms at the surface is insignificant in comparison to the number of atoms within the bulk of the material. As a result, the physical properties of bulk materials are largely independent of size.

Nanoparticles can be found in the form of powders, thin films, suspensions, and they generally exhibit distinctive properties as compared with their bulk counterparts. The remarkable properties of nanoparticles are mainly due to the large surface area of the material, which dominates the small contributions made by the bulk of the material. Thus, size-dependent behaviours are often observed for nanosized materials as the percentage of atoms at the surface of a material becomes significant. The small size of nanoparticles often result in electron confinement and other quantum effects that leads to unanticipated optical properties [53]. For example, the absorption of solar radiation is much higher in materials composed of nanoparticles than it is in sheets of the bulk material. Thus, in solar applications, it is possible to control solar absorption by controlling the size, shape, and material used [54] – [55]. Other size-dependent property changes include quantum confinement in semiconductor particles, surface plasmon resonance [53] in some metal particles and superparamagnetism in magnetic materials. Due to the confinement of the electron wave function, the energy levels of nanoparticles are discrete, whereas in bulk materials they are continuous. The consequence is the size dependency of electronic, optical and magnetic properties.

It is not always desirable to have changes in physical properties of materials. For example, nanosized ferromagnetic materials smaller than 10 nm can switch their magnetisation direction using room temperature thermal energy, thus making them unsuitable for memory storage [56].

The term “nanopowder” is defined in a variety of ways [57]:

- (1) A solid powder-like substance of artificial origin that may contain a combination of nanoobjects or aggregates of nanoobjects
- (2) An assembly of nanoparticles
- (3) A powder, all particles of which are smaller than 100 nm.

Nanoscale grains are contained, to a certain extent, in most submicron powders, but their content is usually very insignificant. The presence of these nanodispersed particles does not mean that the entire volume of such powders may be referred to as “nanopowders”. In certain types of nanopowders, submicron agglomerates are made up of nanoscale crystallites and/or blocks, but they may break down into separate nanoparticles under certain physical effects (e.g., ultrasonic disintegration, mechanical activation, etc.) [57].

Nanopowders are characterised by [57]:

- the mean size of particles and size distribution of particles
- the mean size of crystallites and size distribution of crystallites
- the rate of agglomeration of particles (in case of weak agglomeration, particles hold together due to Van der Waals type of interactions, while strong aggregation is characterised by strong bonding of particles)
- the specific area of the surface
- the chemical composition of a bulk of particles
- the sectional composition for core-shell particles
- the morphology of particles
- the chemical composition of the surface
- the crystalline structure of nanoparticles
- the content of moisture and other adsorbates
- looseness (flow properties)
- the packed density
- colour.

As a main focus for many recent research efforts, significant progress has been achieved in the control of the particle size and degree of aggregation during the production of nanopowders.

2.5 PROPERTIES OF NANOSTRUCTURED TITANIA

2.5.1 Structural Properties of Nanosized Titania

The unit cell structures of the anatase and rutile TiO_2 polymorphs, shown in Figure 1, can be described in terms of chains of TiO_6 octahedra. Here, an octahedron of six O^{2-} ions surrounds each Ti^{4+} ion.

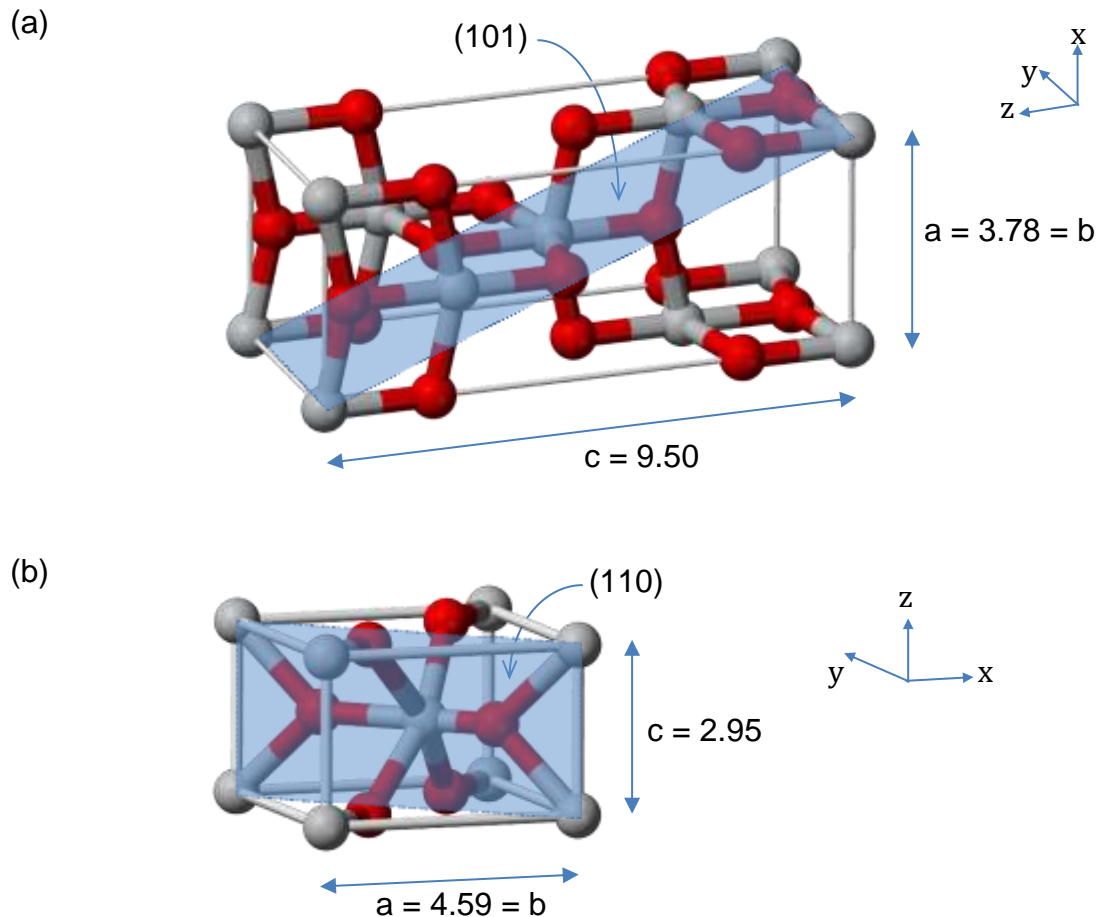


Figure 1. Primitive tetragonal unit cell of (a) anatase TiO_2 and (b) rutile TiO_2 . Oxygen and titanium atoms are coloured red and grey respectively. Anatase (101) and rutile (110) surface planes are shaded. The x , y and z axes correspond to the $[100]$, $[010]$ and $[001]$ directions respectively. Lattice constants are indicated in Å.

The two forms of TiO_2 exhibit different mass densities and electronic band structures as a result of the differences in their lattice structures. This follows from the distortion of each octahedron and the assembly pattern of the octahedra chains. The rutile octahedron shows a slight orthorhombic distortion whereas the distortion in the anatase octahedron is significant, such that its symmetry is lower than orthorhombic.

The Ti-O distances in anatase are shorter, while the Ti-Ti distances are larger than those in rutile. Further, in the rutile structure, there are 10 neighbouring octahedrons in contact with each octahedron – two sharing edge oxygen pairs and eight sharing corner oxygen atoms. However, in the anatase structure, each octahedron is in contact with eight neighbours – four sharing an edge and four sharing a corner.

In their investigations using K-edge XANES, Chen *et al.* [58] observed severe distortions in Ti site environments in the structures of 1.9 nm titania nanoparticles compared to those octahedral Ti sites in bulk anatase titania. As a result of the truncation of the lattice, the distorted Ti sites were presumed to have a pentacoordinate square pyramidal geometry. Distortions in the TiO₂ lattice were found to be mainly located on the surface of the nanoparticles and they accounted for binding with other small molecules.

Based on a surface photovoltage spectroscopy study, Qian *et al.* [59] found that the details of the preparation methods may influence the density of the surface states on titania nanoparticles. The nanoparticles of TiO₂ prepared from acidic sol were found to have fewer surface states as compared with those prepared from basic sol.

A number of theoretical studies have looked into the crystal structures of the polymorphs of TiO₂ as well. With a combination of simulated heat treatment, Monte Carlo basin hopping simulation, and genetic algorithms methods, Hamad *et al.* [60] performed a theoretical calculations on Ti_nO_{2n} clusters ($n = 1, 2, \dots, 15$). They concluded that the calculated global minima consisted of compact structures, with Ti atoms rapidly reaching high coordination with increasing n . For $n > 10$, the particles were found to have at least a central octahedron surrounded by a shell of surface tetrahedra, trigonal bipyramids, and square base pyramids.

Swamy *et al.* [61] examined the metastability of anatase titania as a function of pressure and found that it was size dependent – with smaller crystallites preserving the structure even at higher pressures. The three size categories that were recognised for the pressure-induced phase transition of anatase at room temperature were (a) an anatase amorphous transition regime at the smallest crystallite sizes, (b) an anatase-baddeleyite transition regime at intermediate crystallite sizes, and (c) an anatase- α -PbO₂ transition regime made up of large nanocrystals to macroscopic single crystals [61].

A series of theoretical studies on the phase stability of titania nanoparticles in different environments were carried out by Barnard *et al.* [62] – [63] using a thermodynamic model. Their results showed that surface passivation had a significant influence on the morphology and phase stability of the nanocrystals. They also revealed that surface hydrogenation induced significant changes in the shape of rutile nanocrystals, but not in anatase. When the undercoordinated surface Ti atoms were H-terminated, the size at which the phase transition is expected showed a sharp increase. The crossover point was about 2.6 nm for spherical particles, below which the anatase phase was more stable than the rutile phase [64]. Their study on titania nanoparticles, in vacuum and water environments, revealed that the phase transition size in vacuum (9.6 nm) was smaller than that under water (15.1 nm) [65]. On their estimates on the transition enthalpy of nanocrystalline anatase and rutile, thermochemical results were found to vary as a function of shape, size, and degree of surface passivation [66]. They studied TiO₂ polymorphs passivated with complete monolayers of adsorbates by varying the ratio of hydrogen to oxygen with respect to a neutral, water-terminated surface. Here, the water termination resulted in the lowest values of surface free energy consistently, when with a higher fraction of H on the surface on both anatase and rutile surfaces or when hydrated. On the other hand, the surfaces generally had a higher surface free energy when they were O-terminated or when they had an equal ratio of H and O in the adsorbates [63]. They also established that the phase transition size of a titania nanoparticle varied from 6.9 to 22.7 nm, under different pH conditions from acid to basic. This was accompanied with shape changes of the titania nanoparticles (Figure 2) [62].

Using the density-functional-based tight binding method (DFTB), a theoretical investigation on the structural stability of TiO₂ layer modifications (anatase and lepidocrocite) was conducted by Enyashin and Seifert [67]. They established that the most stable modifications were anatase nanotubes, in a comparison to single walled nanotubes, nanostrips and nanorolls. With the energies of each of the titania nanostructures relative to the infinite monolayer followed an inverse square $1/r^2$ curve thus indicating that their stability increased as their radii grew.

TiO ₂ Surfaces	← More acidic		Neutral	More basic →	
	Hydrogenated surfaces	Hydrogen-rich surface adsorbates	Hydrated surfaces	Hydrogen-poor adsorbates	Oxygenated surfaces
Anatase					
Rutile					

Figure 2: Predicted morphology for anatase and rutile TiO₂ under different pH conditions from acid to basic [62].

2.5.2 Thermodynamic Properties of Nanosized Titania

The metastable anatase and brookite polymorphs of TiO₂ are commonly realised in nanoscaled natural and synthetic samples. Rutile, on the other hand, is the stable phase that is established at high temperatures. Upon heat treatment, the observed phase transitions (which are accompanied by coarsening) are as follows [12]:

- a. Anatase → brookite → rutile
- b. Brookite → anatase → rutile
- c. Anatase → rutile, and
- d. Brookite → rutile.

These transformation sequences are evident of the very closely balanced energetics as a function of particle size. The three polymorphs have sufficiently different surface enthalpies such that crossover in thermodynamic stability may occur under non-coarsening conditions, with anatase and/or brookite stable at small particle size [41], [68]. Irregular behaviours and inconsistent results are however sometimes observed.

As the work by Hwu *et al.* [69] revealed, the crystal structure of nanosized TiO₂ depend largely on the method of preparation. For titania nanoparticles smaller than 50 nm, anatase appeared to be more stable and transformed to rutile at temperatures greater than 700°C. Anatase and/or brookite structures prepared by Banfield *et al.* [68], [70] were found to transform to rutile after reaching a certain particle size. Upon formation, rutile grew much faster than anatase and became more stable for particle size greater than 14 nm.

Below the temperature of 780°C, Ye *et al.* [71] observed a slow transition from brookite to anatase phase, along with grain growth, but a rapid brookite to anatase and anatase to rutile transformations between this temperature and up to 850°C, beyond which a rapid grain growth of rutile was dominant. They concluded that brookite to rutile transformation is not direct but via an anatase intermediate step. However, direct transition of brookite nanocrystals to rutile was observed above 700°C by Kominami *et al.* [72].

In a later study on the phase transformation behaviour of nanocrystalline aggregates during their growth for isothermal and isochronal reactions, Zhang and Banfield [41] found that the thermodynamic phase stability and the transformation sequence depended on the initial particle sizes of anatase and brookite. They arrived at the conclusion that, for equally sized nanoparticles, anatase was thermodynamically stable for sizes smaller than 11 nm, brookite was stable from this size up to 35 nm, and rutile was stable for sizes greater than 35 nm.

The investigation of the energetics of titania polymorphs by high-temperature oxide melt drop solution calorimetry was carried out by Ranade *et al.* [73]. They found that the energetic stability crossed over between the three phases. Brookite was found to be energetically stable for surface areas between 7 m²/g and 40 m²/g, and particle sizes between 200 nm down to 40 nm, rutile being below these ranges and anatase above. The crossover for anatase and rutile energetics took place at 18 m²g⁻¹ (66 nm). By assuming spherical particles, average diameters of 201 nm and 206 nm were calculated for rutile and brookite for a 7 m²g⁻¹ surface area. For a 40 m²g⁻¹ surface area the diameters of brookite and anatase are 36 nm and 39 nm. These differences in particle size as well as surface area are believed to result from density differences. If no further coarsening takes place during the phase transformation, the particle size should be smaller thereafter. In a thermodynamic sense, Gibbs free energy ($\Delta G = \Delta H - T\Delta S$), rather than the enthalpy, governs the phase stability. Anatase and rutile titania have the same entropy. As a result, the $T\Delta S$ will not upset the sequence of stability seen from the enthalpies significantly. Nanocrystalline brookite TiO₂, formed initially with a surface area greater than 40 m²g⁻¹, was found to be metastable with respect to both anatase and rutile, and the brookite → anatase → rutile sequence during coarsening was energetically effortless. On the other hand, if anatase was formed initially, upon coarsening it could transform first to brookite (at

40 m²g⁻¹) and then to rutile. The energetic force that drives the latter reaction (brookite → rutile) was considered to be very small, thus accounting for the natural persistence of coarse brookite. In contrast, a much larger driving force may explain the absence of coarse-grained anatase in its transformation to rutile [73].

Li *et al.* [74] established that only anatase to rutile phase transition occurred in the temperature range of 700°C – 800°C. The particle sizes of these two polymorphs increased with the increasing temperature, but with rutile having a much higher growth rate than anatase. The growth rate of anatase flattened off at 800°C. Upon nucleation, rutile particles grew rapidly, whereas for anatase, the particle size remained practically unaffected. It was observed that as the initial particle size decreased, so did the onset transition temperature. Also lattice compression of anatase was found to increase with temperature. But samples with smaller particle size showed larger distortions. For particles with sizes 23 nm, 17 nm and 12 nm they obtained activation energy values of 299 kJ/mol, 236 kJ/mol and 180 kJ/mol respectively. They attributed the decrease in thermal stability of finer nanoparticles as largely due to the reduction in the activation energy with increasing stress energy and size-related surface enthalpy.

2.5.3 X-ray Diffraction Properties of Nanosized Titania

The determination of crystallinity and the crystal structure of nanomaterials are frequently carried out with XRD. The Scherrer equation, $\tau_{(hkl)} = \frac{K\lambda}{\beta_{(hkl)} \cos \theta}$, is often used in estimating the mean size $\tau_{(hkl)}$ of the ordered crystallite domains from $\beta_{(hkl)}$, the XRD line broadening at half the maximum intensity (or the full-width-at-half-maximum, FWHM) in radians [75]. Here, hkl are the miller indices associated with a particular planar reflection from within the crystal unit cell. θ is the Bragg angle and λ , the X-ray wavelength, which is about 1.540598 Å for the Cu K α radiation. The shape parameter (or roundness factor) K assumes a value of 0.9 for spherically shaped nanoparticles [76], [77].

The crystallite size of nanomaterials is inversely related to the FWHM of an individual peak, so that the narrower the peak, the larger the crystallite size. As is normally the case for nanomaterial systems, the peaks are broader for crystals that are randomly arranged or have low degrees of periodicity. High periodicity of the individual crystallite domains reinforces the diffraction of the X-ray beam, resulting in a tall narrow peak.

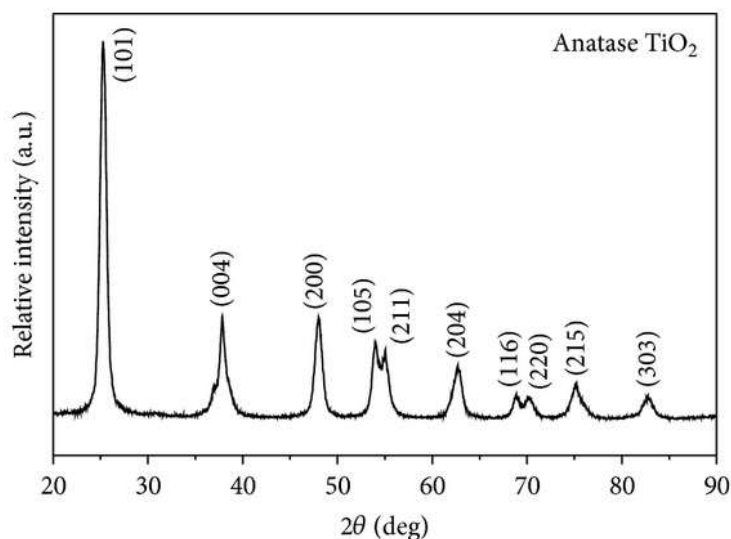


Figure 3: Typical XRD pattern of anatase TiO₂ nanoparticles.

Figure 3 shows a typical XRD pattern for the anatase titania nanoparticles, while the most prominent characteristic peaks are identified in Table 1 for the three main polymorphs of titania – anatase, brookite and rutile. For differently sized nanoparticles [78] and titania nanorods of different lengths [79], the diffraction peaks became narrower with increasing size of the nanoparticle. Zhang *et al.* [79] developed anatase nanoparticle and nanorods with diameters around 2.3 nm. Elongations of the nanorods were observed along the [001] direction (with preferred anisotropic growth along the *c*-axis of the anatase lattice). This was indicated by the narrow width and strong peak intensity of the (004) reflection, as well as broader width and relatively lower intensity for the other reflections. The (004) diffraction peak became much stronger and sharper as the length of the nanorods increased, whereas other peaks remained the same in shape and intensity. Other groups displayed similar results [80] – [81].

Table 1: Characteristic anatase, brookite and rutile XRD peak positions (2θ), featuring their relative intensities and miller indices. The values are from Cu-target diffractometers with a wavelength $\lambda = 1.540598 \text{ \AA}$. Corresponding d-spacing are also displayed, alongside the cell parameter and space group values.

Poly morph	2θ ($^\circ$)	Relative Intensity (%)	d- Spacing (\AA)	Miller Indices			Cell Parameters (\AA)				Space Group
				h	k	l	a	b	c	$\alpha = \beta = \gamma$	
Anatase	25.71	100.00	3.4655	1	0	1	3.730	3.730	9.370	90.00	I4 ₁ /amd
	38.43	15.15	2.3425	0	0	4					
	39.20	7.85	2.2983	1	1	2					
	48.83	25.00	1.8650	2	0	0					
	54.82	16.04	1.6745	1	0	5					
	55.99	16.14	1.6423	2	1	1					
	63.79	9.81	1.4591	2	0	4					
	70.02	6.87	1.3438	1	1	6					
	71.55	5.56	1.3188	2	2	0					
	76.45	8.63	1.2460	2	1	5					
Brookite	25.37	100.00	3.5109	2	1	0	9.184	5.447	5.145	90.00	Pbca
	25.72	77.62	3.4640	1	1	1					
	30.83	97.22	2.9000	2	1	1					
	36.26	23.86	2.4772	1	0	2					
	37.36	17.71	2.4071	0	2	1					
	40.18	14.94	2.2443	2	0	2					
	42.40	15.44	2.1319	2	2	1					
	46.09	19.97	1.9695	3	0	2					
	48.09	32.24	1.8922	3	2	1					
	49.19	20.20	1.8521	3	1	2					
Rutile	27.50	100.00	3.2435	1	1	0	4.587	4.587	2.954	90.00	P4 ₂ /mnm
	36.17	46.72	2.4836	1	0	1					
	39.28	7.11	2.2935	2	0	0					
	41.34	18.28	2.1840	1	1	1					
	44.15	6.45	2.0514	2	1	0					
	54.46	57.99	1.6849	2	1	1					
	56.77	17.32	1.6217	2	2	0					
	62.93	8.18	1.4770	0	0	2					
	64.21	8.66	1.4505	3	1	0					
	69.18	20.83	1.3579	3	0	1					

2.5.4 Raman Vibration Properties of Nanosized Titania

As the size of titania nanomaterials decreases, the featured Raman scattering peaks become broader [82], [83]. The size effect on the Raman scattering in nanocrystalline TiO₂ is interpreted as arising from phonon confinement [61], [84] – [85], nonstoichiometry [86], [87], or internal stress/surface tension effects [88]. Among these schemes, the three-dimensional confinement of phonons in nanocrystals is the most convincing [61], [84] – [85], [89]. The phonon confinement model, also referred to as the momentum (\mathbf{q}) vector relaxation model or spatial correlation model, relates the \mathbf{q} vector selection rule for the excitation of Raman active optical phonons with long-range order and crystallite size [61], [90]. In a perfect “infinite” crystal, conservation of phonon momentum requires that only optic phonons near the Brillouin zone (BZ) centre ($\mathbf{q} \approx 0$) are involved in first-order Raman scattering. In an amorphous material lacking long-range order, the \mathbf{q} vector selection rule breaks down and the Raman spectrum bears a resemblance to the phonon density of states. The strict “infinite” crystal selection rule for nanocrystals is replaced by a relaxed version which results in a range of accessible \mathbf{q} vectors (as large as $\Delta\mathbf{q} \approx 1/L$ (L diameter)) as a consequence of the uncertainty principle [12].

Of the 6 six Raman-active fundamentals in the anatase TiO₂ vibrational spectrum (Figure 4), three E_g modes (designated as E_{g(1)}, E_{g(2)}, and E_{g(3)}) are centered around 144, 197, and 639 cm⁻¹ respectively. Two B_{1g} modes (labelled B_{1g(1)} and B_{1g(2d)}) are at 399 and 519 cm⁻¹, and an A_{1g} mode is at 513 cm⁻¹. As the particle size decreases, the Raman peaks display increased broadening and systematic frequency shifts [61]. The most intense E_{g(1)} mode shows significant broadening and maximum blue shift as the crystallite size decreases. Both the E_{g(2)} and B_{1g(1)} modes display small blue shifts, with the latter being much smaller. The B_{1g(2)}+A_{1g} (which represents a combined effect of two individual modes) exhibits a red shift. Increased broadening and reduced crystallite size are clearly observed for the A_{1g} and B_{1g} modes, even though their frequency shifts are not very pronounced. On the other hand, as the crystallite size decreases, the E_{g(3)} mode displays a red shift with significant broadening.

Choi *et al.* [91] reported a volume contraction effect for anatase titania nanoparticles, which results from radial pressure increasing with decreasing particle size. They

attributed the broadening and shifts of the Raman bands (with decreasing particle diameter) to the effects of decreasing particle size on the force constants and vibrational amplitudes of the nearest neighbor bonds.

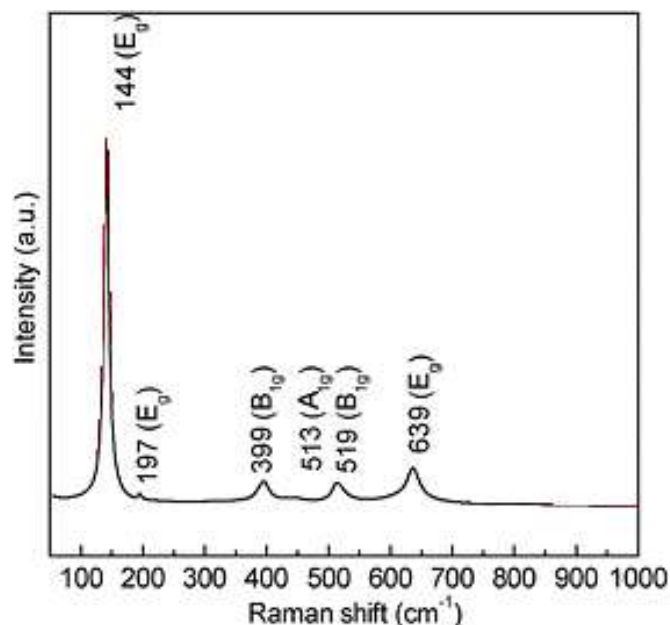


Figure 4: Typical Raman spectra for anatase TiO_2 nanoparticles, featuring peaks at 144 cm^{-1} (corresponding to the $E_{g(1)}$ mode), 197 cm^{-1} (corresponding to the $E_{g(2)}$ mode) and 639 cm^{-1} (corresponding to the $E_{g(3)}$ mode).

2.5.5 Electronic Properties of Nanosized Titania

Asahi *et al.* [92] carried out a detailed investigation of the electronic and optical properties of the anatase TiO_2 structure using first-principles calculations with the full-potential linearised augmented plane-wave method. The calculated band structure, along the high symmetry directions of the BZ is shown in Figure 5. Here, the top of the valence band is taken as the energy zero. They further presented (in Figure 6) the corresponding density of states (DOS) of TiO_2 as being composed of Ti e_g , Ti t_{2g} (d_{yz} , d_{zx} , and d_{xy}), O p_σ (in the Ti_3O cluster plane), and O p_π (out of the Ti_3O cluster plane). The upper valence bands were decomposed into three main sections: (i) The lower energy region in which the σ bonding is mainly due to O p_σ bonding (ii) the middle energy region with the π bonding and (iii) the higher energy region with the non-bonding O p_π states that reside at the top of the valence bands, where hybridisation with d states is insignificant. With weaker contributions from the π

bonding (as compared to the σ bonding) the conduction bands can be separated into Ti e_g (above 5 eV) and t_{2g} (below 5 eV) bands. The d_{xy} states dominate the bottom of the conduction bands (as indicated by the dashed vertical line in Figure 6). The remainder of the t_{2g} bands antibonds with p states, with the main peak mostly constituted by d_{yz} and d_{zx} states.

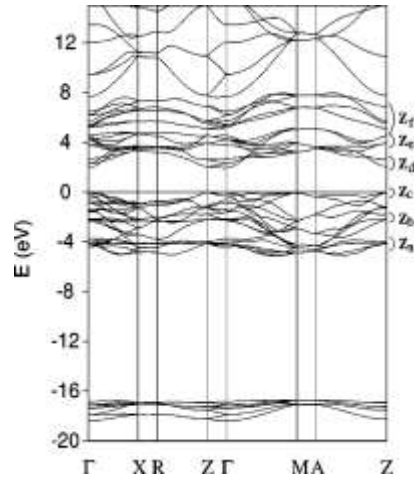


Figure 5: Self-consistent band structure of the anatase TiO_2 structure. The top of the valence band is taken as the zero of energy [93].

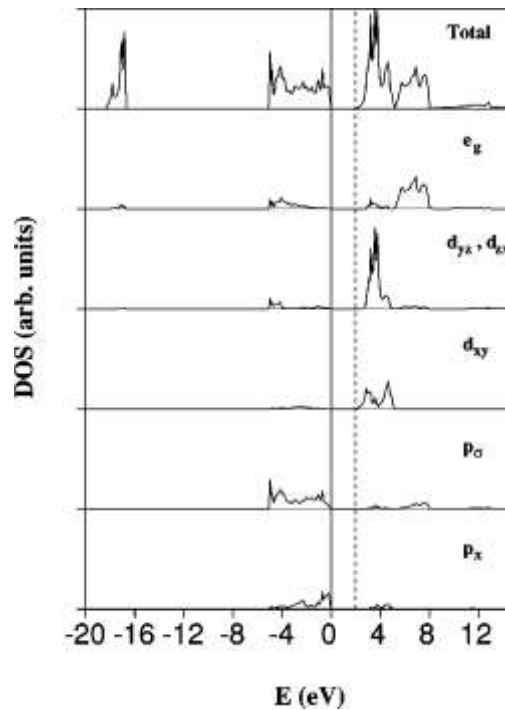


Figure 6: Total and projected densities of states (DOS) of the anatase TiO_2 structure. The vertical solid line represents the top of the valence band (the zero of energy). The vertical dashed line indicates the conduction-band minimum [93].

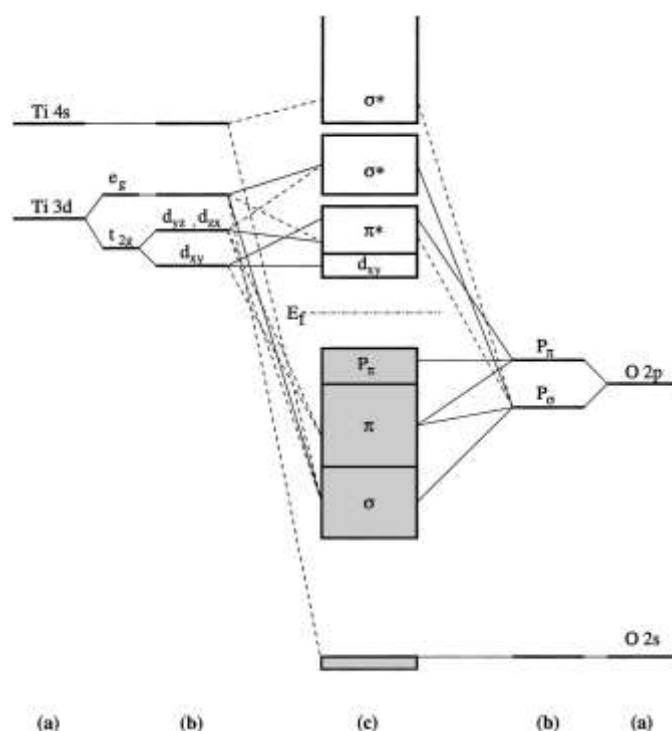


Figure 7: Molecular-orbital bonding for the anatase TiO_2 structure: (a) atomic levels, (b) crystal-field split levels, and (c) final interaction states. The thin-solid and dashed lines represent large and small contributions, respectively [93].

Evident in the non-bonding states near the band gap of Figure 7 (the diagram for molecular-orbital bonding for anatase TiO_2) are the non-bonding O pp orbital (top of the valence bands) and the non-bonding d_{xy} states (bottom of the conduction bands). In rutile TiO_2 , which shows a similar feature but to a lesser extent [93], each octahedron shares corners with eight neighbours and shares edges with two other neighbours, forming a linear chain. Whereas with anatase, a zigzag chain with a screw axis is formed with each octahedron sharing corners with four neighbours and edges with four other neighbours. This accounts for why rutile has a higher density than anatase. Further, with anatase having a large metal-to-metal distance of 5.35 \AA , the t_{2g} orbitals at the bottom of the conduction band in rutile provide the metal-to-metal interaction with a smaller distance of 2.96 \AA while the Ti d_{xy} orbitals at the bottom of the conduction band are quite isolated [93].

A variety of experimental techniques (X-ray photoelectron and X-ray absorption and emission spectroscopies) have been employed in studying the electronic structure of

TiO₂ [69], [94] – [95]. Figure 8 shows a schematic energy level diagram of the lowest unoccupied MOs of a [TiO₆]⁸⁻ cluster with O_h, D_{2h} (rutile), and D_{2d} (anatase) symmetry. The Ti K-edge XANES and O K-edge ELNES spectra for rutile and anatase [94] are shown in Figure 9. In the tetragonally distorted octahedral anatase structure, the elongated octahedral geometry (D_{2d}) features six oxygen atoms surrounding each titanium cation. Both rutile and anatase structures shown further splitting of the 3d levels of Ti³⁺ due to the asymmetric crystals. The Ti K-edge X-ray-absorption near-edge structure (XANES) can be used to directly probe the fine electronic structure of TiO₂. The O K-edge experimental electron-energy-loss near edge structure (ELNES) spectra is displayed in the right panel of Figure 9 [94].

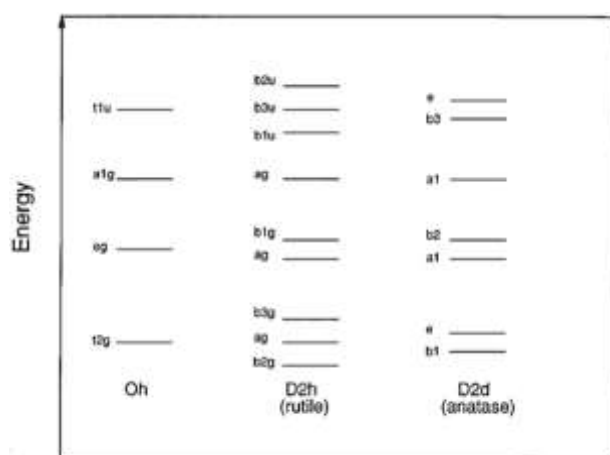


Figure 8: Schematic diagram of the energy levels of the lowest unoccupied MO's of a [TiO₆]⁸⁻ cluster with O_h, D_{2h} (rutile), and D_{2d} (anatase) symmetry [94].

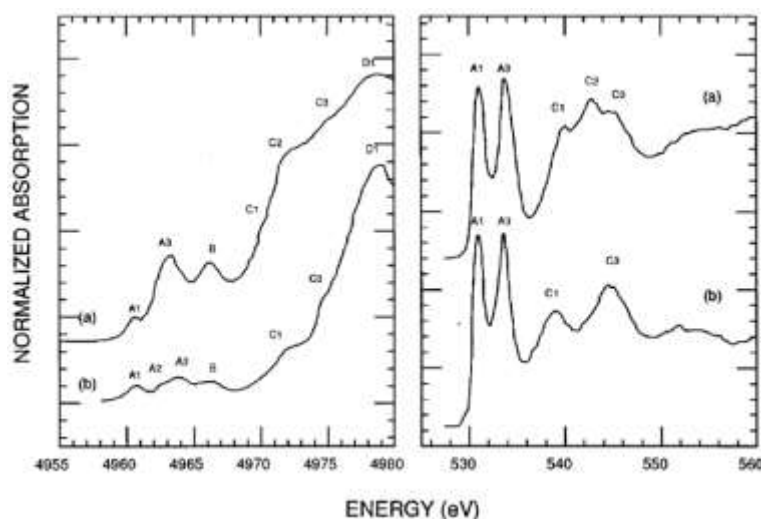


Figure 9: Experimental curves for (a) rutile and (b) anatase TiO₂. The left panel is the Ti K-edge XANES spectra, while O K-edge ELNES spectra is on the right [94].

Hwu *et al.* [69] established that the field splitting of nanocrystal TiO₂ was about 2.1 eV; slightly smaller than that of bulk TiO₂. Also for titania nanoparticles, Luca *et al.* [96] reported the broadening of 1s → np transitions with changes (increase or decrease) in particle size within the postedge region of the X-ray absorption spectroscopy. A clear trend in the X-ray absorption spectroscopy for different sized titania nanoparticles was observed in the study by Choi *et al.* [97] as well.

It is well-known that as nanoparticles decrease in size the band gap energy increases and the energy band becomes more discrete [98] – [99]. As the size of a semiconductor nanoparticle becomes comparable to the de Broglie wavelength of the charge carriers (or falls below the Bohr radius of the first excitation state), the charge carriers begin to behave quantum mechanically such that the charge confinement introduces a series of discrete electronic states [100]. With titania nanomaterials having indirect band gaps, a discrepancy however exists for the critical size below which quantisation effects are observed. The estimated critical diameter depends acutely on the effective masses of the charge carriers [101]. The excitation radii for titania particles were estimated by Kormann *et al.* [98] to be between 7.5 and 19 Å. Here, small band gap blue shifts less than 0.2 eV, attributed to quantum confinement size effects, were observed for spherical titania nanoparticles with sizes as small as 2 nm [102], [103]. Such small effects are attributed mainly to an exciton radius in the range 0.75 – 1.90 nm, and the relatively high effective mass of carriers in TiO₂ [98]. Serpone *et al.* [104], on the other hand, concluded that quantum confinement effects may not be responsible for the blue shifts in the effective band gap of TiO₂ with particle sizes of 21 Å, 133 Å, and 267 Å. The excellent study by Monticone *et al.* [105] found no quantum size effect in anatase titania nanoparticles of sizes $2R \geq 1.5$ nm. However, it did find unusual variation of the oscillator strength of the first allowed direct transition with particle size [105].

2.5.6 Optical Properties of Nanosized Titania

The main mechanism of light absorption in pure semiconductors is generally assumed to be direct interband electron transitions. In indirect semiconductors such

as TiO₂, where the direct electron transitions between the band centres are prohibited by the crystal symmetry, this absorption is particularly very small [12]. Enhancement of light absorption has been observed in small TiO₂ crystallites as a result of indirect electron transitions involving non-conservation momentum at the interface [106]. At rough interfaces, where the relative amount of the interface atoms is larger, this effect is more pronounced. The large dipole matrix element and the large density of states for the electron in the valence band, accounts for the allowed indirect transitions.

Where the proportion of the interface atoms is large enough, considerable improvement in the absorption is anticipated in porous and microcrystalline semiconductors. A rapid increase in the absorption takes place at low photon energies ($h\nu$) where $h\nu < E_g + W_c$, E_g being the gap between valence and conduction bands, and W_c the conduction band width. Electron transitions to any point in the conduction band is probable when $h\nu = E_g + W_c$. Absorption is further enhanced by an increase in the electron density of states in the valence band only. For crystallites that are smaller than 20 nm, the interface absorption becomes the main mechanism of light absorption [106].

Through measurements and calculations, Sato *et al.* [107] showed that titania nanosheets have a larger band gap than the bulk TiO₂, owing to transitions of lower dimensionality (i.e., a 3-D to 2-D). The work revealed that the lower edge of the conduction band for the titania nanosheet was about 0.1 V higher than that of anatase TiO₂, while the upper edge of the valence band was lower by 0.5 V. In addition to size quantisation effect, a strong photoluminescence of well-developed fine structures that extends into the visible light region, were found to be responsible for the blue shift (>1.4 eV) in the absorption of the titania nanosheet colloid, relative to that of bulk TiO₂ crystals (3.0 – 3.2 eV) [108]. The band gap energy shift, ΔE_g , due to exciton confinement in anisotropic two-dimensional crystallites, is formulated as
$$\Delta E_g = \frac{h^2}{8\mu_{xz}} \left(\frac{1}{L_x^2} + \frac{1}{L_z^2} \right) + \frac{h^2}{8\mu_y L_y^2}$$
, where h is Plank's constant, μ_{xz} and μ_y are the reduced effective masses of the excitons, and L_x , L_y , and L_z are the crystallite dimensions parallel and perpendicular with respect to the sheet, respectively. The blue shift is largely controlled by the sheet thickness (as the first term can be ignored). The onset

of a 270 nm peak in the photoluminescence of titania nanosheets was attributed to resonant luminescence. Interband energy levels, introduced by the intrinsic Ti site vacancies, were seen to be responsible for the observed series of peaks extending into a longer wavelength region. The contrasting sharp peaks were also ascribed to the sub-nanometre thickness and its uniformity [108].

In their study of optical absorption and photoluminescence, Bavykin *et al.* [109] found similar optical properties for colloidal titania nanotubes with different internal diameter (between 2.5 nm and 5 nm). This apparent 2D behaviour of titania nanotubes was attributed to the complete smearing of all 1-dimensional effects which resulted from the large effective mass of charge carriers in TiO₂. The energy spectrum of 2D titania nanosheets was expressed as:

$$E_{2D}^{\pm} = \pm \frac{E_g}{2} \pm \frac{\hbar^2 k^2}{2m_{e,h}} \quad 2-1$$

In this effective mass model, the “+” and “-” signs correspond to the conduction and valence bands respectively, m_e and m_h are the effective masses of the electrons and holes, respectively, \hbar is related to Planck’s constant as $\hbar = \frac{h}{2\pi}$ and E_g is the energy gap. By zone-folding, the electronic band structure of a titania nanotube can be obtained from this relation. Different n indices can be used to represent a series of quasi-1D sub-bands, such that $E_{n1D}^{\pm} = \pm \frac{E_g}{2} \pm \frac{\hbar^2}{2m_{e,h}} \left[k_{||}^2 + \left(\frac{2n}{d} \right)^2 \right]$. This transition from the 2D to the quasi-1D energy spectrum has a marked effect on the energy density of states. For the 2D case, the density of states, $G_{2D} = m_{e,h}/\pi\hbar^2$, is constant for energies lying outside the energy gap. The quasi-1D case, however, features van Hove singularities due to diverging density of states of each sub-band, $G_{n,1D}(E) = \pm \left\{ \frac{m_{e,h}}{2\pi^2 \hbar^2 [E - E_n(0)]} \right\}$ at the band edge $E_n(0)$. The density of state results from a series of sharp peaks having long overlapping tails. In the quasi-1D situation, the energy gap between the valence and conduction bands is wider than in the parental 2D material. The difference increases as the diameter of the nanotube decreases. The difference in the energy gaps between a nanosheet and a nanotube is given by $\Delta E_g = E_G^{1D} - E_G^{2D} = \frac{2\hbar^2}{d^2} \left(\frac{1}{m_e} + \frac{1}{m_h} \right)$. In TiO₂, the effective masses of electrons m_e can vary between $5m_0$ and $30m_0$, and the mass of holes m_h is more than $3m_0$.

2.5.7 Photon-Induced Electron & Hole Properties of Nanosized Titania

Absorption in titania nanoparticles involves the excitation of electrons from the valence band into the unoccupied conduction band by impinging photons with energies equal to or higher than its band gap (>3.0 eV). This results in excited electrons in the conduction band and positive holes in the valence band. The charge carriers can either recombine radiatively or nonradiatively (dissipating the input energy as heat), or get trapped and react with electron donors or acceptors adsorbed on the surface of the photocatalyst. The interplay between these fundamental processes (Table 2) determines the overall efficiency of titania nanoparticles in various applications [110].

Table 2: Fundamental photon-induced electron and hole processes [110].

Reaction	Process
$\text{TiO}_2 + h\nu \rightarrow e^- + h^+$	Photon absorption
$e^- + \text{Ti(IV)O} - \text{H} \rightarrow \text{Ti(III)O} - \text{H}^- (\text{X})$	Photocatalytic redox
$h^+ + \text{Ti(IV)O} - \text{H} \rightarrow \text{Ti(IV)O}^* - \text{H}^+ (\text{Y})$	Photocatalytic redox; competition pathways for holes (leads to bound OH radicals); Reverse reaction generates O adatom intermediates upon exposing defective surfaces to $\text{O}^{2-}(\text{g})$
$h^+ + \frac{1}{2}\text{O}_{\text{lattice}}^{2-} \leftrightarrow \frac{1}{4}\text{O}_2(\text{g}) + \text{vacancy}$	Photocatalytic redox; competition pathways for holes (leads to bound O vacancies)
$e^- + \text{O}_{2,\text{s}} \rightarrow \text{O}_{2,\text{s}}^-$	Photocatalytic redox
$\text{O}_{2,\text{s}}^- + \text{H}^+ \leftrightarrow \text{HO}_{2,\text{s}}$	Photocatalytic redox
$h^+ + \text{Ti(III)O} - \text{H}^- \rightarrow \text{Ti(IV)O} - \text{H}$	Recombination channel
$e^- + \text{Ti(III)O}^* - \text{H}^+ \rightarrow \text{Ti(IV)O} - \text{H}$	Recombination channel
$\text{O}_{2,\text{s}} + \text{Ti(IV)O}^* - \text{H}^+ \rightarrow \text{Ti(IV)O} - \text{H} + \text{O}_{2,\text{s}}$	Recombination channel

The localisation of electrons and holes generated in titania nanoparticles are at different defect sites on the surface and in the bulk. The results of electron paramagnetic resonance (EPR) show that electrons are trapped as two Ti(III) centres, while the holes are trapped as oxygen-centred radicals covalently linked to surface titanium atoms [110].

In the study by Hurum *et al.* [111], the holes that appeared at the surface upon band gap illumination recombined preferentially with electrons in surface trapping sites for mixed-phase Degussa P25 TiO_2 . The surface reactions that followed charge migration were dominated by recombination reactions.

The investigation of the UV light-induced electron-hole pair excitations in anatase titania nanoparticles by Berger *et al.* [112] was carried out with electron paramagnetic resonance (EPR) and IR spectroscopy. EPR spectroscopy was able to identify the localised states, such as holes trapped at oxygen anions (O^-) and electrons trapped at coordinatively unsaturated cations (Ti^{3+} formation). The delocalised electrons in the conduction band that could not be detected by EPR were exposed by IR absorption through their electronic excitation within the conduction band in the infrared region. During continuous UV irradiation, photogenerated electrons were either trapped at localised sites (giving paramagnetic Ti^{3+} centres) or remained in the conduction band as EPR silent species which may be observed by their IR absorption. It was also established that the EPR-detected holes produced by photoexcitation were O^- species which were generated from the lattice O^{2-} ions. The majority of photoexcited electrons were found to remain in the conduction band under high-vacuum conditions, although, all stable hole and electron states were lost at 298 K [112].

2.5.8 Gas Sensing Properties of Nanosized Titania

Since Seiyama [113] first observed gas sensing properties of ZnO, binary *n*-type semiconductor oxides such as tin oxide (SnO_2), titanium dioxide (TiO_2) and indium oxide (In_2O_3) have been extensively investigated as gas sensing materials. In the devices based on these materials, the reactions which occur at the surface of the metal oxide with the gas molecules, governs the gas sensing mechanism. This process involves the chemisorption of oxygen on the oxide surface and is followed by charge transfer during the reaction of chemisorbed oxygen with target gas molecules [114]. Depending on whether they are reducing or oxidising agents, the adsorbed gas atoms respectively inject electrons into or extract electrons from the metal oxide. As a result, metal oxide sensors can detect (through a change in electrical resistance) small amounts of a gaseous species present in air down to ppb. Oxygen molecules adsorb onto the surface of the metal-oxide semiconductor (MOS) layer to form O_2^- , O^- and O^{2-} ions by extracting electrons from the conduction band, depending on the temperature [114], [115]. A depletion region is formed at the surface due to the positively charged surface of the MOS and the negatively charged

adsorbed oxygen ions. At high temperatures, the interaction of the target gaseous molecules with the adsorbed oxygen changes the depletion layer or the barrier height of the metal oxide grains, particles or nanostructures. These changes are converted into an electrical output signal that depends on the transducing platforms. The output signal, which takes into account the whole sensitive layer is determined by the grain size (nanostructured forms), the porosity of the film and the different grain/nanostructure intersections.

The conventional thick-film based gas sensors operate on the basis of both surface and bulk conductivity changes [116]. This type of sensor has poor dynamic sensitivity as gas molecules cannot penetrate and interact with the whole bulk of the film within a short period of time. In thin film gas sensors, gas molecules do not have to diffuse deep within the layer since response is primarily based on changes in the conductivity of the surface. Sensitivity is further improved if such sensors are based on nanostructured metal oxides, since these have high surface to volume ratios [116]. Additionally, for thin films that show porosity (such as nanowires, nanorods and nanofibers) the whole depth of the sensitive thin film can interact with the gas species, rather than just the surface. Lastly, conventional polycrystalline thin film sensors do not have long term stability due to the gradual deformation of these films at high temperatures [116].

2.5.8.1 Gas Sensing Technology

Generally, there exists a considerable effort in the optimisation of sensing devices for improving environmental and safety control of gases both in domestic as well as industrial applications. Various branches of gas sensing technology have been established by different studies in the past half century. The three major areas that receive the most attention are (i) the investigation of different kinds of sensors, (ii) research about sensing principles, and (iii) fabrication techniques.

Gas sensing technologies may be broadly classified as either involving methods based on variation of electrical properties or other non-electrical properties [117] as shown in Figure 10.

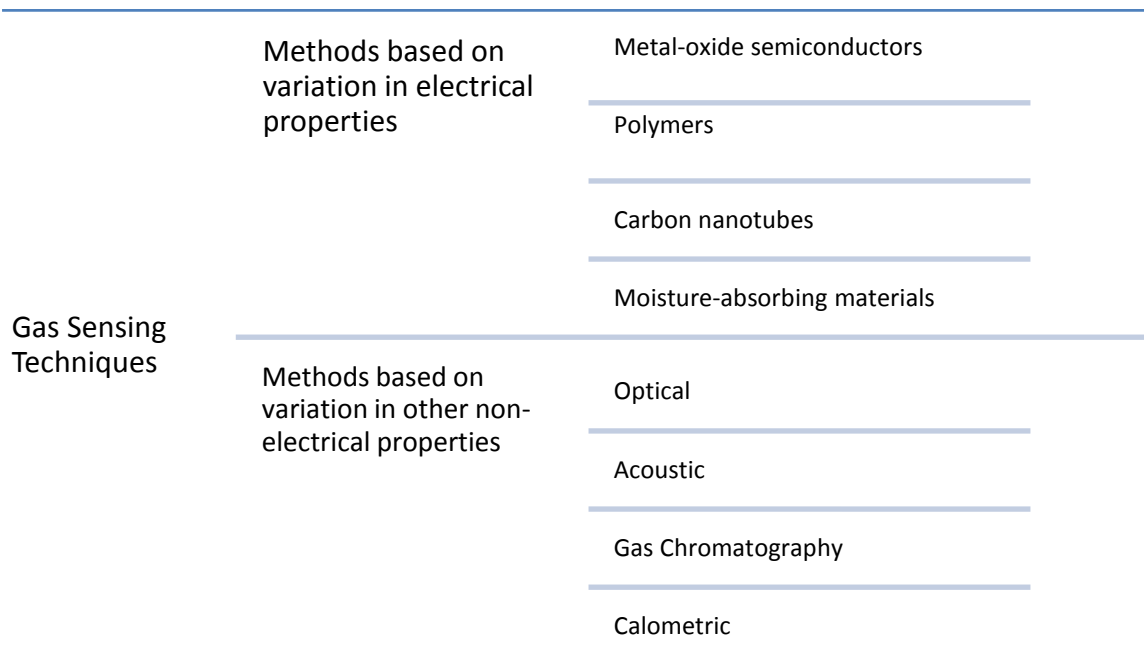


Figure 10: Classification of gas sensing methods [118].

Depending on the development technology used, the more common gas sensing devices are often one of three types, namely:

- Solid State – in which sensing is based on the change of the physical and/or chemical properties of the sensing materials when exposed to different gases
- Spectroscopic – such as mass chromatography and mass spectrograph. These systems, which are based on the direct analysis of the molecular mass or vibrational spectrum of the target gas, are capable of quantitatively measuring the composition of the different gases with a good precision.
- Optic – in which the sensors measure absorption spectra after the target gas has been stimulated by light. These systems requires a complex arrangement of a monochromatic excitation source and an optical sensor for the analysis of the absorbed spectra.

While spectroscopic and optic systems are very expensive for domestic use and sometimes difficult to implement in reduced spaces (such as car engines), solid state sensors offer great benefits due to their fast sensing response, simple implementation and low cost [119] – [120].

Several indicators are considered in evaluating the performance of gas sensors or gas sensing methods. These include

- Sensitivity – the minimum volume concentration value of the target gases required for detection
- Selectivity – the ability of the gas sensor to identify a specific gas among a gas mixture
- Response time – the period from the time when gas concentration reaches a specific value to that when sensor generates a warning signal
- Energy consumption
- Reversibility – whether the sensing materials could return to its original state after detection
- Adsorptive capacity (also affects sensitivity and selectivity)
- Fabrication cost.

Among these, sensitivity and selectivity are the two major indicators.

In addition, gas sensors designed for the market must exhibit a stable and reproducible signal for a period of time (i.e. guarantee the stability of their operation). Several factors may lead to a gas sensor's instability. These include

- Design errors
- Structural changes, such as variations of grain network or size grain
- Phase shifts, which usually refers to the segregation of additives doped with sensing materials
- Poisoning triggered by chemical reactions
- Variation of the surrounding environment

In order to resolve these complications, the elemental composition and grain size of sensing materials should be optimised. Materials with chemical and thermal stability or specific technology during surface pretreatment of sensors could also be used.

A brief summary of the advantages, disadvantages and application fields of the gas sensing materials and methods is provided in Table 3.

Table 3: A comparison of advantages and disadvantages of gas sensing materials and techniques [118].

Material	Advantages	Disadvantage	Target and Applications
Metal Oxide Semiconductor	(a) Low cost (b) Short response time (c) Wide range of target gases (d) Long lifetime	(a) Relatively low sensitivity (b) and selectivity (c) Sensitive to environmental factors (d) High energy consumption	Industrial applications and civil use.
Polymer	(a) High sensitivity (b) Short response time (c) Low cost of fabrication (d) Simple and portable structure (e) Low energy consumption	(a) Long-time instability (b) Irreversibility (c) (c) Poor selectivity	(a) Indoor air monitoring; (b) Storage place of synthetic products as paints, wax or fuels (c) Workplaces like chemical industries
Carbon Nanotubes	(a) Ultra-sensitive (b) Great adsorptive capacity (c) Large surface-area-to-volume ratio (d) Quick response time (e) Low weight.	(a) Difficulties in fabrication and repeatability (b) High cost	Detection of partial discharge (PD)
Moisture Absorbing Material	(a) Low cost (b) Low weight (c) High selectivity to water vapour.	(a) Vulnerable to friction; (b) Potential irreversibility in high humidity.	Humidity monitoring
Optical Methods	(a) High sensitivity, selectivity and stability (b) Long lifetime (c) Insensitive to environment change.	(a) Difficulty in miniaturisation (b) High cost	(a) Remote air quality monitoring (b) Gas leak detection systems with high accuracy and safety (c) High-end market applications
Calorimetric Methods	(a) Stable at ambient temperature (b) Low cost (c) Adequate sensitivity for industrial detection (path range)	(a) Risk of catalyst poisoning and explosion (b) Intrinsic deficiencies in selectivity	(a) Most combustible gases under industrial environment (b) Petrochemical plants (c) Mine tunnels (d) Kitchens
Gas Chromatograph	(a) Excellent separation performance (b) (b) High sensitivity and selectivity	(a) High cost (b) Difficulty in miniaturisation for portable applications	Typical laboratory analysis
Acoustic Methods	(a) Long lifetime (b) Avoiding secondary pollution	(a) Low sensitivity (b) Sensitive to environmental change	Components of Wireless Sensor Networks

The quality of a sensor is mainly defined by the application requirements [121]. So, in addition to the three classical factors of sensitivity, selectivity and stability, another factor which is increasingly considered is suitability. Aside from the target gas or gases, possible cross-interferences and environmental conditions also relate to the cost restrictions of the devices using the sensors.

2.5.8.2 Metal-Oxide Semiconductor Gas Sensors (SGS)

With SGS, the conductivity of the sensing material present changes in presence of a determinate gas [122]. Because the working temperature (which may range from 200°C to 800°C) at which these devices are most efficient, can depend on the gas atmosphere and on properties of the sensor material chosen in a particular case, it is therefore often necessary to implement a heating system in such sensor devices.

Typically, a simple SGS (depicted in Figure 11) will be composed of a substrate (where the sensor material will be supported), the electrodes (to measure the conductivity changes) and the heaters (to achieve the optimum sensing temperatures) [123].

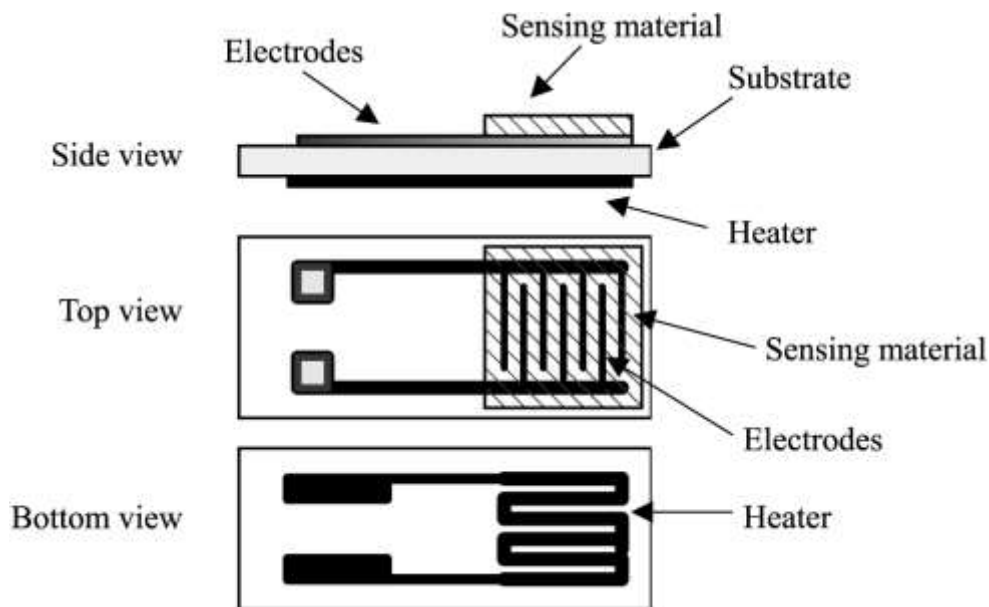


Figure 11: Typical scheme of a semiconductor gas sensing device [124].

Sensors based on metal oxide films have been well studied for their sensitivity effects as a consequence of the sensitive layer morphology, such as grain size, structural formation, surface to volume ratio and film thickness [116]. For sensors based on both polycrystalline and nanostructured materials, the chemistry of metal oxide is similar to that of gas molecule interactions. Thus, the conventional gas sensing theories, to some extent, still apply to the nanostructured MOS based sensors. However, in nanostructured sensors, quantum effects and crystallinity do influence the gas sensing mechanism.

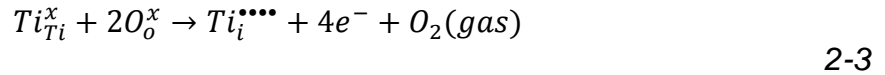
Metal oxide semiconductors are the most common sensing materials because of their low cost and high sensitivity as well as several other advantages. Generally, they can be classified as either transitional (containing elements with several oxidation states) or non-transitional (containing only one oxidation state – much more energy is required to form other oxidation states) [117]. Metal oxides, such as SnO₂, CuO, Cr₂O₃, V₂O₅, WO₃ and TiO₂, can be used in sensors which are based mainly on the resistance-change responses to the target gases, to detect combustible, reducing, or oxidising gases. Several influencing factors, such as the characteristics and structure of the sensing layer, affect the redox reactions and thus decide the sensitivity of metal oxides as gas sensing materials [47], [117].

2.5.8.3 Response Mechanism to Oxygen in the Adsorption Model

The bulk and surface conductivity of a MOS film can be altered by modulating the conductance of the materials used in making the film. The changes in conductivity depend largely on the partial pressure of the ambient oxygen [47]. At high temperatures, the stoichiometry of semiconducting oxides is also dependent on the atmospheric oxygen. Through the adsorption of ambient oxygen, *n*-type MOS gas sensors register a high resistance, whereas lower resistance is observed for the *p*-type metal oxides. The change in stoichiometry affects the electrical conductivity of the materials, σ , which can be expressed by the following equation [125]:

$$\sigma = \sigma_0 e^{-E_a/kT} p(O_2)^{1/n} \quad 2-2$$

where k denotes Boltzmann's constant, T is the Kelvin temperature, E_a is the activation energy of conduction electrons and $p(O_2)$ is the partial pressure of the gaseous oxygen. The activation energy is the sum of the energy required to form the ionic defects and the subsequent ionisation to form charge carriers in the conduction or valence band. The value and sign of n in Equation 2-2 depend on the nature of the point defects arising upon the removal of oxygen from the lattice. For oxygen sensors based on TiO₂, exposure to low pressure gaseous oxygen at temperatures high enough to create defects, leads to the reduction of TiO₂ which in turn results in the formulation of *Ti* interstitials ($Ti_i^{\bullet\bullet\bullet}$), such that [125]:



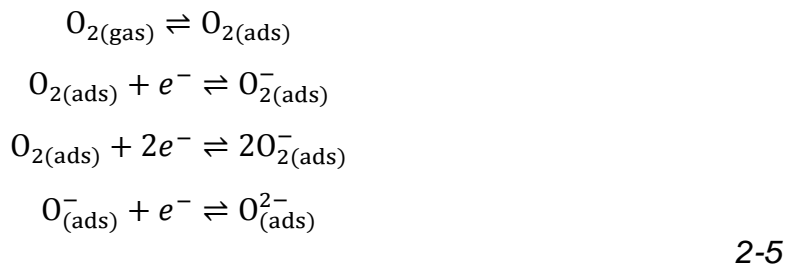
where the charge neutrality is given by $4 \cdot [Ti_i^{\bullet\bullet\bullet\bullet}] = n$. The reduction reaction yields an equilibrium constant, $K_R = [Ti_i^{\bullet\bullet\bullet\bullet}] \cdot n^4 \cdot p(O_2)$, which leads to:

$$n = \{4K_R \cdot [p(O_2)]^{-1}\}^{1/5} \quad 2-4$$

A comparison of Equation 2-4 with Equation 2-2 indicates a dependence on oxygen pressure of $n = -5$ for the reduction of TiO_2 by formulation of Ti interstitial defects. The conductivity of the TiO_2 based oxygen sensor not only depends on temperature (since the defect chemical equilibrium constants are exponentially dependent on temperature), but also on the oxygen partial pressure $p(O_2)$ [47]. Designing oxygen gas sensors will require the equilibrium between oxygen in the gas phase and lattice oxygen. However, for sensing other gases most metal oxide sensors will rely mainly on surface conduction [47].

2.5.8.4 Surface Conductance in Semiconducting Oxide Films

Semiconductor Sensing Materials exhibit a change of their electrical properties in presence of a determinate gas. Depending on the materials, this change can be due to *surface conductance effects* or due to *bulk effects* [47]. In semiconducting oxides, surface conductance does not depend so much on the defect chemistry or oxygen partial pressure of the oxide. Rather, it is a consequence of the changes in the equilibrium condition of the surface processes (which are not at equilibrium with the bulk) due to a reactive gas [125]. The negatively charged oxygen ions (O_2^- , O^- and O^{2-} adsorbates) play an important role in detecting gases such as H_2 and CO . The following equations describe these adsorptions [126]:

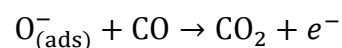
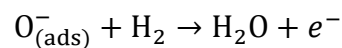


For *n*-type semiconducting oxides, the depletion region formed by the positively charged oxide surface and negatively charged adsorbed oxygen ions results in a high resistance, due to the development of a potential barrier. Due to the electron depletion at the surface by chemisorption, a space charge layer of thickness λ_D (or the Debye length) is formed according to [125]:

$$\lambda_D = \frac{Q_S}{eN_D} = \sqrt{\frac{2K\varepsilon_0 V_S}{eN_D}} \quad 2-6$$

In this Poisson's equation, Q_S is the surface charge density, N_D is the number of ionised donor states per unit volume, e is the carrier charge, K is the static dielectric constant of the oxide, ε_0 is the permittivity of free space, and V_S is the surface potential barrier height. For typical values of $\varepsilon_0 \approx 10^{-12} \text{F} \cdot \text{cm}^{-1}$, $N_D \approx 10^{18} - 10^{20} \text{cm}^{-3}$ and $V_S \approx 1 \text{V}$, the space charge layer thickness is estimated to be between 1 nm and 100 nm [125].

The space charge region around the surface of a porous semiconducting oxide film is depicted in Figure 12. This region, being depleted of electrons, is more resistive than the bulk of the material. In the band model shown, the potential barrier formed at inter-grain contacts varies with the amount of adsorbed oxygen [127]. For inter-grain transport, the charge carriers are subjected to a barrier of eV_S . Further, the surface barrier V_S is dependent on temperature and the atmospheric pressure of oxygen. The steady-state surface coverage of the adsorbates is lowered, whenever an *n*-type metal oxide surface is exposed to a reducing gas such as H_2 or CO at elevated temperatures. This is because of the removal of oxygen adsorbates by the reduction reaction. Close to 300°C , the reactions are given by [127]:



2-7

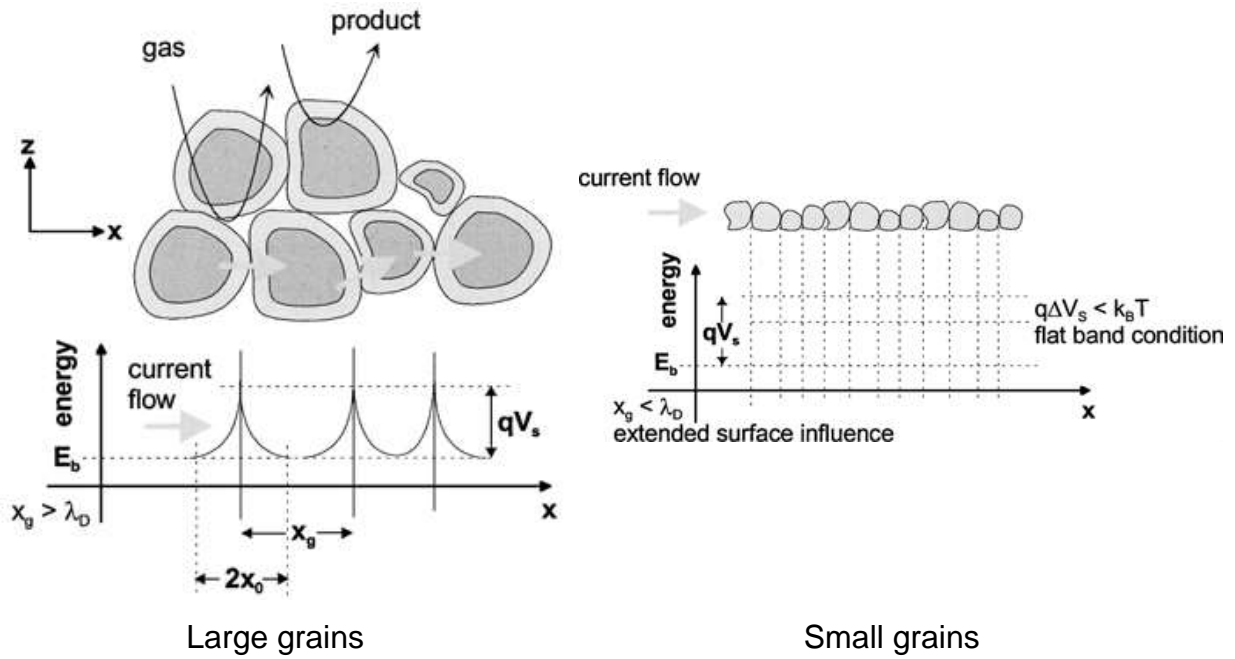


Figure 12: A representation of porous semiconducting oxide grains and the space charge region around the surface of each grain and at intergrain contacts. The band model for the corresponding grain model is also shown. X_g refers to grain size and λ_D refers to the Debye length [128].

During the reaction process, the potential barrier height reduces and the resistance decreases as the electrons trapped by the oxygen adsorbates return to the oxide grains. Thus, these changes in resistance constitute a measurement parameter of the semiconductor gas sensor. Gas sensing properties are greatly influenced by the mean diameter (X_g) of grains or crystallites in metal oxides. As the grain size decrease, the sensor sensitivity improves [129]. By assuming that a chain of uniform crystallites of size X_g connected each other through necks and grain boundary contacts, the grain size effects of metal oxide polycrystalline materials can be summarised as:

- (a) Grain boundary resistance control, for which $X_g \gg 2\lambda_D$
- (b) Neck resistance control, for which $X_g \geq 2\lambda_D$, and
- (c) Grain resistance control, for which $X_g \ll 2\lambda_D$.

In grain resistance control (the most preferable of the three for gas sensing) the resistance of the whole chain, and consequently the film resistance, is dominated by the grain resistance. Thus, grain structures, morphology or crystallinity are the

prevailing factors for controlling device sensitivity. Essentially, smaller grain would be more sensitive than larger ones [129].

Electrical conduction is controlled by the grain boundaries, since the particle or grain size of a polycrystalline semiconducting oxide gas sensor is considerably greater than the depth of the surface space charge region. Nanostructured materials (grains, rods, wires and belts) however, have dimensions which are comparable to the depletion layer depth [47]. This way, oxygen adsorption to the nanostructures will lead to a complete depletion of conduction-band electrons with a substantial variation in resistance. Upon exposure to gases, the level of conductivity modulation in nanostructures is therefore much higher than in conventional grains [47].

Another factor that influences sensor sensitivity is the morphology of the thin film sensing layer [47]. This may be categorised as either compact or porous. In compact sensing layers, the gas sensing reaction is confined to the surface as gases are unable to penetrate deep into the layer. However, in a porous layer, gases can infiltrate the entire volume of the sensing layer. The gas sensing reaction not only takes place at the surface of individual grains/nanostructures, but also at grain-grain boundaries as well as at interfaces between grains and electrodes. In contrast to bulk compact materials, nanostructured metal oxides, display greatly improved gas molecule diffusion, since they have much greater exposed surface area, as well as much greater penetration depth for gas molecules [47].

For *p*-type semiconducting oxides (whose charge carriers are positive holes) the low resistance in air is as a result of the formation of negatively charged oxygen adsorbates. The electrons extracted from the bulk serve to enhance the hole concentration on the grain surface. The adsorption of oxidising gases on *p*-type semiconducting oxides results in a decrease in resistance. On the other hand, the reverse is the case for *n*-type semiconducting oxides, for which the consumption of oxygen adsorbates by reaction with reducing gases leads to an increase in resistance [47].

2.6 SYNTHESIS OF TITANIA NANOSTRUCTURES

A variety of ingenious methods are available for synthesising titania nanostructures. The method of preparation, as well as the prevailing conditions during synthesis, of titania nanomaterials (nanoparticles, nanorods, nanowires and nanotubes) generally influences the structural, thermal, electronic and optical properties of the final product. As the size, shape, crystal structure and surface stability of titania nanomaterials vary, so does the transition between different phases of TiO_2 under pressure or heat change. The methods of synthesis discussed here are:

- Sol-Gel
- Micelle and Inverse Micelle
- Non-Hydrolytic Sol
- Hydrothermal
- Solvothermal
- Direct Oxidation
- Chemical Vapour Deposition
- Physical Vapour Deposition
- Electrodeposition
- Sonochemical
- Microwave
- Titania Mesoporous/Nanoporous Materials
- Titania Aerogels
- Titania Opal and Photonic Materials
- Titania Nanosheets

2.6.1 The Sol-Gel Method

Ceramic materials are often synthesised using the versatile sol-gel method [130] – [131]. The process generally involves the formation of a sol (colloidal suspension) from the hydrolysis and polymerisation reactions of the precursors. The reactants are commonly inorganic metal salts or metal organic compounds such as metal alkoxides. The liquid sol is transformed into a solid gel phase upon complete

polymerisation and loss of solvent. If desired, thin films can be produced on a piece of substrate by spin-coating or dip-coating. Upon casting the sol into a mould, the wet gel formed, is converted into a dense ceramic when further dried and heat treated. An aerogel (a highly porous material of extremely low-density) is then obtained if the solvent in the wet gel is removed under a supercritical condition. Ceramic fibres can be drawn from the sol after adjusting its viscosity into a proper range. The formation of ultrafine and uniform ceramic powders can then be achieved by precipitation, spray pyrolysis or emulsion techniques. As such, nanomaterials can be obtained under the right conditions.

The sol-gel method is sometimes used to synthesise titania nanomaterials from hydrolysis of a titanium precursor [68], [102], [132] – [133]. This process normally proceeds via an acid-catalysed hydrolysis step of titanium(IV) alkoxide followed by condensation [38], [132], [134], [135]. If the reaction mixture is of low water content, low hydrolysis rates and excess titanium alkoxide, the development of Ti-O-Ti chains is favoured. This development of Ti-O-Ti chains yields 3-dimensional polymeric skeletons with close packing. For a medium amount of water, the formation of Ti(OH)_4 is favoured with high hydrolysis rates. Loosely packed first-order particles are obtained in the presence of a large quantity of Ti-OH and insufficient development of 3-dimensional polymeric skeletons. Polymeric Ti-O-Ti chains are established in the presence of a large excess of water. Closely packed 1st-order particles are produced via a 3-dimensionally developed gel skeleton [38], [132], [134], [135]. The study on the growth kinetics of titania nanoparticles in aqueous solution, using titanium tetraisopropoxide (TTIP) as precursor [38], reveals that the rate constant for coarsening increases with temperature as a result of the dependence of the viscosity, and the equilibrium solubility, on temperature. At longer times and higher temperatures, secondary particles are formed by epitaxial self-assembly of primary particles. Also, the ratio of primary particles to secondary particles increases with time. In line with Lifshitz-Slyozov-Wagner coarsening model [38], the average radius of the titania nanoparticles increases linearly with time.

In the presence of tetramethylammonium hydroxide, highly crystalline anatase titania nanoparticles with different sizes and shapes could be realised with the polycondensation of titanium alkoxide [136], [137]. In a typical process, titanium alkoxide is added to the base at 2°C in alcoholic solvents in a flask and is heated at

50°C – 60°C for 13 days or at 90°C – 100°C for 6 h. A secondary treatment involving autoclave heating at 175°C and 200°C is carried out in order to improve the crystallinity of the titania nanoparticles.

Sugimoto *et al.* [138], [139], [140] conducted a series of studies using the sol-gel method by tuning the reaction parameters to produce titania nanoparticles of different sizes and shapes. Typically, a stock solution of a 0.50 M Ti source is prepared by mixing TTIP with triethanolamine (TEOA) in the ratio 1 : 2. This is then followed by the addition of water. The stock solution is further diluted with a shape controller solution (such as amines) and then aged at 100°C for 1 day and at 140°C for 3 days. Tuning of the pH of the solution can be achieved by the addition of HClO₄ or NaOH solution. The amine (which includes TEOA, diethylenetriamine, ethylenediamine, trimethylenediamine, and triethylenetetramine) also acts as a surfactant. The morphology of the titania nanoparticles changes from cuboidal to ellipsoidal with TEOA, at pH above 11. Above the pH of 9.5 the particle shape evolves into ellipsoidal with diethylenetriamine with a higher aspect ratio than that with TEOA. Secondary amines (e.g. diethylamine) and tertiary amines (e.g. trimethylamine and triethylamine) act as complexing agents of Ti(IV) ions by enhancing the growth of ellipsoidal particles with lower aspect ratios. Sodium oleate and sodium stearate can also be used to tune the shape of the titania nanoparticle from round-cornered cubes to sharp-edged cubes [139]. The tuning of the growth rate of the different crystal planes of titania nanoparticles by the specific adsorption of shape controllers to these planes under different pH conditions may account for the shape control [139].

In order to avoid the agglomeration of the titania nanoparticles during the crystallisation process, a prolonged heating time below 100°C for the as-prepared gel can be used [102], [141]. As reported by Zhang and Banfield [68], large quantities of single-phase anatase titania nanoparticles, with average particle sizes between 7 nm and 50 nm, can be realised by heating amorphous TiO₂ in air. Considerable effort has been put into achieving highly crystallised and narrowly dispersed titania nanoparticles using the sol-gel method with other modifications. One such method is the semicontinuous reaction method by Znaidi *et al.* [133]. Another is a two-stage mixed method and a continuous reaction method by Kim *et al.* [142], [143].

Titania nanorods have been successfully synthesised through a combination of the sol-gel method and an anodic alumina membrane (AAM) template. This was achieved by dipping porous AAMs into a boiled TiO_2 sol, followed by drying and heating processes [144], [145]. Typically, the experiment involves mixing TTIP dissolved in ethanol with a solution containing water, acetyl acetone and ethanol in order to form the TiO_2 sol. After being boiled in ethanol, an AAM is immersed into the sol solution for 10 min and then dried in air before being calcined at 400°C for 10 h. The template is further dipped in a 10 wt% H_3PO_4 aqueous solution. The crystal phase of the titania nanorods formed is controlled by the calcination temperature. Anatase nanorods can be obtained at low temperatures, and rutile at high temperatures. The size of the titania nanorods, which typically range from 100 nm to 300 nm in diameter and several micrometres in length, are controlled by the pore size of the AAM template. The size distribution of the pores of the AAM template appears to control the size distribution of the final titania nanorods. High-quality AAM templates are required for smaller and monosized titania nanorods. The titania nanorods are normally composed of small titania nanoparticles or nanograins [12].

Ordered titania nanowire arrays can be obtained by electrophoretic deposition of TiO_2 colloidal suspensions into the pores of an AAM [146]. In the process, TTIP is typically dissolved in ethanol at room temperature. Glacial acetic acid, mixed with deionised water and ethanol, is then added under a pH between 2 and 3 with nitric acid. The anode is Pt while the cathode is an AAM with an Au substrate attached to Cu foil. With a voltage between 2 V and 5 V, a TiO_2 sol is deposited into the pores of the AAM and annealed at 500°C for 24 h. The AAM template is then dissolved in a 5 wt% NaOH solution to obtain isolated titania nanowires. An AAM with long pores is required to produce titania nanowires as opposed to that of nanorods [146].

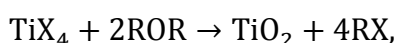
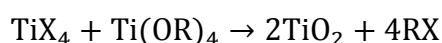
Titania nanotubes can also be fabricated via the sol-gel route using an AAM template [147], [148] and other organic compounds [149], [150]. With an AAM template, for example, a thin layer of TiO_2 sol on the wall of the pores of the AAM is first prepared by sucking TiO_2 sol into the pores of the AAM and removing it under vacuum. Once the sol is fully developed, titania nanowires are obtained upon removing the AAM. The scheme followed by Lee *et al.* [147] involved the preparation of a solution of TTIP with 2-propanol and 2,4-pentanedione. After the AAM is dipped into this solution, it was removed and placed under vacuum until the entire volume of

the solution has pulled through the AAM. The AAM was hydrolysed by water vapour over a solution of HCl for 24 h, dried in air at room temperature, and then calcined for 2 hours at 400°C before being cooled to room temperature at a temperature ramp of 2°C/h. After the AAM was dissolved in a 6 M NaOH solution for several minutes, pure titania nanotubes were obtained [147]. On the other hand, titania nanotubes could be obtained by coating the AAM membranes at 60°C, for a particular period of time between 12 h and 48 h, with dilute TiF₄ under pH of 2.1. The AAM is then removed after titania nanotubes are fully developed [148].

Another sol-gel procedure involves the fabrication of titania nanotubes using a ZnO nanorod array on a glass substrate [151]. Here, TiO₂ sol is deposited on a ZnO nanorod template by dip-coating with a slow withdrawing speed. Drying this at 100°C for 10 min, and heating it at 550°C for 1 h in air, yields ZnO/Titania nanorod arrays. The ZnO nanorod template can then be etched out by immersion in a dilute hydrochloric acid aqueous solution to obtain the titania nanotube arrays. The uniform hexagonal cross-sectional shape and the length of 1.5 µm and inner diameter of 100 nm – 120 nm of the ZnO nanorod template are inherited by the titania nanotubes [12]. Since the concentration of the TiO₂ sol is constant, well-aligned titania nanotube arrays can only be obtained from an optimal dip-coating cycle number in the range of 2 – 3 cycles. For higher dip-coating cycles, a dense porous TiO₂ thick film with holes is obtained instead. One factor that is critical to the formation of titania nanotube arrays is the heating rate [151]. For rapid heating rates (say above 6°C/min) a TiO₂ film with loose, porous nanostructure results. This is because of the large tensile stress that exists between the TiO₂ coat and the ZnO template. This way, the TiO₂ coat cracks easily and flakes off from the ZnO nanorods [12].

2.6.2 Non-Hydrolytic Sol Method

Non-hydrolytic sol-gel processes usually comprise of the reaction of titanium chloride with a variety of different oxygen donor molecules (such as metal alkoxide or organic ether) [78], [152]:



where X is a halide ion (Cl^- , F^- , Br^- , I^-) and R an alkyl group. The Ti–O–Ti bridges are formed as a result of the condensation between Ti–Cl and Ti–OR. The alkoxide groups can be made available by titanium alkoxides or can be formed in situ by reaction of the titanium chloride with alcohols or ethers [12]. Trentler *et al.* [152] used a method in which a metal alkoxide was rapidly injected into the hot solution of titanium halide mixed with trioctylphosphine oxide (TOPO) in heptadecane at 300°C. With dry inert gas as protection, the reactions were completed within 5 min. With a series of alkyl substituents, including methyl, ethyl, isopropyl, and *tert*-butyl, the reaction rate increased significantly with greater branching of R, while average particle sizes remain relatively unaffected [12]. Varying X resulted in a discernible trend in average particle size, but not in the reaction rate. Increasing halide nucleophilicity (or size) yielded smaller anatase nanocrystals [12]. The average sizes ranged from 9.2 nm for TiF_4 to 3.8 nm for TiI_4 . The chemistry was also influenced by the amount of passivating agent (TOPO). Reactions in pure TOPO were slower and they yielded smaller particles, whereas reactions without TOPO were much quicker and yielded mixtures of brookite, rutile, and anatase with average particle sizes larger than 10 nm [152].

In the method used by Niederberger *et al.* [78], under vigorous stirring, TiCl_4 was slowly added to anhydrous benzyl alcohol at room temperature and was kept at 40°C – 150°C for 1 to 21 days in the reaction vessel. The precipitate was calcined at 450°C for 5 h after thorough washing. The reaction between TiCl_4 and benzyl alcohol was found suitable for synthesising highly crystalline anatase titania nanoparticles with fairly uniform size and shape at very low temperatures (~40°C). In the range of 4 nm – 8 nm, the particle size could be selectively adjusted with the appropriate thermal conditions and a suitable choice of the relative amounts of benzyl alcohol and titanium tetrachloride [12]. The particle growth had a strong dependency on temperature. Further, reducing the concentration of titanium tetrachloride led to a substantial decrease of particle size [78].

A variety of nanoparticles with good size distribution and dispersity have been widely used in the preparation of surfactants [12]. For instance, monodispersed titania nanoparticles can be synthesised by adding different surfactants (such as acetic acid and acetylacetone) as capping agents into the reaction matrix. Scolan *et al.* [153]

obtained monodispersed, non-aggregated titania nanoparticles in the 1 nm to 5 nm range, through hydrolysis of titanium butoxide and in the presence of acetylacetonate and *p*-toluenesulfonic acid at 60°C [153]. The resulting nano-xerosols could be dispersed in water-alcohol or alcohol solutions at concentrations higher than 1 M without aggregation. This can be ascribed to the complexation of the surface by acetylacetonate ligands and through an adsorbed hybrid organic-inorganic layer made with acetylacetonate, *p*-toluenesulfonic acid, and water [153].

Different sized and shaped titania nanorods can also be synthesised with the aid of surfactants. For example, Cozzoli *et al.* [80] [154] reported the growth of high-aspect-ratio anatase titania nanorods through controlling the hydrolysis process of TTIP in oleic acid (OA). TTIP was added into dried OA at temperatures between 80°C – 100°C under inert gas (nitrogen) flow and stirred for 5 min. Rapidly injection of an aqueous base (0.1 M – 2 M) solution followed before stirring it at 80°C – 100°C for 6 h to 12 h. Organic amines, such as trimethylamino-N-oxide, trimethylamine, tetramethylammonium hydroxide, tetrabutylammonium hydroxide, triethylamine, and tributylamine, served as some of the bases used. In this reaction, the hydrolysis rate of titanium alkoxide was controlled by chemical modification of the titanium precursor with the carboxylic acid. Through the use of suitable catalysts (tertiary amines or quaternary ammonium hydroxides), fast crystallisation (within 4h to 6 h) in mild conditions was promoted. The kinetically overdriven growth mechanism resulted in the growth of titania nanorods instead of nanoparticles [80]. Zhang *et al.* [79] and Joo *et al.* [155] reported similar procedures for synthesising titania nanorods without using a catalyst. A mixture of TTIP and OA was used to generate OA complexes of titanium at 80°C in 1-octadecene. Differently sized titania nanorods were obtained with the injection of a predetermined amount of oleylamine at 260°C [79].

Jun *et al.* [156] conducted a study on the surfactant-mediated shape evolution of titania nanocrystals in nonaqueous media and found that the shape of titania nanocrystals could be modified by changing the surfactant concentration. An alkyl halide elimination reaction between titanium chloride and titanium isopropoxide was carried out. A dioctyl ether solution containing TOPO and lauric acid was heated to 300°C. This was followed by addition of titanium chloride under vigorous stirring. The reaction was initiated by the rapid injection of TTIP and then quenched with cold toluene. At low concentrations of lauric acid, bullet and diamond-shaped

nanocrystals were obtained, whereas rod-shaped nanocrystals or a mixture of nanorods and branched nanorods was observed at higher concentrations [12]. These nanocrystals and nanorods were aligned along the [001] directions. As the growth time increases, the titania nanorods were found to shrink (due to the minimisation of the overall surface energy by way of the dissolution and regrowth of monomers during an Ostwald ripening [156]).

2.6.3 Micelle and Inverse Micelle Methods

Micelle and inverse micelle methods are commonly employed to synthesise titania nanomaterials [12], [157] – [158]. Micelles are aggregates of surfactant molecules dispersed in a liquid colloid when the surfactant concentration exceeds the critical micelle concentration (CMC). CMC is the concentration of surfactants in free solution in equilibrium with surfactants in aggregated form. Here, the orientations of the hydrophobic hydrocarbon chains of the surfactants are toward the interior of the micelle while those of the hydrophilic groups of the surfactants are toward the surrounding aqueous medium. The self-organisation of the molecules of surfactants and lipids is determined by the concentration of the lipid present in solution. Below the CMC, the lipids form a single layer on the liquid surface and are dispersed in solution. They assemble in spherical micelles at the first CMC (CMC-I), into elongated pipes at the second CMC (CMC-II), and into stacked lamellae of pipes at the lamellar point (LM or CMC-III). The CMC depends on the chemical composition; in particular, on the head area to tail length ratio [12].

Reverse micelles are formed in non-aqueous media, and the hydrophilic headgroups are oriented toward the core of the micelles while the hydrophobic groups are directed outward toward the non-aqueous media. Since the number of aggregates is usually small and they are not sensitive to the surfactant concentration, there is no noticeable CMC for reverse micelles. Although ellipsoids, cylinders, and bilayers are also possible, micelles are often globular and roughly spherical in shape. Factors that determine the shape of a micelle include the molecular geometry of its surfactant molecules and solution conditions such as surfactant concentration, temperature, pH, and ionic strength [12].

Kim *et al.* [157] conducted a statistical experimental method to optimise the conditions for the preparation of titania nanoparticles. Significant parameters that control the titania nanoparticle size and size distribution include the values of H₂O/surfactant, H₂O/titanium precursor, ammonia concentration, feed rate, and reaction temperature. The amorphous titania nanoparticles (having diameters between 10 nm and 20 nm) that were synthesised were converted to anatase TiO₂ at 600°C and then to the more thermodynamically stable rutile at 900°C.

In a reversed microemulsion system consisting of cyclohexane, poly(oxyethylene)₅ nonyle phenol ether, and poly(oxyethylene)₉ nonyle phenol ether, Li *et al.* [159] synthesised titania nanoparticles with the chemical reactions between TiCl₄ solution and ammonia. The produced amorphous nanoparticles transformed into anatase when heat treated at temperatures between 200°C and 750°C, and into rutile at temperatures above 750°C. Particle growth and agglomeration were observed at higher temperatures.

Zhang *et al.* [158] synthesised shuttle-like crystalline titania nanoparticles with the hydrolysis of titanium tetrabutoxide in the presence of acids (hydrochloric acid, nitric acid, sulphuric acid, and phosphoric acid) in NP-5 (Igepal CO-520) – cyclohexane reverse micelles at room temperature. The reaction conditions were found to have a great influence on the morphology, crystal structure and particle size of the titania nanoparticles. The acidity, the type of acid used and the microenvironment of the reverse micelles were the key factors affecting the formation of rutile at room temperature. Agglomeration of the particles were observed as reaction times and the [H₂O]/[NP-5] and [H₂O]/[Ti-(OC₄H₉)₄] ratios increase. Round-shaped titania nanoparticles could also be obtained with the application of suitable acid.

Titania nanoparticles were prepared by Lim *et al.* [160], via the controlled hydrolysis of TTIP in reverse micelles formed in CO₂, with the surfactants ammonium carboxylate perfluoropolyether (PFPECOO⁻NH₄⁺) (MW 587) and poly(dimethyl amino ethyl methacrylate-block-1H,1H,2H,2H-perfluorooctyl methacrylate) (PDMAEMA-b-PFOMA). They found that as the molar ratio of either water to surfactant or precursor to surfactant increased, the crystallite size prepared in the presence of reverse micelles increased [160].

Normally, the titania nanomaterials prepared with the above micelle and reverse micelle methods show amorphous structure [12]. The calcination process, which is often required to induce high crystallinity, usually leads to the growth and agglomeration of titania nanoparticles. From the study of Lin *et al.* [161], it was established that the crystallinity of titania nanoparticles (initially synthesised by controlled hydrolysis of titanium alkoxide in reverse micelles in a hydrocarbon solvent) could be enhanced by annealing in the presence of the micelles, at temperatures substantially lower than those required for the usual solid state calcination treatment [161]. This way, highly crystalline titania nanoparticles, with unchanged physical dimensions and minimal agglomeration can be produced.

2.6.4 Hydrothermal Method

Hydrothermal method of synthesis is normally carried out in autoclaves (steel pressure vessels) with or without teflon liners, under controlled pressure and/or temperature, with the reaction in aqueous solutions. The internal pressure produced is largely determined by the amount of solution added to the autoclave, as well as the temperature (which may be elevated above the boiling point of water, thus reaching the vapour pressure saturation). This hydrothermal method is widely utilised for the fabrication of small particles in the ceramics industry and in research [12]. As an example, titania nanoparticles have been obtained by the hydrothermal treatment of peptised precipitates of a titanium precursor with water [12]. In preparing the precipitates, 0.5 M isopropanol solution of titanium butoxide was added to deionised water ($[H_2O]/[Ti] = 150$), and then peptised at 70°C for 1 h in the presence of tetraalkylammonium hydroxides (peptiser). Upon filtration and treatment at 240°C for 2 h, the as-prepared powders were washed with deionised water and absolute ethanol and then dried at 60°C. With the same concentration of peptiser, the particle size was observed to decrease with increasing alkyl chain length. It was found that the particle morphology was influenced by the peptisers and their concentrations. In another instance, titania nanoparticles were prepared by hydrothermal reaction of titanium alkoxide in an acidic ethanol-water solution [12]. TTIP was added dropwise to a mixed ethanol and water solution at pH 0.7 with nitric acid, and reacted at 240°C for 4 h. This yielded mainly the primary structure in the

anatase phase – without secondary structure. The sizes of the particles were constrained to the range of 7 nm – 25 nm by adjusting the Ti precursor concentration and the composition of the solvent system.

Aside from titania nanoparticles, the hydrothermal method has also been used to prepare titania nanorods [12], [162]. Zhang *et al.* [163] obtained titania nanorods by treating a dilute TiCl_4 solution at 60°C – 150°C for 12 h in the presence of acid or inorganic salts [163]. The morphology of the nanorods obtained can be tuned by changing the solvent compositions or using different surfactants. Feng *et al.* [162] reported a film of assembled titania nanorods deposited on a glass wafer. These were prepared by hydrothermal treatment of a titanium trichloride aqueous solution supersaturated with NaCl at 160°C for 2 hours.

Various groups have also synthesised titania nanowires successfully with the hydrothermal method [12]. These are typically obtained by treating TiO_2 white powders in a 10 M – 15 M NaOH aqueous solution at 150°C – 200°C for between 24 h and 72 h without stirring within an autoclave.

Another hydrothermal method for preparing titania nanowires, this time from layered titanate particles, was reported by Wei *et al.* [164]. In their study, layer-structured $\text{Na}_2\text{Ti}_3\text{O}_7$ was dispersed into a 0.05 M – 0.1 M HCl solution and kept at 140°C - 170°C for 3 to 7 days in an autoclave. Titania nanowires were obtained by washing with H_2O and drying. Three steps are involved when forming titania nanowires from layered $\text{H}_2\text{Ti}_3\text{O}_7$, namely: the exfoliation of layered $\text{Na}_2\text{Ti}_3\text{O}_7$; the formation of nanosheets; and the formation of nanowires [164]. In $\text{Na}_2\text{Ti}_3\text{O}_7$, $[\text{TiO}_6]$ octahedral layers are held by the strong static interaction between the Na^+ cations within the $[\text{TiO}_6]$ octahedral layers and the $[\text{TiO}_6]$ unit. The larger H_3^+O cations replace the Na^+ cations in the interlayer space of $[\text{TiO}_6]$ sheets, thus weakening the static interaction (as a result of the widening of the interlayer distance). Consequently, the layered compounds $\text{Na}_2\text{Ti}_3\text{O}_7$ are gradually exfoliated. As the Na^+ is replaced by H^+ in the dilute HCl solution, numerous $\text{H}_2\text{Ti}_3\text{O}_7$ sheet-shaped products are formed. In the absence of an inversion symmetry, an intrinsic tension exists within the nanosheet which goes to split it to form nanowires – in order to release the strong stress and lower the total energy [164].

Since its introduction by Kasuga *et al.* [165] in 1998, the hydrothermal method has been widely used to prepare titania nanotubes. TiO_2 powders are added to a 2.5 M – 20 M NaOH aqueous solution and held at 20°C – 110°C for 20 h in an autoclave. titania nanotubes are obtained upon washing the products with dilute HCl aqueous solution and distilled water. The formation process of titania nanotubes, as proposed by Kasuga *et al.* [165], involve the following: As the raw TiO_2 material was treated with aqueous solution of NaOH, some Ti-O-Ti bonds are broken and the Ti-O-Na and Ti-OH bonds that are formed thereafter are immediately followed by new Ti-O-Ti bonds. These latter bonds reacted with aqueous HCl solution and distilled water when treated but the Ti-OH bond was unable to form sheets. As the Ti-OH bonds becomes dehydrated by HCl aqueous solution, Ti-O-Ti bonds or Ti-O-H-O-Ti hydrogen bonds are produced. The bond distance from one Ti to the next Ti on the surface is reduced. This results in the folding of the sheets and the connection between the ends of the sheets, thereby leading to the formation of a tube-like structure. In the proposed mechanism, the titania nanotubes were formed in the stage of the acid treatment following the alkali treatment. Du *et al.* [166] however concluded that the nanotubes were formed during the treatment of TiO_2 in NaOH aqueous solution.

A 3D → 2D → 1D formation mechanism of the titania nanotubes was proposed by Wang *et al.* [167]. It suggested that the raw TiO_2 was first transformed into two-dimensional lamellar structures and then bent and rolled to form the nanotubes. For the formation of the titania nanotubes, the lamellar TiO_2 was found to be essential. Based on their HRTEM study, Yao *et al.* [168] further proposed, that titania nanotubes were formed by rolling up the single layer TiO_2 sheets with a rolling-up vector of [001] and attracting other sheets to surround the tubes [12]. Bavykin *et al.* [169] suggested that the nanotube formation mechanism involved the wrapping of multi-layered nanosheets rather than scrolling or wrapping of single layer nanosheets followed by crystallisation of successive layers [12]. In the mechanism put forward by Wang *et al.*, [170] the formation of titania nanotubes involved several steps as follows: During the reaction with NaOH, the Ti-O-Ti bonding between the basic building blocks of the anatase phase, the octahedra, was broken. A zigzag structure was then formed when the free octahedras shared edges between the Ti ions with the formation of hydroxy bridges. This led to the growth along the [100]

direction of the anatase phase. The formation of titania nanotubes then resulted from two-dimensional crystalline sheets that were formed from the lateral growth of the formation of oxo bridges between the Ti centres (Ti-O-Ti bonds) in the [001] direction. These were then rolled up in order to saturate the dangling bonds from the surface and lower the total energy [170].

2.6.5 Solvothermal Method

The solvothermal method has been found to be a versatile method for the synthesis of a variety of nanoparticles with narrow size distribution and dispersity [12]. This method is practically identical to the hydrothermal method except that the solvent used in the solvothermal case is non-aqueous. Since a variety of organic solvents with high boiling points can be selected, the temperature can be raised much higher in the solvothermal method. Further, there is better control over the size and shape distributions, as well as the crystallinity of the titania nanoparticles. The solvothermal method has been used to synthesise titania nanoparticles, nanorods and nanowires with or without the aid of surfactants [12], [171]. For instance, Kim *et al.* [81] mixed TTIP with toluene at the weight ratio of 1-3 : 10 and kept the mixture at 250°C for 3 h. The average particle size of TiO₂ powders appeared to increase with increased composition of TTIP in the solution. Redispersible titania nanoparticles and nanorods were synthesised by Li *et al.* [171], through controlling the hydrolysis reaction of Ti(OC₄H₉)₄ and linoleic acid. Kim *et al.* [81], also produced titania nanorods with narrow size distributions by dissolving TTIP in anhydrous toluene using oleic acid as a surfactant. This was then kept at 250°C for 20 h in an autoclave without stirring. Long dumbbell-shaped nanorods were formed upon adding adequate amount of TTIP or surfactant to the solution. This was ascribed to the oriented growth of particles along the [001] axis. With a fixed precursor to surfactant weight ratio of 1 : 3, the concentration of nanorods in the assembly increased with increasing concentration of the titanium precursor in the solution. They found that the average particle size was smaller, and the size distribution was narrower when compared with particles synthesised without surfactant. Further, the crystalline phase, diameter, and length of these nanorods were largely influenced by the weight ratio of precursor/surfactant/solvent [81].

In a manner similar to the hydrothermal process, the solvothermal method has also been used for the preparation of nanowires [12], [172], [173]. Typically for preparing titania nanowires, a TiO_2 powder suspension in a 5 M NaOH water-ethanol solution is kept in an autoclave at $170^\circ\text{C} - 200^\circ\text{C}$ for 24 h and then cooled to room temperature naturally. Titania nanowires are obtained after washing the obtained sample in an aqueous solution of dilute HCl and drying it at 60°C for 12 h in air [173]. The solvent plays an important role in determining the crystal morphology. Solvents having different physical and chemical properties are able to influence the reactivity, solubility and diffusion behaviour of the reactants. In particular, the morphology and the crystallisation behaviour of the final products can be influenced by the polarity and coordinating ability of the solvent [12]. The presence of high concentration of ethanol brings about a change in the polarity of the solvent as well as the increases in viscosity of the solution. However, in the absence of ethanol, short and wide flakelike structures of TiO_2 were obtained instead of nanowires [173]. When chloroform is used, titania nanorods were obtained instead. Using titanium butoxide as precursor and AgNO_3 as catalyst, bamboo-shaped Ag-doped titania nanowires were also developed [172].

2.6.6 Direct Oxidation Method

Titania nanomaterials can be produced by the oxidation of titanium metal under anodisation or using oxidants such as hydrogen peroxide [174]. Typically, placing a cleaned Ti plate in 50 mL of a 30 wt% H_2O_2 solution at 353 K for 72 h yields titania nanorods on the plate, via a mechanism of dissolution precipitation. The addition of inorganic salts of NaX ($X = \text{F}^-$, Cl^- , and SO_4^{2-}) controls the crystalline phase of the nanorods. Pure anatase is formed by the addition of F^- and SO_4^{2-} , while the Cl^- favours the formation of rutile [174]. Acetone can be used as a good oxygen source for oxidising the Ti plate when preparing highly dense and well-aligned titania nanorod arrays at high temperatures (Peng *et al.* [175]) The role played by the oxygen source an important one. Pure oxygen or argon mixed with oxygen merely produced crystal grain films or grains with random nanofibers growing from the edges. In the titanium oxidation process, the morphology of the TiO_2 largely controls the competition of the oxygen and titanium diffusion [12]. When pure oxygen is used,

because of the high oxygen concentration, oxygen diffusion prevails and the oxidation occurred at the Ti metal and the TiO₂ interface. On the other hand, with acetone as the oxygen source, Ti cations diffuse into the oxide surface and react with the adsorbed acetone species [175].

Anodic oxidation of titanium foil can also produce titania nanotubes [176] – [177]. Using platinum as counterelectrode, a clean Ti plate is typically anodised in a 0.5% HF solution under 10 – 20 V for 10 to 30 min. Upon annealing the anodised Ti plate in oxygen at 500°C for 6 h, crystallised titania nanotubes are obtained [177]. In optimised phosphate/HF electrolytes, the dimensions of the titania nanotubes can be controlled over a wide range (diameter between 15 and 120 nm, and length from 20 nm to 10 µm) with an applied potential between 1 and 25 V [177].

2.6.6.1 Chemical Vapour Deposition

In the vapour deposition process, a material in a vapour state is condensed to a solid-phase. Coatings are usually formed so as to alter the mechanical, electrical, thermal, optical, corrosion resistance, and wear resistance properties of various substrates. The process, which is usually carried out within a vacuum chamber, can also be used to form free-standing bodies, films, and fibres and to infiltrate fabric to make composite materials as well as to fabricate various nanomaterials. If chemical reaction occurs during the process, it is referred to as chemical vapour deposition (CVD), otherwise it is called physical vapour deposition (PVD). In CVD processes, the deposition reaction is driven by the thermal energy which heats the gases in the coating chamber. The pyrolysis of TTIP in a mixed helium/oxygen atmosphere, using liquid precursor delivery can be used to prepare thick crystalline TiO₂ films with grain sizes below 30 nm, as well as titania nanoparticles with sizes below 10 nm [12]. By depositing on the cold areas of the reactor at temperatures below 90°C with plasma enhanced CVD, amorphous titania nanoparticles can be obtained, which upon high temperature annealing, crystallises with a relatively high surface area [12]. Titania nanorod arrays with a diameter of about 50 nm – 100 nm and a length of 0.5 µm – 2 µm can be synthesised by metal organic CVD (MOCVD) on a WC-Co substrate using TTIP as the precursor [12].

Titania nanorods have been grown on fused silica substrates with a template-free and catalyst-free MOCVD method [12]. In a typical procedure, titania nanostructures are grown directly on the substrates by vapourising titanium acetylacetonate ($\text{Ti}(\text{C}_{10}\text{H}_{14}\text{O}_5)$) in the low-temperature zone of a furnace (at $200^\circ\text{C} - 230^\circ\text{C}$). This is then carried by a N_2/O_2 flow into the high-temperature zone of $500^\circ\text{C} - 700^\circ\text{C}$. Tuning the phase and morphology of the titania nanostructures can be achieved by using reaction conditions such as temperature and pressure. Other CVD approaches include electrostatic spray hydrolysis, diffusion flame pyrolysis, thermal plasma pyrolysis, ultrasonic spray pyrolysis, laser-induced pyrolysis, and ultrasonic-assisted hydrolysis [12], [178].

2.6.7 Physical Vapour Deposition

Here, materials are first evaporated and then condensed to form a solid material [12]. Major PVD methods include thermal deposition, ion implantation, ion plating, sputtering, laser surface alloying, and laser vaporisation. In fabricating titania nanowire arrays via a simple PVD method or thermal deposition, pure Ti metal powder is placed on a quartz boat in a tube furnace about 0.5 mm away from the substrate [179], [180]. The furnace chamber is then evacuated down to ~ 300 Torr while the temperature is increased to 850°C under an argon gas flow with a rate of 100 sccm and held for 3 h. The reaction that follows leads to the formation of a layer of titania nanowires [180]. Sometimes, the growth of titania nanowires is preceded by depositing a layer of Ti nanopowders on the substrate, with Au as a catalyst [179].

2.6.8 Electrodeposition

This process involves the production of a coating, usually metallic, on a cathode substrate by the reduction action. The cathode surface to be coated is immersed into a salt solution of the metal to be deposited. The metallic ions are attracted to the cathode where they are reduced to metallic form. To obtain titania nanowires by electrodeposition, an AAM template can be used [84]. A typical process involves a pulsed electrodeposition approach which is carried out in 0.2 M TiCl_3 solution with

pH of 2. Titanium and/or its compound are deposited into the pores of the AAM. Pure anatase titania nanowires are produced by heating the deposited template at 500°C for 4 h and removing the template.

2.6.9 Sonochemical Method

The use of ultrasound in the synthesis of a wide range of nanostructured materials, including high-surface area transition metals, alloys, carbides, oxides, and colloids have been demonstrated. Sonochemistry arises from the formation, growth, and implosive collapse of bubbles in a liquid (or acoustic cavitation) rather than through direct interaction with molecular species. Intense local heating (~5000 K), high pressures (~1000 atm), and enormous heating and cooling rates (>10⁹ K/s) are produced by the cavitation collapse.

The sonochemical method was applied by Yu *et al.* [181] in the preparation of highly photoactive titania nanoparticle photocatalysts with anatase and brookite polymorphs. This is achieved by using the hydrolysis of titanium tetraisopropoxide in pure water or in a 1 : 1 EtOH-H₂O solution under ultrasonic radiation. Huang *et al.* [182] established that, depending on the precursor used and the reaction temperature, anatase and rutile titania nanoparticles (as well as their mixtures) could be selectively synthesised with various precursors using ultrasound irradiation. Titania nanowhiskers and nanotubes, with the assistance of sonication, have been developed by Zhu *et al.* [183]. They established that arrays of whiskers with a diameter of 5 nm and nanotubes with a diameter of about 5 nm and a length between 200 nm and 300 nm, could be obtained by sonicating TiO₂ particles in NaOH aqueous solution and then using deionised water and a dilute HNO₃ aqueous solution to wash the products.

2.6.10 Microwave Method

High-frequency electromagnetic waves between 900 MHz and 2450 MHz can be used to process dielectric materials with energy [12]. At lower microwave frequencies, energy from the microwave field can be transferred to the material via the conductive currents flowing within the material as a result of the movement of

ionic constituents. However, at higher frequencies, the energy absorption is primarily due to molecules with a permanent dipole which tend to reorientate under the influence of a microwave electric field. The inability of the polarisation to follow extremely rapid reversals of the electric field (so the polarisation phasor lags behind the applied electric field) ensures that the resulting current density has a component in phase with the field, thus dissipating power in the dielectric material [12].

The primary benefits of using microwaves for industrial processing include rapid heat transfer, as well as volumetric and selective heating. With microwave radiation, Corradi *et al.* [184] prepared colloidal titania nanoparticle suspensions in periods ranging from 5 min to 1 h. This is in contrast to the 1 h to 32 h needed for the conventional synthesis method of forced hydrolysis at 195°C. High-quality rutile titania nanorods were developed by Ma *et al.* [185], with a microwave hydrothermal method and found that they aggregated radially into spherical secondary nanoparticles. Titania nanotubes, with central hollow, open-ended, and multiwall structure (having diameters of 8 nm – 12 nm and lengths up to 200 nm – 1000 nm) were synthesised by Wu *et al.* [186], using microwave radiation via the reaction of TiO₂ crystals of anatase, rutile, or mixed phase and NaOH aqueous solution.

2.6.11 Mesoporous/Nanoporous Titania Materials

The study of mesoporous/nanoporous TiO₂ materials has been carried out in the past decade, with or without the use of organic surfactant templates [12]. In an experiment reported by Barbe *et al.* [187], on the preparation of a mesoporous TiO₂ film by the hydrothermal method, TTIP was added dropwise at room temperature to a 0.1 M nitric acid solution while stirring vigorously. After the hydrolysis, which yielded a white precipitate, the solution was heated to 80°C and vigorously stirred for 8 h for peptisation. Agglomerates were removed from the solution by filtering on a glass frit. The final concentration of the solids was adjusted to about 5 wt% by added water to the filtrate, before placing the solution in a titanium autoclave for 12 h at 200°C – 250°C. After sonication, a rotary evaporator was used to evaporate the colloidal suspension to a final TiO₂ concentration of 11 wt %. The morphology of the final titania nanoparticles were found to affect factors such as precipitation pH, hydrolysis rate, autoclaving pH, and precursor chemistry. Liu *et al.* [188] and Zhang

et al. [189] have reported alternative procedures that does not make use of hydrothermal processes. In the report by Liu *et al.* pre-hydrolysed 24.0 g of titanium(IV) *n*-butoxide ethanol solution (in the weight ratio of 1 : 7), in the presence of 0.32 mL of a 0.28 M HNO₃ aqueous solution (TBT/HNO₃ ~ 100 : 1) at room temperature for 3 h. This was followed by the addition of 0.32 mL of deionised water to the pre-hydrolysed solution under vigorous stirring and then stirred for an additional 2 h. The sol solution was kept in a closed vessel at room temperature without stirring to gel and age for 14 days. After drying at room temperature, the gel was ground into a fine powder, washed thoroughly with water and ethanol and dried again to produce porous TiO₂. The crystallised mesoporous TiO₂ material was obtained upon calcination at 450°C for 4 h under air. In another investigation, Yu *et al.* [190] were able to prepare thermally stable 3-dimensional mesoporous TiO₂ without the use of any surfactants. Here, monodispersed titania nanoparticles were formed initially by ultrasound-assisted hydrolysis of acetic acid-modified titanium isopropoxide. Controlled condensation and agglomeration of the sol nanoparticles yielded mesoporous spherical or globular particles under high-intensity ultrasound radiation. The wormhole-like mesoporous TiO₂ made up of titania nanoparticles without a long-range order. The template method employed by the Frindell *et al.* [191], used structure-directing agents (or organic templates) for organising network-forming metal oxide species in non-aqueous solutions. The most commonly used organic templates are amphiphilic poly-(alkylene oxide) block copolymers which is typical dissolved in ethanol before vigorously stirring in the TiCl₄ precursor. The resulting solution was gelled in an open Petri dish at 40°C in air for 1 – 7 days. Removing the surfactant species, by calcining the as-prepared sample at 400°C for 5 h in air, yielded the mesoporous TiO₂.

Diblock polymers, instead of triblock copolymers, can also be used as structure-directing agents (Crepaldi *et al.* [192]) Other surfactants employed to direct the formation of mesoporous TiO₂ include tetradecyl phosphate (a 14-carbon chain), commercially available dodecyl phosphate, cetyltrimethylammonium bromide (CTAB) (a cationic surfactant), Gemini surfactant, and dodecylamine (a neutral surfactant). Carbon nanotubes and mesoporous SBA-15286 can also serve as the skeleton for mesoporous titania.

2.6.12 Titania Aerogels

Sol-gel processing, combined with supercritical drying, provides a means the synthesising TiO₂ aerogels having morphological and chemical properties that are not readily realised by other preparation methods (involving high surface area) [12]. Titania aerogels were prepared by Campbell *et al.* [193], via the sol-gel synthesis, from titanium *n*-butoxide in methanol with the subsequent removal of solvent by supercritical CO₂. In a typical procedure, titanium *n*-butoxide is added to 40 mL of methanol in a dry glovebox. This solution is then combined with another solution containing 10 mL of methanol, nitric acid, and deionised water. The concentration of the titanium *n*-butoxide is kept at 0.625 M while the molar ratio of water/HNO₃/titanium *n*-butoxide is 4 : 0.1 : 1. The gel is left to age for 2 h and then extracted in a standard autoclave with supercritical CO₂ at a flow rate of 24.6 L/h, at 70°C under 2.07 x 10⁷ Pa for 2 h to 3 h, resulting in complete removal of solvent. After extraction, the sample is heated in a vacuum oven at 3.4 kPa and 70°C for 3 h to remove the residual solvent and at 3.4 kPa and 210°C for 3 h to remove any residual organics. The pre-treated sample has a brown colour which turned white after calcination at 500°C or above. The resulting TiO₂ aerogel, after calcination at 500°C for 2 h, has a BET surface area greater than 200 m²/g, and contains mesopores in the range 2 nm to 10 nm, and is of the pure anatase phase. Dagan *et al.* [194] found the TiO₂ aerogels obtained by using a Ti/ethanol/H₂O/nitric acid ratio of 1 : 20 : 3 : 0.08 could have a porosity of 90% and surface areas of 600 m²/g, as compared to a surface area of 50 m²/g for Degussa P25 TiO₂ [193].

2.6.13 Opal and Photonic Titania Materials

Various groups [195] – [196] have carried out the syntheses of opal and photonic TiO₂ materials. The preparation of inverse opal TiO₂ from the corresponding metal alkoxides, using latex spheres as templates have been reported by Holland *et al.* [197]. Layers of latex spheres – about a millimetre-thick – were deposited on filter paper in a Buchner funnel under vacuum and soaked with ethanol. While applying suction, titanium ethoxide was added dropwise in order to completely cover the latex spheres. The mass ratios of alkoxide to latex were typical between 1.4 and 3. After drying the composite in a vacuum desiccator for 3 h to 24 h, the latex spheres were

removed by calcination in flowing air at 575°C for 7 to 12 h. This results in hard and brittle powder particles with 320 nm to 360 nm voids. The carbon content of the calcined samples varied from 0.4 wt % to 1.0 wt %; an indication that most of the latex templates had been removed from the 3D host [197].

TiO₂ inversed opals with a skeleton-like structure of TiO₂ rods were prepared by Dong *et al.* [195] in a template-directed method using monodispersed polystyrene particles of size 270 nm. Ti(i-OPr)₄, as a titania precursor was infiltrated in EtOH and then dried and calcined. Precursor concentration was adjusted from 30% to 100%, while the calcination temperature was varied from 300°C to 700°C. The structures were of a highly regular network constituted by rhombohedral windows and TiO₂ cylinders. These cylinders connect the centres of the former octahedral and tetrahedral voids of the opal. The voids themselves form a CaF₂ lattice which is filled with cylindrical bonds linking the Ca and F sites.

Large-scale fabrication of ordered nanostructured titania nanobowl arrays have been reported by Wang *et al.* [196]. The procedure begins with a self-assembled monolayer of polystyrene (PS) spheres, which serves as a template for atomic layer deposition of a TiO₂ layer. The nanobowls are formed upon ion-milling, toluene-etching, and annealing of the TiO₂-coated spheres. Wang *et al.* [196] also produced a 2D photonic crystal by coating patterned and aligned ZnO nanorod arrays with titania. A monolayer mask on a sapphire substrate was made with self-assembled PS spheres. This was then covered with a gold layer. Upon removing the PS spheres with toluene, a vapour-liquid-solid process was used to grow ZnO nanorods. Finally, a TiO₂ layer was deposited on the ZnO nanorods by introducing TiCl₄ and water vapours into the atomic layer deposition chamber at 100°C.

The fabrication of ordered arrays of TiO₂ opals using opal gel templates under uniaxial compression at ambient temperature during the TiO₂ sol/gel process was reported by Ji *et al.* [198]. The compression degree, R was used to control the aspect ratio. Silica opals were used as template to synthesise polystyrene inverse opal and the silica was removed with 40 wt % aqueous hydrofluoric acid. Monomer solutions comprising of dimethylacrylamide, acrylic acid and methylenebisacrylamide in 1 : 1 : 0.02 weight ratios were dissolved in a water/ethanol mixture of 4:7 wt/wt, with 30 wt % total monomer content. The diffusion of the monomer solution into the

inverse opal polystyrene was facilitated using ethanol. A solid composite was obtained upon infiltrating the inverse opal with the monomer solution containing 1 wt % of the initiator AIBN, as well as, a subsequent free radical polymerisation at 60°C for 3 h. The original inverse opal polystyrene template was then removed with chloroform in a Soxhlet extractor for 12 h, thereby forming the opal gel. Opal gels with correspondingly different properties were obtained by using different compositions of the monomer solution, hole sizes, and stacking structures of the starting inverse opal templates [198]. Repeated rinsing of the opal hydrogel with a large amount of ethanol was able to remove the water completely. Following this, the opal gel was immersed in a large quantity of tetrabutyl titanate (TBT) at ambient temperature for 24 h. The TBT-swollen opal gel was then placed in a water/ethanol (1 : 1 wt/wt) mixture for 5 h to sustain the TiO₂ sol/gel process. Upon calcination, TiO₂ opal with distinctive spherical contours was observed. The spacer height was then used to adjust the compression degree, R , upon the compression of the substrates. The deformation of the template-synthesised titania spheres was insignificant for compressions that resulted in up to 20% reduction in the composition opal thickness [198]. Deformed titania opals were obtained when the compression degree was increased to the point of reaching 35% deformation in the opal gel.

2.6.14 Preparation of Titania Nanosheets

Titania nanosheet preparation has been explored by delaminating layered protonic titanate into colloidal single layers [12]. A stoichiometric mixture of Cs₂CO₃ and TiO₂ was calcined at 800°C for 20 h to produce a precursor, caesium titanate, Cs_{0.7}Ti_{1.825}Δ_{0.175}O₄ (Δ being a vacancy). About 70 g of the precursor was treated at room temperature with 2 L of a 1 M HCl solution. This acid leaching was then repeated 3 times by renewing the acid solution every 24 h. The resulting acid-exchanged product was filtered, washed with water, and finally air-dried. The obtained protonic titanate, H_{0.7}Ti_{1.825}Δ_{0.175}O₄•H₂O, was shaken vigorously for 10 days with a 0.017 M tetrabutylammonium hydroxide solution at ambient temperature. The solution-to-solid ratio was adjusted to 250 cm³/g. This process produced a stable opalescent colloidal suspension consisting of titania nanosheets with thicknesses between 1.2 nm – 1.3 nm, which is the height of the titania nanosheet with a monolayer of water molecules on both sides [108].

2.7 MODIFICATIONS OF TITANIA NANOMATERIALS

Several applications of titania nanomaterials are closely dependent on its optical properties. However, the efficient use of these materials is sometimes hindered by the wide band gap. The band gap of bulk TiO_2 (rutile ~ 3.0 eV, anatase ~ 3.2 eV) is located in the UV region of the electromagnetic spectrum, which is less than 10% of the sun's energy [199].

One of the objectives for improving the performance of nanosized titania is to raise the optical activity by shifting the onset of the response from the UV to the visible region [16], [200]. Several methods are available to accomplish this goal. One way is to dope the material with other elements so as to narrow its optical properties. Another way involves sensitizing TiO_2 with other colourful inorganic or organic compounds in order to improve its optical activity in the visible light region. A third way to improve the performance of nanostructured titania-based devices makes use of metal– TiO_2 nanocomposites. Here, the collective oscillations of the electrons in the conduction band of the metal nanoparticle surfaces are coupled with those in the conduction band of the titania nanomaterial. Other methods include altering the charge-transfer properties between TiO_2 and the surrounding environment by modifying the titania surface with other semiconductors [12].

2.7.1 Doping (Bulk Chemical Modification)

The underlying electronic structure of any material largely determines its optical response. Thus, for nanosized materials, the electronic properties are closely related to the chemical nature of the bonds between its atoms or ions (that is, its chemical composition), its atomic arrangement, as well as, its confinement of carriers (or physical dimension). Alteration of the chemical composition of TiO_2 can be achieved by doping. In particular, favourable changes in electronic structure and optical properties of TiO_2 can be realised by replacing the metal (Ti) or the non-metal (O) component, while maintaining the integrity of the crystal structure of the photocatalytic host material. Due to differences in charge states and ionic radii, it is often easier to substitute the Ti^{4+} cation in TiO_2 with other transition metals than to replace the O^{2-} anion with other anions. The small size of the nanoparticle, in

contrast to that of bulk materials, enables a higher tolerance of the structural distortion induced by the inherent lattice strain in nanomaterials. This favours the modification of the chemical composition of TiO₂ nanomaterials [200].

2.7.1.1 Synthesis of Doped Titania Nanomaterials

A variety of metals have been incorporated into titania nanostructures mainly via three preparation methods namely, wet chemistry, high temperature treatment, and ion implantation. Wet chemistry methods generally involve the hydrolysis of a Ti precursor in a mixture of water and other reagents. This is then followed by heating. A systematic study of titania nanoparticles doped with 21 metal ions by the sol-gel method was carried out by Choi *et al.* [24]. This revealed that the presence of metal ion dopants significantly influenced the photoreactivity, charge carrier recombination rates, and interfacial electron-transfer rates. Li *et al.* [201] also used the sol-gel process to develop La³⁺-doped TiO₂ and found that the phase transformation to be inhibited, the thermal stability was enhanced, the crystallite size was reduced, and the Ti³⁺ content on the surface was increased. Nagaveni *et al.* [202] used W, V, Ce, Zr, Fe, and Cu ions in a solution combustion method to dope anatase titania nanoparticles and observed that the solid solution formation was limited to a narrow range of concentrations of the dopant ions. With a hydrothermal method, Wang *et al.* [203] prepared Nd³⁺-doped and Fe(III)-doped titania nanoparticles and established that anatase, brookite, and a trace of hematite, coexisted at lower pH values between 1.8 and 3.6 when the Fe(III) content was as low as 0.5%. There was a non-uniform distribution of Fe ions between particles. At higher pH values (6.0) however, a uniform solid solution of Fe-TiO₂ was formed [12]. Sol-gel and impregnation methods were employed by Bessekhoud *et al.* [204], in their investigation on alkaline-doped titania nanoparticles and found that the crystallinity level of the Li-, Na- and K-doped products to be dependent on both the nature and the concentration of the alkaline. Li-doped TiO₂ displayed the best crystallinity, while the K-doped TiO₂ was lowest. Cao *et al.* [205] used the plasma-enhanced CVD method to prepare Sn⁴⁺-doped nanosized titania films and found increased surface defects after doping. The ion beam induced CVD synthesis by Gracia *et al.* [206] to generate *M*-doped TiO₂ (here *M* is Cr, V, Fe, Co) led to the conclusion that TiO₂ crystallised into the

anatase or rutile structures depending on the type and amount of cations present. Partial segregation of the cations in the form of M_2O_n were observed after annealing. Using oxidative pyrolysis of liquid-feed organometallic precursors in a radiation frequency (RF) thermal plasma, Wang *et al.* [178] synthesised Fe(III)-doped titania nanoparticles and found that the formation of rutile was strongly promoted with iron doping in comparison to the prevalent anatase phase in the undoped TiO_2 .

Several non-metal elements have been successfully incorporated into nanosized titania. For instance, C-doped titania has been achieved by heating titanium carbide [12] and by direct burning of a titanium metal sheet in a natural gas flame. Annealing TiO_2 under CO gas flow at high temperatures ($500^\circ\text{C} - 800^\circ\text{C}$) [207] also yielded similar results. N-doped titania nanomaterials have also been synthesised via a number of ways including (a) direct synthesis from a Ti-bipyridine complex (b) the hydrolysis of TTIP in a water/amine mixture and the post treatment of the TiO_2 sol with amines (c) ball milling of TiO_2 in a NH_3 water solution (d) sputtering/ion-implanting techniques with nitrogen (e) heating TiO_2 under NH_3 flux at $500^\circ\text{C} - 600^\circ\text{C}$ (f) calcination of the hydrolysis product of $Ti(SO_4)_2$ with ammonia as precipitator (g) N^{2+} gas flux and (h) decomposition of gas-phase $TiCl_4$ with an atmosphere microwave plasma torch. Through mixing TTIP with ethanol containing thiourea, S-doped titania nanomaterials have been synthesised. Similar products have also been realised via heating sulphide powder and via using sputtering or ion-implanting techniques with S^+ ion flux [12]. Different doping methods are found to induce the different dopant valence states. For example, direct heating of TiS_2 or sputtering with S^+ induced the S^{2-} anion while the incorporated S from thiourea had S^{4+} or S^{6+} state. Some techniques for synthesising F-doped titania nanomaterials involve the following: Mixing TTIP with ethanol containing H_2O-NH_4F , heating TiO_2 under hydrogen fluoride, spray pyrolysis from an aqueous solution of H_2TiF_6 , and using F^+ ion flux with ion-implantation techniques. By adding $TiCl_4$ to ethanol containing HBr , the combinational doping (co-doping) of titania nanomaterials with Cl^- and Br^- have been achieved [12].

2.7.1.2 Light Absorption Properties of Doped Titania Nanomaterials

Metal doping of TiO₂ have been shown to bring about a red shift in the band gap transition or a visible light absorption in several studies [26], [28], [202], [203], [205], [208]. For instance, the absorption spectra for V-, Mn-, or Fe-doped TiO₂, shifted to lower energies as dopant concentration increased [24], [203]. This red shift was ascribed to the charge-transfer transition between the d electrons of the dopant and the CB (or VB) of TiO₂. Using ion implantation doping of TiO₂ with various transition-metal ions (such as V, Cr, Mn, Fe, and Ni) a large shift in the absorption band toward the visible light region was found, with the magnitude of the red shift being in that order (V to Ni). Anpo *et al.* [209], [26] found that the extent of the red shift in the absorption band of Cr-ion-implanted TiO₂ depends on the amount of metal ions implanted [26]. Impregnated or chemically Cr-ion-doped TiO₂ showed no shift in the absorption edge of TiO₂. However, a new absorption band at around 420 nm which appeared as a shoulder peak was attributed to the formation of an impurity energy level within the band gap, with its intensity increasing with the number of Cr ions [26]. The work by Umebayashi *et al.* [208] ascribed the visible light absorption of V-doped TiO₂ to the transition between the VB and the V t_{2g} level [208]. Holes in the VB were responsible for the production of an anodic photocurrent. Photoexcitation occurred via the t_{2g} level of the dopant, for V-, Cr-, Mn-, and Fe-doped TiO₂. The visible light absorption for Mn- and Fe-doped TiO₂ was as a result of the optical transitions from the impurity band tail into the CB. Since the Mn (Fe) t_{2g} level was close to the VB and easily overlapped in highly impure media, the visible light absorption for the Cr-doped TiO₂ can be ascribed to a donor transition from the Cr t_{2g} level into the CB and the acceptor transition from the VB to the Cr t_{2g} level. The study by Frindell *et al.* [191] found that as much as 8 mol % Eu³⁺ ions could be doped into mesoporous anatase TiO₂. With the mesoporous TiO₂ acting as a sensitizer, the excitation of the TiO₂ electrons within their band gap led to non-radiative energy transfer to the Eu³⁺ ions with a bright red luminescence.

Non-metal doped TiO₂, which normally has a colour from white to yellow or even light grey, also features a red shift to longer wavelengths for the onset of the absorption spectra [23], [75], [200], [208], [210], [211], [212], [213]. Generally, the red shifts in the absorption spectra of doped TiO₂ are attributed to the narrowing of the band gap in the electronic structure after doping [23]. In N-doped titania

nanomaterials, the band gap absorption onset experienced a shift that extended from 380 nm for the undoped TiO₂ up to 600 nm. From density functional theory studies [214], the optical absorption of N-doped TiO₂ in the visible light region was primarily located between 400 and 500 nm, while that of oxygen-deficient TiO₂ was mainly above 500 nm [214]. Co-doping of TiO₂ with N and F, prepared via the spray pyrolysis method [210], was found to absorb light up to 550 nm in the visible light regime. S-doped TiO₂ also exhibited significant absorption in the region from 400 nm to 600 nm [211]. A long-tail absorption spectra in the visible light region have been observed for C-doped TiO₂ [212]. Cl-, Br-, and Cl-Br co-doped TiO₂ have been found to increase the optical response of TiO₂ in the visible region [213]. The work by Livraghi *et al.* [215] also revealed that N-doped TiO₂ contained single atom nitrogen impurity centres localised in the band gap of the oxide which were responsible for visible light absorption with promotion of electrons from the band gap localised states to the CB. The work by Serpone [216] suggested that for doped TiO₂ in general, the red shift of the absorption edge is mainly due to the formation of oxygen vacancies and colour centres that absorb the visible light radiation.

2.7.2 Surface Chemical Modifications

Sensitisation is a process whereby a photocurrent is generated with light energy less than that of the semiconductor band gap. With TiO₂ as a semiconductor with a wide band gap having optical absorption in the UV region (<400 nm), any material with a narrower band gap or absorption in the visible or infrared regime can be used as a light-absorbing dye (sensitizer) for TiO₂ materials [13], [22]. These materials include metals, inorganic semiconductors with narrow band gaps, as well as organic dyes. The efficiency with which the sensitizer interacts with the light determines how efficiently the sensitised TiO₂ can interact with the light. A crucial step in the photosensitisation of TiO₂ is the efficient charge transfer from the excited sensitizer to TiO₂, and the charge separation that results from the transfer. The match between the electronic structures of the sensitizer and TiO₂, as well as the structure of the interface, plays an important role in this process. Grain boundaries and bonding between the sensitizer and TiO₂ also play a major role. Thus careful design is

essential in order to avoid the charge trapping and recombination which may eventually impair the performance of sensitised TiO₂.

Narrow band gap inorganic semiconductor sensitised titania nanomaterials systems are often synthesised by the sol-gel method [12]. Vogel *et al.* [217] studied the sensitisation of nanoporous TiO₂ by CdS, PbS, Ag₂S, Sb₂S₃, and Bi₂S₃ and found that the relative positions of the energetic levels at the interface between the quantum size particles and TiO₂ could be optimised for efficient charge separation by using the size quantisation effect. They also found that the photostability of the electrodes could be significantly improved by surface modification of the titania nanoparticles with CdS nanoparticles.

Ohko *et al.* [218] found that when the titania nanoparticle films were sensitised with metal nanoparticles such as Ag, the colour of the film could be switched back and forth reversely between brownish-gray under UV light and the colour of illuminating visible light. This was attributed due to the oxidation of Ag by O₂ under visible light as well as the reduction of Ag⁺ under UV light. Due to the plasmon-based absorption of Ag and the dielectric confinement of the titania nanoparticle film matrix, the colour of the film under visible light could be tuned from green to red and white by changing the size of the Ag nanoparticles. Kawahara *et al.* [219] proposed the mechanism of charge separation at the interface between Ag and titania nanoparticles. They found that, in the multicolour photochromism of titania nanoporous films loaded with photocatalytically deposited or electrodeposited and commercially available Ag nanoparticles, visible light-induced electron transfer from Ag to oxygen molecules played an essential role.

Organic dyes have also been widely used as sensitizers in dye-sensitised nanocrystalline solar cells (DSSCs) in order to improve the optical properties of titania nanomaterials [178], [220], [221]. These dyes are usually transition metal complexes (such as polypyridine complexes, phthalocyanine, and metalloporphyrins) with low lying excited states, [222]. Ru(II), Zn(II), Mg(II), Fe(II), and Al(III) serve as the metal centres for the dyes, while the ligands include nitrogen heterocyclics with delocalised π or aromatic ring systems. The various interactions between the dyes and the titania nanoparticle substrate that normally link the organic dyes to titania nanoparticle surfaces via functional groups include: (a) covalent attachment by

directly linking groups of interest or via linking agents – the preferred way for most dyes of interest, (b) electrostatic interactions via ion exchange, ion-pairing, or donor-acceptor interactions, (c) hydrogen bonding, (d) van der Waals forces, etc. [12]. Stable linkages with the surface hydroxyl groups on TiO₂ substrates have been observed for groups such as silanyl (–O–Si–), amide (–NH–(C=O)–), carboxyl (–O–(C=O)–), and phosphonato (–O–(HPO₂)–) [12]. Carboxylic and phosphonic acid derivatives react with the hydroxyl groups to form esters, while amide linkages are obtained via the reaction of amine derivatives and dicyclohexyl carbodiimide on TiO₂. The functional groups that are based on carboxylic acids are the most common and successful.

2.8 APPLICATIONS OF TITANIA NANOMATERIALS

Titanium dioxide is very stable, nontoxic, and cheap. It is commonly found in paints, toothpaste and many other materials that requires a white base pigment. Other promising areas of application include photocatalysis, photovoltaics, sensing, electrochromics, as well as photochromics. Since titania nanomaterials normally have a high absorption in the UV region, their electronic band gaps being larger than 3.0 eV, their optical and biologically benign properties allow them to be suitable for UV protection applications [12].

Titania nanomaterials can provide antifogging functions on various glass products (such as mirrors and eyeglasses), with surfaces that are superhydrophilic (water-surface contact angle larger than 130°) [223] or superhydrophobic (water-surface contact angle less than 5°) [224]. For example, Feng *et al.* [162] found that reversible superhydrophilicity and superhydrophobicity could be switched back and forth for titania nanorod films. Owing to the superhydrophilicity or superhydrophobicity, self-cleaning and stain-proofing properties can also be imparted on a variety of surfaces using titania nanomaterials. These extraordinary nanomaterials have also been used as sensors for various gases and humidity due to the electrical or optical properties which change upon adsorption.

The production of electricity and/or hydrogen using efficient materials is one of the most important research areas for future clean energy applications. When sensitised

with organic dyes or inorganic narrow band gap semiconductors, TiO₂ can absorb light into the visible light region and convert solar energy into electrical energy for solar cell applications [12]. For instance, an overall solar to current conversion efficiency of 10.6% has been achieved by the group led by Grätzel [17] with DSSC technology. Given the redox potential of water, titania nanomaterials have been widely studied for water splitting and hydrogen production as a result of their suitable electronic band structure [207]. Dye-sensitised or metal-incorporated titania nanomaterials have also found applications in the building of photochromic devices [219]. The photocatalytic decomposition of various pollutants is yet one of the many applications of nanosized TiO₂ materials.

2.8.1 Photocatalytic Applications

Being the most efficient and environmentally benign photocatalyst, TiO₂ has been most widely used for photodegradation of various pollutants [155], [154], [201]. As it has been carried out with *E. coli* suspensions, photocatalysts based on TiO₂ can also be used to kill bacteria. Further, the strong oxidising capabilities of illuminated TiO₂ can be used to treat cancerous tumour cells. In photocatalytic reaction mechanisms, the absorption of photons with energy larger than the band gap of titania results in electrons being excited from the valence band to the conduction band, thereby creating electron-hole pairs [14], [225], [226]. These charge carriers migrate to the surface where they react by decomposing the chemicals adsorbed there. In this photodecomposition process, one or more radicals or intermediate species (such as •OH, O²⁻, H₂O₂, or O₂) usually play an important role in the photocatalytic reaction mechanisms. The photocatalytic activity of a semiconductor is largely influenced by (i) the light absorption properties, such as light absorption spectrum and coefficient, (ii) electron and hole reduction and oxidation rates on the surface, and (iii) the electron-hole recombination rate. However, the relation between the physical properties and the photocatalytic activities is not a straightforward one. For example, a large surface area with a constant surface density of adsorbents is expected to lead to faster surface photocatalytic reaction rates. Conversely, with the surface being a defective site, the larger the surface area, the faster is the recombination. Also, as the crystallinity increases, the bulk defects reduce and the photocatalytic

activity increase. The enhancement of the crystallinity of titania nanomaterials via high temperature treatment usually brings about the aggregation of small nanoparticles, which in turn decreases the surface area. From considerations such as these, optimal conditions may vary from case to case [226].

The catalytic activity of undoped or “pure” TiO₂ improves as the size of its particles decreases. This is because of the increase in the fraction of atoms located at the surface of these 1st generation nanomaterials, with higher surface area to volume ratios [12]. Further, the increase in the band gap energy as nanoparticle size decreases can potentially improve the redox potential of the valence band holes and the conduction band electrons. This allows photoredox reactions, which might not otherwise occur in bulk materials, to proceed readily [12]. A drawback of titania nanoparticles is that only a small percentage of sunlight can be utilised for photocatalysis. In practice, each photocatalytic reaction has an optimal size [12].

Second generation (metal-doped) titania nanomaterials have been widely studied, over the past decades, for improved photocatalytic performance (under visible light irradiation) on the degradation of various organic pollutants. A systematic study on the photocatalytic activity of titania nanoparticles doped with 21 transition metal elements on the oxidation of CHCl₃ and the reduction of CCl₄ was conducted by Choi *et al.* [24]. They established that photocatalytic activity was related to the electron configuration of the dopant ion. Doping with Fe³⁺, Mo⁵⁺, Ru³⁺, Os³⁺, Re⁵⁺, V⁴⁺, and Rh³⁺ at 0.1 wt % to– 0.5 wt % significantly increased the photoreactivity, whereas wt % Co³⁺ and Al³⁺ doping decreased the photoreactivity. The dopant ions with closed electron shells were shown to have little or no effect on the activity. The charge carrier recombination rates and interfacial electron-transfer rates appeared to be significantly influenced by the presence of metal ion dopants in the TiO₂ matrix. Photoreactivity was found to be a complex function of the dopant concentration, the electron donor concentrations, the energy level of dopants within the TiO₂ lattice, their d electronic configurations, the distribution of dopants and the light intensity. Peng *et al.* [227] found that Be²⁺-doping of titania nanomaterials was beneficial, when the doping ions were in the shallow surface, whereas doping was detrimental deep in the bulk. However, not all the metal-doped titania nanomaterials showed higher photocatalytic activities when compared with the pure, undoped form. Reduced photoreactivity was found for Vanadium-doped titania nanoparticles on the

photooxidation of 4-chlorophenol [12]. Vanadium appeared to achieve the decrease by promoting charge-carrier recombination with electron trapping at VO^{2+} centres or with hole trapping at V^{4+} impurity centres. These serve to shunt charge carriers away from the solid/ solution interface.

A variety of studies on nonmetal-doped titania nanomaterials (third generation photocatalyst) have also revealed improved visible light photocatalytic activities compared to those of pure titania nanomaterials [23], [200]. Nitrogen and Sulphur-doped titania nanomaterials have been demonstrated to display a higher photocatalytic activity in the visible region but lower activity in the UV [12].

2.8.2 Photovoltaic Applications

2.8.2.1 The Nanocrystalline Titania Electrode in DSSCs

At the heart of a DSSC photovoltaics system that is based on nanocrystalline titania electrodes is the nanocrystalline mesoporous TiO_2 film with a monolayer of the charge transfer dye attached to its surface [17], [18], [22]. The film is placed in contact with a redox electrolyte or an organic hole conductor. Figure 13 depicts the structure and operating principles of the DSSC. The photoexcitation of the sensitising dye (S) serves to inject an electron into the conduction band of TiO_2 film. The electron can be conducted to the outer circuit to drive the load and provide electric power. The electrolyte (usually an organic solvent containing a redox system, such as the iodide/triiodide couple) donates electrons which serves to restore the original state of the dye. The recapture of the conduction band electron by the oxidised dye is prevented by the regeneration of the sensitiser by the iodide. The iodide itself is regenerated by the reduction of triiodide at the counterelectrode. Finally, the circuit is completed via electron migration through the external load. The open circuit voltage of the solar cell generated under illumination corresponds to the difference between the redox potential of the mediating electrolyte and the Fermi level of the nanocrystalline TiO_2 film indicated with a dashed line. Overall, the device generates electric power from light without suffering any permanent chemical transformation [17], [18], [22]. According to Cahen *et al.* [228] the basic cause for the

photovoltage is the change in the electron concentration in the nanocrystalline electron conductor that results from photoinduced charge injection from the dye.

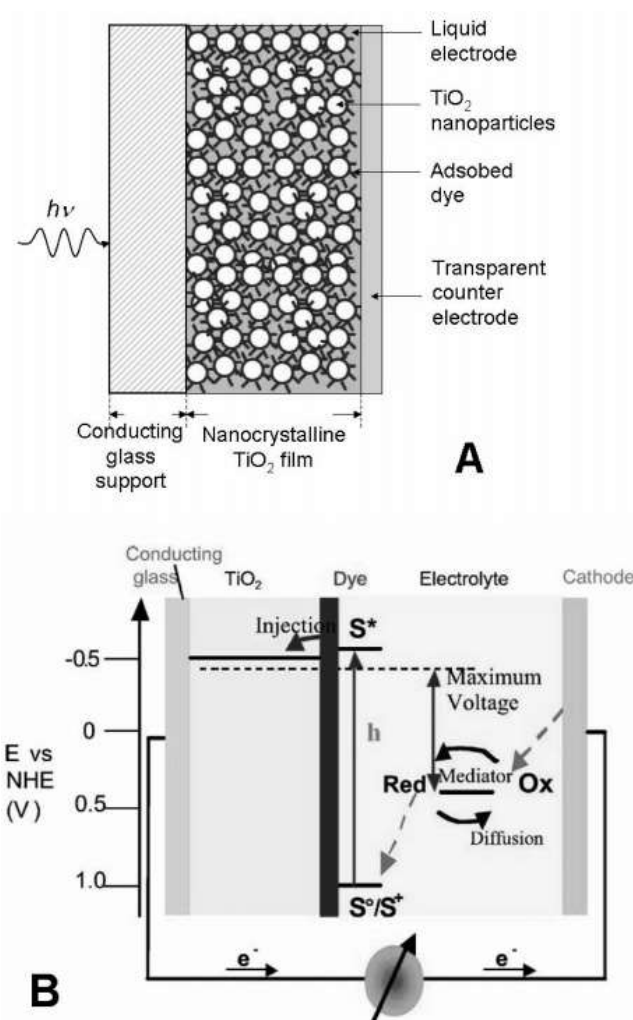


Figure 13: Schematic representation of the structure (A) and operating principles (B) of the DSSC (or dye-sensitised nanocrystalline solar cell).

In the past decades, a large amount of effort was made in trying to optimise the organic dyes in DSSCs [221], [222], [229], [230], [231]. Only recently has attention been given to the titania nanocrystalline electrode. Some of the important results that were obtained include the following:

Solar conversion efficiency enhancement of about 50% was recorded by Zukałova *et al.* [221] for ordered mesoporous titania nanocrystalline thin film electrodes, as compared to traditional films of the same thickness made from randomly oriented

anatase nanocrystals. This improvement resulted from a remarkable enhancement of the short circuit photocurrent, due to the huge surface area accessible to both the dye and the electrolyte. From the study by Adachi *et al.* [222], dye-sensitised solar cells with electrodes made of disordered single-crystalline titania nanotubes (10-nm diameter, 30 nm to 300 nm in length) displayed an efficiency of about 5% [222]. This is more than twice the short-circuit current density in comparison with those made of Degussa P-25 titania nanoparticles in a similar thin-film thickness region. Somani *et al.* [229] achieved an increase in light conversion efficiency of at least 1 order of magnitude by utilising inversed opal TiO₂ films (rather than nanocrystalline TiO₂ films) as electrodes in fabricating solid-state dye-sensitised organic-inorganic hybrid Grätzel solar cells. This improvement was attributed to the wide and well-connected pores in mesoporous TiO₂ films that facilitated easy permeation of the hole transporting material, allowing good contact with the dye and hence the optimal cell efficiency. Higher performance (solar-to-electric energy conversion efficiency $\eta \approx 7\%$) have been reported by Han *et al.* [230], for a hybrid titania nanocrystalline electrode, composed of a mixture of anatase (71%) and rutile phases, than one made of pure anatase.

Various methods have been adopted to prevent losses due to the recombination of photoinjected electrons with oxidised dye molecules or a redox couple at the surface of nanocrystalline TiO₂, which stand to reduce the conversion efficiency of a DSSC. Kang *et al.* [231] introduced a buffer layer of a TiO₂-WO₃ composite material, between a TCO substrate and a TiO₂ layer, which effectively prevented dye molecules and electrolytes from contacting the conducting substrate directly. Performance enhancement were noted for the buffer layer having 15 mol % to 75 mol % WO₃. Core-shell TiO₂ electrodes consisting of a nanoporous TiO₂ covered with a shell of another metal oxide have been shown to slow recombination processes through the formation of an energy barrier at the TiO₂ surface [12]. The conduction band potential of the shell needs to be more negative than that of TiO₂ in order to generate an energy barrier for the reaction of the electrons present in TiO₂ with the oxidised dye or the redox mediator in solution. Two methodologies are employed in the fabrication of the nanoporous core-shell electrodes. One involves synthesis of core-shell nanoparticles that are applied onto the conducting substrate [12]. Here, an energy barrier forms at both the electrode/electrolyte interface as well

as between the individual titania nanoparticles. The second approach involves a nanoporous TiO₂ electrode coated with the thin shell layer [12]. The direct connection between titania nanoparticles enables electron transport through the TiO₂ material.

Improving the spectral response of photosensitisers at the low-energy end of the solar spectrum has proven unsuccessful because dye molecules with high red absorbance have lower excited-state excess free energy, thus reducing the quantum yield for charge injection. By increasing the thickness of the film (beyond 10 μm – 12 μm) in order to increase the absorbance in the red light regime only results in an increase in the electron transport length and the recombination rate, as well as a reduction in the photocurrent. One approach in improving efficiency (which involves electrode coupling using photonic crystals) is to enhance the light scattering in the TiO₂ films so as to increase the path length of light. The small size of titania nanoparticles (10 nm – 30 nm) which ensures high surface areas however makes conventional nanocrystalline TiO₂ films poor light scatterers. Improvement in light scattering, and hence harvesting, have been achieved through applying a scattering layer to the nanocrystalline film and through the mixing of nanoparticles with larger particles [12].

2.8.2.2 Metal/Semiconductor Junction Schottky Diode Solar Cell

A multilayer photovoltaic device structure in which photon absorption occurred in photoreceptors deposited on the surface of an ultrathin metal/semiconductor junction Schottky diode has been reported by McFarland *et al.* [232]. The device featured a solid-state multilayer with a photoreceptor layer deposited on a 10 nm – 50 nm Au film, which capped 200 nm of TiO₂ on an ohmic metal back contact. There are four stages involved in photon-to-electron conversion. In stage 1, light absorption takes place in the surface-absorbed photoreceptors, thus giving rise to energetic electrons [232]. Next, these excited-state-photoreceptor-electrons are injected into the conduction levels of the neighbouring conductor, where they travel ballistically through the metal at an energy ($1e$) above the Fermi energy, E_f [232]. The thirdly stage is internal electron emission. Here the electrons traverse the metal and enter the conduction levels of the semiconductor – provided that $1e$ was greater than the Schottky barrier height, f , and the carrier mean-free path was long compared to the

metal thickness [232]. Finally, the absorbed photon energy, preserved in the remaining excess electron free energy when it was collected at the back ohmic contact, gives rise to the photovoltage, V [232]. The photooxidised dye is then reduced by transfer of thermalised electrons from states near E_f in the adjacent metal [232]. By using a variety of materials, this alternative approach to photovoltaic energy conversion might provide the basis for durable low-cost solar cells [12].

2.8.2.3 Doped Nanotitania-Based Solar Cell

Nitrogen-doped titania nanocrystalline porous thin films have been shown by Lindgren *et al.* [75] to have visible light absorption in the wavelength range from 400 nm to 535 nm. The generated incident photon-to-current efficiency response was found to be in good agreement with the optical spectra. At moderate bias, the increase in photoinduced current due to visible light, was up to 200 times as compared with -TiO_2 electrode.

2.8.3 Photocatalytic Water Splitting

Since its discovery in 1972 by Fujishima and Honda [12], the photocatalytic splitting of water into hydrogen and oxygen using TiO_2 electrode has brought much hope for achieving clean and sustainable energy sources [233]. In the process, the TiO_2 material absorbs light having energy larger than the band gap, generating electrons in the conduction band and holes in the valence band. These photogenerated charge carriers bring about redox reactions in which water molecules are reduced by the electrons to form H_2 and oxidised by the holes to form O_2 . For successful water splitting, the width of the band gap must be such that the bottom level of the conduction band is more negative than the reduction potential of H^+/H_2 (0 V vs NHE), while the top level of the valence band is more positive than the oxidation potential of $\text{O}_2/\text{H}_2\text{O}$ (1.23 V) [233]. The potential of the TiO_2 band structure just matches what is required thermodynamically. Factors that influence the photocatalytic properties of TiO_2 include charge separation, mobility, and lifetime of photogenerated electrons and holes [233]. Others involve surface properties such as surface states, surface chemical groups, surface area, and active reaction sites [233]. The local pH

environment and surface structures of the TiO₂ electrode are also affected by the water-splitting process [12].

Fast, undesirable electron-hole recombination reaction is often a hindrance to the splitting of water into H₂ and O₂ in the simple aqueous suspension system [107], [234]. To control the electron-hole recombination process, thereby improving photoefficiency, “sacrificial” reagents can be added as reversible redox mediators, [234]. These reagents include various compounds such as methanol, ethanol, EDTA (an ethylenediaminetetraacetic derivative), Na₂S, and Na₂SO₄ or ions such as I⁻, IO₃⁻, CN⁻, and Fe³⁺. In their study of water splitting over a Pt-TiO₂ catalyst using various sacrificial reagents, Galinska *et al.* [235] found that the sacrificial reagents played a key role in hydrogen production via the photocatalysed water-splitting reaction. EDTA and Na₂S acted as effective hole scavengers, inhibiting O₂ formation and hence the recombination reaction of oxygen with hydrogen.

Highly ordered titania nanotube arrays have been found, by Mor *et al.* [236], to decompose water efficiently under UV radiation. The nanotube wall thickness was found to be a key parameter that influences the magnitude of the photoanodic response and the overall efficiency of the water-splitting reaction. A photoconversion efficiency of 12.25% was also claimed for illumination at 320 nm – 400 nm (98 mW/cm²). Park *et al.* [207] further established that, when doped with carbon, TiO_{2-x}C_x nanotube arrays exhibited greater efficient water splitting under UV and visible light illumination (>420 nm) than pure titania nanotube arrays [207].

Water splitting under visible light can be realised with doped titania nanomaterials. Since the band gaps of oxide semiconductor photocatalysts with the potential for H₂ evolution inevitably become wide. Accordingly, strategies that can be considered for the development of visible light-driven photocatalysts include: (i) forming a donor level above a valence band by doping some element into conventional photocatalysts with wide band gaps such as TiO₂; (ii) creating a new valence band employing some element; and (iii) controlling the band structure by making a solid solution. By using a radio frequency magnetron sputtering method, Matsuoka *et al.* [237] were able to develop visible light responsive titania nanocrystalline thin films. This method involves the decomposition of water when Pt-loaded and in the presence of a sacrificial reagent such as methanol or silver nitrate under visible light.

It is also possible to achieve water splitting over dye-sensitised TiO₂. For instance, Park *et al.* [238] were able to design two different kinds of cells with bipolar dye-sensitised TiO₂/Pt panels connected so that their photovoltages added to provide vectorial electron transfer for unaided water splitting.

As found by Akikusa *et al.* [239], coupled/composite self-driven system for water splitting under illumination could be achieved with the combination of single-crystal p-SiC and nanocrystalline n-TiO₂ photoelectrodes. Both photoelectrodes (p-SiC and n-TiO₂) are placed side by side facing the light source and in contact with an electrolyte of 0.5 M H₂SO₄. The open circuit potential between the n-TiO₂ and p-SiC photoelectrodes was found to be 1.24 V, with a maximum photocurrent density of 0.05 mA cm⁻² under a closed circuit potential of 0.23 V, corresponding to an efficiency of 0.06%. The low cell photocurrent density and the photoconversion efficiency for the water splitting reaction were ascribed to the high band gap energies of both semiconductors and high recombination of photogenerated carriers mainly in the covalently bonded p-SiC [239].

2.8.4 Electrochromic Devices

Electrochromism refers to the ability of a material to experience colour change upon oxidation or reduction. Electrochromic devices are capable of varying their output of visible light and solar radiation upon electrical charging and discharging, using a low voltage [12]. For instance, by regulating the amount of energy passing through a “smart window” the need for air conditioning in a cooled building can be reduced substantially. A small voltage applied to the windows will cause them to darken, whereas reversing the voltage causes them to lighten [12]. With an adequate control strategy, the energy efficiency inherent in this technology can be substantial. In addition, the transmittance regulation can facilitate glare control as well as user control of the indoor environment. Because it is the absorbance that is modulated, rather than the reflectance, electrochromic devices tend to heat up in their low-transparent state [240] – [241].

Titania nanomaterials have been extensively investigated as electrochromic devices, such as electrochromic windows and displays [12]. Reported electrochromism of

nanocrystalline thin film TiO₂ electrodes fall into two categories. One type involves Li-containing electrolytes related to the reversible insertion of Li⁺ into the anatase lattice of the nanoparticles. The second type electrodes modified with viologens and/or anthraquinones equipped with a surface anchoring group [12]. This latter category usually possess fast switching times and substantial optical dynamics. This is due to the combination of good conductivity between the titania nanoparticles and the fast electron exchange between TiO₂ and the monolayer of the electrochromic compound covering each particle. Bach *et al.* [242] was able to demonstrate high-quality paper-like electrochromic displays based on nanostructured TiO₂ films modified with electrochromophores with excellent ink-on-paper optical qualities, fast response times, and low power consumption. Using a completely transparent counterelectrode based on mesoporous antimony tin oxide coated with CeO₂, Moeller *et al.* [243] established electrochromic pictures with appreciable resolution of 360 dpi in transparent and reflective electrochromic displays (ECD) based on ink-jet printing technology and cascade-type crosslinking reactions of viologens in the mesopores of a TiO₂ electrode.

2.8.4.1 Fundamentals of Electrochromic Devices

The principle of the electrochromism of a molecular monolayer adsorbed on TiO₂ involves a molecule which functions as the electrochromophore that exhibits different colours in different oxidation states [12]. This molecule is chosen such that its redox potential lies above the conduction band edge of the titania nanocrystalline electrode at the liquid/solid interface. By this, electrons can be transferred reversibly from the conduction band to the molecule and the TiO₂ electrode can behave like a conductor for the adsorbed electroactive species. (The reduction process will be irreversible if the redox potential is situated below the conduction band edge.)

Nanocrystalline TiO₂ film electrodes are highly attractive electrochromic elements for a number of reasons [12]. Amongst them are the high conductivity of the nanocrystalline TiO₂ particles, the fast electron exchange with the molecular monolayer, optical amplification by the porous structure and fast charge compensation by ions in the contacting liquid [241]. The principle of efficiency relies on fast interfacial electron transfer between the nanocrystalline TiO₂ and the

adsorbed modifier as well as on the high surface area of the TiO₂ support that amplifies optical phenomena by 2 or 3 orders of magnitude [241]. By loading nanoporous films with Ag nanoparticles through photocatalytic means, Ag-TiO₂ films have been found to exhibit multicolour photochromism, which relates to the oxidation and reduction of Ag nanoparticles under UV and visible radiation [241].

Closed cells can be built by combining a transparent nanocrystalline electrode with a counterelectrode which is able to provide enough electrons to allow complete reduction of viologen [12]. The simplest counterelectrode is conducting glass. For displays applications, Zn can be used as a counterelectrode. Short-circuiting the two electrodes leads to electron flow from the zinc (which oxidises to Zn²⁺ ions) to the viologens of the nanocrystalline electrode [12]. Reversing this process can be achieved under a potential of about 1 V – 2 V [241].

Photoelectrochromic smart window with flexible substrates and solid-state electrolytes has been demonstrated by Pichot *et al.* [240]. It is based on a dye-sensitised TiO₂ electrode spin-coated onto In-Sn oxide-coated polyester substrates coupled with a WO₃ electrochromic counterelectrode, separated by a cross-linked polymer electrolyte containing lithium iodide (LiI). In the bleached state, the device typically transmitted 75% of visible light but after exposure to white light for a few minutes, the window turned dark blue, transmitting only 30%. Upon the removal of the light source, the device bleached back to their initial uncoloured state spontaneously. Essentially, the photoelectrochromic device behaved like a capacitor as no mobile oxidised species (i.e., I₂) was initially present in the electrolyte.

2.8.5 Hydrogen Storage

Titania nanotubes has the ability to reproducibly store up to approximately 2 wt % hydrogen at room temperature and 6 MPa – according to the study by Lim *et al.* [160]. Approximately 75% of this stored H₂ is released as a result of physisorption when the hydrogen pressure reduces to ambient conditions. About 13% of the hydrogen is weakly chemisorbed and is released at 70°C, and roughly 12% is strongly bonded to oxide ions and released only at temperatures above 120°C as H₂O.

Bavykin *et al.* [244] investigated the sorption of hydrogen between the layers of the multilayered wall of nanotubular TiO₂ in the temperature range of -195°C – 200°C and at pressures of 0 bar to 6 bar. Intercalation of H₂ was noted between layers in the walls of titania nanotubes forming host-guest compounds TiO₂•xH₂, where $x \leq 1.5$ and decreasing at higher temperatures. The rate of hydrogen uptake was a reversible process which increased with temperature, and the characteristic time for hydrogen sorption in titania nanotubes was several hours at 100°C. Heating the sample in a vacuum to 200 °C led to a complete desorption of hydrogen, returning the weight of the sample to its initial value.

2.8.6 Gas Sensing Applications

Metal oxides have been used for nearly four decades for gas sensing applications. The main principle behind the gas sensing mechanism being the change in their electrical resistance on exposure to a gas, as a result of electronic exchange. The discoveries by Seiyama *et al.* [113] in 1962, and in the same year, by Taguchi *et al.* [245] were the beginning of what has been a rapid gas sensor developmental phase. Since 1968 Taguchi sensors have been commercially available through the establishment of Figaro Engineering Inc. in 1969 [246]. Solid state sensors need to be selective to the target gas and stable in their performance in the sensing environment. Selectivity, stability and repeatability in the sensing environment are important parameters that are normally investigated for the sensor.

Nanocrystalline titania has been widely studied as sensors for various gases. Grimes *et al.* [177], [176] found that titania nanotubes were excellent room-temperature hydrogen sensors not only with a high sensitivity of 10⁴, but also with an ability to self-clean photoactively after environmental contamination. The sensors showed a fully reversible change in electrical resistance of approximately 175,000% in response to 1000 ppm of hydrogen at 24°C. The hydrogen-sensing capabilities of the sensors were largely restored by exposure to UV light after being completely extinguished through contamination with 10W-30W motor oil.

Schottky barrier modulation of devices like Pd/TiO₂ or Pt/TiO₂ form the basis for many types of room-temperature, titania nanomaterial based, hydrogen sensors [12]. High-temperature hydrogen sensors have been used to examine the change in electrical resistance with hydrogen concentration. In the study by Birkefeld *et al.* [247], the resistance of anatase TiO₂ was found to vary in the presence of CO and H₂ at temperatures above 500 °C. However, on doping with 10% alumina, selectivity for hydrogen was realised.

Anodised nanoporous titania films with a Pd Schottky barrier that were sensitive to hydrogen at 250°C, have been reported by Shimizu *et al.* [248]. In their investigation of the mechanism of hydrogen sensing by Pd/TiO₂ Schottky diodes, Kobayashi *et al.* [249] found that the formation of adsorbed water from adsorbed oxygen at the Pd/TiO₂ interface was the dominant reaction for the Pd/TiO₂(001) diodes throughout the hydrogen concentration range of 0 to 3000 ppm. This reaction was dominant only for hydrogen concentrations below 100 ppm when using the Pd/TiO₂(100) diodes. At higher hydrogen concentrations, hydrogen adsorption on bare Pd atoms became dominant. By measuring the change in the electrical resistance of the sensor upon exposure to different hydrogen concentrations under a constant hydrogen gas flow rate, Carney *et al.* [250] established that sensors based on SnO₂-TiO₂ with higher surface areas were more sensitive to hydrogen in the presence of oxygen. Ordered mesoporous TiO₂ have been shown, by Devi *et al.* [251], to exhibit higher H₂ and CO sensitivities than sensors made from common TiO₂ powders due to increased surface area, and improvement in the sensitivity could be enhanced by loading the sensor with 0.5 mol % Nb₂O₅. Higher performance in H₂ sensing for nanoscaled TiO₂ over microscale TiO₂ (as a consequence of the larger surface area) was also reported by Gao *et al.* [252].

Oxygen sensing based on Pt-doped TiO₂ nanomaterials show improved gas sensitivity, low operation temperature (350°C – 800°C), and short response time (<0.1 s) [12]. The mechanism involves the combination of Pt/TiO₂ interfaces in a Schottky-barrier mechanism and an oxygen-vacancy bulk effect. Normally, at high temperatures, titania-based devices can be used as thermodynamically controlled bulk defect sensors to detect oxygen over a large range of partial pressures. However at low temperatures, extremely sensitive O₂ detection is made possible

with Pt/TiO₂ Schottky diodes. Oxygen-sensing sites, formed from photoirradiation of oxygen vacancies have been observed in Ta-doped TiO₂ sensors. Nb⁵⁺-doped titania nanomaterials have been shown to enhance sensitivity by a factor of 65 as compared with the undoped material at a lower operating temperature.

La-doped titania nanoparticles are showing promise in the sensing of ethanol [12]. The addition of Cu or Co titania nanoparticles was also shown to be good candidates for CO sensing. Improved performance for ethanol sensing was found by Garzella *et al.* [253] for W-doped TiO₂ over γ -TiO₂. Ta-doped and Nb-doped TiO₂ were found to be beneficial for the stabilisation of the nanophase, resulting in selectivity enhancement toward CO and NO₂. The enhancement of sensitivity toward ethanol and methanol was also observed for TiO₂ films when doped with Pt and Nb.

From the study by Benkstein *et al.* [254], high-sensitivity conductometric gas sensor materials could be realised with mesoporous titania nanoparticle thin films prepared on MEMS micro-hot-plate platforms. Here, nanoparticle films were deposited onto selected micro-hot-plates in a multielement array via microcapillary pipet before being sintered with the micro-hot-plate. The relative thickness of the films was varied by using one, two, three, or four drops of 6% mass fraction TiO₂ to cast the film. The ratio of the film conductance in the presence of an analyte to the baseline conductance measured in dry air define the sensitivity ($S = G/G_0$). The thicker films showed a higher baseline conductance and a higher overall sensitivity to methanol. The high internal surface area of the porous nanoparticle films were considered to be responsible for the higher sensitivity to target analytes [254].

Montesperelli *et al.* [255] found K-doped nanocrystalline titania films showed high sensitivity of magnitude of 10⁷ with great stability over time. Optical humidity sensors, based on the variations in the intensity of light with in humidity changes were fabricated by Yadav *et al.* [256] using nanocrystalline titania films as well. A thin U-shaped borosil glass rod, with a film of TiO₂ deposited on it, served as the sensor element.

Several promising results on TiO₂ nanotube based sensors for H₂ sensing have been reported by Grimes *et al.* [176]. They developed a room temperature hydrogen sensor comprised of a TiO₂ nanotube array which can recover substantially from poisoning by environmental contamination. The nanotube arrays are fabricated by

anodising titanium foil in an aqueous electrolyte solution containing hydrofluoric acid and acetic acid. A 10 nm coating of Pd was evaporated onto the surface of the titania nanotube array film to enhance the hydrogen sensitivity of the sensor. Upon exposure to 100 ppm hydrogen at 25°C the sensor exhibited over 4 orders of magnitude in electrical resistance change.

2.9 CHARACTERISATION TECHNIQUES

The material properties of nanostructured metal oxide and conducting polymer thin films are strongly dependant on the deposition techniques and deposition parameters, and are known to vary considerably from bulk material properties [257]. For example, synthesising nanostructured materials with highly oriented single crystal forms require extremely precise and controlled deposition parameters. Thus, acoustic and electrical properties of the nanostructured material based thin films are directly affected by the synthesis and deposition technique and associated deposition parameters. Additionally, the properties of the nanostructured materials can be varied significantly depending on the substrate on which they are grown. Thus, to understand the fundamental properties of various nanosystems, it is necessary to characterise their structures at a nanometre or atomic level. This, in turn, allows understanding of the synthesis-structure-properties relationships of nanosystems, such as nanomaterial based gas sensors.

To observe, measure, and tailor the properties of nanostructured materials for fundamental analysis and various potential applications, high precision characterisation instruments are increasingly required. Extreme accuracy, as well as atomic level resolution is needed for the characterisation and manipulation of individual nanostructures. Remarkable efforts have therefore been given to develop and upgrade various microscopic and spectroscopic techniques that will play a central role in characterisation and measurement of nanostructured materials. Some of the instruments are concerned with what lies within a few Angstroms of the sample surface (i.e. surface-sensitive), while others characterise the bulk of the material. The various techniques that are most widely used in characterising nanostructured materials can be broadly classified as either structural or chemical as shown in Table 4.

Table 4: Classification of the various characterisation techniques that are most widely used in characterising nanostructured materials.

Characterisation Techniques	Structural Characterisation	X-ray Diffraction (XRD)	
		Electron Microscopy (EM)	Scanning electron microscopy (SEM) Transmission electron microscopy (TEM)
		Scanning Probe Microscopy (SPM)	Scanning tunnelling microscopy (STM) Atomic force microscopy (AFM)
		Chemical Characterisation	Optical Spectroscopy
		Electron Spectroscopy	Energy dispersive X-ray spectroscopy (EDS) Auger electron spectroscopy (AES) X-ray photoelectron spectroscopy (XPS)
		Ion Spectroscopy	Rutherford backscattering spectrometry (RBS) Secondary ion-mass spectrometry (SIMS)

Nanomaterials and nanostructures can be analysed and characterised by any combination of the above techniques depending on the specific applications. For example, XRD has been widely used for the determination of crystallinity, crystal structures and lattice constants of nanostructured materials and thin films. SEM and TEM, together with electron diffraction pattern have been commonly used for observing the images of materials and structures on the nanometre scale.

The characterisation techniques that are used in the current research include the following:

- X-Ray Diffraction (XRD)
- Raman Spectroscopy
- Scanning Electron Microscopy (SEM)
- Energy-Dispersive X-ray Spectroscopy (EDS, EDX, or XEDS)
- Ultraviolet–Visible spectroscopy (UV-Vis or UV/Vis)
- Photoluminescence (PL)
- Gas Sensing

More information is provided on each technique in Section 3.3.

RESEARCH METHODOLOGY

3.1 INTRODUCTION

In the present study, single-doped, double-doped and undoped titania nanoparticles have been successfully synthesised. This was attained via the sol-gel method of sample preparation. All the samples were characterised using a variety of techniques, in order to render the associated properties. The investigation also examined the performance of the synthesised materials in gas sensing applications. In this chapter, the synthesis of the powder samples and their characterisation are described. The theories used in calculations are also discussed thereafter. Background information on synthetic methods and overviews on characterisation techniques are provided in Chapter 2.

In the following, we briefly describe the techniques, showing their main characteristics, comparing their analytical properties and discussing the advantages or disadvantages of every technique.

3.2 POWDER SAMPLE SYNTHESIS

TiO₂ has been synthesised by several methods, (as described in Section 2.6). Of these, the precipitation of alkoxides, followed by hydrothermal treatment or calcination (also known as the sol-gel method) is the most widely preferred method in the production of TiO₂-based materials because of the advantages derived from its ability to synthesise nanosized crystallised powder of high purity at relatively low temperature.

The method of synthesis used in this study is the sol-gel approach [258]. The method was developed in the 1960s mainly due to the need of new synthesis methods in the nuclear industry. According to Hench and West [131], the goal of the method is to control the structure of a material on a nanometre scale from the earliest stages of processing. With this wet-chemical synthesis approach, the composition and microstructure of the nanomaterials can be controlled by the precursors and processing conditions regime. Sol-gel processing not only has the ability to synthesise nanosized crystallised powders of high purity, but also provides for excellent chemical homogeneity and the possibility of deriving unique metastable

structures at relatively low reaction temperatures. It is composed of two sets of simultaneous reactions (namely hydrolysis and polycondensation) which involves the formation of a metal-oxide-polymer/gel network from molecular precursors such as metal alkoxides or metal salts [259]. Typically, sol-gel-derived precipitates are amorphous in nature, requiring further heat treatment to induce crystallisation. The calcination process, which may induce phase transformation, often gives rise to particle agglomeration and grain growth [259].

Further discussion of the sol-gel method is presented in Section 2.6.1 (page 45) of this thesis.

3.2.1 Materials

In preparing the nanocrystalline titania samples used in this research, the following precursors were used in the sol–gel formulation:

- | | |
|-------------------------------|--|
| a. Titanium (IV) Isopropoxide | $\text{Ti}\{\text{OCH}(\text{CH}_3)_2\}_4$ |
| b. Silver Nitrate | AgNO_3 |
| c. Copper Chloride | CuCl_2 |

The analytical reagent-grade chemicals were sourced from Sigma-Aldrich [260]. The specification sheets of these chemicals are provided in Appendix D. All chemicals purchased from the supplier were used without further purification.

3.2.2 Quantities

A program for determining the quantities of precursors needed was designed in Microsoft Excel® 2010. The main inputs for the program include an estimate of the mass of the final product desired, as well as the dopant concentration or levels. The calculated quantities, by mass or volume, are then displayed as outputs, for each precursor material. Further details of the worksheet are given in Appendix E.

Table 5 displays the quantities of precursors used in synthesising the TiO_2 nanopowders. The calculations were estimated to yield about 100 g of each final sample species if losses are ignored.

Table 5: Quantities of precursors used in the preparation of doped and undoped TiO₂ powder species. Ignoring losses, the calculations were estimated to yield about 100 g of each final sample species.

Species	Dopant Level (wt%)	AgNO ₃ (g)	CuCl ₂ (g)	Ti{OCH(CH ₃) ₂ } ₄ (cm ³)
TiO ₂ (pure)	–	–	–	381.95
Ag\TiO ₂	5	8.29	–	381.95
Cu\TiO ₂	5	–	11.14	381.95
Ag+Cu\TiO ₂	5 + 5	8.75	11.76	381.95
½Ag+Cu\TiO ₂	2.5 + 2.5	4.14	5.57	381.95

3.2.3 Procedure

The basic steps involved in synthesising the nanosized titania powders via the sol-gel formalism are as follows:

- a. About 10 ml ethanol is added to each 80 cm³ of titanium isopropoxide solution
- b. The mixture is stirred for 60 minutes
- c. 30 ml of water is added for each 80 ml of the mixture
- d. The precipitate (xerogel) is filtered and left to dry overnight at room temperature for 16 hours
- e. The solid is dried at 100°C
- f. The solid is ground in a pestle and mortar.

For doped titania nanopowders, the dopant solution (to be added to the ethanol + titanium isopropoxide solution) is first prepared. In a typical synthesis, the dopant salt (AgNO₃, CuCl₂) is primed by first dissolving it in as little water as possible. About 10 ml of ethanol is then added to a portion (10 g of AgNO₃, 20 g of CuCl₂) of the dissolved salt precursor. This dopant solution is then added, dropwise, to the titanium isopropoxide solution – prepared in step (a) above – while vigorously stirring. The steps following (a) above then resumes thereafter.

To prepare the double-doped powders, the AgNO₃ and CuCl₂ dopant solutions were first combined before adding the mixture to the ethanol + Titanium Isopropoxide solution of step (a).

3.2.4 Sample Species

The five species of titania nanopowders, namely TiO_2 , $\text{Ag}\backslash\text{TiO}_2$, $\text{Cu}\backslash\text{TiO}_2$, $\text{Ag}+\text{Cu}\backslash\text{TiO}_2$, $\frac{1}{2}\text{Ag}+\text{Cu}\backslash\text{TiO}_2$, that were synthesised are shown in Table 6. Four portions of each species were further heat treated for 1 hour at temperatures of 300°C, 600°C, 900°C and 1100°C. In all, there were a total of 22 samples including the ‘as-prepared’ (dried at 100°C) as well as the double-doped $\frac{1}{2}\text{Ag}+\text{Cu}\backslash\text{TiO}_2$ which is of lower dopant concentration (2.5 wt %) compared with the $\text{Ag}+\text{Cu}\backslash\text{TiO}_2$ species.

Table 6: List of the five titania species, dried at 100°C and further annealed at 300°C, 600°C, 900°C and 1100°C – four of which titania is a host to Ag and/or Cu.

Species Label	Doping Type	Dopants	Dopant Level (wt %)	Annealing Temperatures (°C)			
				300	600	900	1100
TiO_2	Undoped	–	0.0	√	√	√	√
$\text{Ag}\backslash\text{TiO}_2$	Single	Ag	5.0	√	√	√	√
$\text{Cu}\backslash\text{TiO}_2$	Single	Cu	5.0	√	√	√	√
$\text{Ag}+\text{Cu}\backslash\text{TiO}_2$	Double	Ag, Cu	5.0, 5.0	√	√	√	√
$\frac{1}{2}\text{Ag}+\text{Cu}\backslash\text{TiO}_2$	Double	Ag, Cu	2.5, 2.5	√	√		

3.3 SAMPLE CHARACTERISATION (EXPERIMENTAL)

Undoped TiO_2 -based systems, as well as those doped with various metals and non-metals, are generally characterised by a wide range of physical techniques. Those used in this study are mentioned in Section 2.9 in terms of theory and literature review. Here, the experimental aspects of using these techniques for sample characterisation are discussed.

3.3.1 X-Ray Diffraction (XRD)

Various studies related to the current research, invariably carry out analyses by XRD methods. This technique is capable of revealing diverse information such as lattice parameters, particle sizes, elemental constituents and crystal phases.

XRD is a technique for analysing the interaction of X-rays with the crystalline matter through their diffraction. It involves shining X-ray on a crystalline sample, Figure 14 [261], to produce diffractogram – a pattern characteristic of the structure of the sample material. The X-ray beam diffracts when crossing the crystal and produces beams at different angles depending on the X-ray wavelength, the crystal orientation and the structure of the crystal. If the sample is a crystalline powder, rather than a single crystal, a diffraction pattern (which is a plot of intensity against the angle of the detector, 2θ) for the bulk material of the crystalline solid is obtained [262].

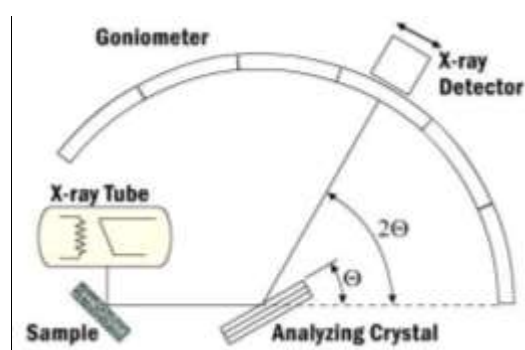


Figure 14: Schematic of the x-ray diffractometer setup. The spectrograph consists of a high voltage power supply (50KV or 100KV), a broad band X-ray tube, usually with a tungsten anode and a beryllium window, a specimen holder, an analysing crystal, a goniometer, and an X-ray detector device [261].

In X-ray crystallography, the outgoing X-rays have the same energy, and thus same wavelength, as the incoming X-rays, only with altered direction – a form of elastic scattering [262]. (In contrast, inelastic scattering involves energy transfer from the incoming wave to the sample, thus exciting an inner-shell electron to a higher energy level and reducing the energy (or increasing the wavelength) of the outgoing beam.) Though inelastic scattering is suitable for probing such excitations of matter, it is however not useful in determining the distribution of scatterers within the matter, which is the objective of X-ray crystallography [262]. Other forms of elastic X-ray scattering include powder diffraction, small-angle X-ray scattering (SAXS) and

several types of X-ray fiber diffraction, which was used by Rosalind Franklin in determining the double-helix structure of DNA. Generally, single-crystal X-ray diffraction offers more structural information than the other techniques; however, it requires a suitably large and regular crystal, which is often not available [262].

The scattering methods normally use single-wavelength (monochromatic) X-rays. Broad spectrum (multiple wavelengths) X-rays can also be utilised in carrying out X-ray diffraction – a technique known as the Laue method. The wavelength range of X-rays is from 10 nm to 0.01 nm and a typical wavelength used for crystallography is 1 Å or 0.1 nm. (The common X-rays wavelengths used are Mo K_{α} at 0.7136 Å, the Cu K_{α} at 1.5406 Å and the Co K_{α} at 1.7889 Å.) This is on the scale of covalent chemical bonds and the radius of a single atom. Longer-wavelength photons (such as UV) would not have sufficient resolution to determine the atomic positions [262]. On the other extreme, shorter-wavelength photons such as gamma rays are difficult to produce in large numbers, difficult to focus, and interact too strongly with matter, producing particle-antiparticle pairs. Therefore, X-rays are of the appropriate wavelength for determining atomic-resolution structures from the scattering of electromagnetic radiation [262].

Other particles, such as neutrons and electrons, may also be used to produce a diffraction pattern. Even though electron, neutron, and X-ray scattering are based on different physical processes, the same coherent diffraction imaging techniques is used for analysing the resulting diffraction patterns.

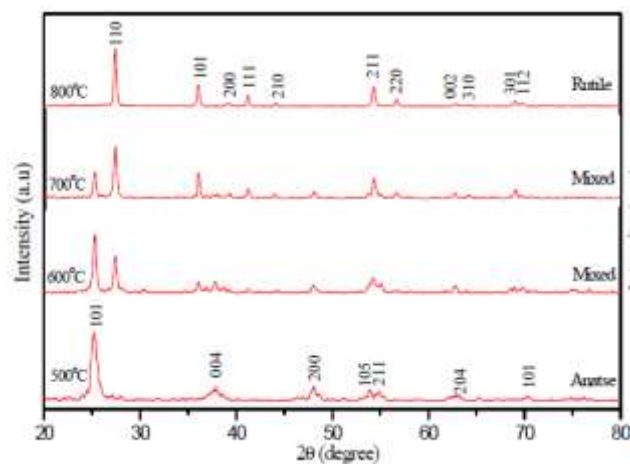


Figure 15: Typical x-ray diffraction patterns (for anatase, rutile and mixed-phase TiO_2) featuring the miller indices corresponding to the prominent peaks of the samples [263].

XRD patterns allow us to identify and analyse any crystalline matter. Typical patterns for anatase, rutile and mixed-phase TiO₂ are shown in Figure 15. The degree of crystallinity conditions the quality of the result obtained. The application of XRD technique to polycrystalline materials such as SGS nanopowders gives us a set of peaks with angular separations satisfying the Bragg's law. These peaks can be indexed and related to a determinate crystalline structure using some patron tables such as the well-known PDD (Powder Diffraction Data), published by the International Centre for Diffraction Data (ICDD) [264], Crystallography Open Database (COD) [265] or American Mineralogist Crystal Structure Database (AMCSD) [266].

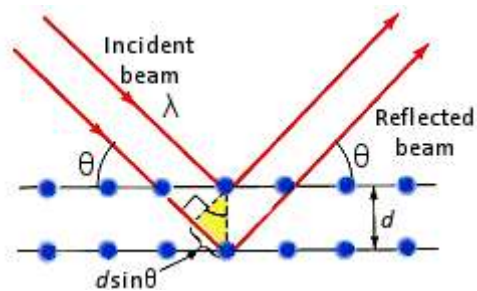


Figure 16: Scheme of the x-ray diffraction geometry [262].

Bragg (William Lawrence Bragg) model of diffraction provides an intuitive understanding of X-ray diffraction. In this model, a set of evenly spaced planes, usually defined by the centres of the atoms in the crystal lattice (Figure 16), are associated with a specific reflection [262]. The orientation of a particular set of planes is identified by its three Miller indices (h, k, l), and their spacing, by d . The model proposes that the incoming X-rays are scattered specularly (mirror-like) from each plane [262]. With this assumption, constructive interference of X-rays scattered from adjacent planes will result when the angle θ between a plane and the X-ray is such that the path-length difference is an integer multiple n of the X-ray wavelength λ , and [262]:

$$2d \sin \theta = n\lambda$$

Reflections are indexed by associating Miller indices (or more appropriately, reciprocal lattice vector components) with the scattering angle 2θ and the X-ray wavelength. Such indexing gives the unit-cell parameters, the lengths and angles of the unit-cell, as well as its space group. Since Bragg's law does not interpret the relative intensities of the reflections, it is however generally inadequate in determining the arrangement of atoms within a unit-cell. To solve for that, a Fourier transform method is required [262].

The XRD analytical technique provides an easy quantification of the crystalline phases that compose the samples, as well as the possibility of evaluating the mean grain size of the nanopowders in polycrystalline samples. However, in order to obtain accurate results in this quantification, we have to be sure of the sample structure, and some initial patron models are needed. This technique has been widely used for the identification of material structural phase [119] [267]. In this way, Turkoviæ *et al.* [120] carried out their TiO₂ nanophase sample structural characterisation by means of this technique, identifying a mixture of anatase and brookite in their pre-annealed material and showing the feasibility of the technique in this field. Further, an accurate analysis of phase transitions in SGS materials can be carried out when analysing samples treated at different annealing temperatures or even performing in-situ XRD analysis. Depero *et al.* [122] employed this technique in their studies on anatase to rutile phase transitions when metal additives had been loaded onto the samples.

In the current research, XRD was employed to determine crystallite phases and the structural properties of the nanostructured sensing materials. The crystal phase composition (XRD powder diffractogram) data were recorded in the 2θ scan range of $10^\circ - 90^\circ$ (with a step size of 0.026°) with PANalytical X'Pert PRO diffractometer (Figure 17). The system was operated with a Cu, Ni-filtered K α radiation, of wavelength $\lambda = 1.540598 \text{ \AA}$ monochromatic radiation source at voltage 45 kV and the current at 40 mA. Plotting the intensity of the radiation produced by interference of diffracted X-rays as a function of diffraction angle, provides a pattern characteristic of the crystal structure.



Figure 17: The XRD instrumentation – PANalytical X'Pert PRO diffractometer – made available by the CSIR.

For phase identification, peak indexing was carried out with reference data from American Mineralogist Crystal Structure Database (AMCSD) [266]. 'Match! 2' [268], a computer program specially designed for this purpose, was also used in conjunction with the reference data from Crystallography Open Database (COD) [265].

The Scherrer equation, $\tau_{(hkl)} = \frac{K\lambda}{\beta_{(hkl)} \cos \theta}$ was used in estimating the mean size $\tau_{(hkl)}$ of the ordered crystalline domains from $\beta_{(hkl)}$, the line broadening at half the maximum intensity (or the full-width-at-half-maximum, FWHM) in radians. Here, θ is the Bragg angle and λ , the X-ray wavelength, which in this case is 1.5418740 Å for the Cu K α radiation. By considering the synthesised nanoparticles to be fairly spherically shaped, a value of 0.9 was assumed for the shape parameter (or roundness factor) K [76], [77]. For quantitative comparative analyses, instrumental and strain broadening were neglected and Gaussian fitting of the most intense peaks of the individual phases – (101) and (200) for anatase and (110) and (211) for rutile – were carried out [31], with the aid of the statistical package called Origin®.

Lattice parameters a , b and c , were calculated from Bragg's law, $2d_{(hkl)} \sin \theta = m\lambda$, and the formula for the crystal system: $\frac{1}{d_{(hkl)}^2} = \frac{h^2}{a^2} + \frac{k^2}{b^2} + \frac{l^2}{c^2}$. Here, the Miller indices h , k and l , define the Bragg planes of which $d_{(hkl)}$ is the interplanar spacing of the

lattice. For anatase and rutile systems $a = b \neq c$ (tetragonal) while for the orthorhombic brookite system, $a \neq b \neq c$.

The phase content (mass fraction f_X) of each sample was calculated from the integrated intensities I_A , I_R and I_B of the respective peaks of anatase (101), rutile (110) and brookite (121) as [41]:

$$f_A = \frac{k_A I_A}{k_A I_A + I_R + k_B I_B}, f_R = \frac{I_R}{k_A I_A + I_R + k_B I_B}, f_B = \frac{k_B I_B}{k_A I_A + I_R + k_B I_B}, \quad 3-2$$

where the coefficients k_A and k_B assume the values 0.886 and 2.721 respectively.

3.3.2 Raman Spectroscopy

Raman Spectroscopy (named after Sir C. V. Raman) is a spectroscopic technique used to observe vibrational, rotational, and other low-frequency modes in a system [269]. It involves the Raman (inelastic) scattering of monochromatic light (usually from a laser source) in the visible, near infrared or near ultraviolet range. The impinging light interacts with molecular vibrations, phonons or other excitations in the system. As a result, the energy of the photons are shifted up or down, thus providing information about the vibrational modes in the system. The information obtained from infrared spectroscopy is similar, and complementary.

Raman spectroscopy is commonly used in chemistry to provide an identification fingerprint for molecules [270]. It is based in the diffusion processes given by the electronic polarisation caused by ultraviolet or visible light. Raman gives information at molecular level allowing the vibrational and rotational analysis of chemical species [270]. The light scattering phenomena involves the interaction of the electromagnetic radiation with a pulsating polarisable electron cloud, and thus interaction with the molecular vibrational energy levels via the bonds of the molecule in the phase (solid, liquid or gaseous) and environment in which the molecule finds itself [269]. As a consequence of the diffusion effect, this technique presents several advantages. On one hand, no sample preparation is needed, thus making its implementation easier. Moreover, it provides a nondestructive and quantitative microanalysis of structures and electronic properties [270].

As with XRD, the Raman technique has been widely used for the identification of material structural phase, as in those works carried out by Tompsett *et al.* [271], and moreover for the analysis of phase transitions. But it can also be used to determine whether the catalytic species are located inside the semiconductor lattice, by analysing the Raman peaks shift [270].

In a typically Raman setup, a sample is illuminated with a laser beam and the electromagnetic radiation from the illuminated spot is collected with a lens and sent through a monochromator. Elastic scattered radiation at the wavelength corresponding to the laser line (Rayleigh scattering) is filtered out, while the rest of the collected light is dispersed onto a detector by either a notch filter or a band pass filter [269]. Since the spontaneous inelastically scattered Raman light is generally very weak, the main challenge of Raman spectroscopy is therefore separating the intense Rayleigh scattered laser light from the weak light [269].

In the spontaneous Raman Effect, a photon excites the molecule in either a ground or an excited rovibronic (rotational and vibrational energy levels) state [270]. This results in the molecule being in a short-lived “virtual” energy state. The rovibronic state of the molecule that result from Raman scattering differs from the original rotational or vibrational state of the molecule before the encounter with the incoming photon [270]. That is, the resulting inelastically scattered photon is emitted with an energy either lower or higher than the incoming photon. The energy difference between the two states leads to a shift in the emitted photon's frequency away from the excitation wavelength, thereby resulting in a Rayleigh line. If the final vibrational state of the molecule is more energetic than the initial state, the inelastically scattered photon will be shifted to a lower frequency for the total energy of the system to remain balanced. This shift in frequency is designated as a Stokes shift (Figure 18) [270]. For a final vibrational state that is less energetic than the initial state, the shift (an anti-Stokes shift) is to a higher frequency.

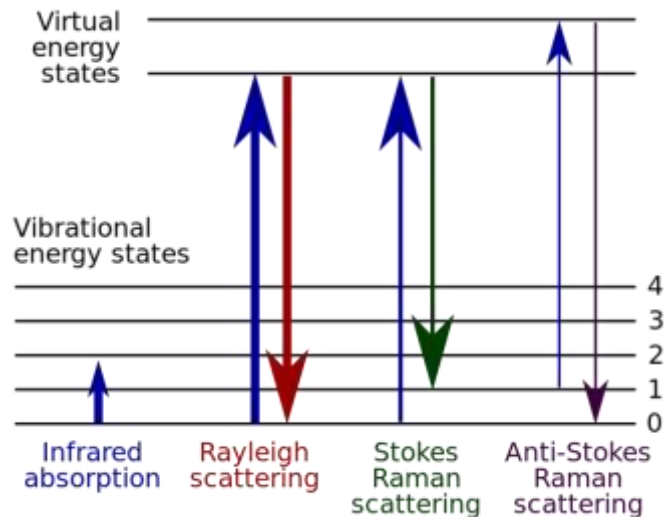


Figure 18: Energy-level scheme of the states involved in the Raman signal. The relative strength of the signal for the different transitions is roughly proportional to the thickness of the lines.

The inelastic scattering Raman is an example of inelastic scattering because of the energy and momentum transfer between the photons and the molecules during the interaction. The effect should not be confused with emission fluorescence (or phosphorescence) in which a molecule in an excited electronic state emits a photon of energy and returns to the ground electronic state; often to a vibrationally excited state on the ground electronic state potential energy surface [270]. On the other hand is Rayleigh scattering which is an example of elastic scattering. Here, the energy of the scattered photon has of the same frequency and wavelength as the incoming electromagnetic radiation [270].

For a molecule to exhibit a Raman Effect, there has to be a change in the molecular electric dipole (or the electric polarisability) with respect to the vibrational coordinate corresponding to the rovibronic state. The intensity of the Raman scattering is proportional to this change [270]. Thus, Raman spectra (i.e. Raman scattering intensity as a function of the Stokes and anti-Stokes frequency shifts) depends on the rovibronic states of the sample. In infrared spectroscopy however, the dependence is not on the electric dipole polarisability derivative, but on the atomic polar tensor (APT) – an electric dipole moment derivative. With this contrasting feature, transitions that might not be IR active can be analysed via Raman

spectroscopy, in accordance with the rule of mutual exclusion in centrosymmetric molecules. The Raman bands with weak intensities generally turn out to have large infrared intensities and vice versa. For molecules that are very symmetric, certain vibrations may be both Raman and infrared inactive (within the harmonic approximation). In those cases, an inelastic incoherent neutron scattering (IINS) technique can be used to determine the vibrational frequencies [270].

The Raman IINS selection rules are different from those of infrared [270]. Hence the three types of vibrational spectroscopy are complementary, all giving in theory the same frequency for a given vibrational transition, but the relative intensities giving different information due to the types of interaction between the molecule and the electromagnetic radiation for infrared and Raman spectroscopy and with the neutron beam for IINS [270].

Raman shifts are normally reported in wavenumbers, which have units of inverse length, as this value is directly related to energy. In order to convert between spectral wavelength and wavenumbers of shift in the Raman spectrum, the following formula can be used [270]:

$$\Delta w = \left(\frac{1}{\lambda_0} - \frac{1}{\lambda_1} \right) \tag{3-3}$$

Where Δw is the Raman shift expressed in wavenumbers, λ_0 is the excitation wavelength and λ_1 is the Raman spectrum wavelength. Most commonly, the unit chosen for expressing wavenumbers in Raman spectra is inverse centimetres (cm^{-1}). Since wavelength is often expressed in units of nanometres (nm), the formula in equation 3-3 can scale for this unit conversion explicitly, giving

$$\Delta w(\text{cm}^{-1}) = \left(\frac{1}{\lambda_0(\text{nm})} - \frac{1}{\lambda_1(\text{nm})} \right) \times \frac{(10^7 \text{ nm})}{(\text{cm})} \tag{3-4}$$

In chemistry, Raman spectroscopy provides a fingerprint by which the molecule can be identified. For organic molecules, the fingerprint region is in the wavenumber range of $500 - 2000 \text{ cm}^{-1}$. The technique is also used in studying changes in chemical bonding, such as when a substrate is added to an enzyme [270].

Spontaneous Raman spectroscopy is used in solid-state physics to measure temperature, characterise materials and find the crystallographic orientation

of a sample, amongst others [270]. Just as it is with single molecules, solid materials have characteristic phonon modes that can be used in identifying it. Further, the Raman technique can be used to detect plasmons, magnons, superconducting gap excitations and other low frequency excitations of a solid [270]. Information on the population of a given phonon mode in the ratio between the downshifted (Stokes) intensity and upshifted (anti-Stokes) intensity can be provided by the Raman signal. The polarisation of the Raman scattered light by an anisotropic crystal (with respect to the crystal) as well as the polarisation of the impinging laser light, can give information on the crystal orientation, if the point group of the crystal is known [270].

For samples that do not exhibit high thermal background, Raman spectroscopy results can be used to support XRD results. For instance, spectroscopic characteristics of Raman peaks are known to be related to crystal size [84], [272]. Raman microspectroscopy can also be used to effectively differentiate the phases, in mixed-phase compositions.

In the current investigations, Raman spectra from 50 to 1200 cm^{-1} were obtained with a Jobin Yvon LabRAM HR 800 UV-VIS-NIR spectrometer (Figure 19) equipped with an Olympus Microscope. The excitation wavelengths are 488 nm, 514 nm, 647 nm, 785 nm and 1064 nm. The 800 mm-focal-length spectrometer is capable of 0.33 cm^{-1} resolution at 633 nm excitation. Plots of the intensity (in arbitrary units) against the wavenumber (cm^{-1}) were carried in the Microsoft Excel® spreadsheet program.



Figure 19: The Raman spectrometry instrumentation – Jobin Yvon LabRAM HR 800 UV-VIS-NIR – made available by the CSIR.

3.3.3 Scanning Electron Microscopy (SEM)

SEM is a type of electron microscopy that produces images of a sample by scanning it with a focused beam of electrons [273]. As the electrons interact with atoms in the sample, various signals that contain information about the sample's surface topography and composition, can be detected. The electron beam is generally made to scan the sample in a raster fashion. The image is then produced by combining the beam's position with the detected signal. With resolutions better than 1 nanometre, SEM specimens can be observed in high vacuum, in low vacuum, in wet conditions, and at a wide range of cryogenic or elevated temperatures [273].

The most common mode of detection is by secondary electrons (SE) emitted by atoms excited by the electron beam. On a flat surface, the trail of secondary electrons is mostly contained by the sample, but on a tilted surface, this trail is partially exposed and more electrons are emitted [273]. An image displaying the topography of the surface is thus created by scanning the sample and detecting the secondary electrons. In addition to SE, other types of signals produced by SEM include back-scattered electrons (BSE), light cathodoluminescence (CL), specimen current, characteristic X-rays and transmitted electrons. It is rare that a single machine would have detectors for all possible signals, thus secondary electron detectors are standard equipment in all SEMs [273]. The signals result from interactions of the electron beam with atoms at or near the surface of the sample. The most common detection mode involves secondary electron imaging or SEI. Here, details less than 1 nm in size can be revealed by the high-resolution images of a sample surface produced. SEM micrographs have a large depth of field (as a result of the very narrow electron beam) thus yielding a characteristic 3-dimensional appearance – which is useful for understanding the surface structure of a sample. Magnifications range from about that of a powerful hand-lens (10x) to more than 250 times the magnification limit of the best light microscopes (500,000x) [273].

For the characterisation of nanomaterials and nanostructures, SEM is one of the most versatile and widely used instruments. It is capable of providing structural and morphological information of organic and inorganic materials at nanoscale resolution [273]. The popularity of the SEM can be attributed to several factors such as the very modest requirement for sample preparation and conditioning, the relatively

straightforward interpretation of the acquired images, the high levels of automation with user friendliness, the versatility of its various modes of imaging, as well as the exceptional spatial resolution [273].

The spatial resolution of the SEM depends on the size of the electron spot, which in turn depends on both the wavelength of the electrons and the electron-optical system that produces the scanning beam [273]. A limiting factor on the resolution is the size of the volume of specimen material that interacts with the electron beam (the interaction volume). If the spot size and the interaction volume are both large compared to the distances between atoms, the resolution of the SEM will not be high enough to image individual atoms (as is possible in the shorter wavelength/higher energy transmission electron microscope) [273]. Some compensating advantages SEM includes the ability to image a comparatively large area of the specimen, the ability to image bulk materials (not just thin films or foils), and the variety of analytical modes available for measuring the composition and properties of the specimen. Depending on the instrument, the resolution can fall somewhere between less than 1 nm and 20 nm [273].

Morphology and microstructure (surface composition, agglomeration, and particle sizes) are parameters that are often deduced from SEM as well as TEM (Transmission Electron Microscopy). SEM micrographs have a very large depth of field resulting in a well-defined characteristic three-dimensional appearance useful for understanding the surface structure of a sample. (In general, the samples placed in the SEM chamber must be either conducting or coated with a thin metal layer in order to avoid electric charging by the electron beam.

SEM micrographs of the samples were obtained with an Auriga Cobra FIB FESEM Scanning Electron Microscope (Figure 20). The instrument is a cross-beam workstation that combines a high resolution scanning electron microscope (HRSEM) with the precision milling and nanofabrication abilities of high resolution focused ion beam (FIB). This multifunctional instrument can be used for SEM imaging, TEM lamella preparation, milling, cross-sectioning and imaging with either FIB or SEM. It also has a charge compensation system which is used when imaging non-conductive samples or insulating materials without coating, as well as the STEM

detector and Energy and Angle Selective EsB detector that allows an almost pure compositional image to be obtained by filtering out unwanted surface information.



Figure 20: The SEM instrumentation – Auriga Cobra FIB FESEM – made available by the CSIR.

Scanning was done at low pressure so that the electrons are not scattered by the gas molecules. All samples were taken at 3 kV at magnifications varying from 5000x to 10000x for differing views. The detailed results of the SEM investigation of the nanomaterials are given in Chapter 4 (page 126).

3.3.4 Energy-Dispersive X-ray Spectroscopy (EDS, EDX, or XEDS)

EDS – sometimes referred to as Energy Dispersive X-ray Analysis (EDXA) or Energy Dispersive X-ray Microanalysis (EDXMA) – is an analytical technique used for chemical characterisation of samples or for performing elemental analysis. By allowing a source of X-ray excitation to interact with a specimen, the EDS characterisation capabilities are due mainly to the fundamental principle that each element has a unique atomic structure which results in a distinctive set of peaks on its X-ray emission spectrum [274]. The technique involves focusing a high-energy beam of charged particles (such as electrons or protons) or a beam of X-rays, on a sample in order to stimulate the emission of characteristic X-rays from it. Within a sample, the electrons in an atom at rest, are in unexcited or ground state discrete energy levels (or electron shells bound to the nucleus). If the impinging beam ejects (excites) an electron from an inner shell, a ‘hole’ is left behind may be filled by

another electron from an outer, higher-energy shell. An X-ray having energy equal to the difference in energy between the higher-energy shell and the lower-energy shell, may be released. An energy-dispersive spectrometer may be used to measure the number and energy of the X-rays emitted from a specimen [274]. Since the energy of the X-rays is characteristic of the difference in energy between the two shells, and of the atomic structure of the element from which they were emitted, this makes it possible to determine the elemental composition of the sample [274].

The principle involved in EDS is schematically shown in Figure 21. The excess energy of the electron that migrates to an inner shell to fill the newly created hole may be available to eject a third electron (called an Auger electron) from another outer shell. The method for the analysis in this case is known as Auger electron spectroscopy (AES) [274].

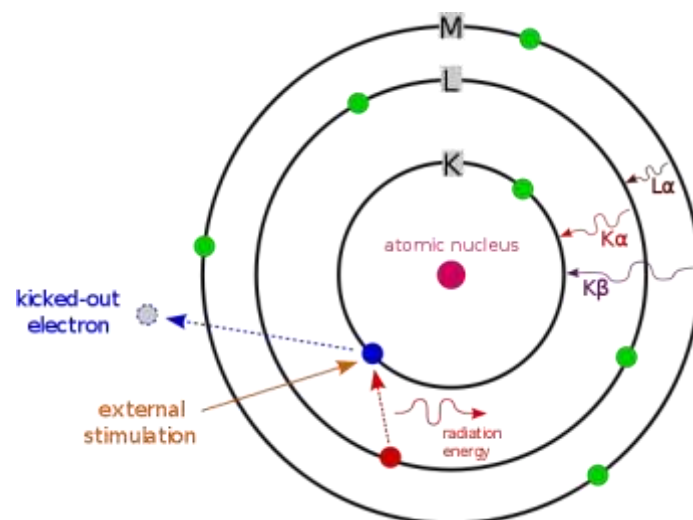


Figure 21: A schematic representation of the EDS principle [274].

X-ray photoelectron spectroscopy (XPS) is another method that is closely related to EDS. It utilises ejected electrons in a manner similar to that of AES. Information on the kinetic energy and quantity of ejected electrons is used to determine the binding energy of these now-liberated electrons, which is element-specific thus allowing for chemical characterisation of a sample [274].

The main aspects of the EDS setup are [274]:

- the excitation source (electron beam or x-ray beam)
- the X-ray detector
- the pulse processor
- the analyser.

The electron beam excitation procedure is commonly used in electron microscopes, scanning electron microscopes (SEM) and scanning transmission electron microscopes (STEM). X-ray beam excitation is employed in X-ray fluorescence (XRF) spectrometers, in which a detector is used to convert X-ray energy into voltage signals. This information is passed to a pulse processor to measure the signals and then sent to an analyser for data display and analysis [274].

One of the several factors that affect the accuracy of the EDS spectrum results from many elements (such as Ti K_{β} and V K_{α} , Mn K_{β} and Fe K_{α}) having overlapping peaks. The nature of the sample is another factor that may affect the accuracy of the spectrum. X-rays generated by an atom in the sample, that is sufficiently excited by the incoming beam, can be emitted in any direction and may therefore not all escape the specimen to be detected and measured [274]. The probability of an X-ray escaping the sample (and thus becoming available for detection) depends on the energy of the X-ray as well as the amount and density of material it has to pass through. Thus the accuracy of the EDS spectrum can be reduced, particularly in inhomogeneous and rough samples [274].

Elemental chemical composition analysis, using Energy Dispersive X-ray Spectrometry (EDS), may confirm the distribution of dopant nanoparticles in the TiO₂ lattice. This technique is a powerful tool that provides a nanostructural material characterisation, such as chemical composition and structure. EDX can also be used to determine the approximate fractions of an element within the surface of a composite coating, and to measure the dispersion of an element within a sample.

In this project, EDS micrographs and relative composition analyses have been carried out using a JEOL Field Emission Scanning Electron Microscope, Model: JSM-7500F, equipped with a ThermoScientific UltraDry EDS (Figure 22). The

resulting EDS spectra were analysed using the database supplied with the instrument software.



Figure 22: The EDS instrumentation – JEOL JSM-7500F FESEM / ThermoScientific UltraDry EDS – made available by the CSIR.

3.3.5 Ultraviolet–Visible spectroscopy (UV-Vis or UV/Vis)

UV-Vis or ultraviolet-visible spectrophotometry refers to absorption or reflectance spectroscopy that employs light in the visible and near-visible (near-UV and near-infrared [NIR]) spectral regions [275]. In the visible range the perceived colour of the materials involved is directly affected as the molecules undergo electronic transitions. The UV-Vis technique is complementary to fluorescence spectroscopy, in which transitions from the excited state to the ground state are measured, whereas absorption transitions deal with the ground state to the excited state [275].

UV-Vis spectroscopy is routinely used for the quantitative determination of different analytes, such as transition metal ions, highly conjugated organic compounds, and biological macromolecules [275]. Though the spectroscopic analysis is usually carried out in solutions, absorbance of solids and gases may also be studied by UV-Vis. The concentrations of an absorbing species in solution can be quantitatively determined using the Beer-Lambert law [275]:

$$A = \log_{10}(I_0/I) = \epsilon cL, \quad 3-5$$

where A is the measured absorbance, in absorbance units (AU), I_0 is the intensity of the incident light at a given wavelength, I is the transmitted intensity, L the

pathlength through the sample, and c the concentration of the absorbing species. The parameter ϵ is a constant (for each species and wavelength) known as the molar absorptivity or extinction coefficient. In a given solvent, this constant is a fundamental molecular property at a particular temperature and pressure, and has units of $1/M \cdot \text{cm}$ or $\text{AU}/M \cdot \text{cm}$. The absorbance and extinction ϵ are sometimes defined in terms of the natural logarithm instead of the base-10 logarithm. Though the Beer-Lambert Law is useful for characterising many compounds, it does not hold as a universal relationship for the concentration and absorption of all substances [275]. For very large, complex molecules such as organic dyes (e.g. Xylenol Orange or Neutral Red) a 2nd order polynomial relationship between absorption and concentration is sometimes found [275].

The UV-Vis spectrophotometer (the instrument used in ultraviolet-visible spectroscopy) normally measures the intensity of light passing through a sample (I), and compares it to the intensity of light incident on the sample (I_0). The ratio I_0/I , called the transmittance, is usually expressed as a percentage ($\%T$). The absorbance, A , depends on the transmittance as:

$$A = -\log(\%T/100\%). \quad 3-6$$

In addition to absorbance, the UV-Vis spectrophotometer can also be configured to measure reflectance. Here, the intensity of light reflected from a sample (I), measured and compared to the intensity of light reflected from a reference material (I_0). The ratio I_0/I is now the reflectance, which may also be expressed as a percentage ($\%R$) [275].

Typically samples for UV-Vis spectrophotometry (often liquids) are placed in a rectangular-shaped transparent cell (or cuvette). The internal width of the cuvette (commonly 1 cm) represents the path length, L , in the Beer-Lambert law. Test tubes can also be used as cuvettes in some instruments. The type of sample container used must allow radiation to pass over the spectral region of interest [275].

In less sophisticated spectrophotometers, the absorption is determined one wavelength at a time and later compiled into a spectrum by the operator. By eliminating the concentration dependence, the extinction coefficient (ϵ) can then be

determined as a function of wavelength. In more advanced instruments, a complete spectrum of the absorption at all wavelengths of interest can often be produced directly [275].

Generally, the measurement of the band gap energy, (E_g) in doped titania is by UV-Vis adsorption spectroscopy or by applying the Kubelka-Munk [276] treatment to diffuse reflectance spectra. Morales *et al.* gives a comparison of these approaches [277]. Although precise determination of the band gap may not always be possible, the absorption coefficient α (and hence the band gap) is often determined from inversion of the measurements of diffuse reflectance by using the spectral-projected gradient-method to invert the Kubelka-Munk expression for the diffuse reflectance [278]. The fundamental absorption, which corresponds to electron excitation from the valence band to conduction band, can be used to determine the nature and value of the band gap. For crystalline solids with an indirect band gap, such as rutile TiO₂ [104], [105], the dependence of the absorption coefficient α on the frequency ν , near the absorption edge (in the strong absorption zone), can be approximated as the power law behaviour of Tauc's relation [279]:

$$(\alpha h\nu) = B(h\nu - E_g)^r \tag{3-7}$$

where B is the edge width parameter (an energy-independent constant), h is the Planck's constant (so that $h\nu$ is the photon energy) and r is a constant, which determines type of optical transition. (It is equal to 2 in the case of 'allowed indirect' transitions.) Other values assumed by r for electronic transitions include $\frac{1}{2}$ (allowed direct), $\frac{3}{2}$ (forbidden direct) or 3 (forbidden indirect).

Using Equation 3-7, it is clear that the band gap E_g can be obtained by extrapolating the linear region of Tauc's plot – a plot of $(\alpha h\nu)^{1/r}$ against $h\nu$ – to zero (Figure 23) [280] – [281]. The $h\nu$ factor on the left-hand side of equation 3-7 is sometimes excluded by some authors [282] as it does not alter significantly the value of E_g obtained.

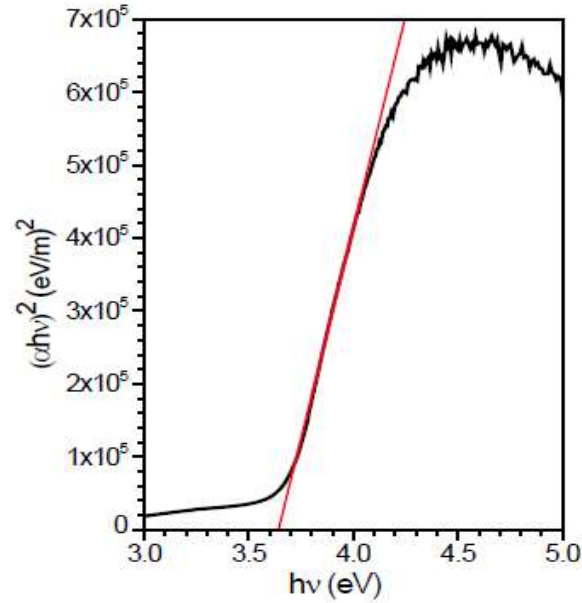


Figure 23: A typical Tauc's plot of the variation of $(\alpha h\nu)^2$ with excitation energy $h\nu$ for a TiO_2 film, in order to identify direct transitions [283]. The straight line extrapolation of the linear region of the plot, yields the band gap energy E_g at the intersection with the $h\nu$ axis.

The frequency-dependent absorption coefficient is sometimes calculated from the Beer-Lambert's law as [284]:

$$\alpha(\lambda) = 2.303 \left(\frac{A}{t} \right) \quad 3-8$$

Here A is the adsorbance and t , the sample thickness, is not well defined since the penetration depth of the beam in the sample depends on factors such as particle sizes, packing density and the amount of the absorbing material present in the sample. The absorption coefficient α is related to the measured reflectance R through [284]:

$$\alpha = F(R) \left(\frac{s}{2V_R} \right) \quad 3-9$$

where s is the scattering coefficient, V_R is the volume fraction of the absorbing species, and the Kubelka-Munk function $F(R)$ is of the form $F(R) = \frac{(1-R)^2}{2R}$. If the dependence of the scattering coefficient s on wavelength is neglected, then $\alpha(\lambda) \propto$

$F(R)$ and from Equation 3-7, it follows that a plot of $(F(R)h\nu)^{1/r}$ against $h\nu$ can be extrapolated to $(F(R)h\nu)^{1/r} = 0$, as was done with Tauc plots [104] [105].

UV-visible light absorption measurements were undertaken to derive band-gap information on the TiO_2 nanopowders. This analytical technique allows for photoabsorbance band gap determination and provides some insights into the interactions of photocatalytic materials with photon energy [285]. The double-beam Perkin-Elmer Lambda 750S UV/Vis Spectrometer (Figure 24) have been used in collecting the optical absorbance spectra of the prepared nanoparticles. This was carried out by placing diluted solutions of target samples in 1 cm path length UV quartz cuvettes and then recording the absorption within the scan range of 200 – 800 nm, with a spectral resolution of 1 nm and at room temperature. The spectra were taken against the pure solvent reference for each different sample.



Figure 24: The UV-vis instrumentation – Perkin-Elmer LAMBDA 750S – made available by the CSIR.

Generally, Tauc's formula [279], which relates the optical absorption coefficient to the photon energy, is often used to deduce the band gap energy E_g from extrapolations on Tauc's plots for indirect transitions near the absorption edge (Section □, page 89). However, in the present study, the absorption spectra fitting (ASF) procedure [280] was applied to the Tauc's model in order to estimate the optical band gap of the TiO_2 nanostructural powders. This method requires only the measurement of the absorbance spectrum, and no additional information such as the thickness or reflectance spectra is needed.

Here, the absorption coefficient is related to the incident photon energy via Tauc's relation (Equation 3-7 of page 112) may be rewritten as a function of wavelength λ :

$$\alpha(\lambda) = B(hc)^{r-1} \left(\frac{1}{\lambda} - \frac{1}{\lambda_g} \right)^r \quad 3-10$$

where h , c and λ_g are Planck's constant, speed of light and wavelengths corresponding to the optical band gap, respectively. Using the Beer-Lambert's law (Equation 3-8 of page 113), the absorbance A is then expressed as:

$$A(\lambda) = B'\lambda \left(\frac{1}{\lambda} - \frac{1}{\lambda_g} \right)^r \quad 3-11$$

where $B' = B(hc)^{r-1} \frac{t}{2.303}$. Thus the value of the band gap can be determined as

$$E_g = \frac{1239.83}{\lambda_g}. \quad 3-12$$

Curves of $\left(\frac{A(\lambda)}{\lambda} \right)^{1/r}$ versus $\frac{1}{\lambda}$ can be plotted for the different electronic transitions – allowed direct ($r = \frac{1}{2}$), forbidden direct ($r = \frac{3}{2}$), allowed indirect ($r = 2$) and forbidden indirect ($r = 3$). By extrapolating the linear portion of the curves, λ_g can be determined at the zero of the $\left(\frac{A(\lambda)}{\lambda} \right)^{1/r}$ axis.

3.3.6 Photoluminescence (PL)

PL is the spontaneous light emission from any form of matter under optical excitation or absorption of photons. Different regions and excitation concentrations in the sample can be probed by selecting the excitation energy and intensity. PL spectroscopy can be used to characterise a variety of material parameters as it provides electrical characterisation, as opposed to mechanical. This selective and extremely sensitive probe for discrete electronic states, reveals features of the emission spectrum which can be used for the identification of surface, interface, and impurity levels and to gauge alloy disorder and interface roughness [286].

Information on the quality of surfaces and interfaces can be obtained from the intensity of the PL signal. Under pulsed excitation, the transient PL intensity yields the lifetime of nonequilibrium interface and bulk states. The variation of the PL intensity under an applied bias can be used to map the electric field at the surface of a sample. In addition, thermally activated processes cause changes in PL intensity with temperature [286].

The PL analysis is a nondestructive technique that requires very little sample manipulation or environmental control. Because the specimen is optically excited, electrical contacts and junctions are not required and materials of high resistivity present no practical difficulty. Further, time-resolved PL can be very fast, making it useful for characterising the most rapid processes in a material. [287] The fundamental limitation of PL analysis is its reliance on radiative events. Materials with poor radiative efficiency, such as low-quality indirect band gap semiconductors, are difficult to study via ordinary PL. Similarly, identification of impurity and defect states depends on their optical activity. Although PL is a very sensitive probe of radiative levels, to study states that couple weakly with light secondary evidence from other techniques is often necessary [287].

PL, initiated by excitation of photons (photoexcitation), is one of several forms of light emission (luminescence) [287]. Following excitation, various relaxation processes typically occur in which other photons are re-radiated. Time periods between absorption and emission may vary – ranging from short femtosecond-regime for emission involving free-carrier plasma in inorganic semiconductors [288] up to milliseconds for phosphorescent processes in molecular systems. Under special circumstances delay of emission may even span to minutes or hours [287].

Observing photoluminescence at a particular energy may be seen as indication that an excited state associated with this transition energy is excitation populated. Even though this is common in atoms and similar systems, correlations and other more complex phenomena also act as sources for photoluminescence in many-body systems (such as semiconductors). A theoretical approach to deal with this is given by the semiconductor luminescence equations [287].

A typical PL experiment (Figure 25) uses a light-source that releases photons with energy greater than the band gap energy to excite a semiconductor with a

polarisation that can be described with the semiconductor Bloch equations [287]. Upon the absorption of photons, electrons and holes are formed with finite momenta \bar{k} in the conduction and valence bands, respectively. The excitations then undergo energy and momentum relaxation towards the band gap minimum. Typical mechanisms include Coulomb scattering and the interaction with phonons. The electron-hole recombination finally results in the emission of photons [287].

Ideal (defect-free) semiconductors may be represented by many-body systems in which, in addition to the light-matter coupling, the interactions of charge-carriers and lattice vibrations have to be considered also. Generally, the PL properties are also extremely sensitive to internal electric fields, as well as to the dielectric environment (such as in photonic crystals) which impose further degrees of complexity. A precise microscopic description is given by the semiconductor luminescence equations [287].

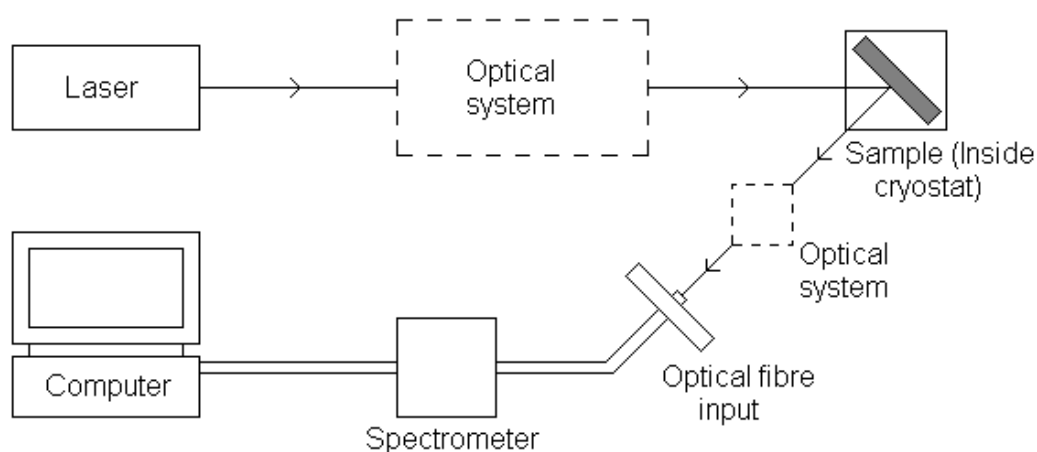


Figure 25: Typical experimental setup for PL measurements [289].

It is well known that the surface composition and structure can greatly influence the photocatalyst activity of materials [290]. PL (Photoluminescence) spectrum is an effective way to investigate the electronic structure and optical characteristics of semiconductor nano-materials, by which the information such as surface oxygen vacancies and defects as well as separation and recombination of photoinduced charge carriers can be obtained. Therefore, it is of great significance for preparing the photocatalyst with higher activity to carry out PL spectra research on semiconductor nano-materials.

In the current study, the emission properties were acquired using a Perkin-Elmer LS 55 Fluorescence Spectrometer (Figure 26) in the range from 310 – 532.5 nm with an excitation source of 446 nm. This spectrometer offers flexibility, versatility, reliability and ease-of-use. The monochromator-based LS 55 uses a high energy pulsed Xenon source for excitation. Its variable slit and holographic gratings provide flexibility with very low stray radiation.



Figure 26: The UV-vis instrumentation – Perkin-Elmer LS 55 Fluorescence Spectrometer – made available by the CSIR.

The synthesised powders were diluted with ethanol and placed in 1 cm path length UV quartz cuvettes before measuring the PL spectra with the steady-state fluorescence system, equipped with a Xenon flash lamp that is pulsed at 50 Hz line frequency. 450-W Xe lamp. The data was accumulated with a computer. All spectra were taken at room temperature.

3.3.7 Gas-Sensing

In order to generate a sensor signal, a sensor element normally incorporates a sensitive layer, deposited over a substrate, which is provided with electrodes for the measurement of the electrical characteristics. The device is generally heated by its own heater which is separated from the sensing layer and the electrodes by an electrical insulating layer [121].

Experimental techniques may be broadly grouped as either phenomenological or spectroscopic [121]. The former gives access only to the macroscopic effects as

opposed to microscopic knowledge e.g. change of sensor resistance or change of the composition of the ambient atmosphere that follow the detection of CO. However, distinguishing between CO reaction with oxygen ions or hydroxyl groups, if at all possible, cannot be made without spectroscopic input. On the other hand, ascribing a sensor effect to a certain surface reaction is not possible on the basis of spectroscopic input alone [121].

The typical phenomenological measurement technique normally involves conductance or resistance of the sensors as it relates to the composition of the surrounding atmosphere that is used for gaining the desired chemical information [121]. The measurements are performed in different modes of operation spanning from constant operation temperature and permanent polarisation to modulated operation temperature and periodic dc tests (with long or short pulses) [121]. Typical configurations of the electrodes are depicted in Figure 27.

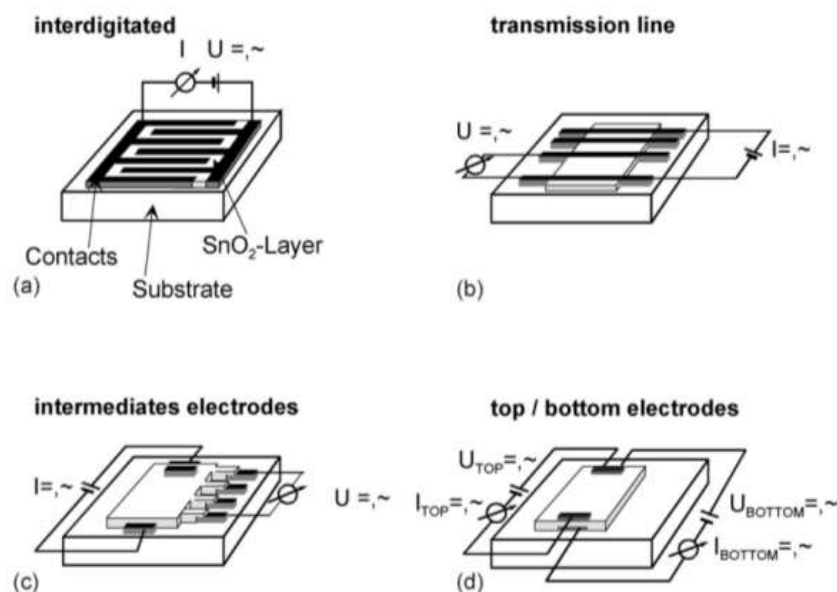


Figure 27: Electrode configurations [121].

3.3.7.1 Static and Dynamic Measurements

Gas sensors are normally characterised by two methods, namely (i) a static system in which the sensor temperature is held constant with a d.c. heater and (ii) a dynamic system in which the sensor temperature is modulated through a changing heater voltage [118]. In general, the information obtained from static measurements by

chemical sensors is one-dimensional – such as the change in the electrical resistance of a semiconductor gas sensor (ΔR) or response and recovery time. However, most chemical sensors are not very selective because of the principle involved in detection. For example, detection in a semiconductor gas sensor is based on the oxidation or combustion of a gas species. Although several attempts have been made to enhance this selectivity, it is impossible to oxidise only a specific substrate. Instead, we determine how to obtain much more information from molecular recognition by a single sensor [118].

A dynamic system contains abundant information. The key point in this system is the use of nonlinear dynamics in the chemical sensor [118]. The nature of a dynamic system depends on the wave shape of the frequency, the duty ratio and the applied voltage. Many useful items of information about the sensing reaction, including amplitude and frequency, can be obtained; it is beneficial to analyse the sensing mechanism for the gases to be tested and to enhance the selectivity. A time trace of the output signal is Fourier transformed to the frequency domain. The deformation of the output signal compared to the input corresponds to the nonlinearity of the experimental system and is quantitatively evaluated as the higher harmonics of a Fourier transformation [118].

Certain conditions are necessary for dynamic measurements. Gas sensing materials of a surface-controlled type (such as SnO_2 , TiO_2 and ZnO) have special sensing behavior during oscillating measurements [118]. On the other hand, bulk effect-controlled materials (such as Fe_2O_3) do not demonstrate an interesting sensing behavior, even though the surface temperature changes when a variable voltage is applied. It is widely believed that the overall surface stoichiometry has a decisive influence on the surface conductivity for the oxides. Oxygen vacancies act as donors, increasing the surface conductivity, whereas adsorbed oxygen ions act as surface acceptors, binding electrons and diminishing the surface conductivity [118].

With static measurements, the oxygen adsorbates are partly consumed by oxidation of target gases on the sensing material surface [118]. An increase in conductance is induced by a decrease in the amount of chemisorbed oxygen. In the dynamic system, in which the sensor temperature is modulated with a rectangular heating mode, the complicated response transients are considered to be closely related to

different reaction kinetics of individual target molecules on the surface of the sensing material. While the temperature is being modulated, no equilibrium exists among the surface oxygen species. Consequently, reactions between reducing and oxidising gases are dramatically influenced by temperature modulation, thus resulting in complicated response transients characteristic of individual target molecules. This makes, the method of dynamic measurement to be quite beneficial for the identification of sample gases and analysing sensing mechanisms [118].

Further, the structure of the element must be suitable for heating and radiating, and a smaller volume and thermal capacity are required. Easy desorption is also expected to follow the reaction of the gas sample with the adsorbed oxygen ions on the surface of the sensing material. Except at high levels, the amplitude of the response increases with the concentration of the gas sample [118].

3.3.7.2 Basic Characteristics of the Chemiresistive Sensor

The electrical resistance of a chemiresistive sensor changes drastically (increase or decrease) when exposed to the molecules of analysing gas. Increase or decrease in resistance depends on the nature of sensor material (*n*-type or *p*-type) and the gas (reducing or oxidizing) [118]. A typical response curve, that is, the variation of resistance of sensor with time of exposure and withdrawal of analysing gas, is schematically depicted in Figure 28. The response curve of a sensor is characterised by five parameters which depend on the sensing material, the interaction between the gas and the sensor, the sensor operating conditions, etc. These are [118]

- (a) *Sensor Sensitivity (S)*, which may be defined as either
 - i. a ratio of resistance in air to that in gas i.e. $S = \frac{R_{air}}{R_{gas}}$. Good sensors are indicated by a high value of *S* for a particular gas, or
 - ii. the percentage difference between the resistance in air and that in gas, i.e. $S (\%) = \frac{R_{air} - R_{gas}}{R_{air}} \times 100$. A positive value of *S* implies that resistance decreases on gas exposure and vice versa.
- (b) *Response Time* – the time interval in which resistance attains a fixed percentage (usually 90%) of final value when the sensor is exposed to full-

scale concentration of the gas. It is represented as t_{90} , t_{80} , t_{50} , etc. A t_{90} of 45 s implies that the sensor exhibits 90% of the saturation value of resistance in 45 s. A small value of response time is indicative of a good sensor.

- (c) *Recovery Time* (usually referred as t_{10}) – the time interval over which sensor resistance reduces to 10% of the saturation value when the sensor is exposed to full-scale concentration of the gas and then exposed to clean air. Good sensors should have a small recovery times for repeated use.
- (d) *Selectivity* (or specificity) of a sensor towards an analysing gas is expressed in terms of dimensions that compare the concentration of the corresponding interfering gas which produces the same sensor signal. This factor is obtained by $Selectivity = \frac{Sensor\ sensitivity\ for\ interfering\ gas}{Sensor\ sensitivity\ for\ desired\ gas}$. Usually most chemiresistive sensors exhibit significantly high value of sensitivity for many gases under similar operating conditions.
- (e) *Long Term Stability* is the ability of the sensor to maintain its properties when operated continuously for long durations in hostile environment. The good sensors are expected to work for several years without showing a drift in any of the above four parameters.

Other indicators that are considered in evaluating the performance of gas sensors (or gas sensing methods) designed for the market include energy consumption and fabrication cost [124].

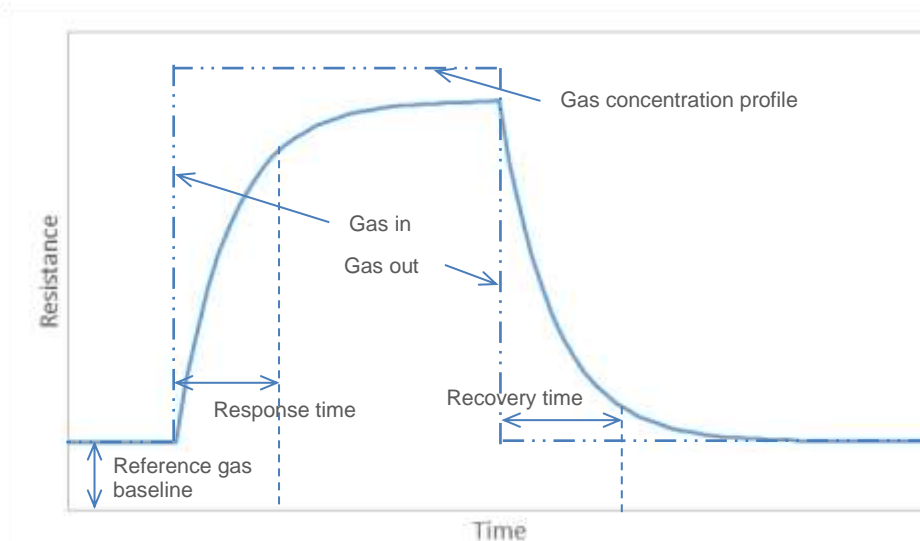


Figure 28: Typical response-curve of a gas sensor [124].

Gas sensors are normally characterised by two methods using (i) a dynamic system and (ii) a static system. In the current study a dynamic computer-automated gas sensing system, KSGAS6S by Kenosistec, Italy, (Figure 29) was used. The system is equipped with a 500 ml sensing chamber that accepts a total gas flow rate of 500 sccm. The voltage source for the heater is a TTi PL303QMD-p quad mode power supply while voltage source and current measurements across the sensor electrodes are made by Keithley 6487 picoammeter/voltage source.



Figure 29: Gas sensor testing system by Kenosistec [291].

The Kenosistec gas sensor testing system [291] features three independent test cells, each with its own sensors to constantly monitor pressure, temperature, relative humidity and flow speed. Thermally regulated chamber allows an accurate setting of the temperature and a microprocessor program is used to control every valve and to calculate gas flows and gas mixtures at desired concentration, humidity and temperature. Total control of dry and wet flows makes it possible to obtain specified relative humidity values [291]. There is also a computer-controlled mass spectrometer to monitor actual gas concentrations. The climate chamber is equipped with three air-sealed, vacuum-tested, testing cells to guarantee the gas sensor heads an interference-free space. The system provides an automatic gas flow control using three mass flow controllers – 2 air (to give dry and wet air) and 1 gas – with a valve system to distribute gas mixture flow. It further provides a thermoregulated humidifier, to provide 100% wet mixture and a thermoregulated condenser to eliminate extra humidity [291]. This allows maximum flexibility on preparing gas flows at a given concentration, humidity and temperature. With these parameters, the control program provides complete automatic sequences to verify all tests in conformity with CEI norms. The PPT430 software allows constant monitoring of cell contents, showing actual system concentration of gas. It is also possible to log data on disk, filling in reports on system activity. The unique close-source software allows good readings even at low concentrations (a few PPM) of gas mixture [291].

The sensing strip for holding the nanosamples is a 20 mm x 5 mm x 1 mm alumina strip with pre-printed with platinum electrodes on one side and resistive heater on the other. The various RH levels (between 8% and 84%) were achieved by bubbling water with synthetic air and monitored using an inbuilt humidity sensor. The ppm levels of target gases were adjusted by controlling the flow rate ratio with synthetic air. The total flow rate of 500 sccm ensured that the sensing chamber was filled in a minute. The response and recovery were each measured for 5 minutes.

To study the sensing properties, one anatase powder sample (annealed at 300°C) and one rutile powder sample (annealed at 900°C) were selected from each of the species -TiO_2 , $\text{Ag}\text{-TiO}_2$, $\text{Cu}\text{-TiO}_2$ and $\text{Ag+Cu}\text{-TiO}_2$. The functional properties of the titania nanopowders were screened for the detection of humidity, and reducing gases (NH_3 and H_2). Impedances were measured for ten humidity levels (between 5.4% RH and 88.4% RH) at 'Room' temperature (20.8°C ~ 28.0°C). The powders

were also exposed to seven different concentrations of NH₃ and H₂ gases, at operating temperatures of Room, 250°C, 300°C and 350°C – 25, 50, 75, 100, 250, 375, 500 sccm for NH₃ and 10, 20, 30, 40, 100, 150, 200 sccm for H₂. A summary of the samples tested are provided in Table 7. In it, it will be noted that the anatase powders were not subjected to working gas temperatures beyond their annealing temperature of 300°C. Sensor response time measurements were obtained by alternating between “gas-in” and “gas-out” modes.

Table 7: The scheme for the TiO₂ samples available for gas testing measurements.

Sample @ Annealing Temperature	Crystallographic Phase	Sensing Gas			Temperature (°C)			
		Humidity	NH ₃	H ₂	Room	250	300	350
-TiO ₂ @ 300°C	Anatase	√	√	√	√	√	√	
Ag\TiO ₂ @ 300°C	Anatase	√	√	√	√	√	√	
Cu\TiO ₂ @ 300°C	Anatase	√	√	√	√	√	√	
Ag+Cu\TiO ₂ @ 300°C	Anatase	√	√	√	√	√	√	
-TiO ₂ @ 900°C	Rutile	√	√	√	√	√	√	√
Ag\TiO ₂ @ 900°C	Rutile	√	√	√	√	√	√	√
Cu\TiO ₂ @ 900°C	Rutile	√	√	√	√	√	√	√
Ag+Cu\TiO ₂ @ 900°C	Rutile	√	√	√	√	√	√	√

Dynamic response and recovery profiles were plotted for each situation and the graphs for the sensitivity, as well as the response and recovery times were constructed from calculated values. The sensor sensitivity S (%), was measured by comparing the impedance of the sensor in air R_{air} to that in the target gas R_{gas} using the equation:

$$S (\%) = \frac{R_{air} - R_{gas}}{R_{gas}} \times 100$$

3-13

Response and recovery behaviours (Figure 28) are important characteristics for evaluating the humidity sensor performances. These parameters were evaluated at the time taken by a sensor to attain 90% of the maximum (or minimum) impedance change when the resistance is increasing (or decreasing).

RESULTS & DISCUSSION I: STRUCTURAL PROPERTIES

4.1 INTRODUCTION

The increasing interest and need to develop a deeper understanding of the nature and behaviour of nanostructured TiO₂, in energy and the environment, is driven by the increased use of engineered nanoparticles, as well as the increased pressure to commercialise the growing field of nanotechnology. Understanding the factors that affect material properties is essential for the successful and meaningful application of nanostructured TiO₂ and in predicting the behaviour of other nanomaterials of similar characteristics.

High precision characterisation instruments are increasingly required to observe, measure, and shape the properties of nanostructured materials for fundamental analysis and various potential applications. Characterisation and manipulation of individual nanostructures require great accuracy as well as atomic level resolution. Remarkable efforts have therefore been given to develop and upgrade the various microscopic and spectroscopic techniques that will play a central role in characterisation and measurement of nanostructured materials. Some of the instruments are surface sensitive, i.e. concerned with what lies within a few Angstroms of the sample surface, while others characterise the bulk of the material.

In this chapter, the structural properties of single-doped, double-doped and undoped TiO₂ nanoparticles are discussed. These sol-gel-derived sample species used in this study are listed in Table 6, which also reveals the various annealing temperatures they have been subjected to. Issues relating to the crystal structure of the nanopowders, including lattice constants, are addressed. Key focus of the discussion involves polymorphism (that is, the existence of the different crystal kinds of the TiO₂ compound). The current chapter also attempts to analyse the influence of annealing temperature, as well as the metal loading on the phase transition and phase mixing. In the end, a comparison of the spectroscopic results for the different species of TiO₂ nanoparticles would have been performed. The materials and methods used in obtaining the results discussed here have been covered in Chapter 3, which also describes the characterisation techniques (XRD, Raman Spectroscopy, SEM and EDS) involved in the analyses.

In the chapter that follows (Chapter 5), a discussion of the results relating to the optical characteristics of the TiO₂ nanopowders is presented. Chapter 6 is devoted to the analysis of the gas sensing properties of the various TiO₂ species.

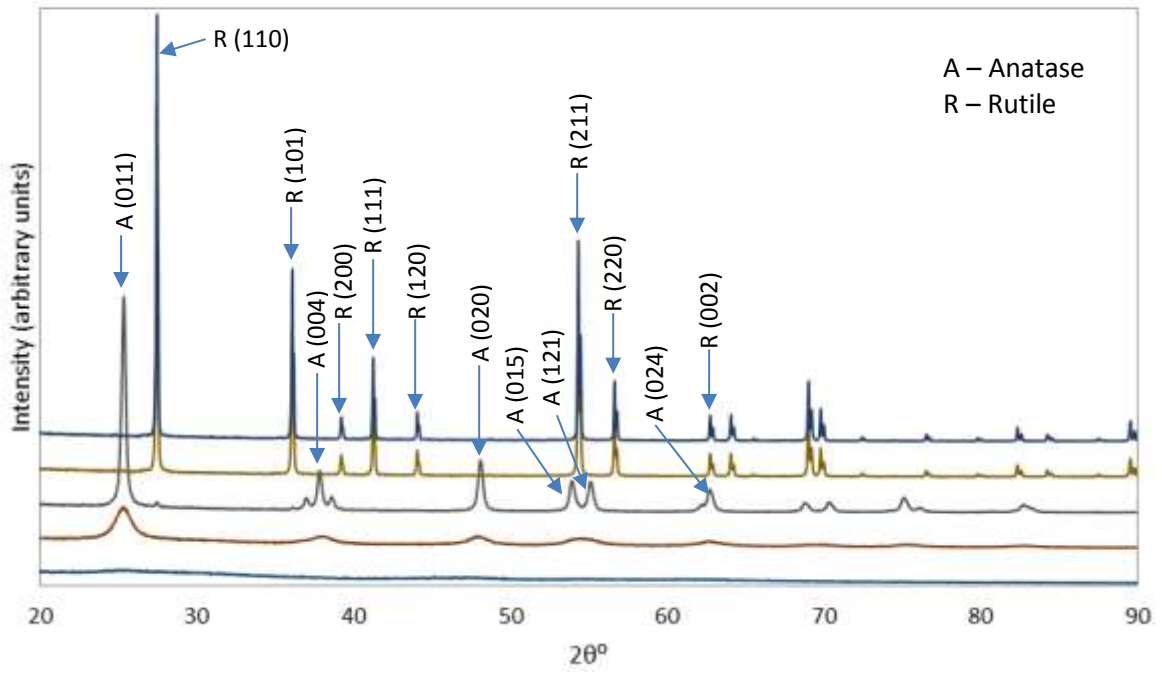
4.2 PHASE INDEXING

4.2.1 XRD Data

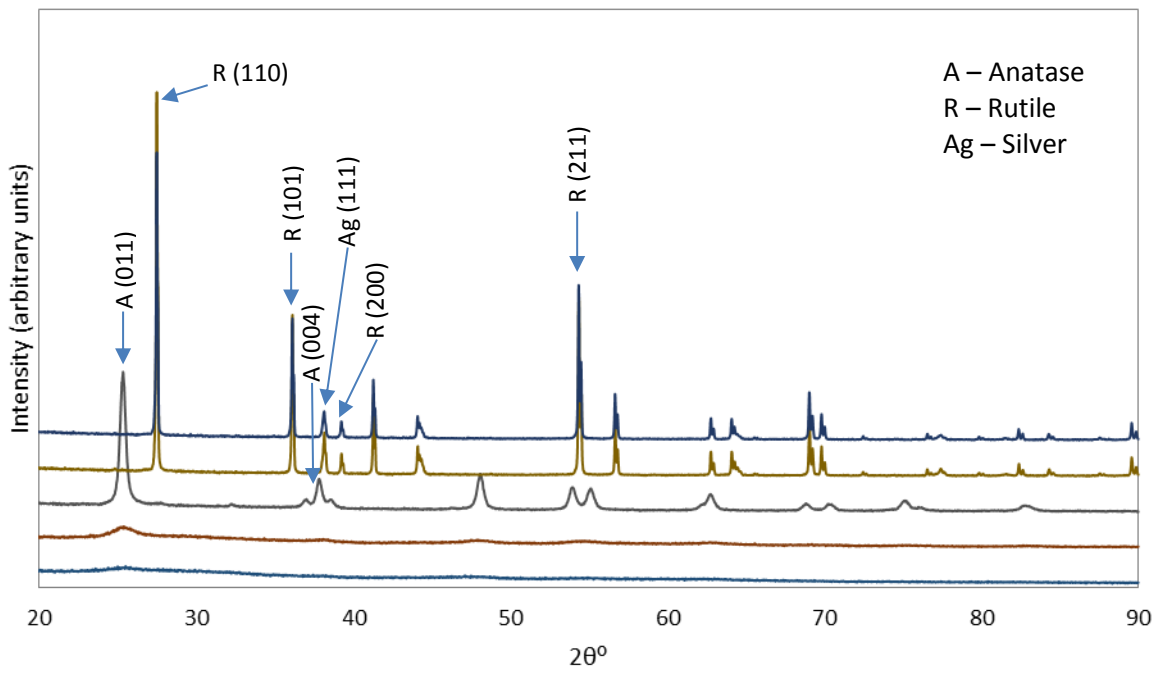
The starting point for analyses in this study involves verifying that the method of synthesis used (the sol-gel formalism) yielded the desired products. To this end, phase identification, by indexing the pattern obtained from the XRD data, was carried out. The XRD diffractograms of Figure 30 display the patterns for the titania species investigated in this study. In each case, samples annealed at 1100°C, 900°C, 600°C, 300°C, 100°C (drying) are arranged from top to bottom, respectively. The last sample, being that which was only dried at 100°C, is largely amorphous and therefore devoid of sharp TiO₂ peaks.

Manual indexing was carried out using reference data from the American Mineralogist Crystal Structure Database (AMCSD) [266]. The characteristic anatase, brookite and rutile XRD peak positions (2θ) obtained from AMCSD, are featured in Table 1. Software-assisted indexing was done with the Match! 2 (Version 2) computer application [268], with reference data from the Crystallography Open Database (COD) [265]. Table 8 summarises the COD entries for the various phases (namely anatase TiO₂, brookite TiO₂, rutile TiO₂, Ag (silver), CuO (tenorite) and AgCl (chlorargyrite)) that were identified in the TiO₂ powder samples investigated in the current study. (A more detailed specification of the entries can be found in Appendix D.) The table also displays the prominent peaks listed for each entry as 2θ positions ($^{\circ}$) and Miller indices (hkl). Estimates of the fraction (in %) of each phase found in a sample, as determined by the Match! 2 Program, are shown in Table 9.

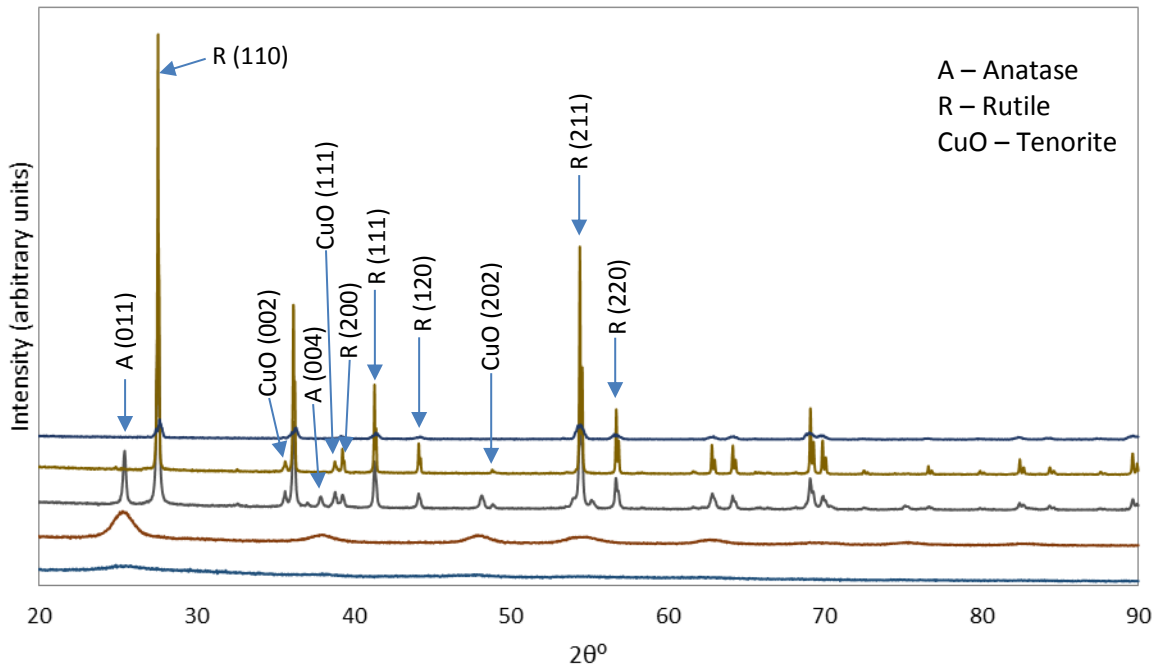
(a) TiO_2



(b) Ag/TiO_2



(c) $\text{Cu}\backslash\text{TiO}_2$



(d) $\text{Ag+Cu}\backslash\text{TiO}_2$

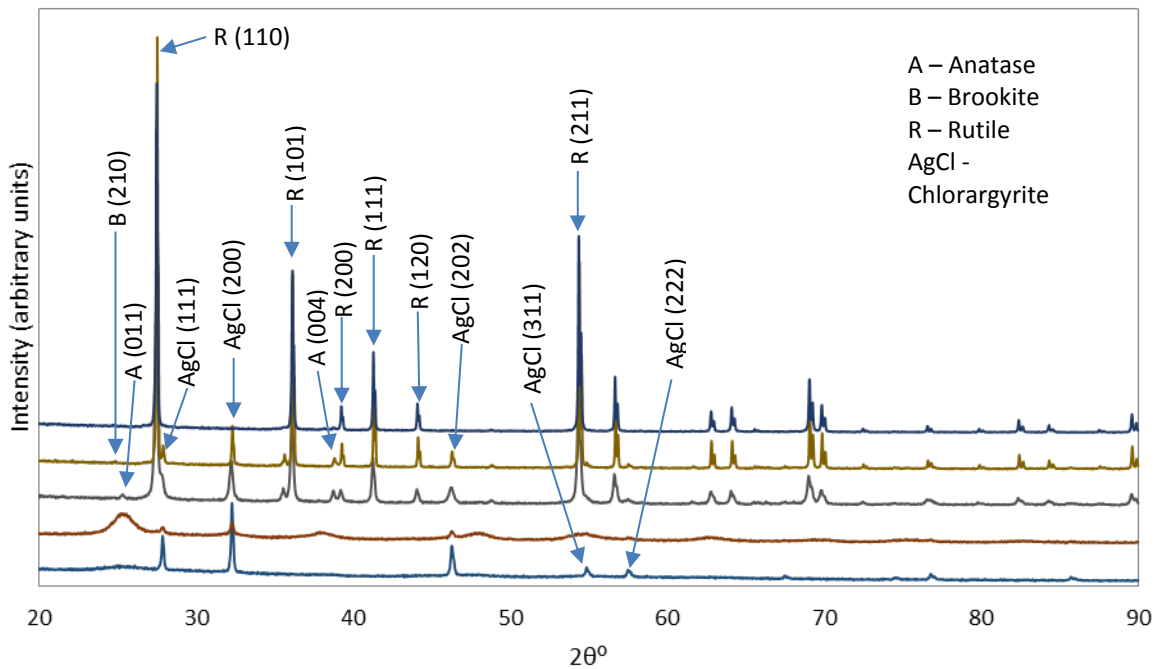


Figure 30: The XRD diffractograms of the various TiO_2 species, namely, (a) Pure (undoped) -TiO_2 , (b) $\text{Ag}\backslash\text{TiO}_2$, (c) $\text{Cu}\backslash\text{TiO}_2$ and (d) $\text{Ag+Cu}\backslash\text{TiO}_2$. In the pattern for each species, and the samples annealed at 1100°C , 900°C , 600°C , 300°C , 100°C (drying), are arranged from top to bottom respectively.

Table 8: A list of the phases found in the TiO₂ powder samples and their COD entry codes. Their major XRD peaks are included in the last column.

Phase	COD Reference	Major Reference Peaks (2 θ positions & Miller Indices)
Anatase TiO ₂	#96-901-5930	25.31 ⁰ (011), 37.79 ⁰ (004), 48.04 ⁰ (020), 53.88 ⁰ (015), 55.07 ⁰ (121), 62.69 ⁰ (024)
Brookite TiO ₂	#96-900-4140	25.31 ⁰ (210), 25.64 ⁰ (111), 30.75 ⁰ (211), 36.15 ⁰ (102), 47.94 ⁰ (321)
Rutile TiO ₂	#96-900-7532	27.43 ⁰ (110), 36.08 ⁰ (101), 41.24 ⁰ (111), 54.32 ⁰ (211), 56.62 ⁰ (220), 69.00 ⁰ (301)
Silver (Ag)	#96-900-8460	38.11 ⁰ (111), 44.30 ⁰ (200), 64.44 ⁰ (202), 77.4 ⁰ (311), 81.54 ⁰ (222)
CuO (Tenorite)	#96-901-6327	35.41 ⁰ (002), 35.50 ⁰ (11 $\bar{1}$), 38.69 ⁰ (111), 38.89 ⁰ (200), 48.66 ⁰ (20 $\bar{2}$), 61.46 ⁰ ($\bar{1}$ 13)
AgCl (Chlorargyrite)	#96-901-1667	27.84 ⁰ (111), 32.25 ⁰ (200), 46.26 ⁰ (202), 54.85 ⁰ (311), 57.52 ⁰ (222), 76.79 ⁰ (402)

Table 9: Quantities (in %) of the phases (anatase TiO₂, brookite TiO₂, rutile TiO₂, Ag (silver), CuO (tenorite) and AgCl (chlorargyrite)) as determined by the Match! 2 program for the TiO₂ powder samples.

Sample		Fraction of Phase in Sample (%)					
Species	Annealing Temperature	Anatase TiO ₂	Brookite TiO ₂	Rutile TiO ₂	Ag	CuO	AgCl
-TiO ₂	100°C	100					
	300°C	100					
	600°C	87.7		12.3			
	900°C			100			
	1100°C			100			
AgTiO ₂	100°C	100					
	300°C	100					
	600°C	98.5		1.6			1.5
	900°C			97.4	2.6		
	1100°C			97.7	2.3		
CuTiO ₂	100°C	100				n/a	
	300°C	100				n/a	
	600°C	15.8		80.8		3.4	
	900°C			97.9		2.1	
	1100°C			96.3		3.6	
Ag+CuTiO ₂	100°C	34.5					65.5
	300°C	72.6					27.4
	600°C	0.1		88.8		3.8	7.3
	900°C			93.9		2.0	4.1
	1100°C			100			
½Ag+CuTiO ₂	300°C	51.6	39.2				9.2
	600°C	n/a	8.5	78.9		4.6	8.0
	700°C		44.2	53.2		0.9	1.7
	900°C			99.2	n/a	0.8	

n/a – expected data not available.

4.2.2 Anatase and Rutile Phases

For all the sample species studied, the lower temperature patterns feature peaks at $2\theta = 25.3^\circ$, 37.3° , 48.1° , 53.9° , 55.1° , 62.6° , and 75.0° , that can be indexed to the (101), (004), (200), (105), (211), (204) and (215) planes of the anatase titania structure (AMCSD 0019093) [266], thus confirming the presence of this phase of titania. The phase identification carried out with the Match! 2 program [268] produced the pattern shown in Figure 31 for the -TiO_2 annealed at 600°C . The vertical lines represent the COD #96-901-5930 [265] anatase TiO_2 2θ peak positions and their relative intensities (given by the height of the lines). The Miller indices for each peak are displayed next to each line in this figure.

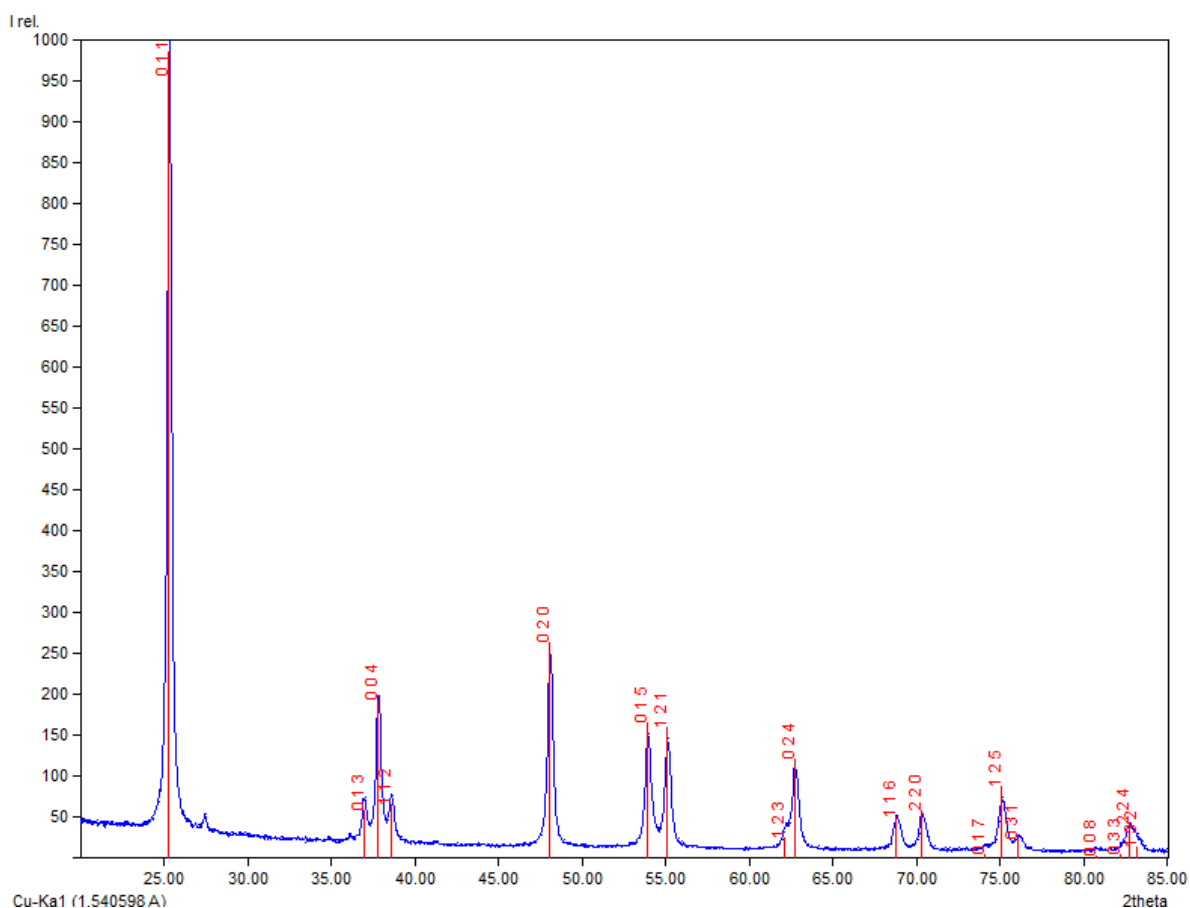


Figure 31: Phase identification results for the undoped -TiO_2 annealed at 600°C , as carried out on the Match! 2 program. The vertical lines represent the COD #96-901-5930 anatase titania 2θ peak positions and their relative intensities (given by the height of the lines). The Miller indices for each peak are displayed near the top of each line.

However, at higher temperatures (900°C and 1100°C, in the case of the -TiO_2 species of Figure 30 (a)), the peaks at $2\theta = 27.5^\circ$, 36.1° , 41.3° , 54.4° , 56.6° , 69.0° , and 69.8° – corresponding to the (110), (101), (111), (211), (220), (301) and (112) planes – can be indexed to the rutile titania structure (AMCSD 0001737) [266]. In the pattern shown in Figure 32 (produced using the Match! 2 phase identification program [268]) the vertical lines for the -TiO_2 annealed at 900°C, are for the COD 96-901-5930 [265] rutile TiO_2 2θ peak positions. As before, their relative intensities are represented by the relative height of the lines.

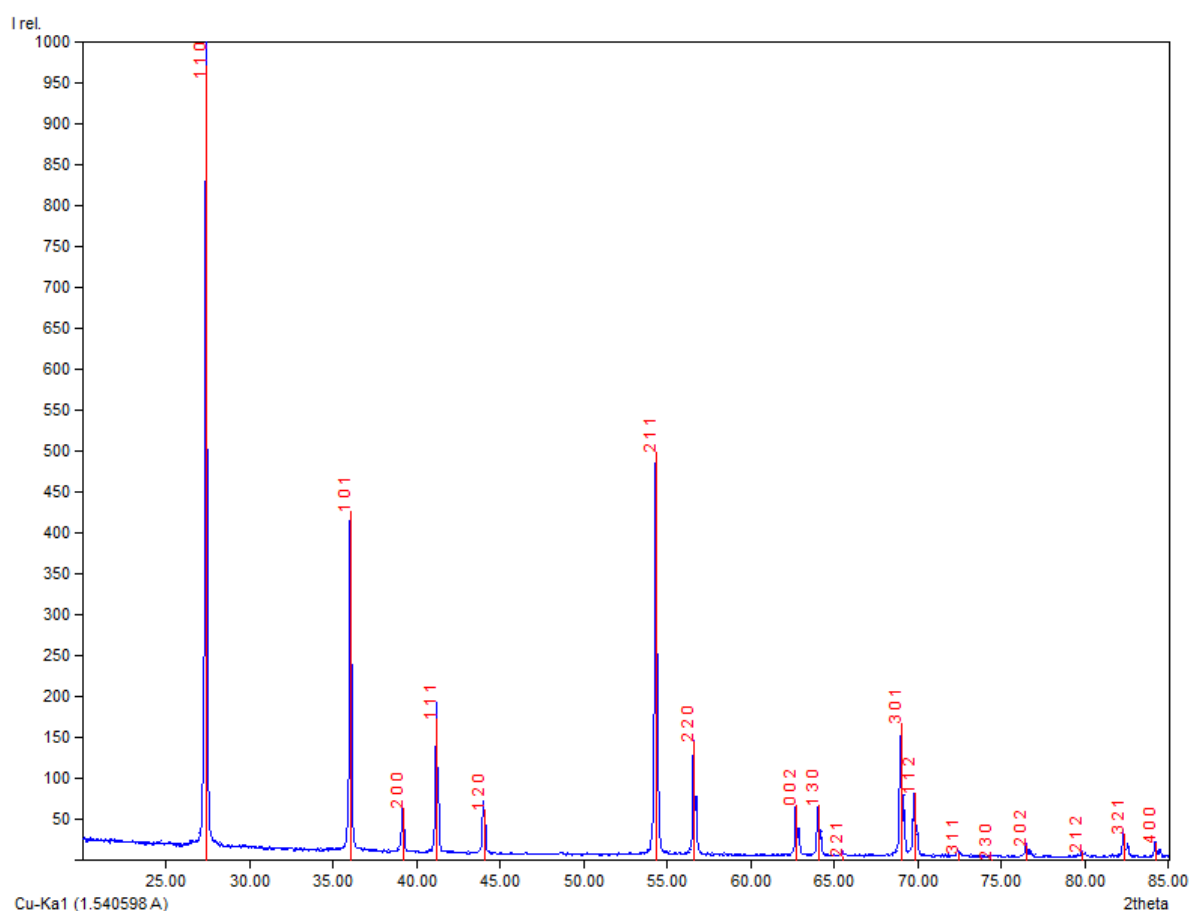


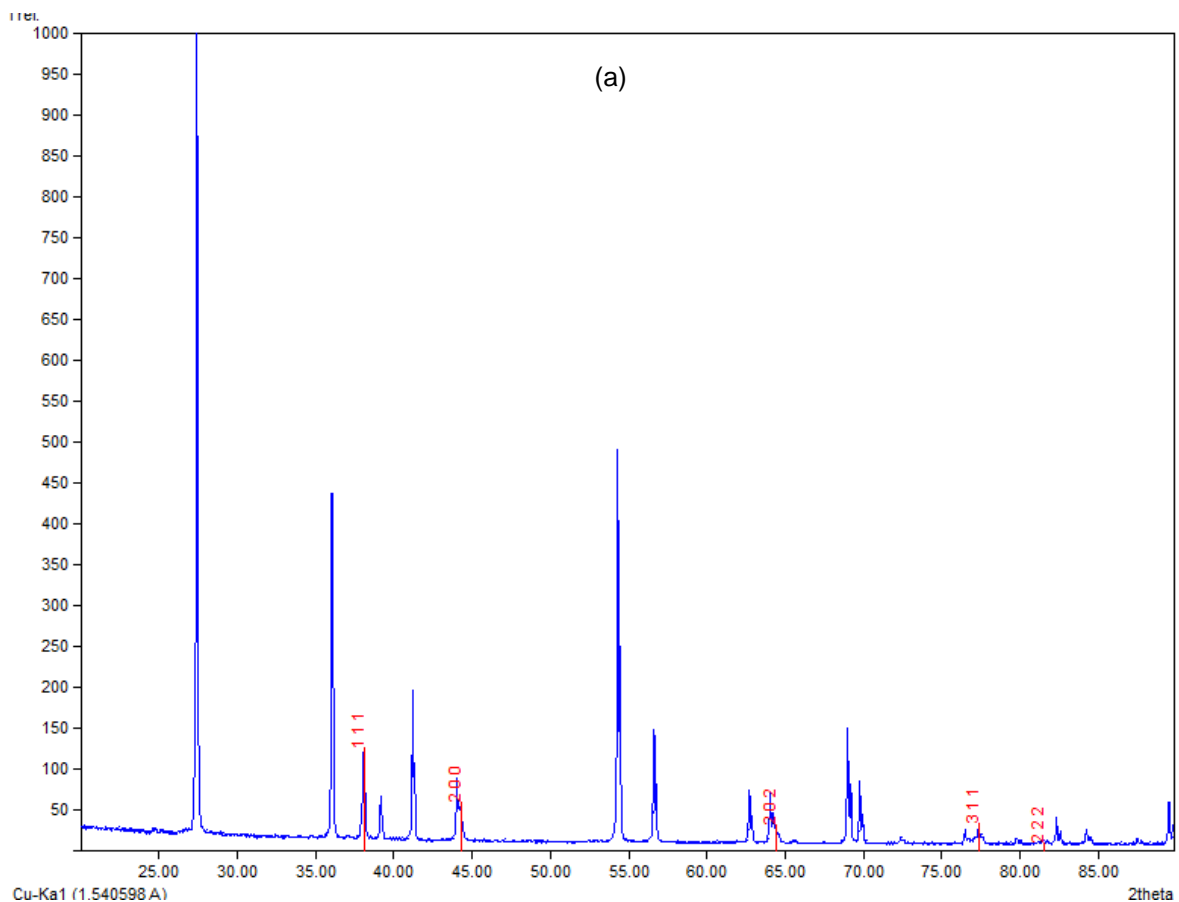
Figure 32: Phase identification results for the undoped -TiO_2 annealed at 900°C, as carried out on the Match! 2 program. The vertical lines represent the COD 96-900-7532 rutile titania 2θ peak positions and their relative intensities (given by the height of the lines). The Miller indices for each peak is displayed near the top of each line.

4.2.3 Extraneous Phases

Understandably, the XRD patterns for the doped samples feature peripheral peaks that cannot be identified with the any of the phases of TiO_2 . Since the undoped samples (TiO_2) are devoid of these peaks, it implies that they arise essentially from the introduction of the dopant materials of Ag and Cu. The extraneous phases were found to be due to reflections off lattice planes belonging to silver (Ag), CuO (tenorite) and AgCl (chlorargyrite), as quantified in Table 9.

4.2.3.1 Silver (Ag)

Figure 33 reveals the extraneous peaks due to silver (COD 96-900-8460) [265] that were found in the single-doped AgTiO_2 , 900°C and 1100°C patterns, at $2\theta = 38.1^\circ$, 44.3° , 64.4° , 77.4° , and 81.5° , corresponding respectively to Miller indices (111), (200), (220), (311) and (222). The absence of the Ag peaks in the lower-temperature AgTiO_2 patterns (dried at 100°C or annealed at 300°C and 600°C) suggests that the silver atoms might have migrated to the surface at temperatures above 600°C.



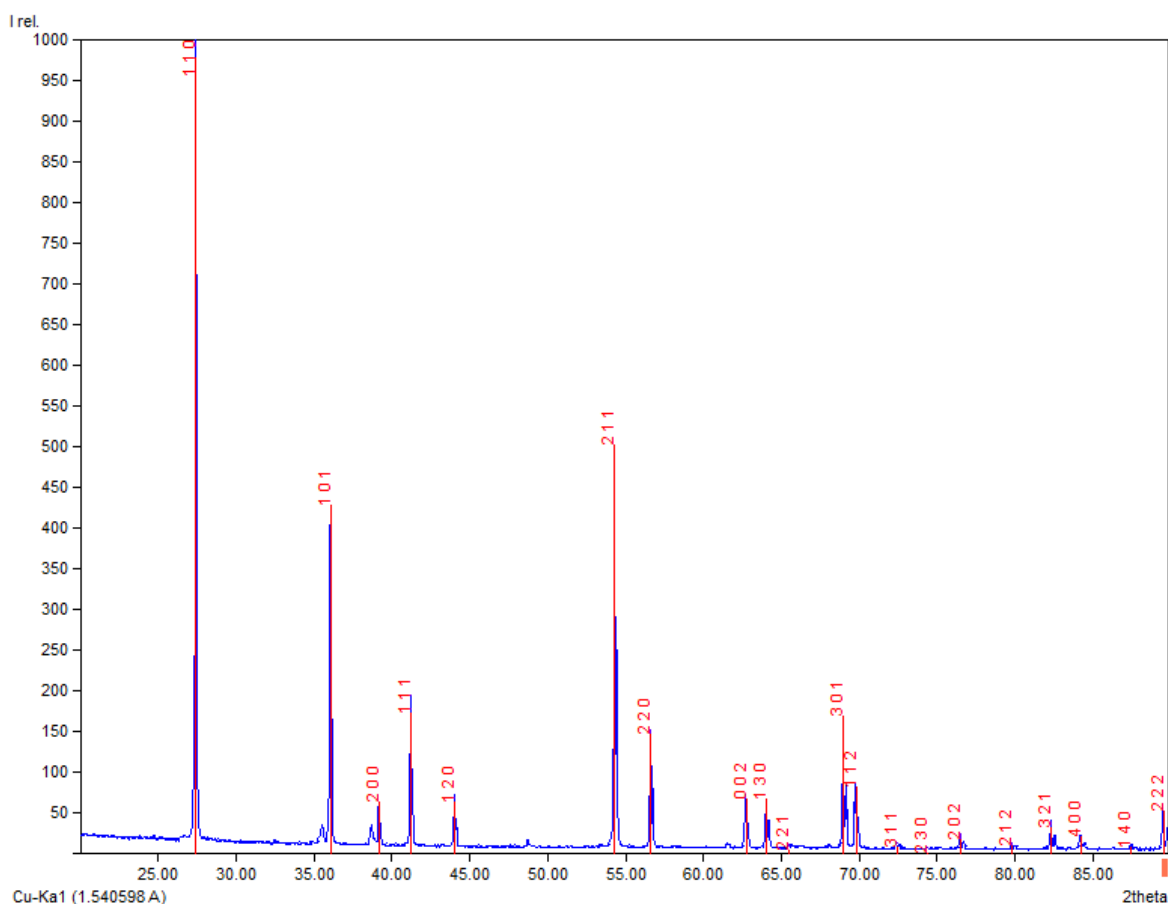
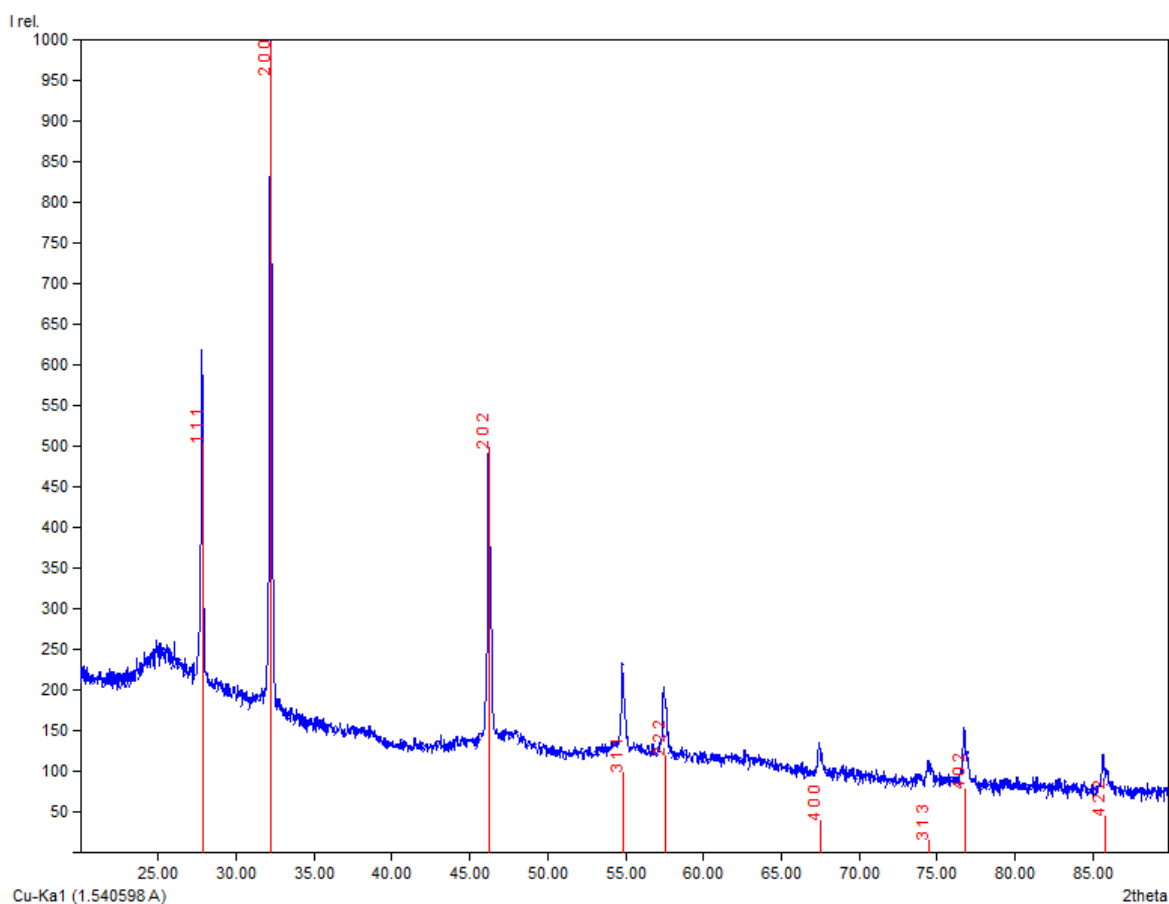


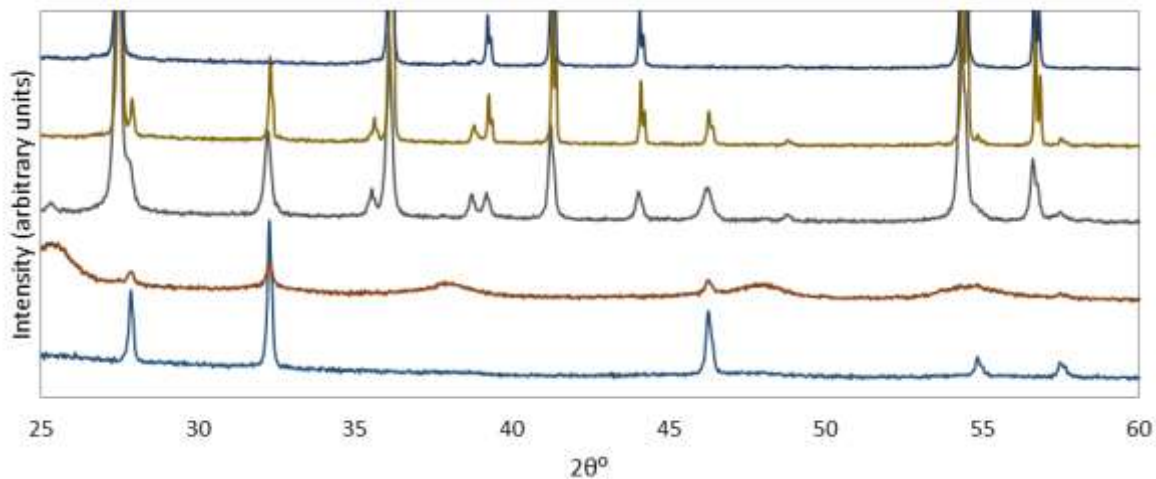
Figure 34: The XRD diffractogram of the $\text{Cu}\backslash\text{TiO}_2$ sample annealed at 900°C containing the peaks belonging to rutile TiO_2 . The unmarked extraneous peaks at 35.41° (002), 35.50° ($11\bar{1}$), 38.69° (111), 38.89° (200), 48.66° ($20\bar{2}$) and 61.46° ($\bar{1}13$) are identified with CuO (tenorite) – COD entry #96-900-6327.

4.2.3.3 AgCl

AgCl (whose mineral form is chlorargyrite) is present in all the $\text{Ag}+\text{Cu}\backslash\text{TiO}_2$ powders, at annealing temperatures of 900°C and below. Its peaks (Figure 35 (a)) were mapped to the COD entry of #96-901-1667 [265] and are located at 27.84° (111), 32.25° (200), 46.26° (202), 54.85° (311), 57.52° (222) and 76.79° (402), 2θ and Miller indices. However, at the very high annealing temperature of 1100°C , the AgCl phase is practically non-existent (Figure 35 (b)), whereas its peaks are relatively quite noticeable at the lower temperatures (100°C to 900°C), as indicated in Table 9.



(a)



(b)

Figure 35: (a) The AgCl peaks in the Ag+Cu\TiO₂ for the powder dried at 100°C, are found at 2θ and Miller indices of 27.84° (111), 32.25° (200), 46.26° (202), 54.85° (311), 57.52° (222) and 76.79° (402), using COD reference of #96-901-1667. (b) XRD patterns for the Ag+Cu\TiO₂ powder at temperatures 1100°C, 900°C, 600°C, 300°C, 100°C (top to bottom) showing the relative amounts of AgCl as it decreases with increasing annealing temperature. AgCl is no longer present at 1100°C.

4.3 CRYSTALLINITY

In all the TiO_2 species investigated in current study, the XRD diffraction patterns display sharp peaks – which is indicative of the high purity and crystallinity of the sol-gel derived nanoparticles [292]. Further, improved resolution is observed as the annealing temperature increases. A typical situation is shown in Figure 36 for anatase titania patterns of the -TiO_2 species at annealing temperatures of 100°C (bottom), 300°C (middle) and 600°C (top). However, doped and undoped powders from the various species do not show any appreciable difference in crystallinity (Figure 37) at the same phase and annealing temperature. The influence of doping with Ag and/or Cu on the crystallinity can be assumed to be intangible.

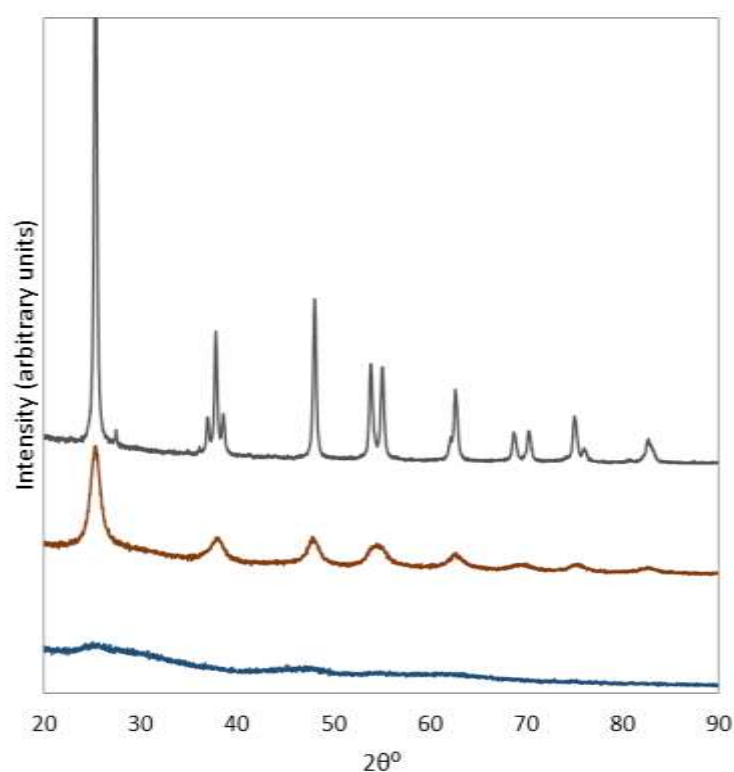


Figure 36: XRD diffractograms of the undoped -TiO_2 species dried at 100°C (bottom), heated at 300°C (middle) and at 600°C (top). The anatase TiO_2 patterns show improved resolution of the peaks as temperature increases.

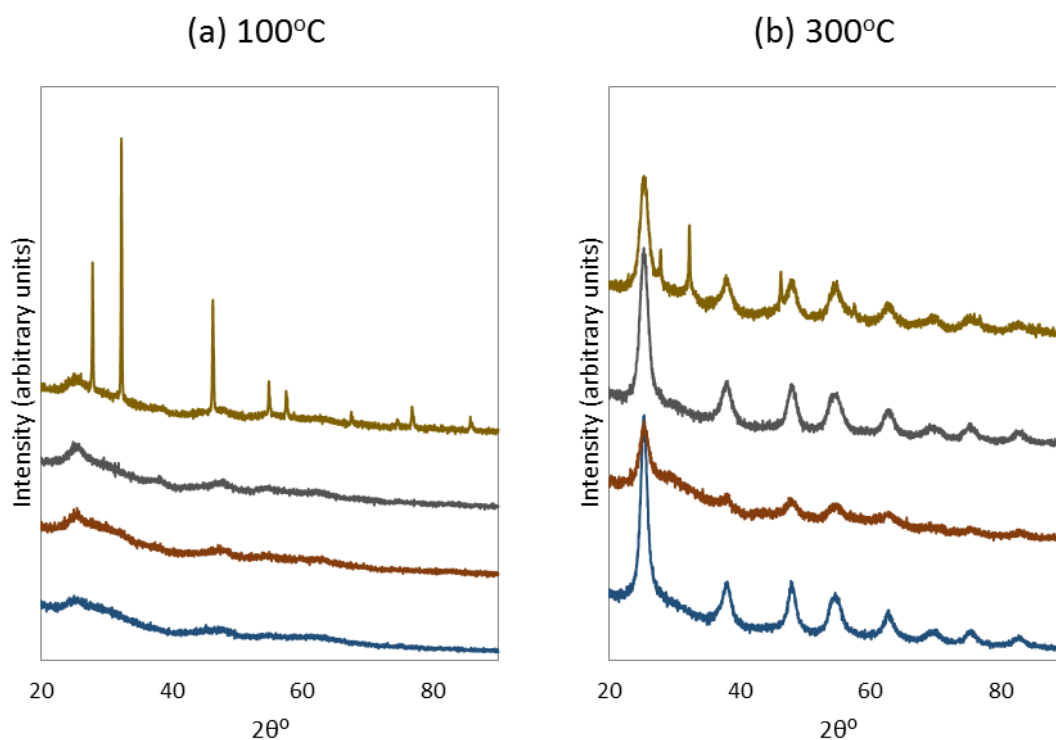


Figure 37: Anatase TiO_2 XRD diffractograms of all the titania species (a) dried at 100°C and (b) heated at 300°C . The patterns for $\text{Ag+Cu}\backslash\text{TiO}_2$, $\text{Cu}\backslash\text{TiO}_2$, $\text{Ag}\backslash\text{TiO}_2$, and $\text{-}\backslash\text{TiO}_2$, are arranged from top to bottom respectively. The sharp peaks in the $\text{Ag+Cu}\backslash\text{TiO}_2$ (top-most) pattern are due to the presence of AgCl .

4.4 CRYSTALLITE SIZE

The broadening of XRD peaks for all powder samples is indicative of the small size of the sol-gel derived nanoparticles. As it is often the case [4], [293], [294], analysis of the TiO_2 grain size evolution reveals that the Scherrer-derived crystallite or domain sizes (Table 10) increases with increasing annealing temperature – as the samples evolve from the anatase phase to rutile. The variation of the crystallite size with annealing temperature for the various titania species can be fitted (Figure 38) with 4th order polynomials as follows:

$$\text{-}\backslash\text{TiO}_2: \quad \tau_{(hkl)} = -2 \times 10^{-10}T^4 + 4 \times 10^{-7}T^3 - 2 \times 10^{-4}T^2 + 0.0371T + 0.6467$$

$$\text{Ag}\backslash\text{TiO}_2: \quad \tau_{(hkl)} = -9 \times 10^{-10}T^4 + 2 \times 10^{-6}T^3 - 0.0011T^2 + 0.2587T - 12.591$$

$$\text{Cu}\backslash\text{TiO}_2: \quad \tau_{(hkl)} = -5 \times 10^{-10}T^4 + 5 \times 10^{-7}T^3 + 5 \times 10^{-5}T^2 - 0.057x + 8.2617$$

$$\text{Ag+Cu}\backslash\text{TiO}_2: \tau_{(hkl)} = -9 \times 10^{-11}T^4 - 1 \times 10^{-7}T^3 + 4 \times 10^{-4}T^2 - 0.1234T + 12.388$$

Generally, for the anatase structures, the crystallites of doped powders are found to be slightly smaller than those of the undoped TiO_2 . This grain growth inhibition through doping is in agreement with previous studies that discussed the reduction mechanism [5], [6]. On the other hand, the doped rutile samples show larger crystallites than the rutile powders of the $\text{-}\backslash\text{TiO}_2$ species.

Table 10: Crystallite sizes (in nm) of the major TiO_2 phases of anatase and rutile in the TiO_2 powder samples – as estimated with the aid of the Origin® program and Scherrer equation.

Sample		Crystallite Size (nm)	Predominant TiO_2 Phase
Species	Calcination Temperature		
$\text{-}\backslash\text{TiO}_2$	100°C	3.20	Anatase
	300°C	7.39	
	600°C	28.84	
	900°C	65.46	Rutile
	1100°C	77.57	
$\text{Ag}\backslash\text{TiO}_2$	100°C	3.74	Anatase
	300°C	6.17	
	600°C	21.38	
	900°C	74.93	Rutile
	1100°C	74.56	
$\text{Cu}\backslash\text{TiO}_2$	100°C	3.53	Anatase
	300°C	6.32	
	600°C	47.05	
	900°C	78.53	Rutile
	1100°C	26.21	
$\text{Ag+Cu}\backslash\text{TiO}_2$	100°C	3.79	Anatase
	300°C	6.53	
	600°C	43.22	
	900°C	79.70	Rutile
	1100°C	74.86	

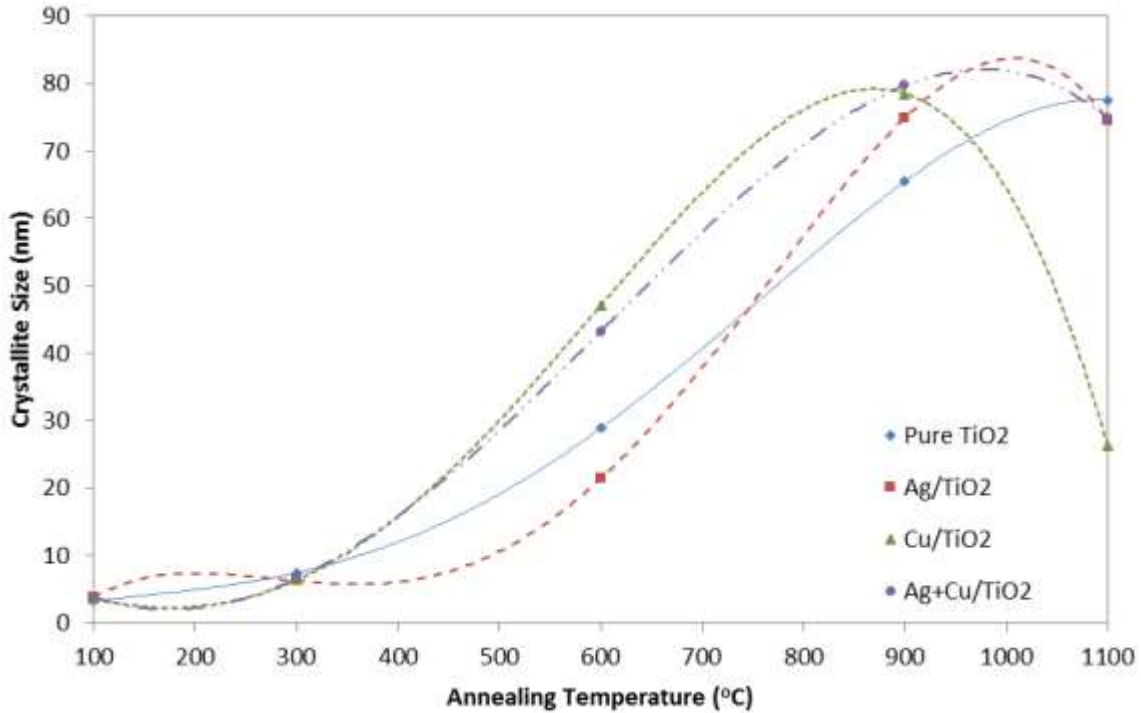


Figure 38: The variation of the crystallite size with annealing temperature for the various TiO_2 species (TiO_2 , Ag/TiO_2 , Cu/TiO_2 and Ag+Cu/TiO_2) fitted with 4th order polynomials.

4.5 LATTICE SIZE

As previously mentioned in Section 2.5.1, the primitive unit cell of anatase and rutile TiO_2 have tetragonal structures, with the cell parameters of anatase being $a = b = 3.78 \text{ \AA}$, $c = 9.50 \text{ \AA}$, while those of rutile are $a = b = 4.59 \text{ \AA}$, $c = 2.95 \text{ \AA}$ (Figure 1). The respective cell volumes are thus 135.74 \AA^3 and 62.15 \AA^3 . This is in agreement with COD entries #96-901-5930 (Appendix C1) and #96-900-4140 (Appendix C2) [295].

The unit cell parameters of all the anatase and rutile tetragonal structures in the current study are displayed in Table 11. In general, the values suggest that the titania lattice is not significantly deformed by doping, particularly at the higher annealing temperatures of 600°C , 900°C and 1100°C . Below these temperatures however, a slight reduction in the c -parameter is observed for the doped TiO_2 samples that incorporated Ag. This may be due to the shorter bond lengths of the AgCl (or smaller c -parameter $a = b = c = 5.5463$) structures which is found in these samples [296]. The CuO ($a = 4.6927 \text{ \AA}$, $b = 3.4283 \text{ \AA}$, $c = 5.1370 \text{ \AA}$, $\beta =$

99.546°) found in the samples doped with Cu may also account for the slight shrinking of the c-parameter.

Table 11: The unit cell parameters of all the tetragonal anatase and rutile titania structures. The last column compares their cell volumes with expected values (anatase: 135.74, rutile: 62.15).

Sample			Lattice Constants (Å)		Cell Volume (Å ³)	
Phase	Calcination Temperature	Species	a = b	c	Calculated	% Difference
Anatase (Lit.: a = b = 3.78 Å, c = 9.50 Å)	100°C	-TiO ₂	3.80	9.31	134.44	0.96
		Ag\TiO ₂	3.81	8.71	126.44	6.85
		Cu\TiO ₂	3.80	9.07	130.97	3.51
		Ag+Cu\TiO ₂	3.89	8.18	123.78	8.81
	300°C	-TiO ₂	3.79	9.37	134.59	0.85
		Ag\TiO ₂	3.80	9.07	130.97	3.51
		Cu\TiO ₂	3.79	9.37	134.59	0.85
		Ag+Cu\TiO ₂	3.80	9.11	131.55	3.09
	600°C	-TiO ₂	3.78	9.49	135.60	0.10
		Ag\TiO ₂	3.78	9.53	136.17	0.32
		Cu\TiO ₂	3.77	9.37	133.17	1.89
		Ag+Cu\TiO ₂	3.78	9.52	136.03	0.21
Rutile (Lit.: a = b = 4.59 Å, c = 2.95 Å)	600°C	Ag+Cu\TiO ₂	4.59	2.96	62.36	0.34
	900°C	-TiO ₂	4.59	2.96	62.36	0.34
		Ag\TiO ₂	4.59	2.96	62.36	0.34
		Cu\TiO ₂	4.57	2.97	62.03	0.19
		Ag+Cu\TiO ₂	4.58	2.96	62.09	0.10
	1100°C	-TiO ₂	4.59	2.96	62.36	0.34
		Ag\TiO ₂	4.59	2.96	62.36	0.34
		Cu\TiO ₂	4.53	3.00	61.56	0.95
Ag+Cu\TiO ₂		4.58	2.97	62.30	0.24	

4.6 POLYMORPHISM

4.6.1 Phase Transition

The transformation of the metastable anatase and brookite polymorphs of TiO₂ to rutile, upon heat treatment, has been extensively discussed in Section 2.5.2. Generally, under standard calcinations conditions, the phase transformation of anatase to rutile is observed between 600°C and 700°C. Figure 39 (a zoom in on Figure 30 (a)) presents the XRD diffractograms of samples from the -TiO₂ species synthesised for the current study. Here, the anatase-to-rutile transition actually began just below 600°C, as evidenced by the weak (110) rutile peak at this

calcination temperature, and was already complete before 900°C was reached. The same trend is observed for the single-doped Ag\TiO₂ as well.

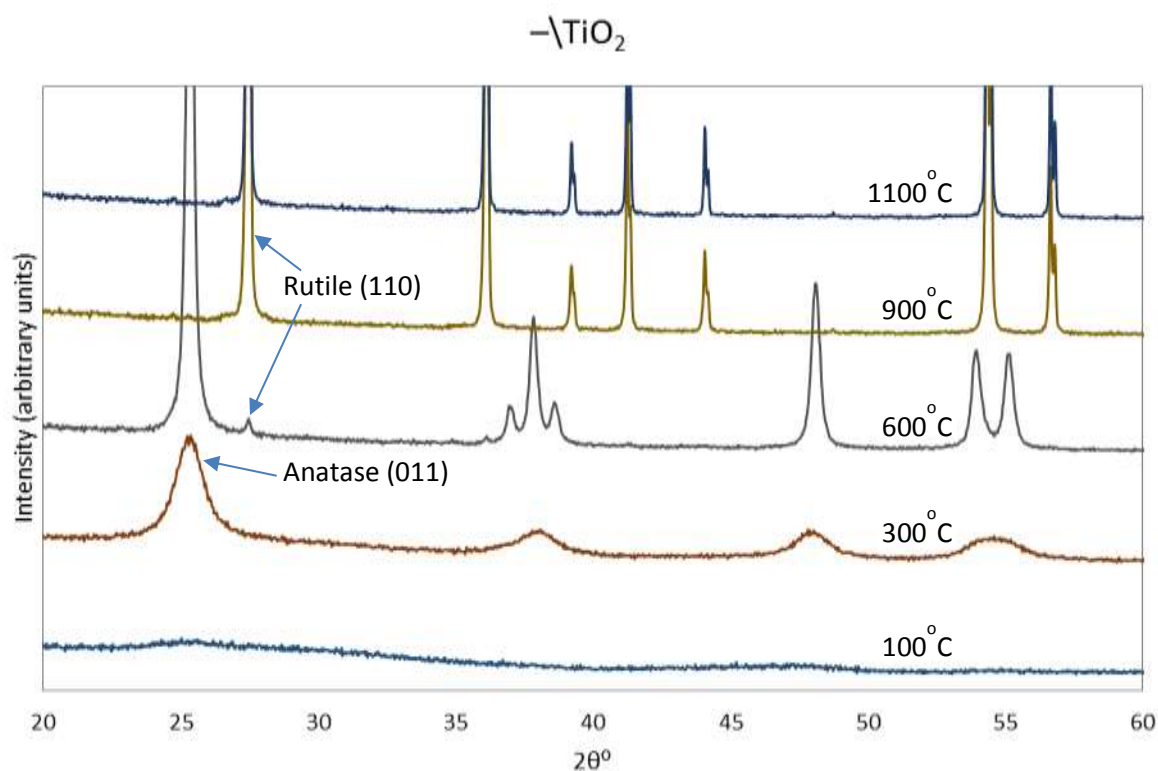


Figure 39: XRD diffractograms for the undoped -TiO_2 species samples showing the occurrence of the anatase-to-rutile phase transition between the calcination temperatures of 600°C and 900°C.

The $\text{Cu}\text{-TiO}_2$ powder however displays a well-formed rutile structure at 600°C (Figure 40), in addition to the anatase peaks. This suggests that the phase transition started well below the transition temperatures of the undoped -TiO_2 and $\text{Ag}\text{-TiO}_2$ samples (that is 600°C). A close inspection of the XRD patterns for the double-doped $\text{Ag+Cu}\text{-TiO}_2$ species (Figure 41) reveals a very weak reflection for the (011) anatase peak at 600°C. The almost-complete anatase-to-rutile transformation at this temperature implies that the transition must have started much earlier than the $\text{Cu}\text{-TiO}_2$ case. Figure 42 summarises the anatase-to-rutile transition scheme, at different annealing temperatures, for each of the TiO_2 species. Cu impurities are seen here to lower the transformation temperature, while the combination of Ag and Cu goes even further in reducing this temperature.

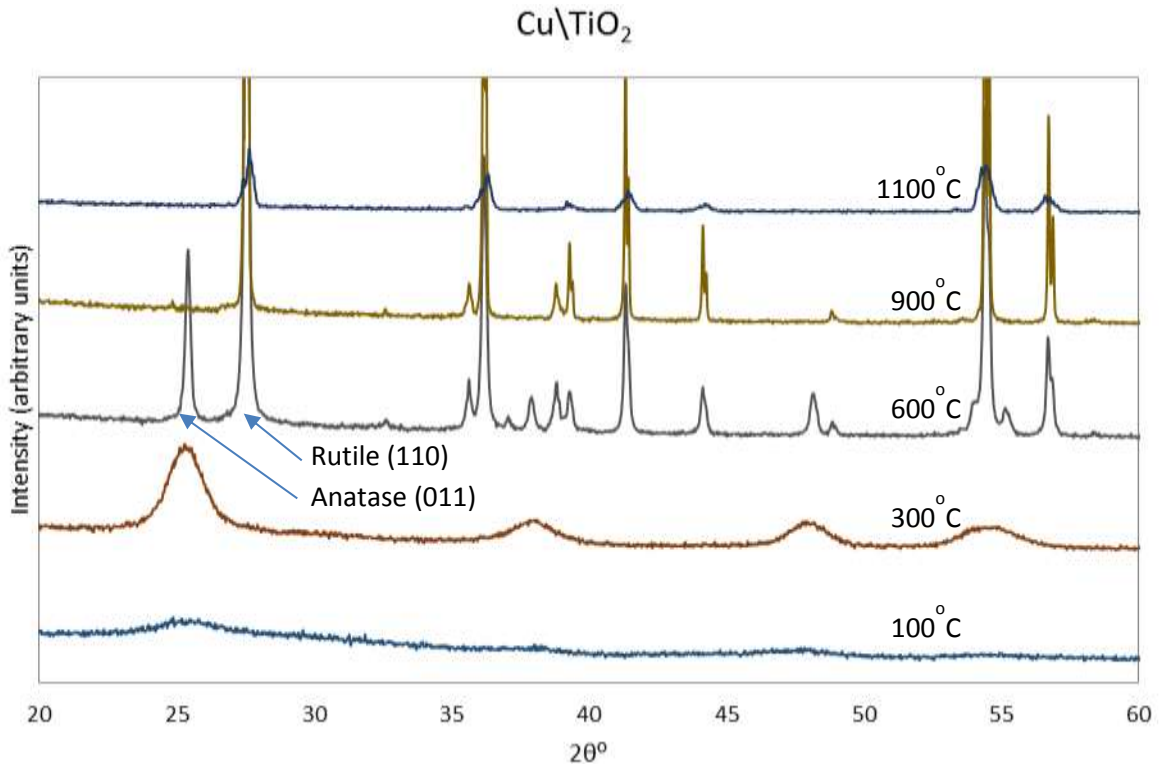


Figure 40: XRD diffractograms for the single-doped $\text{Cu}\backslash\text{TiO}_2$ species indicating the commencement of the anatase-to-rutile phase transition between the calcination temperatures of 300°C and 600°C.

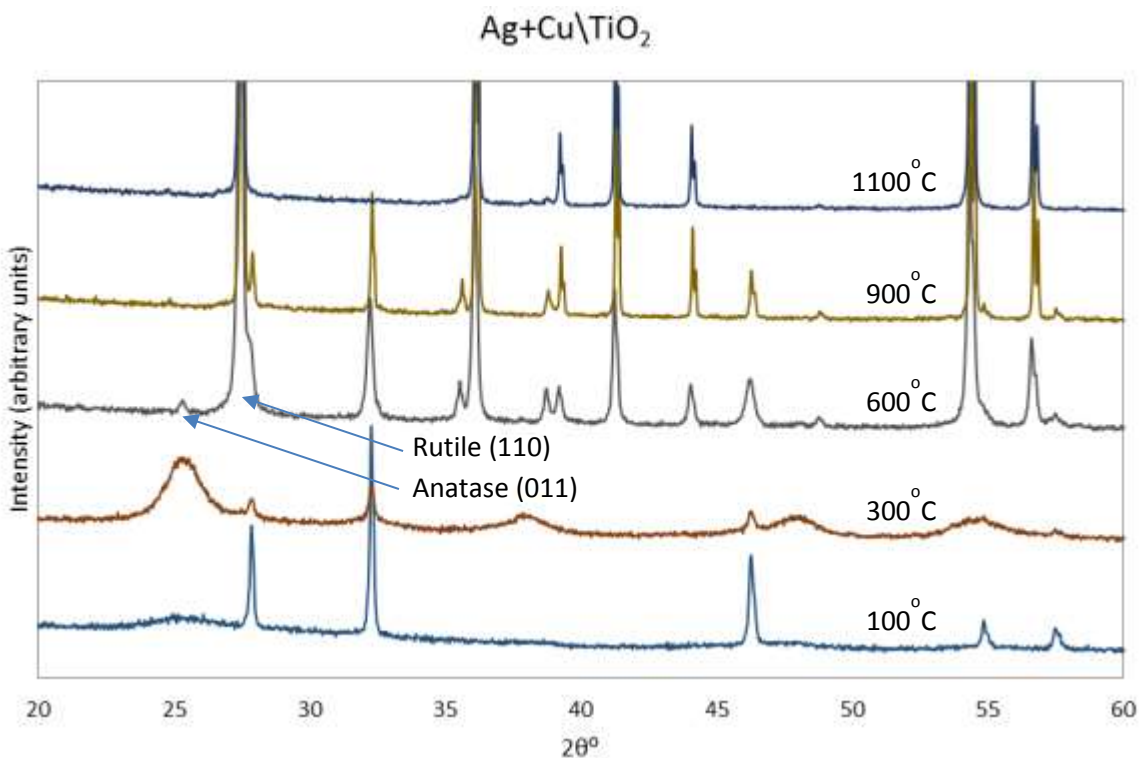


Figure 41: XRD diffractograms for the double-doped $\text{Ag}+\text{Cu}\backslash\text{TiO}_2$ species indicating the nearly completed anatase-to-rutile phase transition at the calcination temperatures of 600°C.

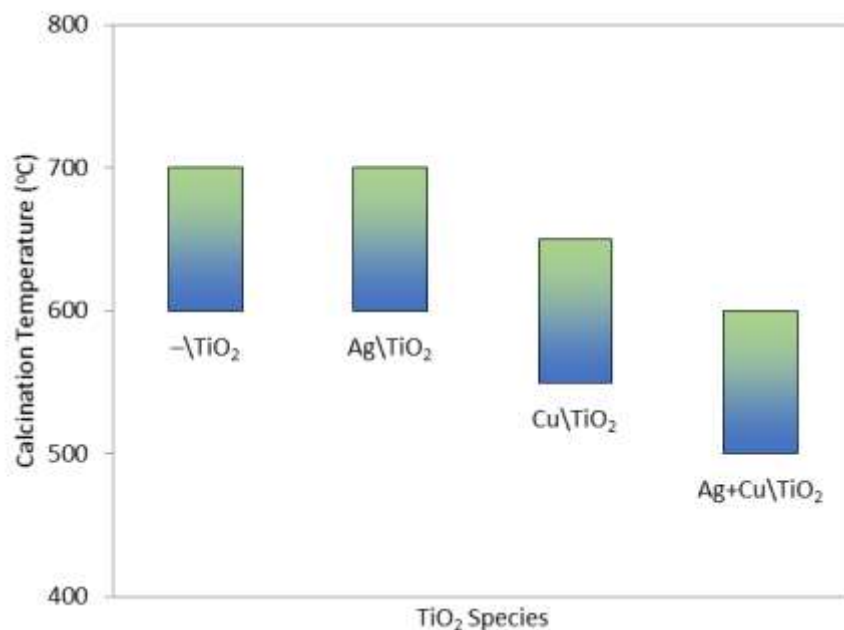


Figure 42: A depiction of the anatase-to-rutile (blue-to-green or bottom-to-top) phase transition at various calcination temperatures, for the different TiO_2 species.

4.6.2 Phase Mixing

Table 9 of Section 4.2.1 reveals that the TiO_2 species contained a mixture of anatase, brookite or rutile at some point in their phase evolution with calcination temperature. For all the species, a mixture of anatase and rutile phases (in various ratios) can be identified directly from their XRD patterns, at the calcination temperature of 600°C. The phase contents are discussed in Section 4.6.3.

At first glance, TiO_2 phase transformations appear to involve only anatase-to-rutile transitions only. Upon closer inspection however, the double-doped $\text{Ag}+\text{Cu}\text{TiO}_2$ structure (Figure 30 (d)) reveals the presence of brookite peaks (in addition to those of anatase) at 300°C, with the two most intense ($2\theta = 25.38^\circ$, 25.73°) being overlapped by the anatase (101) peak at $2\theta = 25.33^\circ$. Another double-doped structure ($\frac{1}{2}\text{Ag}+\text{Cu}\text{TiO}_2$), which was synthesised with a lower dopant concentration (2.5 wt% of each dopant, as opposed to the 5 wt% in the $\text{Ag}+\text{Cu}\text{TiO}_2$). This sample reveals the presence of this brookite phase to a greater degree between the annealing temperatures of 300°C and 700°C (Figure 44). Brookite, having been transformed to rutile, was no longer noticeable at 900°C and higher.

The extraneous (non-TiO₂) phases of Ag (boiling point of 2126°C), CuO (boiling point of 2000°C) and AgCl (boiling point of 1547°C) are also found in the doped TiO₂ species – as outlined in Section 4.2.3. The species containing impurities of Ag ions (that is, Ag\TiO₂ and Ag+Cu\TiO₂) were found to contain AgCl, which at the higher temperatures (~1100°C) appear to reduce to pure silver (in the case of Ag\TiO₂), or vapourise completely (in the case of Ag+Cu\TiO₂). The inclusion of Cu as a dopant (which introduces CuO into the powder samples) thus seems to influence the transformation of AgCl to other products at very high temperatures. CuO itself is present only in the 600°C and 900°C samples of the Cu\TiO₂ and Ag+Cu\TiO₂ species. Cu impurity ions may also account for the strong peaks of AgCl in the 100°C and 300°C samples of the double-doped Ag+Cu\TiO₂.

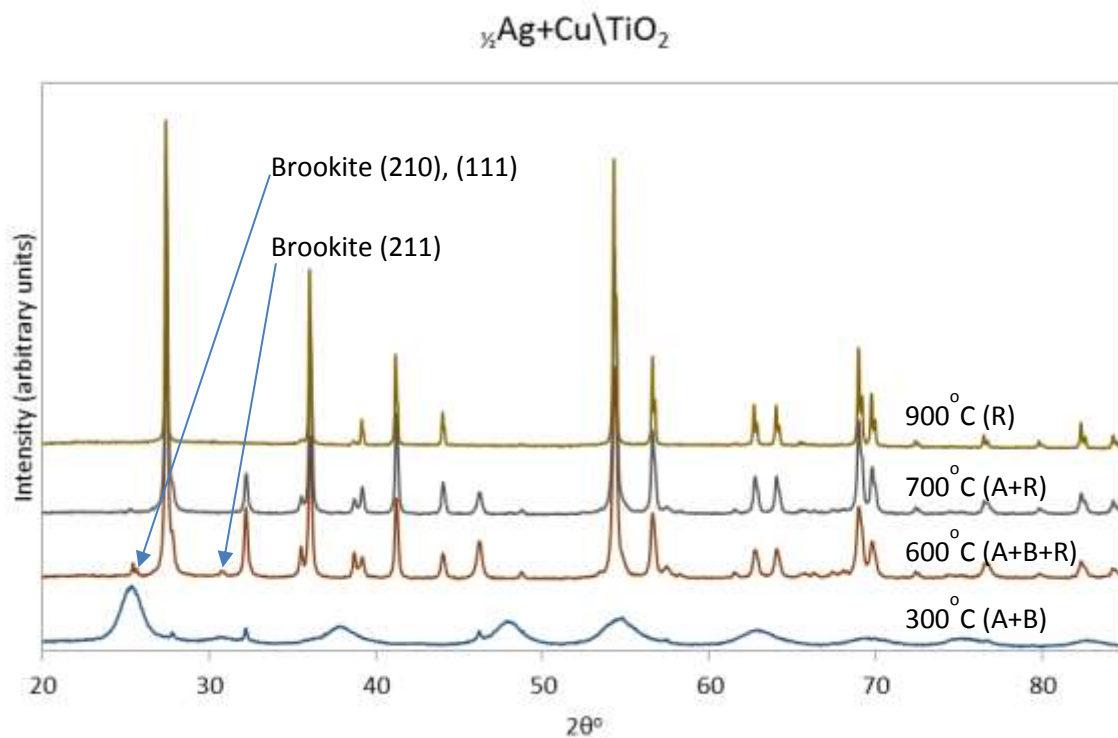


Figure 43: Brookite peaks in the XRD diffractogram of the $\frac{1}{2}\text{Ag+Cu}\backslash\text{TiO}_2$ species.

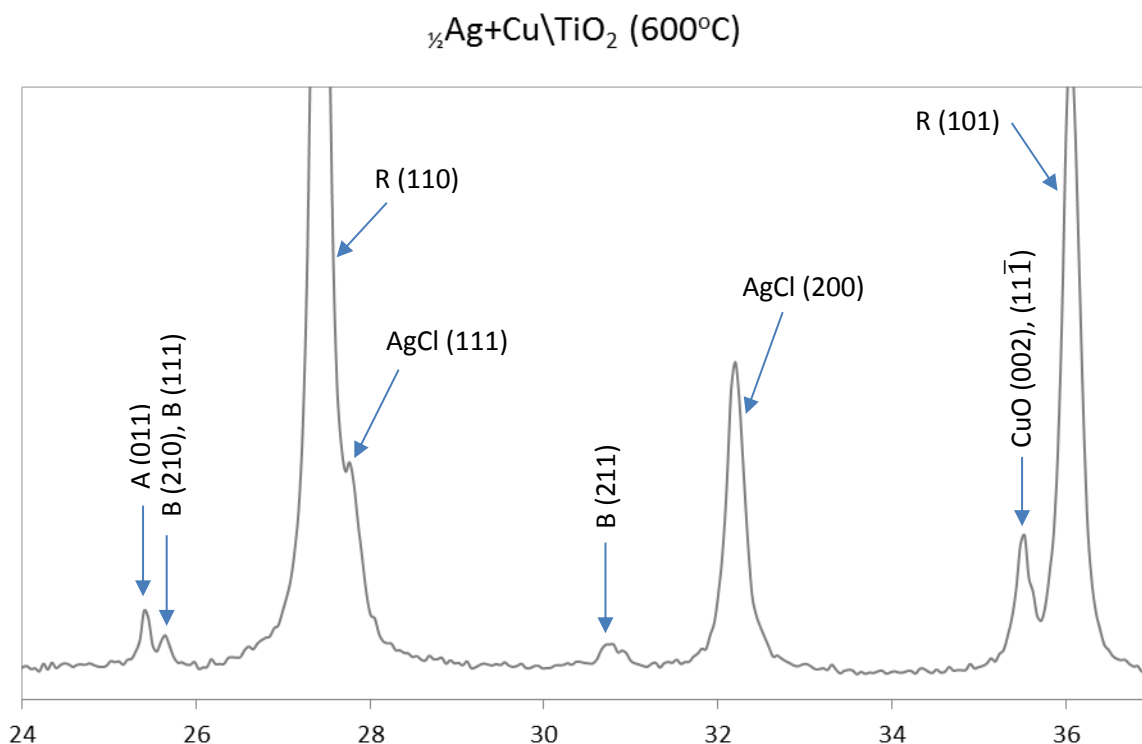


Figure 44: The anatase (A), brookite (B), rutile (R), CuO and AgCl phases present in the XRD diffractogram of the $\frac{1}{2}\text{Ag}+\text{Cu}\backslash\text{TiO}_2$ species annealed at 600°C.

4.6.3 Phase Content

Table 12 displays the estimates of the phase content (or mass fraction) of anatase, brookite and rutile in each sample – as described in Section **Error! Reference source not found.** The results are comparable to those given by the Match! 2 Program [268] in Table 9. The double-doped Ag+Cu\TiO₂ revealed about 1% of the phase mix as brookite for the powder annealed at 300°C. This suggests that some of the anatase present below 300°C were transformed to brookite. At 600°C, most of the anatase – with only about 2% left – has been converted to rutile. The persistence of this brookite phase beyond this anatase-to-rutile transition (that is beyond 600°C), is indicated as 2.72% in the table. By 900°C, the transformation of both anatase and brookite to rutile was complete. The phase-evolution of the $\frac{1}{2}\text{Ag}+\text{Cu}\backslash\text{TiO}_2$ powders also confirms these processes, but in greater detail when examined through XRD data.

Table 12: Anatase, brookite and rutile contents in the TiO₂ samples as calculated from the integrated intensities of the respective peaks of anatase (101), brookite (121) and rutile (110) [47].

Sample		TiO ₂ Phase Content (%)		
Species	Calcination Temperature	Anatase	Brookite	Rutile
-TiO ₂	100°C	100		
	300°C	100		
	600°C	100		
	900°C			100
	1100°C			100
Ag\TiO ₂	100°C	100		
	300°C	100		
	600°C	100		
	900°C			100
	1100°C			100
Cu\TiO ₂	100°C	100		
	300°C	100		
	600°C	20.47		79.53
	900°C			100
	1100°C			100
Ag+Cu\TiO ₂	100°C	100		
	300°C	98.96	1.04	
	600°C		2.72	97.28
	900°C			100
	1100°C			100
½Ag+Cu\TiO ₂	300°C	96.13		3.87
	600°C	3.91	5.88	90.21
	700°C			100
	900°C			100

4.7 SURFACE MICROSCOPY

4.7.1 Raman Microspectroscopy

Raman spectroscopy is a powerful tool for investigating the modification of the vibrational structure of materials. Its peaks derive only from the local structure, they are not influenced by either grain size or surface roughness.

Figure 45 shows the results of the Raman studies, carried out to confirm the phase, crystallinity and possible defects. Characteristic Raman modes of the anatase TiO_2 structure, exhibiting a strong band at 142 cm^{-1} and others at 196, 396, 518 and 635 cm^{-1} , were observed for all the sample species at the annealing temperature of 300°C (Figure 45 (a)). The rutile phase is evident in the spectra for the 900°C samples (Figure 45 (b)). Here, the major peaks were found at 240, 446 and 610 cm^{-1} while minor peaks are at 818, 707 and 319 cm^{-1} as expected [296], [297]. The broad second order peak at 240 cm^{-1} is due to scattering or disorder effects. The various vibration modes for the anatase and rutile structures are displayed in Figure 45 (c).

Raman peaks are known to shift in response to bulk (physical constraint), microstructural (intragrain), and chemical stresses (contaminants). Figure 45 (d) reveals a blue-shift of the about 6.3 cm^{-1} in the lowest frequency E_g mode towards higher wavenumbers for the anatase phases of both CuTiO_2 and $\text{Ag}+\text{Cu}\text{TiO}_2$. This can be attributed mainly to the symmetric stretching of the O–Ti–O [298], as the grains come under tension.

The sharpness and intensity of the Raman peaks signify that the samples are highly crystalline and pure. The Raman spectroscopy results are found to be complimentary to those obtained from XRD.

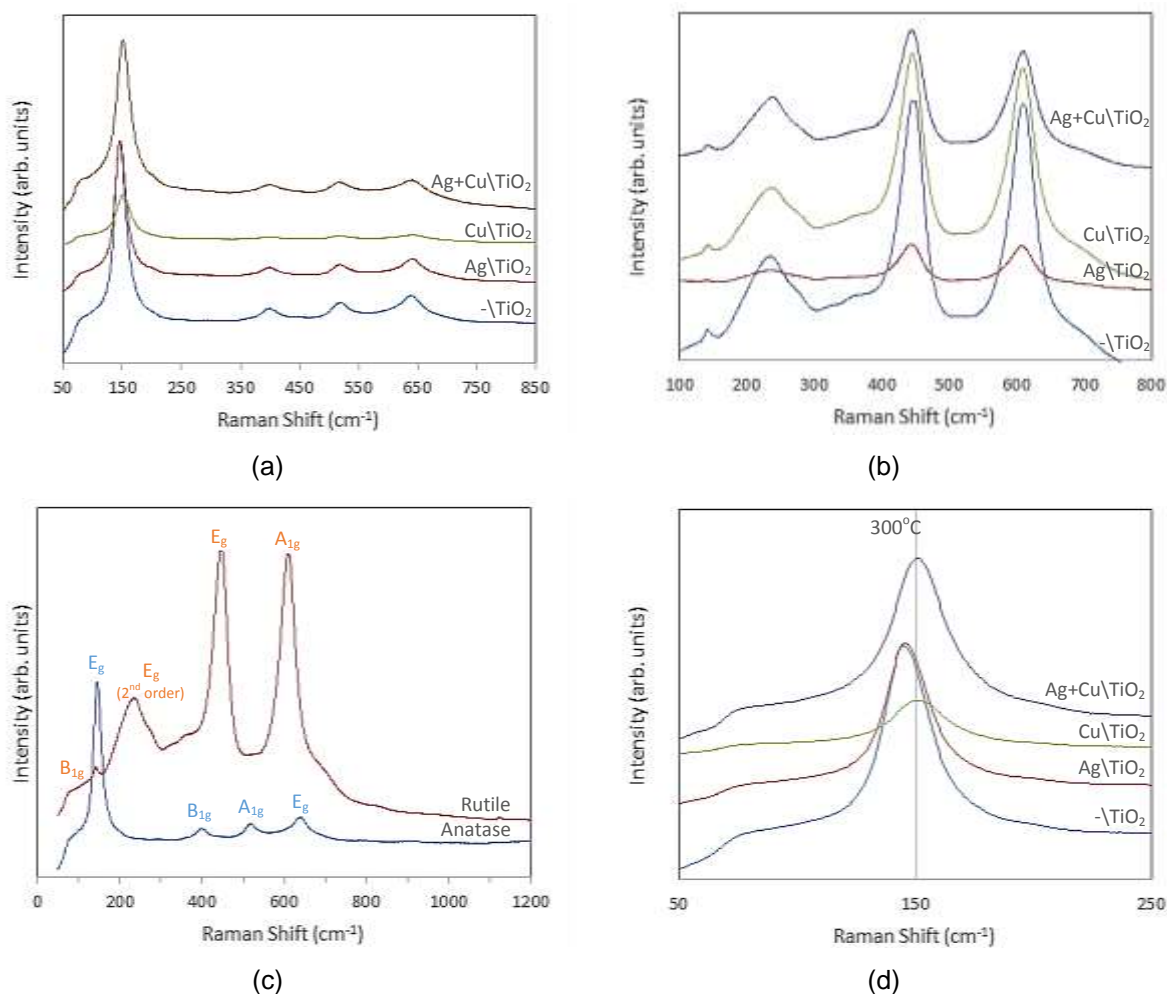


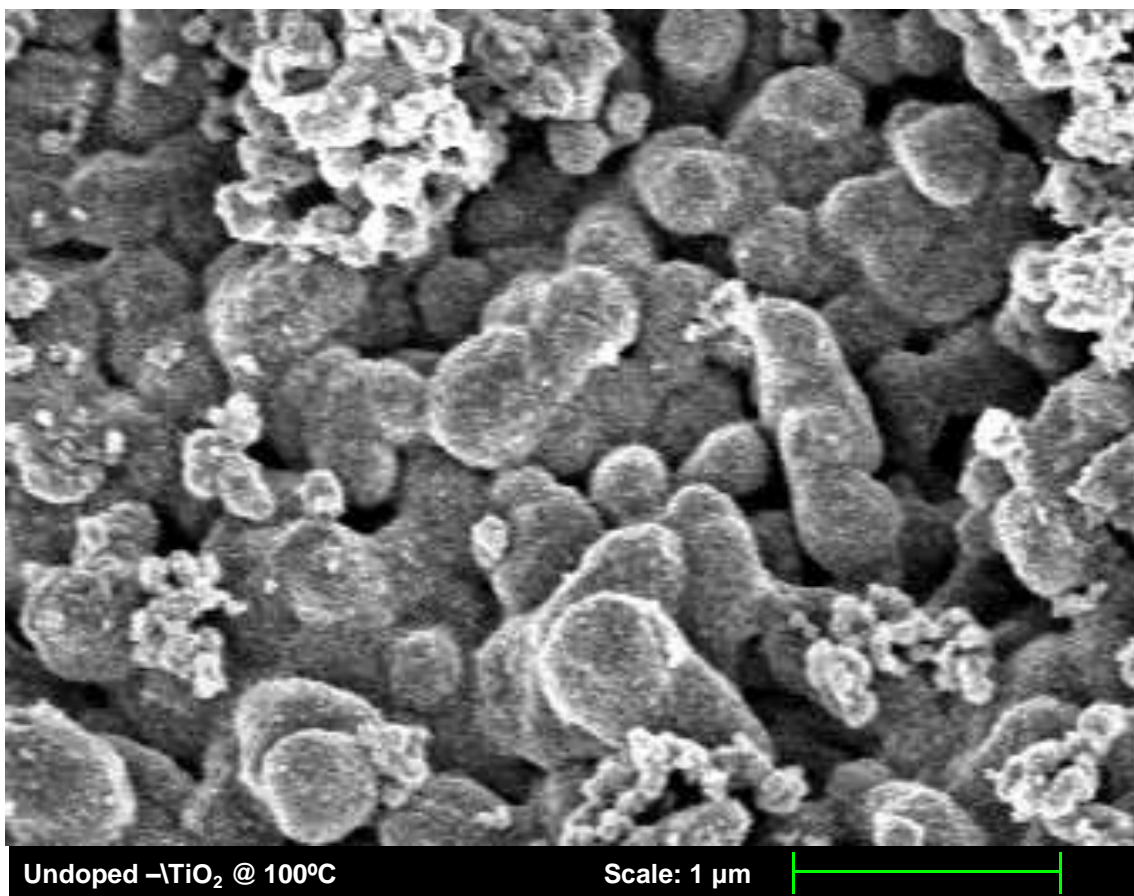
Figure 45: Raman spectra of all sample species at the annealing temperature of (a) 300°C and (b) 900°C. (c) Typical vibrational modes for the anatase and rutile phases. Shown are the Raman spectra for the undoped TiO₂ at 300°C (anatase) and at 900°C (rutile). (d) Blue-shift for all the sample species annealed at 300°C.

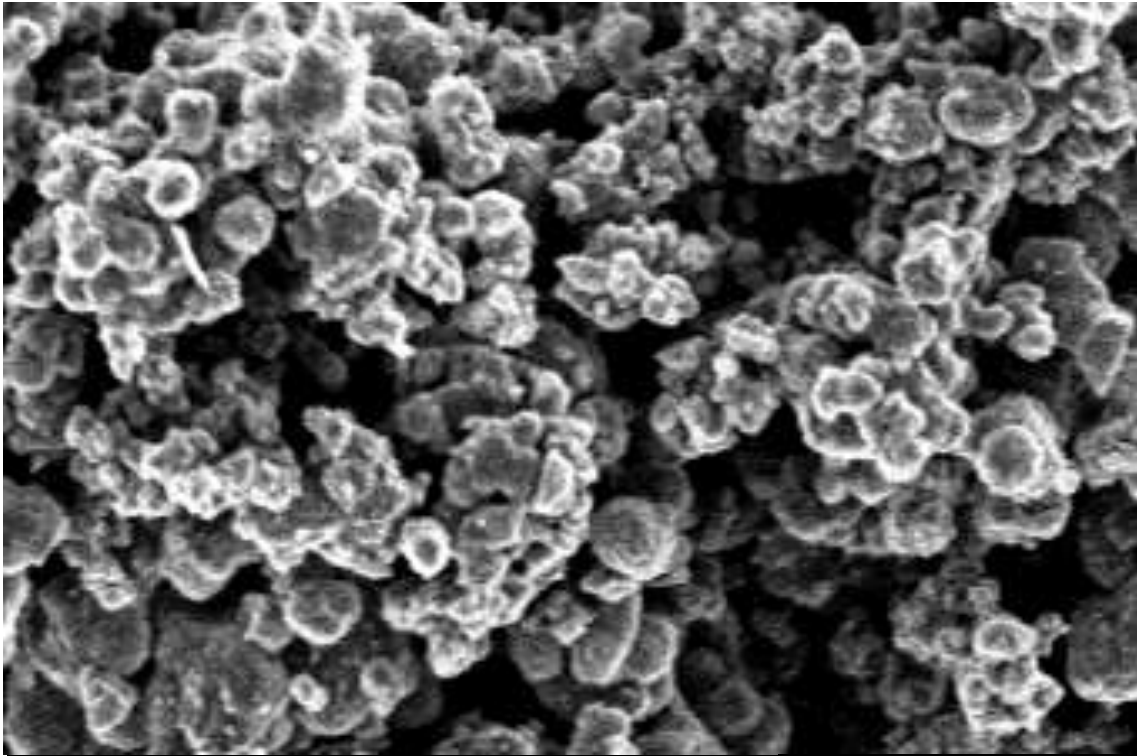
4.7.2 SEM Surface Morphology

The set of SEM micrographs shown in Figure 46 typifies what was observed for the sample species at the anatase (100°C, 300°C, 600°C) and rutile (900°C, 1100°C) phases. The agglomeration of fairly spherically-shaped particulate structure was observed for all samples at the various annealing temperatures. As a result, calculating the crystallite sizes from XRD data using the Scherrer's equation was considered appropriate, at least for comparative purposes [76], [77]. Irregular clustering of the particles (with large voids between aggregates and mesopores within) was apparent at the lower temperatures (anatase phase). In particular, the

images (at 600°C) show the presence of porous aggregates composed of smaller spherical individual particles. Intra-particle pores are indicated by the pores within the aggregates, while the voids between the aggregates themselves represent the inter-particle pores [299]. However, at the higher-temperature rutile phase, the aggregation was more in the form of coagulation, with clearly defined domain boundaries which grew with temperature. This coalescence is well pronounced at 1100°C in which there are fewer and smaller aggregation pores and voids.

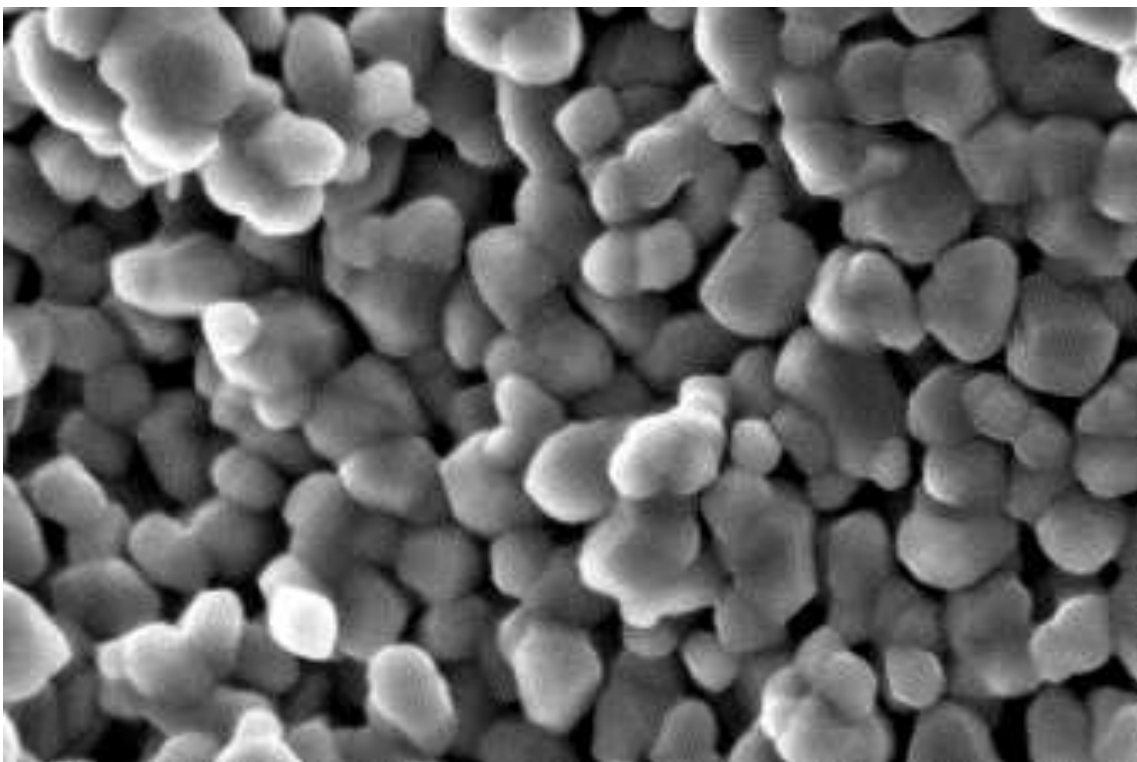
The microstructures of the nanopowders annealed at 900°C reveal a mixture of individual grains and agglomerates. Here, it is deemed likely that the agglomerates are rutile precursors to the large rutile grains observed in the samples annealed at 1100°C, since both Raman microspectroscopy and XRD data indicate the presence of a mixture of anatase and rutile at 900°C, and as rutile-only phase at 1100°C.





Undoped TiO_2 @ 300°C

Scale: 1 μm



Ag+Cu/TiO₂ @ 600°C

Scale: 0.1 μm



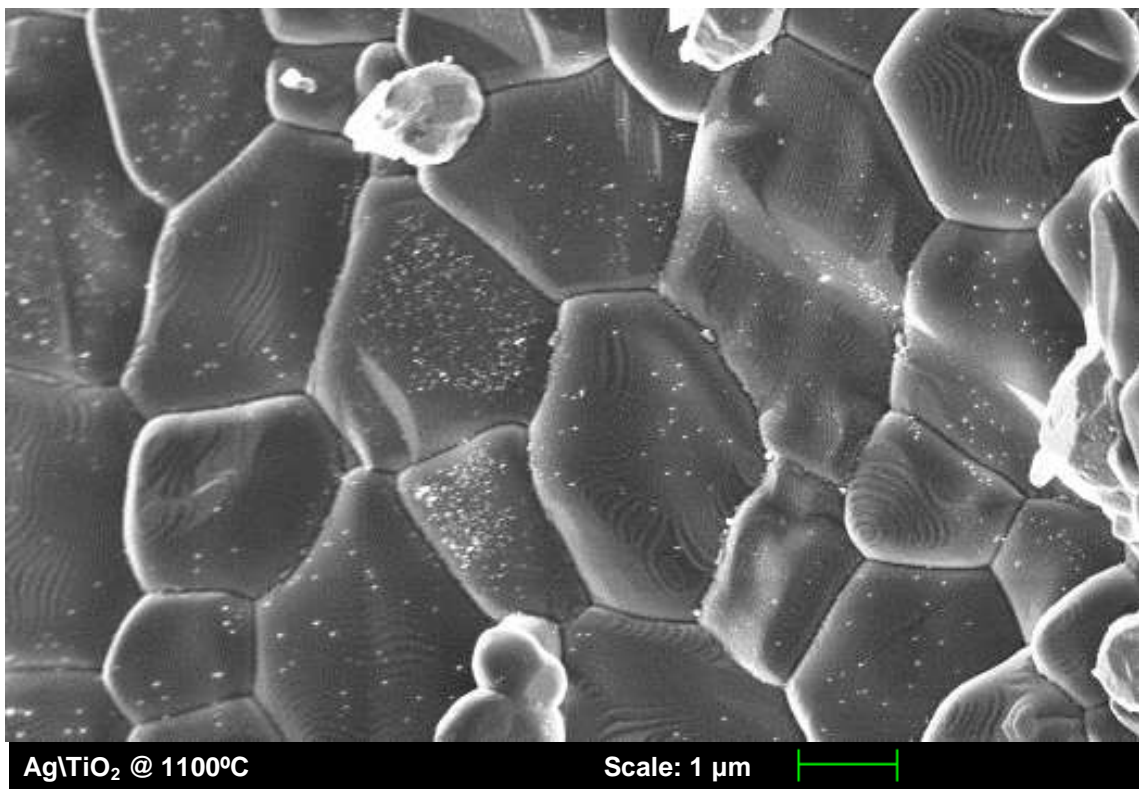
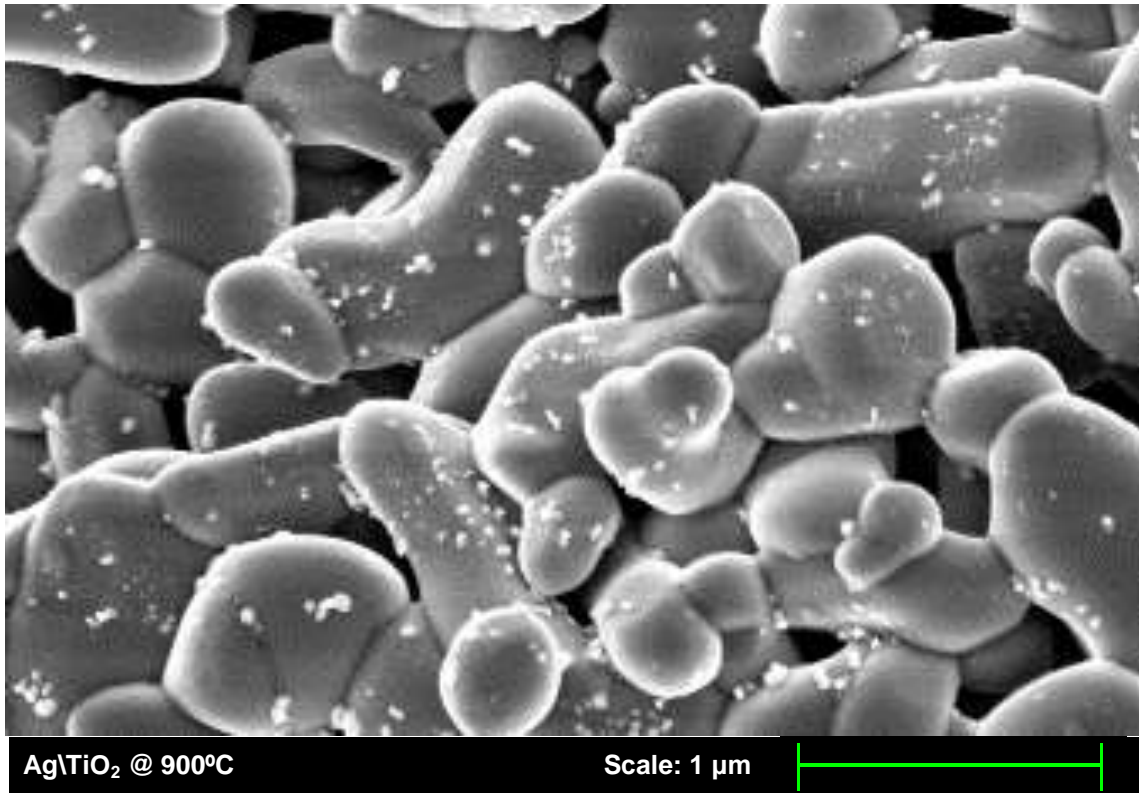


Figure 46: Typical SEM micrographs for the microstructural evolution of the titania nanoparticle species as the annealing temperature increased from 100°C to 1100°C.

Table 13 compares the crystallite sizes obtained from XRD data with the grain sizes deduced from SEM micrographs. Since a grain may be composed of more than one crystallite, the grain sizes are generally larger than the crystallite sizes. Nonetheless, the grain sizes increased with increasing annealing temperature as expected, particularly after the phase transformation from anatase to rutile [300].

Table 13: Crystallite sizes (obtained from XRD data) and grain sizes (obtained from SEM micrographs) of the dominant phases in the TiO₂ powder samples.

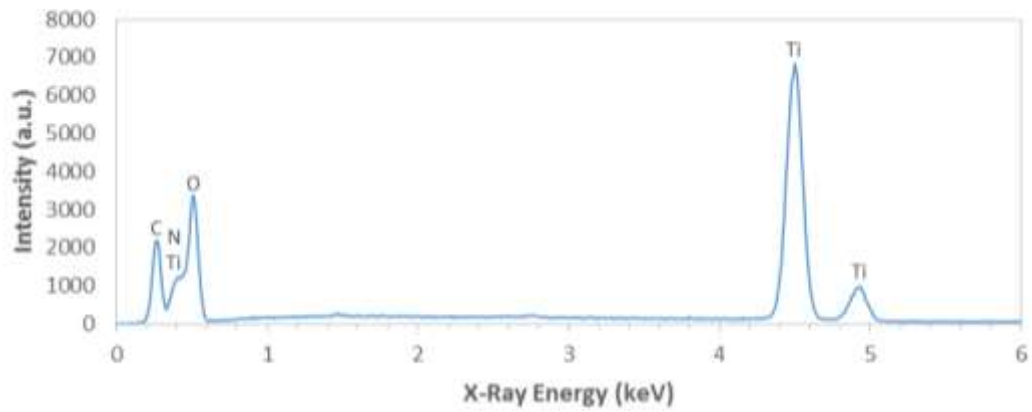
Sample		XRD Crystallite Size (nm)	SEM Grain Size (nm)	Predominant TiO ₂ Phase
Species	Annealing Temperature			
-TiO ₂	100°C	3.20	48.39	Anatase
	300°C	7.39	65.32	
	600°C	28.84	79.95	
	900°C	65.46	207.47	Rutile
	1100°C	77.57	729.6	
Ag\TiO ₂	100°C	3.74	29.03	Anatase
	300°C	6.17	39.55	
	600°C	21.38	71.97	
	900°C	74.93	704.63	Rutile
	1100°C	74.56	2304.88	
Cu\TiO ₂	100°C	3.53	50.6	Anatase
	300°C	6.32	84.68	
	600°C	47.05	210.68	
	900°C	78.53	759.04	Rutile
	1100°C	26.21	1849.4	
Ag+Cu\TiO ₂	100°C	3.79	66.67	Anatase
	300°C	6.53	80.82	
	600°C	43.22	203.28	Rutile
	900°C	79.70	1513.1	
	1100°C	74.86	2218.07	

4.8 ELEMENTAL ANALYSIS

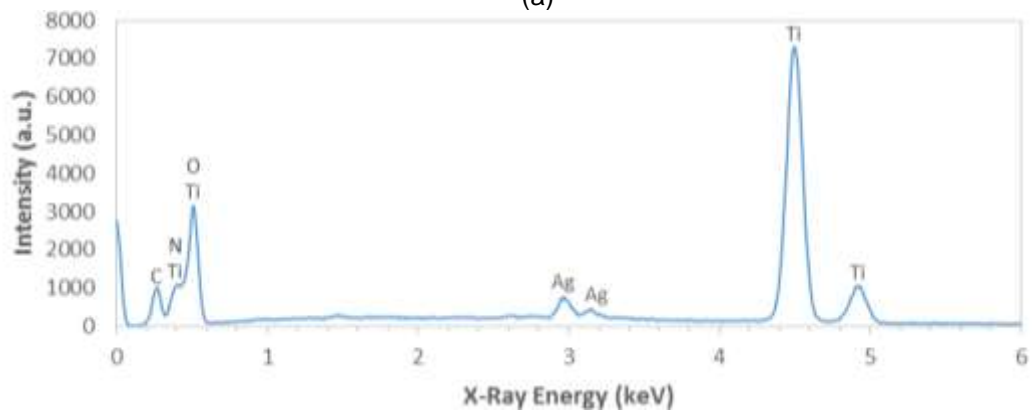
4.8.1 Energy Dispersive Spectroscopy (EDS)

EDS microanalysis was used to confirm that the samples contained elemental titanium and oxygen, as well as the dopants Ag and Cu. Figure 47 (a) is the EDS result for the base sample, which is constituted by the undoped TiO_2 nanoparticles that were dried at 100°C . The pattern reveals two peaks at 4.51 keV and 0.53 keV which are indicative of the presence of Ti and O at atomic percentages of 27 and 68 respectively. This composition of Ti and O confirms the formation of non-stoichiometry TiO_2 with oxygen vacancies – which stands to enhance its photocatalytic activity performance [301]. Further, the intense Ti peak relates to the bulk TiO_2 , while the less intense peaks (at 0.40 keV and 4.94 keV) are attributed to the TiO_2 surface [301]. Other elements (impurities) that are within the detection limit of EDS – Carbon (0.0001 at%) and Nitrogen (5.14 at%) – are believed to derive from the precursor reactants.

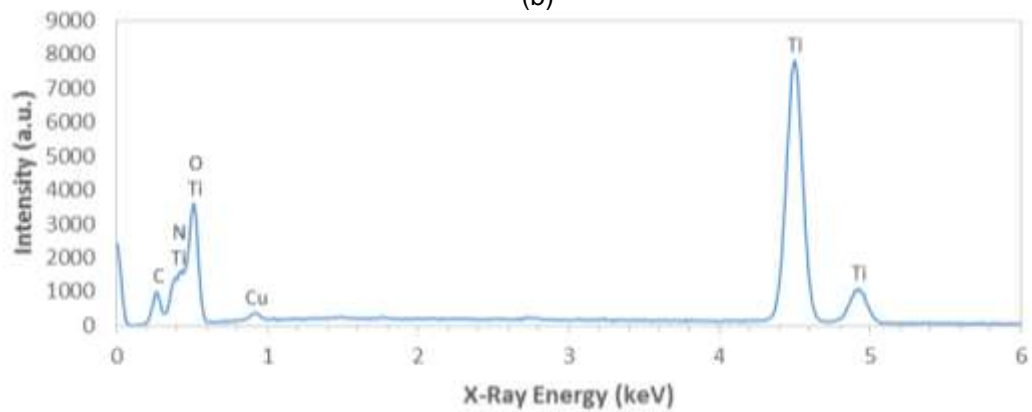
As expected, the silver-doped samples (AgTiO_2) feature less than 1 at% of Ag at 4.98 keV in their EDS spectra (Figure 47 (b)). The Ag element identified here may include the extraneous silver peaks presented in the XRD diffractograms of Section 4.2.3.1. The XRD analyses of the samples also identified the presence of tenorite (CuO) in the rutile TiO_2 samples annealed at 600°C and 900°C . The Cu atoms are also confirmed here (at 0.94 keV in Figure 47 (c) & (d)), for all those samples that incorporated Cu as a dopant. Finally, the double-doped $\text{Ag}+\text{Cu}\text{TiO}_2$ powders at annealing temperatures of 900°C and below contain Cl atoms at 2.62 keV which, together with Ag atoms, form chlorargyrite (or AgCl), as declared by the XRD data.



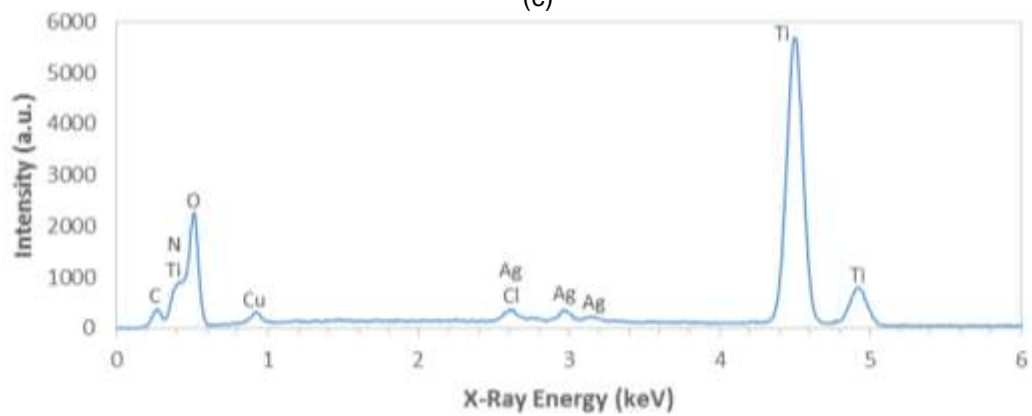
(a)



(b)



(c)



(d)

Figure 47: EDS spectra of (a) undoped TiO_2 calcined at 300°C (b) AgTiO_2 calcined at 300°C (c) CuTiO_2 calcined at 900°C (d) Ag+CuTiO_2 calcined at 600°C .

4.9 DISCUSSION

In general, the results from the various characterisation techniques in this chapter are consistent with each other. The elements identified through EDS were already predicted by XRD analysis which were in turn corroborated by Raman spectroscopy. Further XRD was also influential in revealing the mixing of phases amongst anatase, brookite and rutile TiO₂. With this, it was discovered that the introduction of brookite into the mix actually brought about enhancement in the properties of titania.

RESULTS & DISCUSSION II: OPTICAL PROPERTIES

5.1 INTRODUCTION

Unique optical properties of nanoparticles can be studied using UV–Visible spectroscopy. This is because the phenomenon of surface plasmon occurs only with nanoparticles and not in case of bulk metallic particles [302]. Further, the size and shape of nanoparticles could be qualitatively described by the peak position and shape of the absorption spectrum of UV-Vis, the general tendency being that the absorption at long wavelengths was due to the scattering of light by large particles. For photocatalysis, especially when dealing with doped materials, it is very important to estimate the optical band gap of a semiconductor material. This is the minimum photon energy required to promote electrons from the valence band to the conduction band. The energies of band gaps of semiconductors depend upon a number of factors, such as crystal structure, non-stoichiometric defects per unit volume and the thermalisation of the crystal lattices. The band gap of both anatase (3.2 eV) and rutile (3.0 eV) are indirect, although there is also a direct forbidden transition near 3 eV in rutile which accounts for small oxygen deficiencies (considered as impurities) that affords the *n*-type doping to the semiconducting material [92].

PL is primarily used to determine the effectiveness of trapping, migration and transfer of charge carriers, as well as to understand the fate of the e^-h^+ pairs in semiconductors [303]. In this study, PL is used to understand the optical properties, surface states, oxygen vacancy and/or defects, and to locate the position of the additional energy level within the band gap of the metal-doped TiO_2 nanoparticles. In general, metal doped metal-oxides are expected to show lower PL intensities compared to the undoped ones [303].

5.2 UV-VIS LIGHT ABSORPTION

Figure 48 (a) displays a representative UV-visible absorption spectra that was recorded in the wavelength range 200 nm – 900 nm at room temperature, for the undoped TiO_2 samples that were annealed at various temperatures from 100°C to 1100°C. An additional absorption edge can be found in the anatase samples annealed at the lower temperatures of 100°C and 300°C. The presence of this

weaker absorption shoulder in the visible-light range (around 500 nm) suggests that the anatase powders could be active under visible-light illumination, although this has not been reported before for undoped TiO_2 nanoparticles. However, the second absorption shoulders are not as pronounced in Ag-loaded anatase samples (Figure 48 (b)). In particular, the anatase $\text{Ag}\backslash\text{TiO}_2$, which was dried at 100°C , blends the two shoulders sufficiently to form almost a single absorption edge.

The anatase samples that incorporated Cu as dopants (in both $\text{Ag}\backslash\text{TiO}_2$ and $\text{Ag}+\text{Cu}\backslash\text{TiO}_2$ species) also reveal a similar hump around 440 nm (Figure 48 (c) & (d)). On the other hand, all the rutile powders (heated to the higher temperatures of 900°C and 1100°C) in all species, feature sharper increases below 400 nm but with much weaker tails.

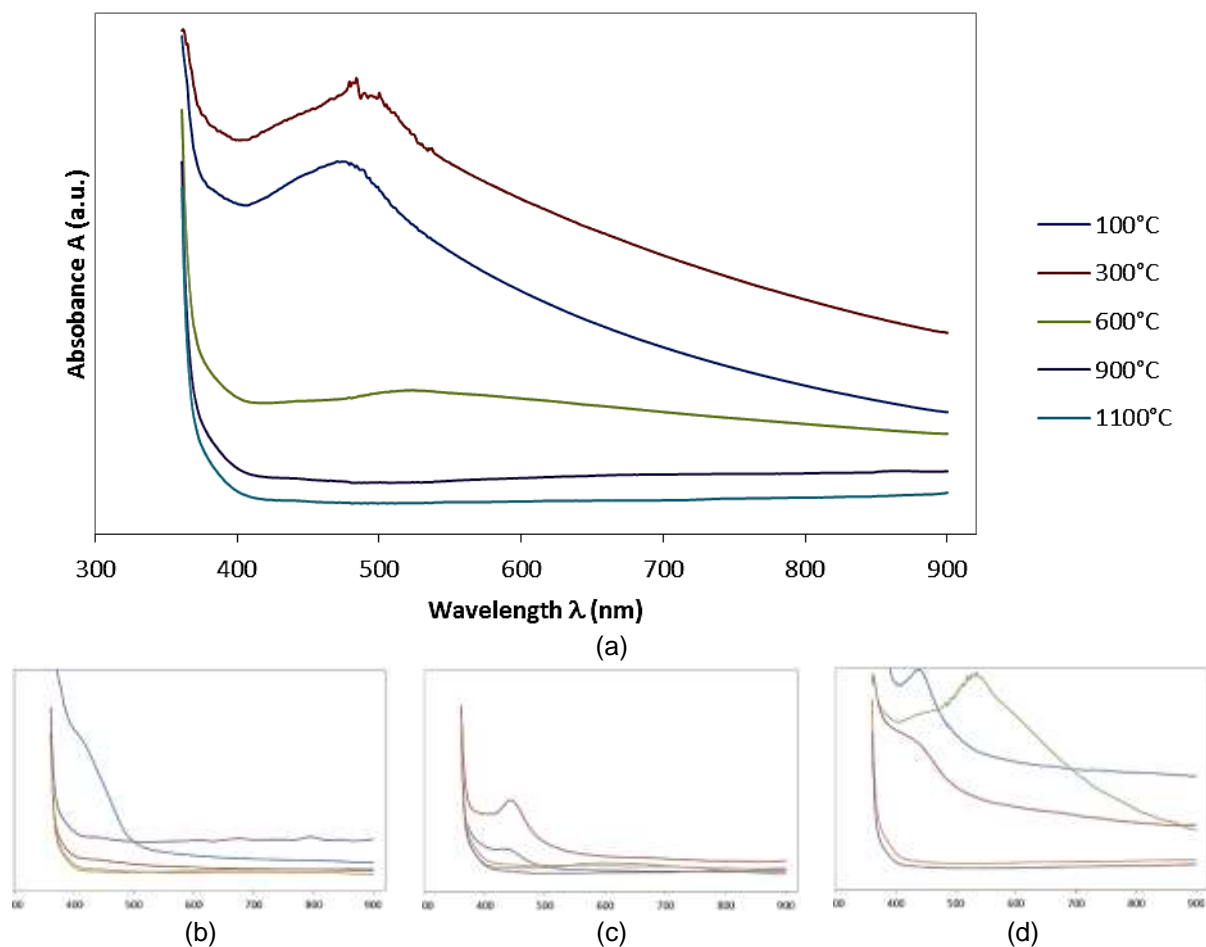


Figure 48: Optical absorption spectra of the TiO_2 samples annealed at various temperatures (from 100°C to 1100°C) for each of the species (a) undoped TiO_2 , (b) $\text{Ag}\backslash\text{TiO}_2$, (c) $\text{Cu}\backslash\text{TiO}_2$ and (d) $\text{Ag}+\text{Cu}\backslash\text{TiO}_2$.

In order to produce active photocatalytic species, TiO_2 must absorb photons with energy that is equal to or greater than the band gap energy. For visible-light photocatalysis this requires that the band gap be less than 3.1 eV, which corresponds to wavelengths around 400 nm.

The band gaps of the samples were determined by the Absorption Spectrum Fitting (ASF) method described in Section **Error! Reference source not found.** [280]. Extrapolation of the linear region for the 'allowed-indirect' electronic transitions ($r = 2$) curve is depicted in Figure 49, for the undoped TiO_2 that was annealed at 600°C . Table 14 summarises the calculated band gap energies of the samples investigated in this study. As expected, the single-phase anatase powders yielded band gap values around 3.2 eV, while the rutile ones centred around 3.0 eV. The mixed-phase powders are however, exceptions to this rule. The double-doped $\text{Ag+Cu}\text{TiO}_2$ sample, which was annealed at 300°C , contains a mixture of anatase and brookite and it registered a red-shift towards a lower energy gap of 1.99 eV, which falls squarely within the visible region of the solar radiation spectrum. Another mixed-phase sample (the brookite-rutile, double-doped $\text{Ag+Cu}\text{TiO}_2$ that was annealed at 600°C) also featured a narrower band gap (2.09 eV) in comparison with other rutile-only samples.

The excellent improvement in photo absorptions exhibited by these two powders may be attributed to either phase mixing (in which there are two or more phases present) or the presence of brookite in the mix. The former is less likely since such red-shifts are not observed for the anatase-rutile combinations. Though others [263] have ascribed such shifts (of the absorbance spectra towards the visible light region) to quantum size effects, the introduction of some additional energy levels in the TiO_2 host lattice band gap, by the Ag and Cu impurities, may form a *p*-type semiconductor and cause a shift in Fermi energy towards valence band.

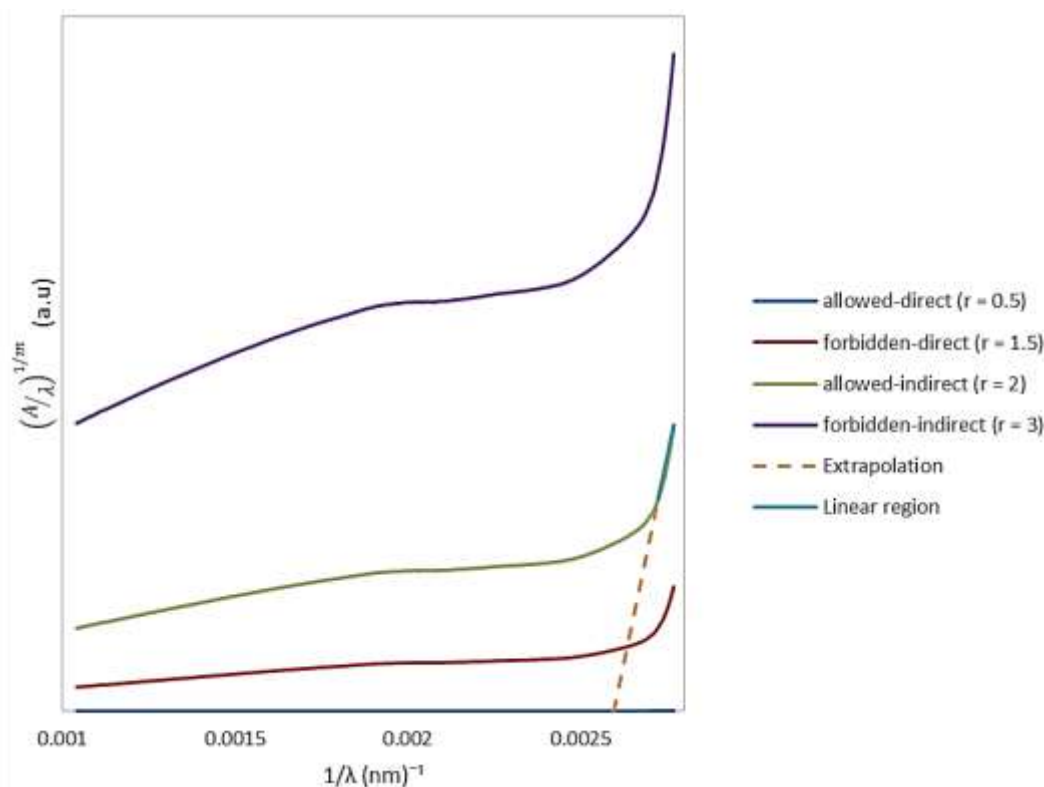


Figure 49: Plots used in the determination of the band gap for the different electronic transitions in the undoped TiO_2 that was annealed at 600°C . Extrapolation of the linear portion of the $r = 2$ (allowed-indirect transitions) curve is shown.

Table 14: Calculated Band gaps of the sample species at various phase structures.

Sample Species	Annealing Temperature	Phases Present	Absorption Edge (nm)	Band Gap E_g (eV)
TiO_2	100°C	Anatase	378.76	3.27
	300°C	Anatase	392.69	3.16
	600°C	Anatase, Rutile	384.95	3.22
	900°C	Rutile	412.30	3.01
	1100°C	Rutile	410.34	3.02
AgTiO_2	100°C	Anatase	395.42	3.14
	300°C	Anatase	380.95	3.26
	600°C	Anatase, Rutile	379.18	3.27
	900°C	Rutile	419.74	2.95
	1100°C	Rutile	412.84	3.00
CuTiO_2	100°C	Anatase	382.14	3.25
	300°C	Anatase	387.94	3.20
	600°C	Anatase, Rutile	412.95	3.00
	900°C	Rutile	413.05	3.00
	1100°C	Rutile	414.22	2.99
$\text{Ag}+\text{Cu}\text{TiO}_2$	100°C	Anatase	341.08	3.64
	300°C	Anatase, Brookite	623.74	1.99
	600°C	Brookite, Rutile	594.69	2.09
	900°C	Rutile	412.27	3.01
	1100°C	Rutile	418.27	2.97

5.3 PHOTOLUMINESCENCE

Figure 50 reports the optical emission (photoluminescence) spectra, derived from an excitation wavelength of 532.5 nm, of the TiO_2 sample species at their various annealing temperatures (100°C, 300°C, 600°C, 900°C and 1100°C). Two emission peaks can generally be identified in each spectrum. Since the excitation energy used was lower than the band gap energy of TiO_2 (anatase or rutile), the PL signal mainly resulted from the electron transitions related to surface defects or surface state energy level rather than the electron transitions between the conduction band and valence band [290].

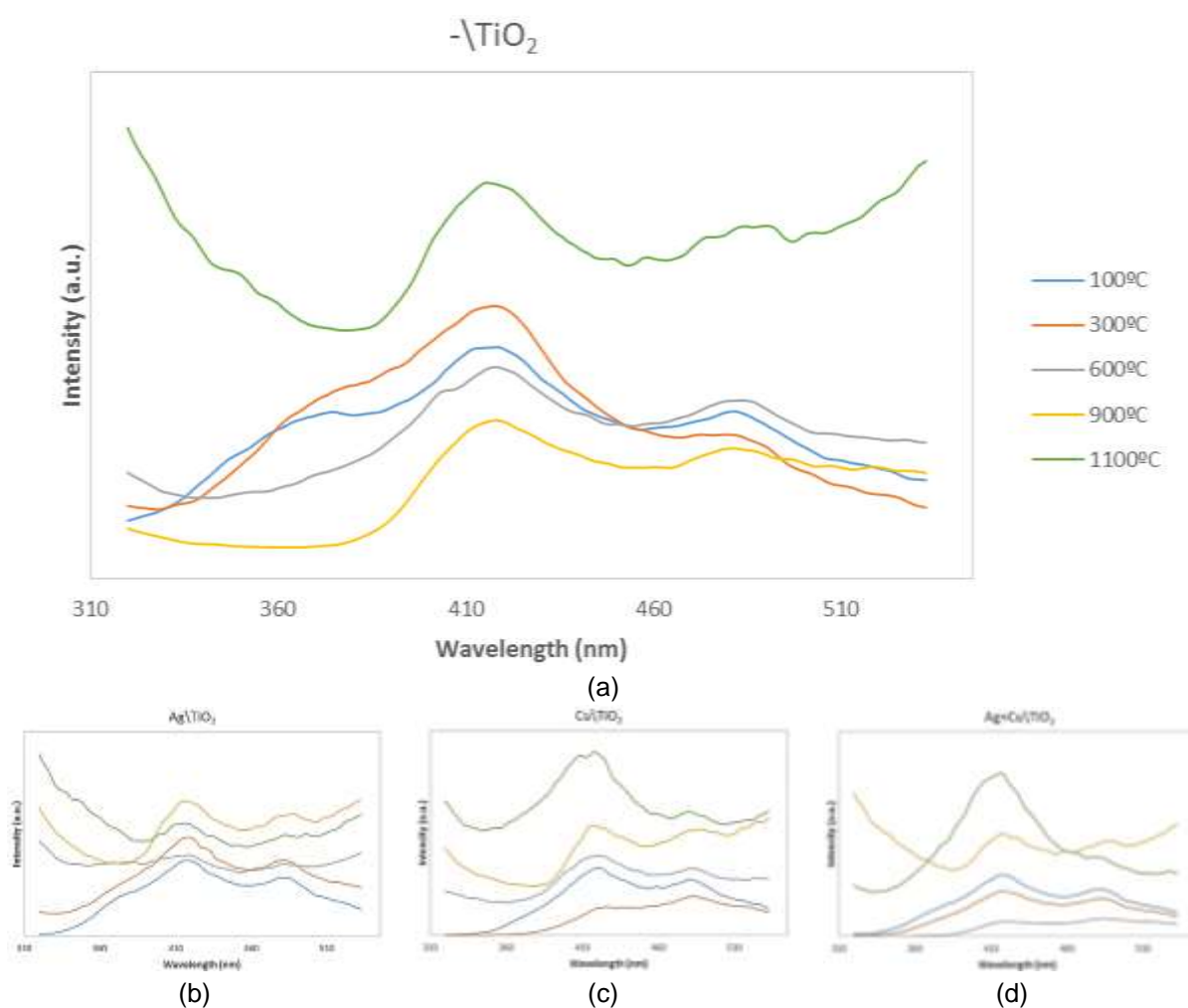


Figure 50: Optical emission (PL) spectra of the TiO_2 species (a) $-\text{TiO}_2$, (b) Ag/TiO_2 , (c) Cu/TiO_2 and (d) $\text{Ag}+\text{Cu}/\text{TiO}_2$, at the various annealing temperatures.

The more prominent peak, located in the around 418 nm (2.98 eV), can be attributed to the near band gap transition of TiO₂ which comes from the recombination of band edge free excitons [290]. The other peak is weaker but broader, and is located deeper in the visible-light emission range at 483 nm (2.56 eV), representing emissions due to the presence of the singly ionised oxygen vacancies (bound excitons) [290]. This is believed to be caused by the radiative recombination of a photogenerated hole with an electron occupying the oxygen vacancy. It can also be observed from Figure 50 that the rutile samples (annealed at 600°C and 1100°C) feature, in most cases, higher intensities than the anatase samples (100°C and 300°C), the only exception here being the undoped TiO₂ that was annealed 900°C.

The difference in particle sizes, between the anatase and rutile powders, may contribute significantly to this observation. Since it is generally believed that the smaller the particle size, the larger is the oxygen vacancy content, which in turn results in higher probability of exciton occurrence and a stronger the PL signal [290]. As the distance available for the free movement of electrons is relatively shorter for smaller particles, it becomes relatively easier for the oxygen vacancies to bind the photo-induced electrons and form excitons. The anatase powders, despite having smaller crystallite/grain sizes as compared with the rutile (Table 10), may feature larger particle sizes than the rutile, as the grains agglomerate. With the rutile nanoparticles having smaller sizes, its PL intensity will be greater than those of the anatase powders.

Figure 51 compares the PL spectra of the doped and undoped powders grouped as either anatase (annealed at 300°C and below) or rutile (annealed at 900°C & 1100°C).

For anatase (Figure 51 (a) & (b)), the intensities registered by doped samples were lower than that of the undoped TiO₂ powder. This decrease of luminescence intensity, upon doping, may be attributed to the localisation of the dopant trapping level in the anatase band gap. On the other hand, the doped rutile powders (Figure 51 (d) & (e)) presented an opposite behaviour to its anatase counterpart. Here, it is the undoped TiO₂ powder that registered the lowest intensities.

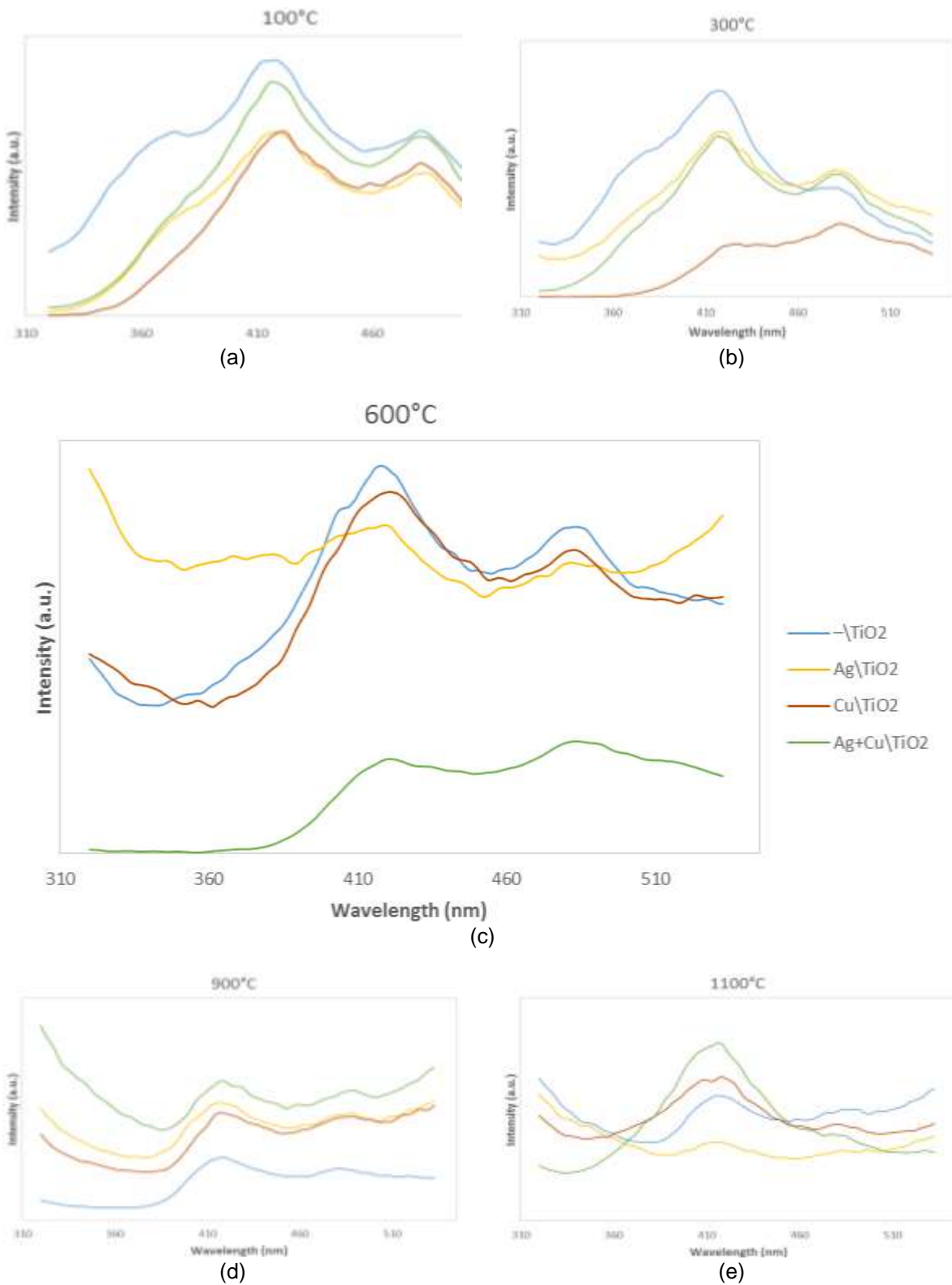


Figure 51: Optical emission (PL) spectra of the TiO_2 species: Respectively, (a) and (b) are anatase samples annealed at 100°C and 300°C, (c) samples annealed at 600°C, while (d) and (e) are rutile samples annealed at 900°C and 1100°C

This suggests the presence of a high concentration of oxygen vacancies and/or defects in the doped samples, which leads to the binding of the photo-induced electrons to easily form excitons. The exciton energy level near the base of the conduction band (Figure 52) are created and the PL band of the excitons are formed on the surface of semiconductor nanoparticles. Thus, the high levels of oxygen vacancies/defects brings about high PL signals.

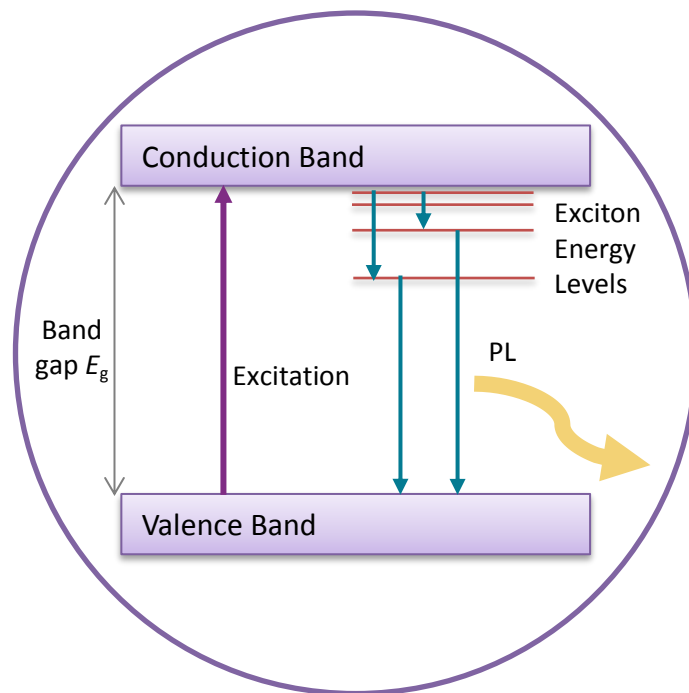


Figure 52: Schematic diagram depicting the exciton energy levels between the conduction band and valence band [290].

RESULTS & DISCUSSION III: GAS-SENSING PROPERTIES

6.1 INTRODUCTION

The usual polymorphs of TiO_2 differ in crystallographic structure – tetragonal anatase and rutile, and orthorhombic brookite – and this difference can exert influences on the sensing properties of TiO_2 based devices [15]. For gas sensors, most of the researchers focus on anatase TiO_2 owing to its appropriate calcining temperature (about 400°C – 500°C), which may enhance the concentration of chemisorbed oxygen species (O_2^- , O^{2-} , and O^-) on its surface [16]. With humidity sensors, as the operating temperature (about 20°C – 25°C) is much lower than the optimised temperature for oxygen active in TiO_2 sensors (about 200 – 400 °C) [17], the oxygen species cannot greatly affect the humidity sensing properties [18]. Thus TiO_2 with other crystallographic structures may also be used as humidity sensing materials.

Humidity, particularly water vapour present in the atmosphere, is highly variable and changes in accordance with several factors. Monitoring and controlling humidity is therefore important, whether it is for human comfort, storage of various goods or industrial process control. The design and fabrication of humidity sensors has become one of the most active research fields.

This chapter is devoted to the analysis of the gas sensing properties of the anatase and rutile nanostructured TiO_2 species. The anatase samples included those TiO_2 species ($-\text{TiO}_2$, $\text{Ag}\backslash\text{TiO}_2$, $\text{Cu}\backslash\text{TiO}_2$ and $\text{Ag}+\text{Cu}\backslash\text{TiO}_2$) that were annealed at 300°C , while the rutile were those annealed at 900°C . A summary of the samples tested are provided in Table 7 of Section 3.3.7. The gas sensing performances of the prepared TiO_2 nanoparticles were tested at various operating temperatures, namely Room, 250°C , 300°C and 350°C , and toward ammonia (NH_3) and hydrogen (H_2) gases, as well as ten humidity levels (between 5.4% RH and 88.4% RH). The response of the TiO_2 species to NH_3 and H_2 presented here serves as case studies for reducing gases.

In what follows, calculations for the performance indices (Sensitivity, Response Time and Recovery Time) of each powder, when exposed to various concentrations of the intervening gas, were carried out (Table 15 to Table 20). The response and recovery

times are respectively defined as the times the impedance takes to decline to 10% of its saturation value from the baseline, when the gas is introduced, and to recover 90% of its final value when the flux of air is restored. The calculations also include estimates of, baseline drifts, which is calculated as the percentage increase or decrease of the resistance before the gas was introduced for the last time, as compared to the first “gas-out” resistance:

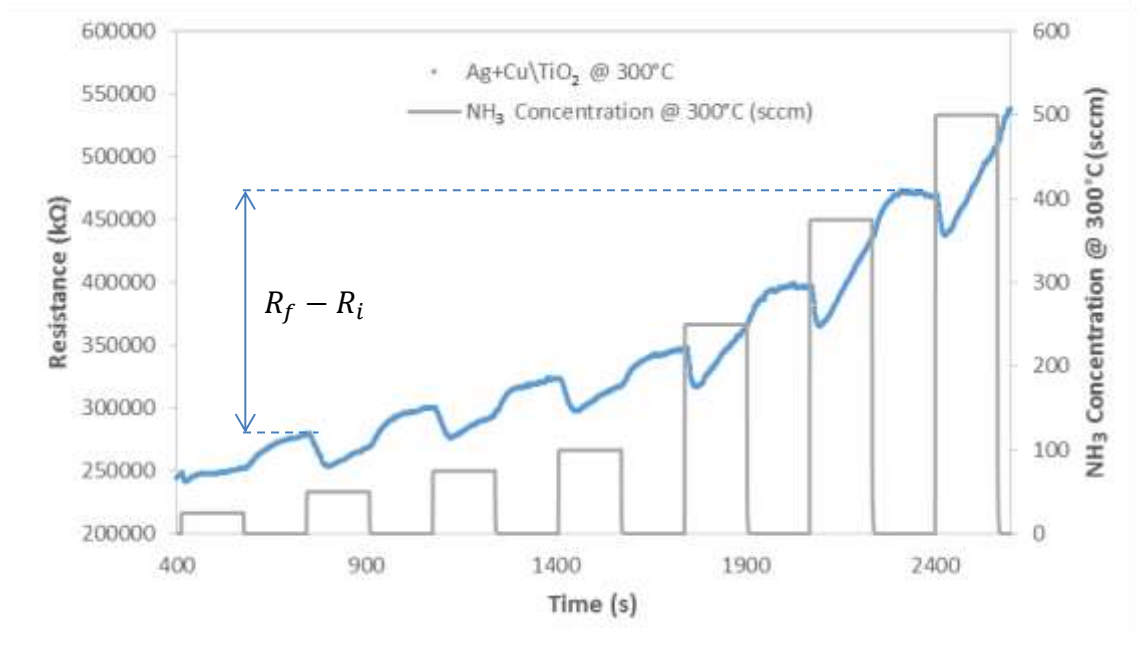
$$\text{Fractional Baseline Drift} = \frac{R_f - R_i}{R_i} \times 100\%$$

6-1

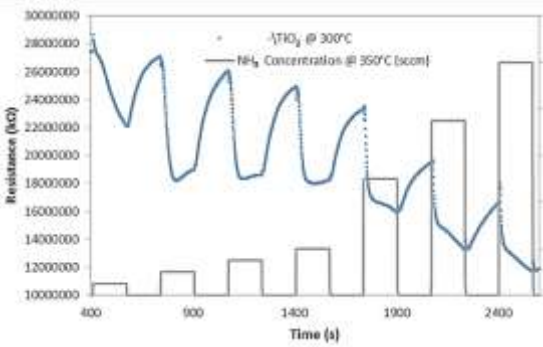
This parameter serves as a rough indication of the ability of the sensor material to restore its initial properties (particularly the resistance) after being repeatedly exposed to pulses of increasing gas concentration. Positive values indicate resistances higher at the last “gas-out” than at the first and vice-versa. For materials that interact chemically with the intervening gas, the baseline shift may be much greater than zero. As an example, a Fractional Baseline Shift of -67% means that the resistance decreased by 67% from the first gas-out to the last. The dynamic response profiles for some sensor materials are shown in Figure 53 (a – c) to demonstrate a Fractional Baseline Shift that is positive, negative and nearly zero respectively.

An extensive display of results from this gas sensing analyses is presented graphically in the Appendix F. These data sheets contain a set of charts that compare the performances of the TiO₂ nanopowders. A representative dynamic response graph is shown in Figure 54 for the anatase samples that were exposed to room-temperature NH₃ gas. In it, the “gas-in”/“gas-out” square concentration profile is depicted on the secondary vertical axis by continuous grey line that roughly resembles a bar-chart. On the other hand, the impedances registered by the sensing materials when exposed to a specific gas, are plotted on the primary vertical axis, and are represented by the ○, △, □ or × markers.

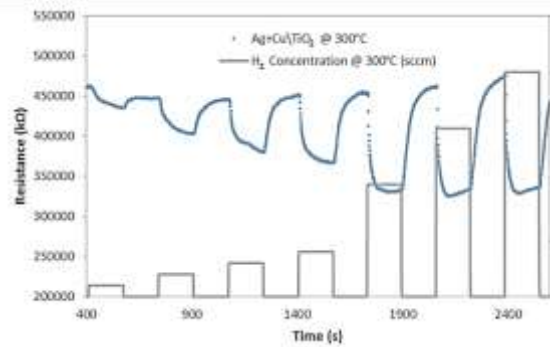
A typical isotherm graph for the sensor characteristics is shown in Figure 55. Here, the sensitivity is plotted on the primary vertical axis with the “●” marker, while the response and recovery times are plotted on the secondary vertical axis with the “□” and “△” markers respectively.



(a)



(b)



(c)

Figure 53: Baseline shift in the initial and final “gas-out” resistances R_f and R_i . The difference may result in a Fractional Baseline Shift value that is (a) positive, (b) negative or (c) zero.

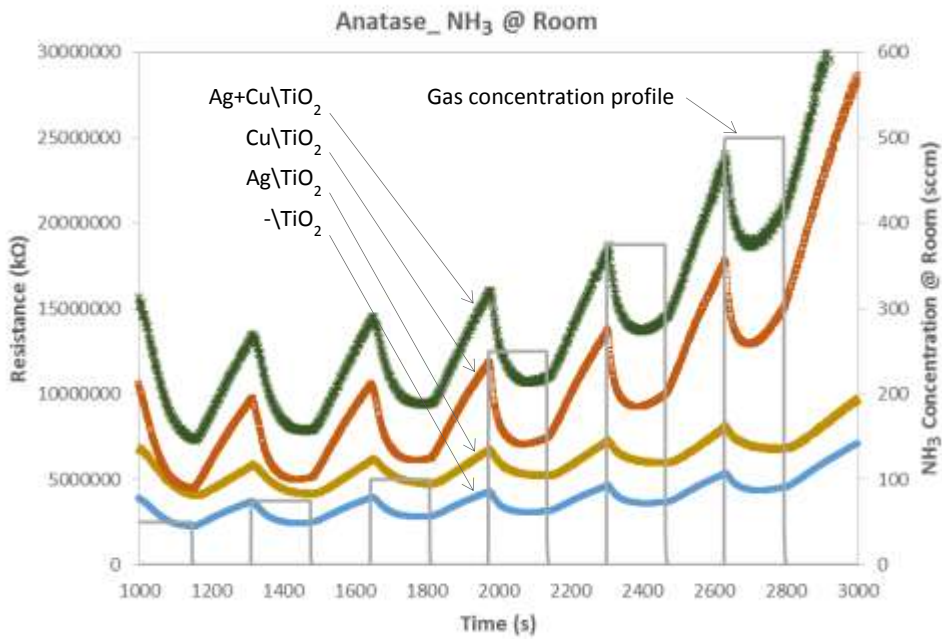


Figure 54: Dynamic response chart for anatase samples exposed to NH_3 gas at room temperature. It features the gas concentration profile plotted on the secondary vertical axis.

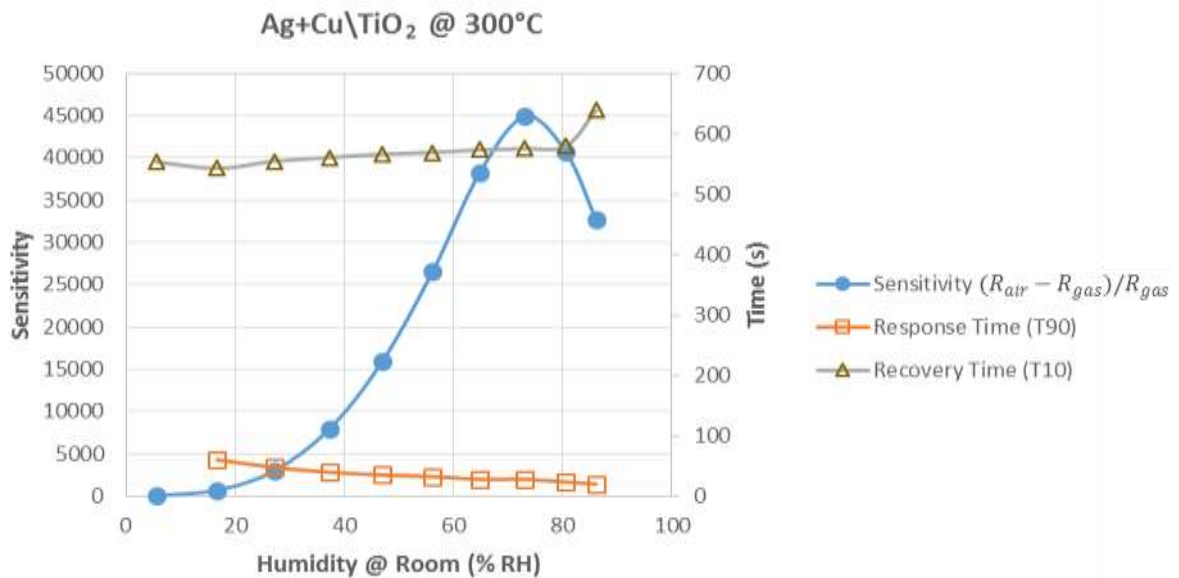


Figure 55: Sensor characteristics plotted for the double-doped anatase sample. It features Sensitivity on the primary vertical axis, while the Response Time and Recovery Time are on the secondary axis.

6.2 HUMIDITY

6.2.1 Response of Anatase TiO₂ to Humidity

The dynamic response of the prepared undoped anatase TiO₂ sensor to humidity levels ranging from 5% RH to 88% RH, measured at room temperature, is shown in Figure 56. The profiles for the doped samples (Ag-TiO₂, Cu-TiO₂ and Ag+Cu-TiO₂) are very similar but with much higher impedances than the undoped TiO₂ (Figure 57). Ag-TiO₂ registered resistances that were roughly 20 times more, Cu-TiO₂ was about 5 times, while the Ag+Cu-TiO₂ sample peaked by a factor of around 24.

All powders showed reversible and reproducible response to all humidity levels with some short-term stability over several hours of measurement. Generally, there is a systematic decrease in the measured resistances of sensor material as the intervening “gas” (humidity) is introduced (“gas-in”). Upon withdrawing the gas (“gas-out”) 5 minutes later an increase in the resistance is observed. However, the time interval required for obtaining stabilised responses (constant resistance) in gas flow of constant humidity level is much more than 5 minutes. Adsorption or desorption processes on the surface of the sensor material can therefore not be fully accounted for with the available data.

Figure 58 displays TiO₂ nanopowder sensor characteristics, featuring the performance indices of Sensitivity, Response Times and Recovery Times. The sensitivity S is found to increase exponentially ($S = 0.624e^{0.0602e}$ in the case of the undoped TiO₂ powder) as the humidity level/concentration c increases (Figure 58 (a)). In spite of the inflexion in the trend, the Cu-doped sample showed the highest sensitivity levels. Ag-TiO₂, on the other hand, was not as sensitive as TiO₂. The combined influence of Ag and Cu impurities can be observed for the double-doped Ag+Cu-TiO₂, in that its sensitivity levels are above those of Ag-TiO₂, but not as high as those of Cu-TiO₂. From the sensitivity dependence on NH₃ concentration (Figure 58), it follows that rate of change (or slope) of this dependence is continually increasing. This implies that at low concentrations a change in concentration leads to a small response, whereas at higher concentrations, the same change yields a relatively larger response. The change in resistance of a sensor at higher

concentrations therefore, constitutes an important part of the dynamic response to humidity.

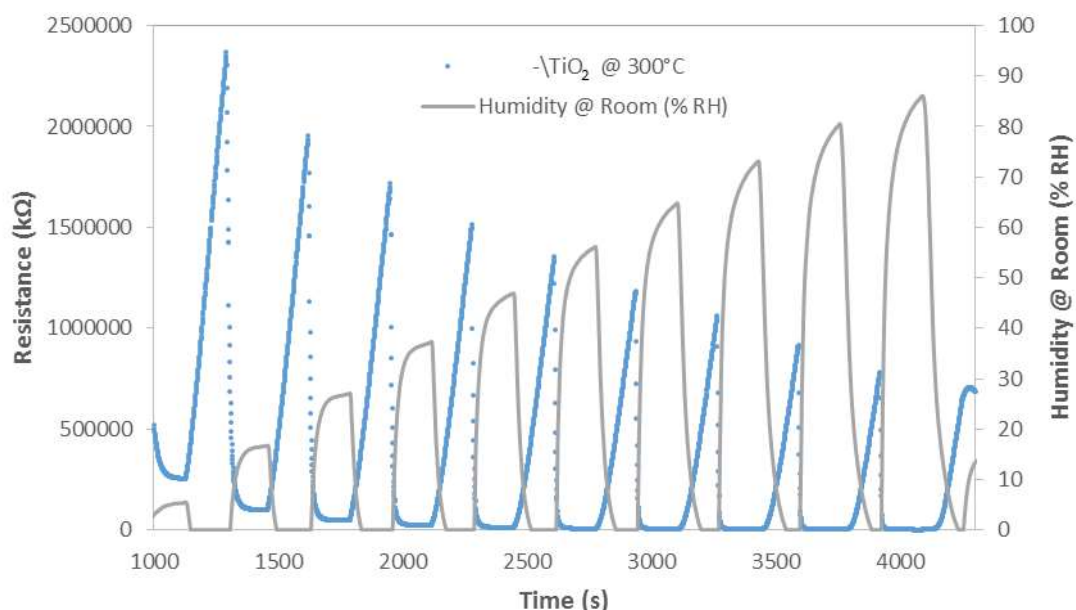


Figure 56: Dynamic response of prepared gas sensors based on undoped $-TiO_2$ nanopowders annealed at $300^\circ C$, when exposed to various room-temperature humidity levels (5.4% RH – 86.1% RH).

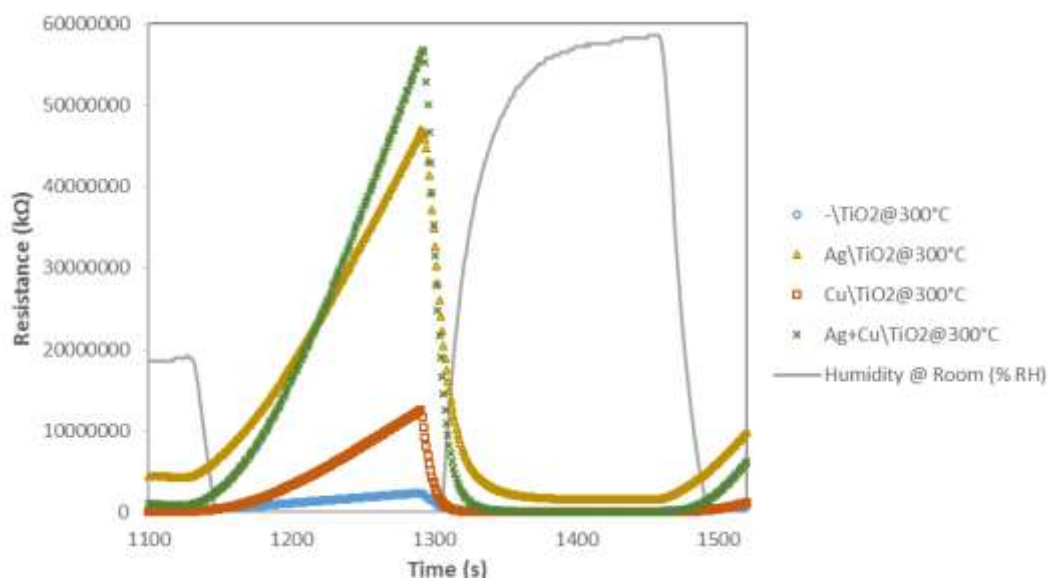
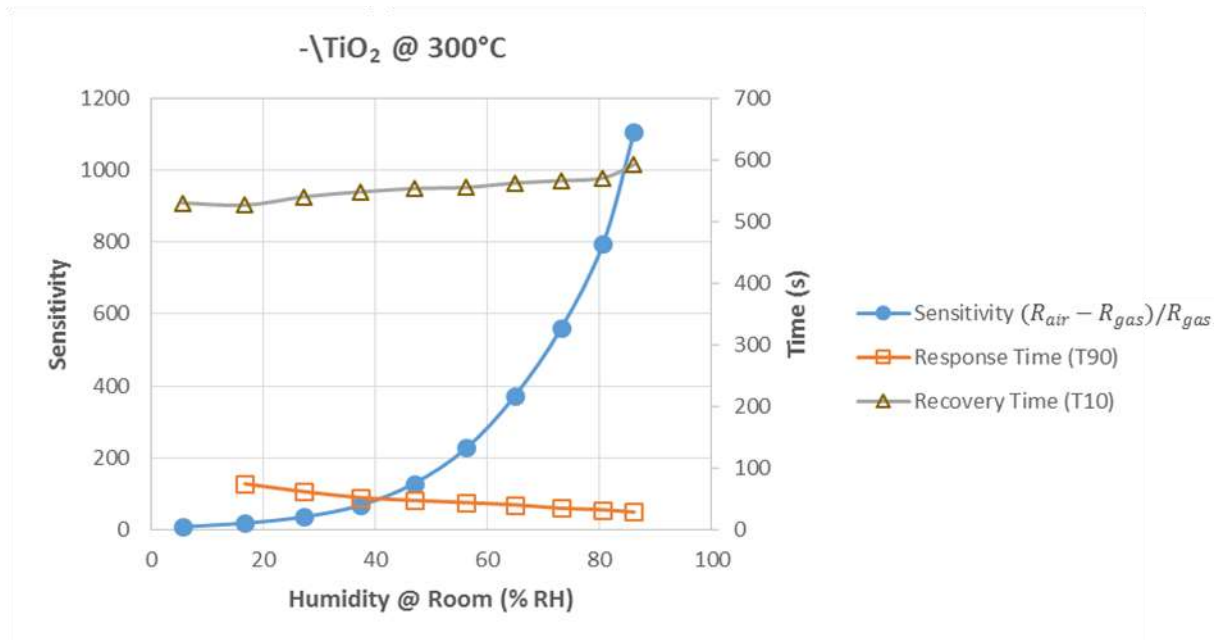


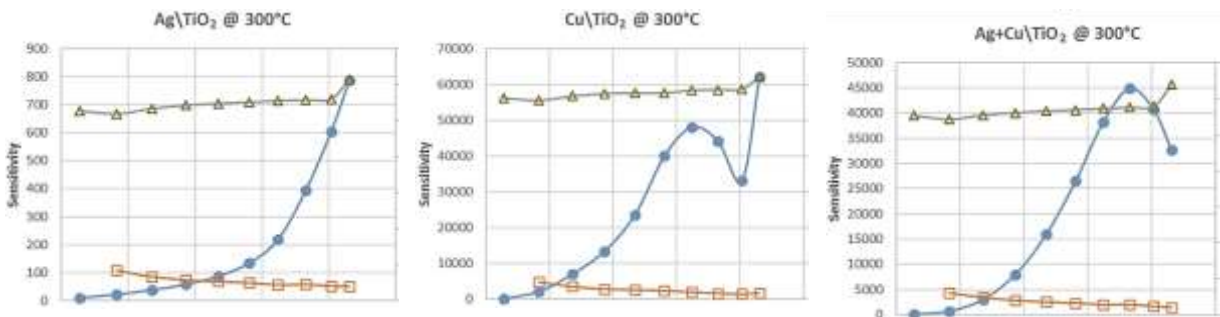
Figure 57: The response-recovery profiles for anatase TiO_2 nanopowders ($-TiO_2$, $Ag\TiO_2$, $Cu\TiO_2$ and $Ag+Cu\TiO_2$) annealed at $300^\circ C$ and exposed to room-temperature humidity of 16.7% RH.

The time taken for the resistance to decrease to 90% of its saturation value (the Response Time) also improved (decreased by more than 60%) with increasing humidity. On the other hand, the recovery of the samples became slightly slower when exposed to increasing humid conditions at room temperature. The response-

recovery patterns therefore appear to follow a symmetric trend with each other in all cases. That is, where the response time is following an increasing trend in the concentration evolution, the recovery tends to decrease, and vice versa.



(a)



(b)

(c)

(d)

Figure 58: Sensor characteristics of the prepared gas sensors based on (a) the undoped $-TiO_2$, (b) $AgTiO_2$, (c) $CuTiO_2$ and (d) $Ag+CuTiO_2$. The anatase nanopowders (annealed at $300^\circ C$) were exposed to various humidity levels (5.4% RH – 86.1% RH) and measured at room temperature.

The performance indices of the anatase TiO_2 nanopowders are displayed in Table 15. The Fractional Baseline Shift for each sample is negative, indicating that the system settled to lower resistances by the time the last humidity level was introduced. Further, more than 60% of the starting resistance was lost in each case.

Table 15: Performance indices of the anatase TiO₂ samples that were exposed to various levels of humidity at room temperature.

Gas: Humidity Operating Temperature: Room Crystallographic Structure: Anatase					
Sample	Humidity Level (% RH)	Sensitivity	Response Time (s)	Recovery Time (s)	Fractional Baseline Drift (%)
-TiO ₂ @ 300°C (Anatase)	5.5	8.38	440.22	530.21	-66.91
	16.7	18.62	74.71	526.61	
	27.1	35.74	62.12	540.09	
	37.3	68.39	52.23	548.22	
	46.9	129.09	47.73	553.61	
	56.2	227.35	44.10	555.43	
	64.8	371.60	40.51	562.62	
	73.1	560.25	35.11	566.25	
	80.6	795.81	32.41	570.73	
	86.1	1105.21	28.81	592.33	
AgTiO ₂ @ 300°C (Anatase)	5.5	9.94	318.61	527.46	-78.72
	16.7	22.59	83.70	519.39	
	27.1	37.82	66.61	533.80	
	37.3	58.16	57.61	542.90	
	46.9	87.40	53.03	548.19	
	56.2	134.74	49.52	551.82	
	64.8	219.41	44.12	555.43	
	73.1	395.13	45.02	558.14	
	80.6	603.85	40.52	560.81	
	86.1	788.21	39.63	615.72	
CuTiO ₂ @ 300°C (Anatase)	5.5	161.17	451.93	561.55	-80.04
	16.7	2140.14	47.71	555.53	
	27.1	6936.02	35.01	567.14	
	37.3	13376.05	27.91	574.35	
	46.9	23573.28	26.11	575.23	
	56.2	39986.99	23.50	576.06	
	64.8	48090.72	19.81	583.37	
	73.1	44095.20	16.21	585.16	
	80.6	33104.92	14.41	586.96	
	86.1	62021.71	17.12	622.03	
Ag+CuTiO ₂ @ 300°C (Anatase)	5.5	59.69	344.68	553.59	-85.98
	16.7	696.86	60.30	542.82	
	27.1	2972.57	47.71	554.52	
	37.3	7975.42	39.61	560.83	
	46.9	15886.37	35.11	566.20	
	56.2	26615.23	32.40	568.98	
	64.8	38272.26	27.91	573.46	
	73.1	44893.16	27.92	575.28	
	80.6	40663.19	23.42	579.74	
	86.1	32696.61	19.91	639.03	

6.2.2 Response of Rutile TiO₂ to Humidity

Although the dynamic responses of both the doped and undoped rutile TiO₂ sensors (annealed at 900°C) to humidity (Figure 59 to Figure 61) also show similar trends, the patterns are not as well-defined as those of their anatase counterpart. In particular, samples with Cu impurities (namely Cu\TiO₂ and Ag+Cu\TiO₂) proved to be least defined (Figure 59). These samples also displayed the highest impedances (Figure 60). Cu\TiO₂ was almost 2900 times more than the undoped -\TiO₂, Ag+Cu\TiO₂ was about 410 times, while the single-doped Ag\TiO₂ sample peaked by a factor of 2400.

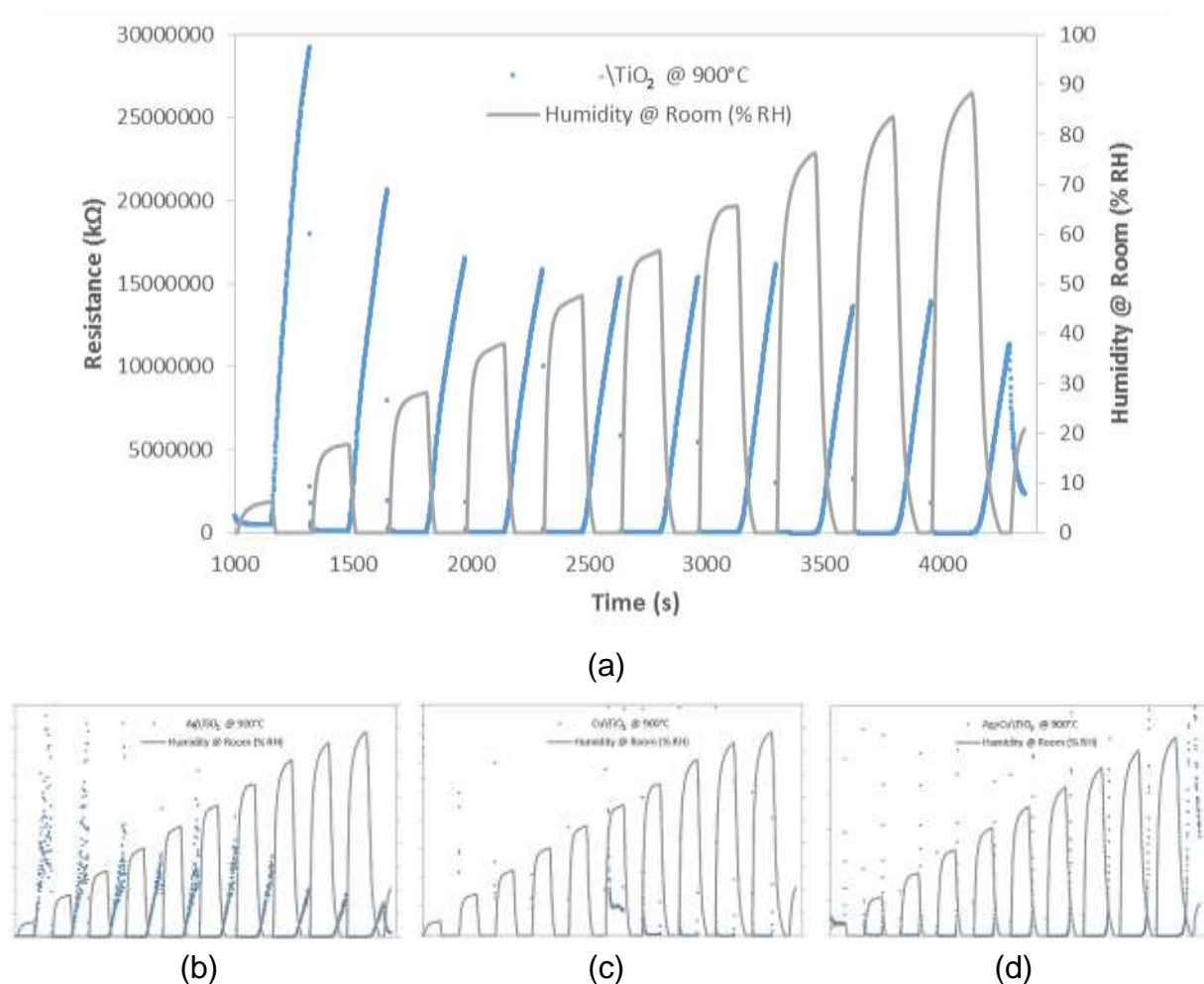


Figure 59: Dynamic response of prepared gas sensors based on rutile -TiO_2 nanopowders (annealed at 900°C), when exposed to various room-temperature humidity levels (5.4% RH – 86.1% RH). (a) Undoped -TiO_2 , (b) Ag\TiO₂, (c) Cu\TiO₂ and (d) Ag+Cu\TiO₂.

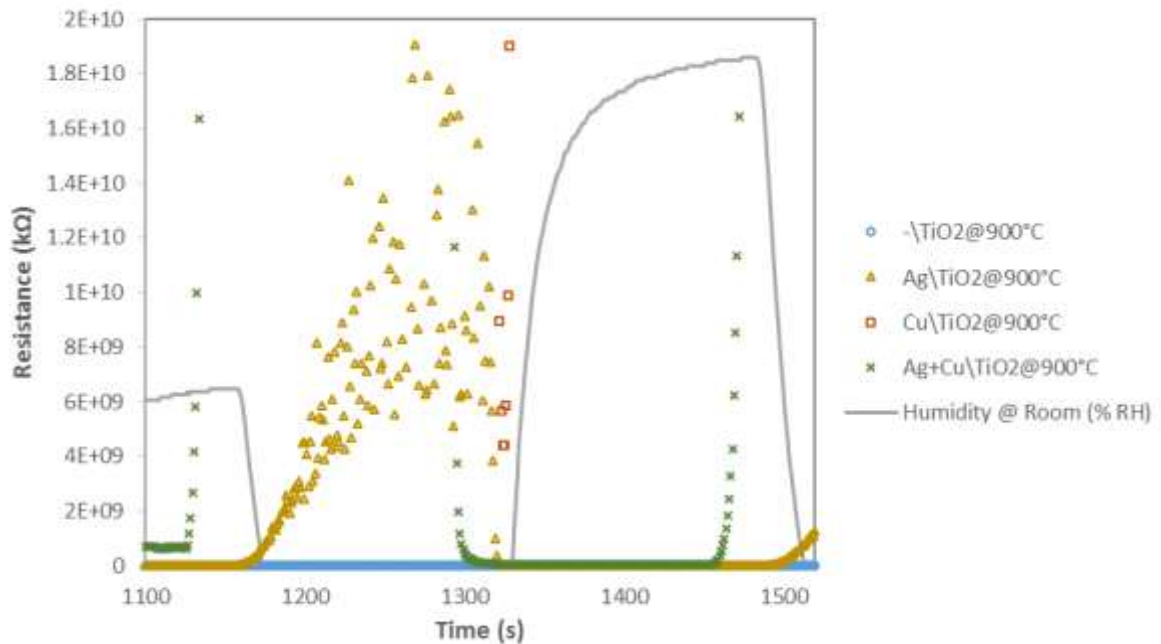
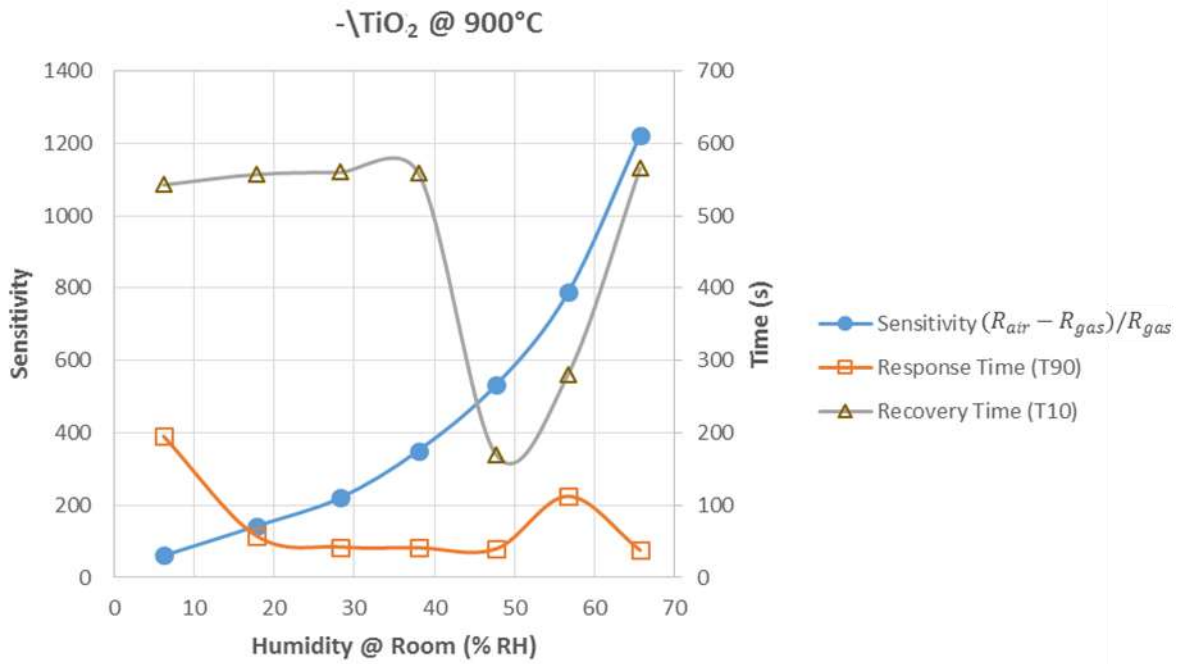
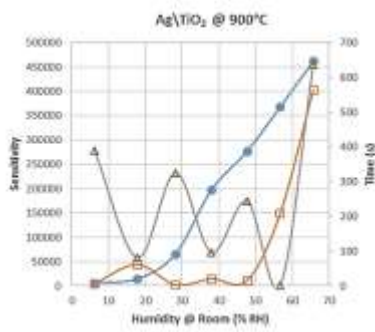


Figure 60: The response-recovery profiles for rutile TiO_2 nanopowders ($-\text{TiO}_2$, AgTiO_2 , CuTiO_2 and $\text{Ag}+\text{Cu}\text{TiO}_2$) annealed at 900°C and exposed to room-temperature humidity of 16.7% RH.

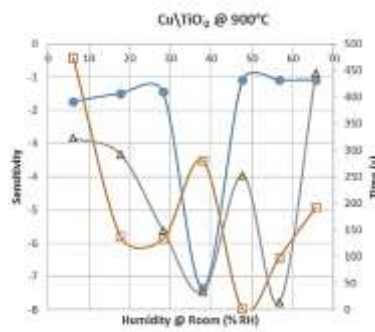
The sensitivities for $-\text{TiO}_2$ and AgTiO_2 were characteristically exponential, while the samples with Cu impurities display anomalies in their performance index patterns (Figure 61). This is a direct consequence of the poorly defined response to humidity by the rutile CuTiO_2 and $\text{Ag}+\text{Cu}\text{TiO}_2$ powders. Above all, the response and recovery times for all samples in this category do not show a clear linear or exponential trend. The five-minute “gas-in” and “gas-out” time intervals may prove to be too short for the sensor materials to register saturation in their impedances. The performance indices of the rutile TiO_2 samples that were exposed to various levels of humidity at room temperature are shown in Table 16.



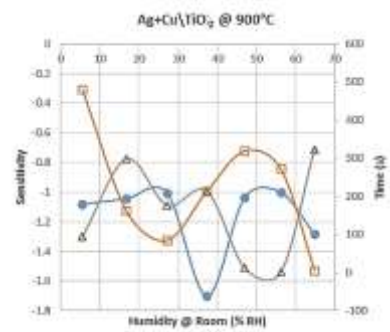
(a)



(b)



(c)



(d)

Figure 61: Sensor characteristics of the prepared gas sensors based on (a) the undoped $-\text{TiO}_2$, (b) AgTiO_2 , (c) CuTiO_2 and (d) Ag+CuTiO_2 . The anatase nanopowders (annealed at 300°C) were exposed to various humidity levels (5.4% RH – 86.1% RH) and measured at room temperature.

Table 16: Performance indices of the rutile TiO₂ samples that were exposed to various levels of humidity at room temperature.

Gas: Humidity Operating Temperature: Room Crystallographic Structure: Rutile					
Sample	Gas Concentration (% RH)	Sensitivity	Response Time (s)	Recovery Time (s)	Fractional Baseline Drift (%)
-TiO ₂ @ 900°C (Rutile)	6.2	60.9	195.3	542.8	-52.41
	17.8	142.7	57.6	557.2	
	28.2	220.0	42.3	560.0	
	38.0	351.0	41.3	559.0	
	47.7	532.5	39.7	563.4	
	56.7	788.0	37.9	565.3	
	65.7	1223.0	34.2	568.0	
	76.3	1602.1	32.5	567.1	
	83.6	2686.2	33.3	570.7	
	88.4	4309.4	29.7	574.4	
Ag\TiO ₂ @ 900°C (Rutile)	6.2	6621.8	1924.5	371.8	-95.90
	17.8	14785.9	5.4	636.3	
	28.2	65835.9	33.3	567.1	
	38.0	197601.3	34.2	592.3	
	47.7	276996.9	7.2	594.1	
	56.7	367944.6	7.2	582.4	
	65.7	461917.6	16.2	593.2	
	76.3	525724.3	7.2	585.0	
	83.6	1001059.38	15.3	592.2	
	88.4	1500907.94	9.0	582.3	
Cu\TiO ₂ @ 900°C (Rutile)	6.2	-1.7	1.8	575.4	-55.31
	17.8	-1.5	1.8	587.0	
	28.2	-1.5	1.8	586.1	
	38.0	-7.4	7.3	595.1	
	47.7	-1.1	113.8	477.5	
	56.7	-1.1	1.8	599.4	
	65.7	-1.1	1.8	592.3	
	76.3	-1.0	3.5	604.9	
	83.6	-1.0	5.5	589.5	
	88.4	-0.9	327.9	5.4	
Ag+Cu\TiO ₂ @ 900°C (Rutile)	5.5	-1.1	337.6	285.9	30609.68
	16.7	-1.1	329.7	5.4	
	27.1	-1.0	261.7	595.9	
	37.3	-1.7	4.5	591.4	
	46.9	-1.0	1.8	595.9	
	56.2	-1.0	1.8	595.9	
	64.8	-1.3	3.6	581.6	
	73.1	-1.0	1.8	380.9	
	80.6	-1.0	231.2	407.9	
	86.1	622642046.40	188.9	561.0	

6.2.3 Performance of Anatase versus Rutile TiO₂ under Humidity

The dynamic responses of the rutile powders are not as well-defined as those of the anatase samples, particularly in cases where Cu impurities are present. The impedances, as well as the sensitivities, of the rutile samples are also higher by several orders of magnitude. However, the sensitivities of the undoped and Ag-doped (whether anatase or rutile) still remained fairly exponential. Further, Ag impurities reduced the sensitivity to humidity in the case of anatase TiO₂, but improved the parameter in the rutile counterpart. It turns out that the anatase samples are generally better suited for detecting humidity, in terms of reliability, repeatability and stability, but the undoped and Ag-doped rutile TiO₂ have superior performance indices (higher sensitivities, lower response and recovery times).

6.3 AMMONIA GAS (NH₃)

NH₃ is a caustic and hazardous colourless gas with a characteristic pungent odour. It is a source of nitrogen to living organisms, nitrogen being present in vital biological molecules such as amino acids (the building blocks of proteins). The gas is present in animal waste, and in particularly high concentrations in chicken faeces. In agricultural environments, where animals can live in unventilated environments, ammonia concentrations can become high enough to kill the animals. An ability to monitor and control these environments is highly desirable [304].

The NH₃ gas concentration profile is more squarely defined than the humidity profile featured in the previous section. Just as before, the dynamic responses of both anatase and rutile (Appendix C) were recorded for the TiO_2 , Ag TiO_2 , Cu TiO_2 and Ag+Cu TiO_2 species, and their performance indices (Table 17 and Table 18) were deduced for NH₃ concentrations of 25, 50, 75, 100, 250, 375, 500 sccm, as well as for four operating temperatures (namely Room, 250°C, 300°C and 350°C) each. It would be noted that the anatase samples were not subjected to gas exposures at operating temperatures exceeding the annealing temperature of 300°C. This is to rule out the possibility of unintended crystallographic phase change to rutile TiO₂ which might take place. In such cases the missing data or chart is simply labelled "Not available".

6.3.1 Response of Anatase TiO₂ to NH₃

The dynamic responses of anatase TiO₂ nanopowders (annealed at 300°C), when exposed to various NH₃ concentrations at different operating temperatures are shown in Figure 62. Figure 63 displays the dynamic profiles of undoped γ -TiO₂ powders as the operating temperature increased. Here, the 5-minute “gas-in” time period is long enough to achieve stabilised responses (constant resistance) in a gas flow of constant concentration.

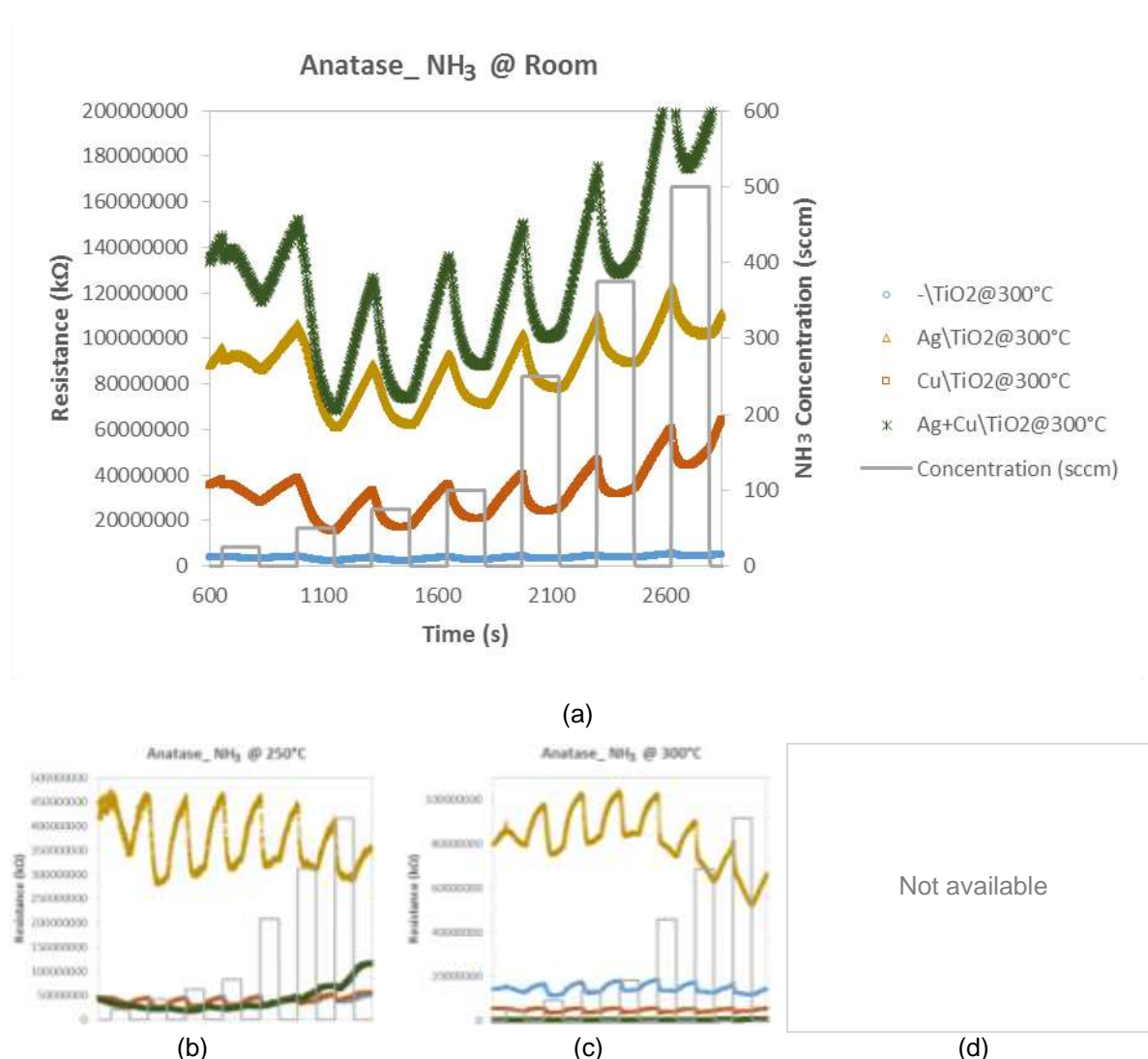


Figure 62: The dynamic responses of prepared gas sensors based on anatase TiO₂ nanopowders (annealed at 300°C), when exposed to various NH₃ concentrations at different operating temperatures. (a) Room temperature, (b) 250°C, (c) 300°C and (d) Not available. The programmed gas concentration profile is displayed as steps in continuous lines.

However, it may be pointed out that the adsorption or desorption processes that take place on the surface of the sensor material, may result in the rise in resistance observed soon after saturation is reached. With a fractional Baseline Drift close to zero, the undoped anatase -TiO_2 delivered the best overall performance in the presence of NH_3 at 300°C . At “Room” temperature, CuTiO_2 was more sensitive to NH_3 than the other anatase powders and also responded quickest, but the double-doped Ag+CuTiO_2 registered the highest resistances (Figure 62). When the operating temperature was increased to 250°C however, the Ag+CuTiO_2 was the most sensitive, while the undoped -TiO_2 was the quickest to respond. The double-doped sample was the least sensitive at 300°C , with the others having comparable trends.

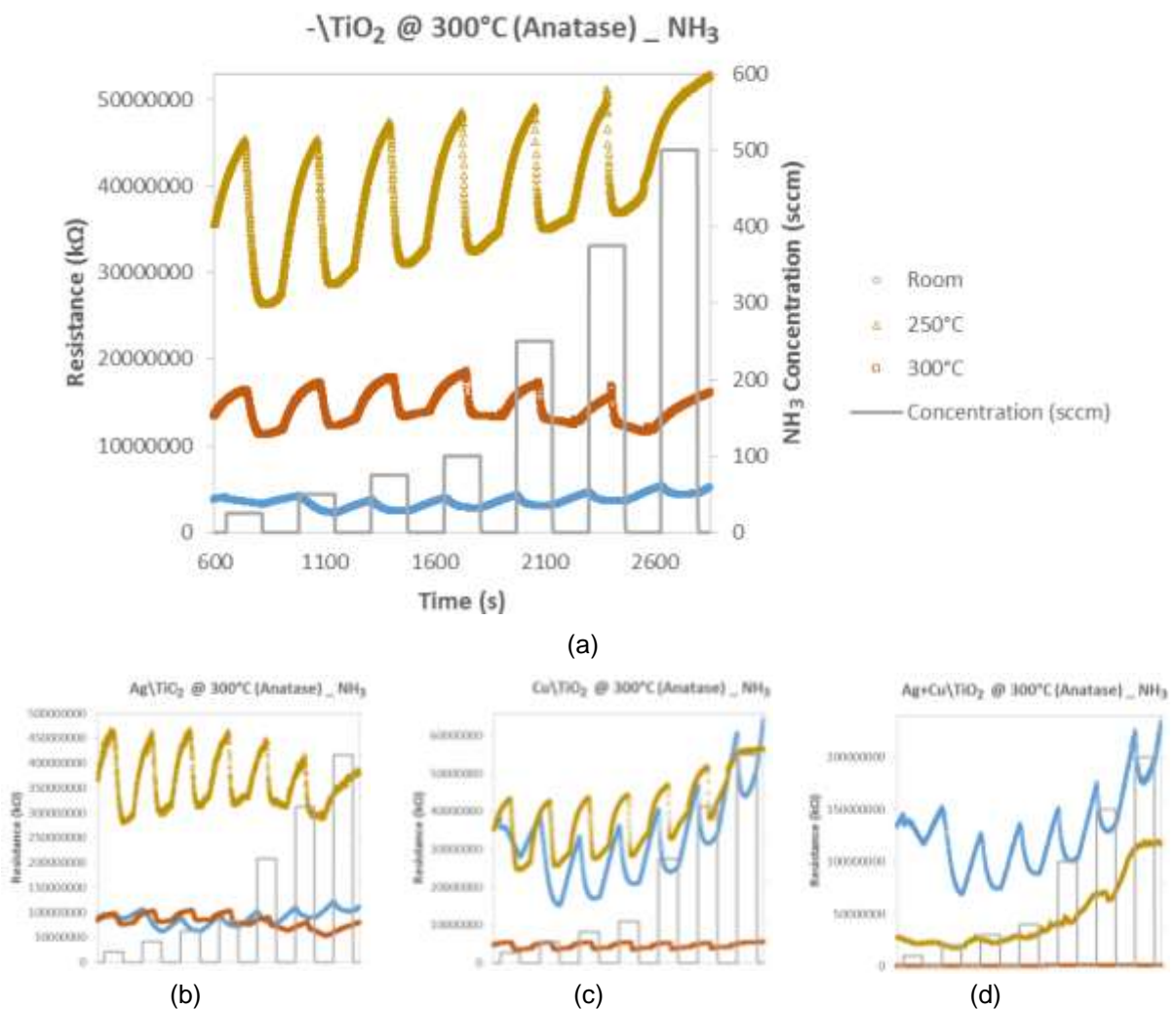


Figure 63: Dynamic response of prepared gas sensors based on anatase TiO_2 nanopowders (annealed at 300°C), when exposed to various concentrations of NH_3 at room temperature, 250°C and 300°C . (a) Undoped -TiO_2 , (b) AgTiO_2 , (c) CuTiO_2 and (d) $\text{Ag+Cu}\text{TiO}_2$.

Table 17: Performance data of the anatase TiO₂ samples that were exposed to various concentrations of NH₃ at different operating temperatures.

Gas: NH ₃ Crystallographic Structure: Anatase						
Sample	Temperature (°C)	Gas Concentration (sccm)	Sensitivity	Response Time (s)	Recovery Time (s)	Fractional Baseline Drift (%)
-TiO ₂ @ 300°C (Anatase)	Room	25	0.28	443.95	317.61	28.30
		50	0.66	240.31	358.26	
		75	0.60	171.12	431.97	
		100	0.51	168.33	431.21	
		250	0.50	139.51	462.67	
		375	0.47	142.23	459.98	
		500	1.04	132.31	814.6	
Ag\TiO ₂ @ 300°C (Anatase)	Room	25	0.22	400.44	308.63	15.50
		50	0.44	255.55	335.63	
		75	0.47	210.64	390.42	
		100	0.42	220.44	378.85	
		250	0.4	179.08	419.32	
		375	0.35	184.47	413.93	
		500	0.86	187.19	825.98	
Cu\TiO ₂ @ 300°C (Anatase)	Room	25	0.37	428.33	302.39	55.98
		50	1.16	213.3	383.46	
		75	1.09	157.5	441.92	
		100	0.92	153.9	443.74	
		250	0.93	124.21	476.17	
		375	0.9	112.42	485.91	
		500	1.88	99.88	857.49	
Ag+Cu\TiO ₂ @ 300°C (Anatase)	Room	25	0.27	165.49	589.39	47.87
		50	0.8	221.35	356.43	
		75	0.8	179.88	421.14	
		100	0.68	170.01	427.43	
		250	0.7	135.9	471.5	
		375	0.72	112.49	469.73	
		500	1.54	107.08	864.58	
-TiO ₂ @ 300°C (Anatase)	250°C	25	0.38	287.99	282.52	12.9
		50	0.71	153.92	427.47	
		75	0.64	149.36	454.49	
		100	0.55	143.08	453.49	
		250	0.51	118.78	484.98	
		375	0.42	112.52	541.63	
		500	0.45	54.9	709.96	
Ag\TiO ₂ @ 300°C (Anatase)	250°C	25	0.38	262.66	266.24	-10.25
		50	0.65	184.41	463.29	
		75	0.58	116.04	456.97	
		100	0.49	143.01	474.92	
		250	0.43	91.77	507.28	
		375	0.34	113.42	510.82	
		500	0.39	107.96	837.5	

Cu\TiO ₂ @ 300°C (Anatase)	250°C	25	0.4	447.22	266.45	19.52
		50	0.73	159.17	407.71	
		75	0.7	174.58	434.73	
		100	0.61	157.47	418.57	
		250	0.66	158.32	448.07	
		375	0.58	146.67	452.58	
		500	0.49	142.22	419.27	
Ag+Cu\TiO ₂ @ 300°C (Anatase)	250°C	25	0.01	289.87	349.27	153.2
		50	0.09	261.09	423.97	
		75	0.69	78.3	80.12	
		100	0.43	#N/A	#N/A	
		250	0.73	78.3	378.83	
		375	0.69	226.84	444.45	
		500	0.89	112.47	#N/A	
-TiO ₂ @ 300°C (Anatase)	300°C	25	0.3	249.35	286.27	2.72
		50	0.54	159.36	426.71	
		75	0.47	158.45	439.32	
		100	0.38	151.21	484.32	
		250	0.29	107.12	491.55	
		375	0.26	165.64	487.96	
		500	0.5	168.32	758.01	
Ag\TiO ₂ @ 300°C (Anatase)	300°C	25	0.24	234.89	311.35	-16.52
		50	0.36	148.49	421.18	
		75	0.3	163.78	444.56	
		100	0.23	147.59	115.18	
		250	0.21	27.92	342.84	
		375	0.26	262.88	322.99	
		500	0.68	300.57	359.98	
Cu\TiO ₂ @ 300°C (Anatase)	300°C	25	0.31	189.95	245.78	-1.75
		50	0.56	246.64	221.47	
		75	0.54	197.13	384.39	
		100	0.5	204.44	381.59	
		250	0.5	210.65	424.89	
		375	0.49	154.83	420.39	
		500	0.52	174.74	491.41	
Ag+Cu\TiO ₂ @ 300°C (Anatase)	300°C	25	0.16	#N/A	#N/A	67.87
		50	0.19	187.25	417.71	
		75	0.17	174.64	457.32	
		100	0.17	119.73	349.31	
		250	0.26	246.67	332.19	
		375	0.3	267.36	314.19	
		500	0.25	617.58	#N/A	

6.3.2 Response of Rutile TiO₂ to NH₃

When using rutile TiO₂ as a sensor material, the undoped sample (–TiO₂) was the only one that revealed (in Figure 64) a reasonable dynamic performance in sensing NH₃ at room temperature, as well as at 250°C. All the rutile samples may be used for detecting NH₃ at the higher temperatures of 300°C and 350°C, except for the Cu\TiO₂ which did not register any clear response or stability. Yet, their sensitivities are much lower than those of their anatase counterparts.

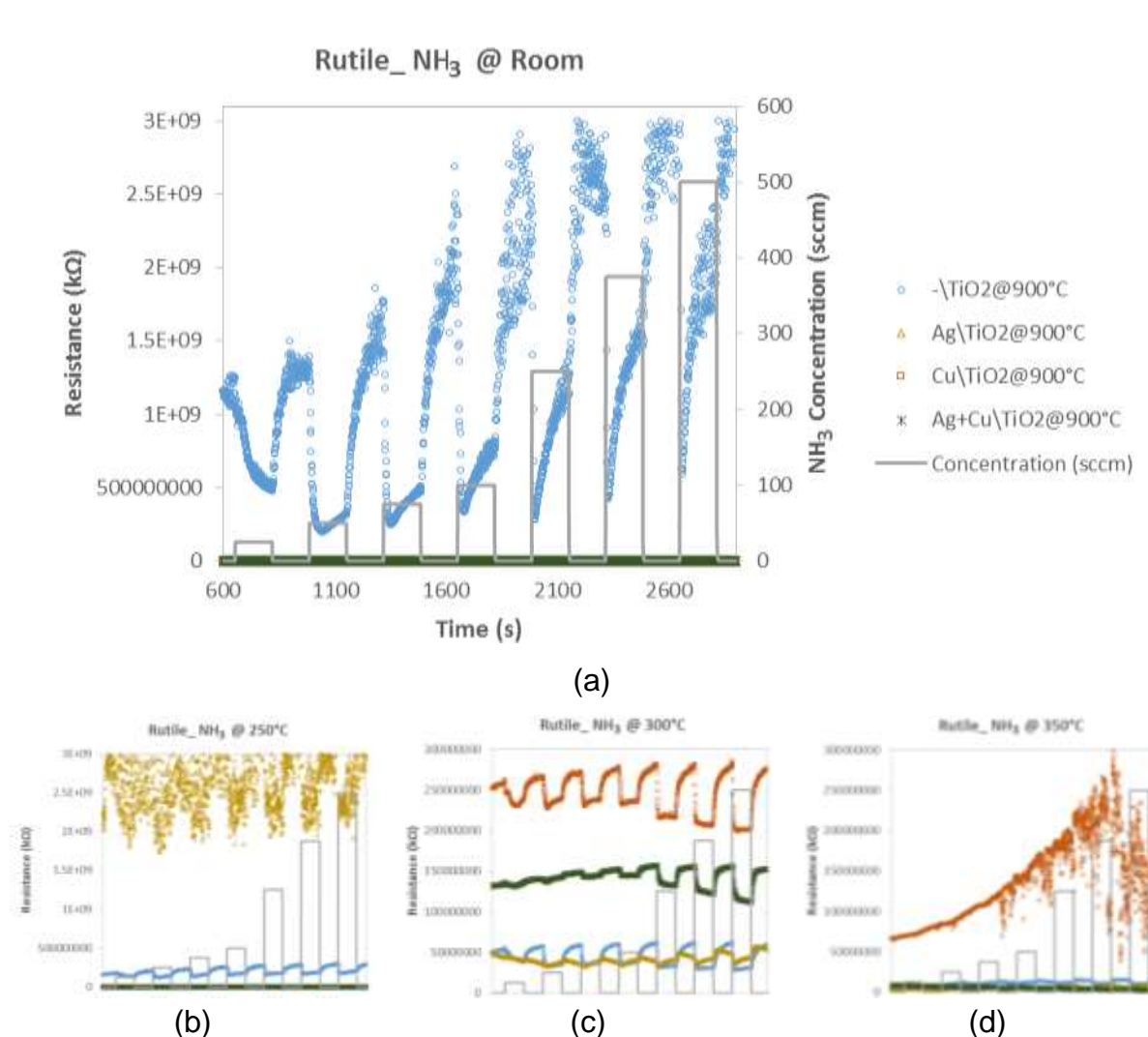


Figure 64: The dynamic responses of prepared gas sensors based on rutile TiO₂ nanopowders (annealed at 900°C), when exposed to various NH₃ concentrations at different room temperatures. (a) Room temperature, (b) 250°C, (c) 300°C and (d) 350°C.

Figure 65 shows that detecting NH_3 at concentrations up to 500 sccm is best carried out by the undoped nanopowder, if rutile TiO_2 is to be used as a sensor material. This sample displays good sensing properties at all the operating temperatures tested and performs best at 300°C . The double-doped sensor material could only function properly at the higher temperatures of 300°C and 350°C , while the Ag-doped fails at all temperatures, except at 350°C .

In general, the sensitivities of samples that exhibit discernable dynamic response profiles were found to increase as the gas concentration increases – in many cases, exponentially.

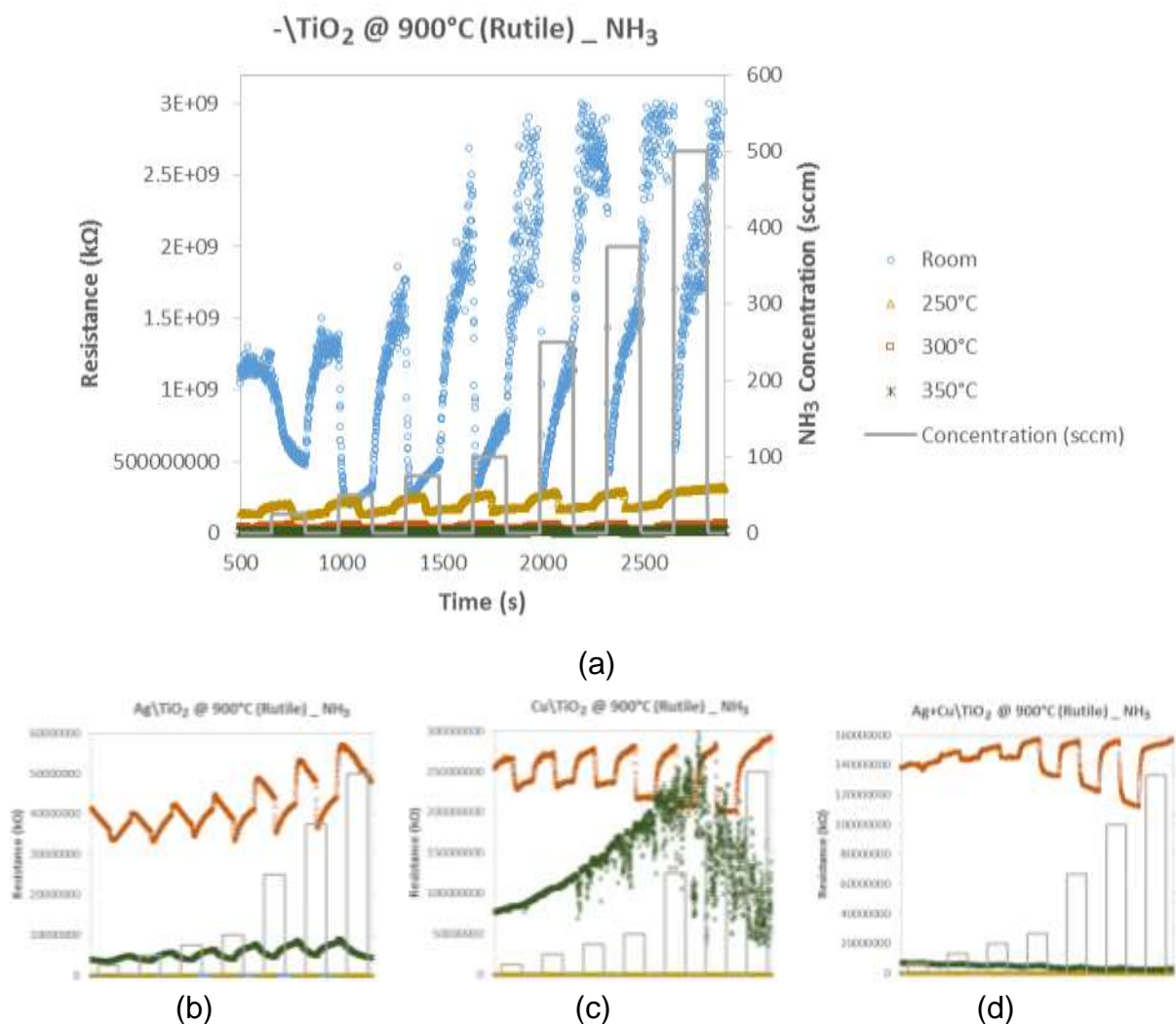


Figure 65: The dynamic response of prepared gas sensors based on rutile TiO_2 nanopowders (annealed at 900°C), when exposed to various concentrations of NH_3 at room temperature, 250°C , 300°C and 350°C . (a) Undoped $-\text{TiO}_2$, (b) AgTiO_2 , (c) CuTiO_2 and (d) $\text{Ag}+\text{Cu}\text{TiO}_2$.

Table 18: Performance data of the rutile TiO₂ samples that were exposed to various concentrations of NH₃ at different temperatures.

Gas: NH ₃ Crystallographic Structure: Rutile						
Sample	Temperature (°C)	Gas Concentration (sccm)	Sensitivity	Response Time (s)	Recovery Time (s)	Fractional Baseline Drift (%)
-TiO ₂ @ 900°C (Rutile)	Room	25	2.12	477.58	402.95	114.13
		50	8.46	65.66	537.94	
		75	9.92	48.57	553.17	
		100	7.72	42.28	417.34	
		250	9.79	173.6	379.55	
		375	9.69E+09	205.99	583.83	
		500	1.4E+10	17.1	474.08	
Ag\TiO ₂ @ 900°C (Rutile)	Room	25	-607.16	126.92	602.1	30.07
		50	-1012.55	9	592.18	
		75	-718.23	1.8	592.2	
		100	-19010.2	1.8	588.67	
		250	-994.2	1.8	321.3	
		375	-819.05	#N/A	#N/A	
		500	-1.1E+14	1.8	763.16	
Cu\TiO ₂ @ 900°C (Rutile)	Room	25	276.75	1.79	1645.22	361.04
		50	275.53	106.64	568.11	
		75	171.75	3.59	518.83	
		100	77.72	74.48	590.45	
		250	128.86	10.75	597.71	
		375	18931.58	3.58	589.65	
		500	-17586.7	5.38	#N/A	
Ag+Cu\TiO ₂ @ 900°C (Rutile)	Room	25	2006.19	0	213.24	-0.22
		50	2011.95	39.43	539.51	
		75	216.73	88.73	564.64	
		100	2003.6	1.84	617.5	
		250	114.86	1.7	571.18	
		375	2007.7	2.42	619.29	
		500	2.8E+10	1.79	581.67	
-TiO ₂ @ 900°C (Rutile)	250°C	25	0.64	213.33	380.51	39.59
		50	1.03	65.68	492.18	
		75	0.99	97.18	428.29	
		100	0.83	168.27	475.07	
		250	0.9	107.97	470.59	
		375	0.78	124.24	524.51	
		500	0.94	75.57	797.16	
Ag\TiO ₂ @ 900°C (Rutile)	250°C	25	9.86E+09	10.79	174.55	0.00
		50	9.98E+09	5.4	111.59	
		75	9.97E+09	3.6	81.06	
		100	9.91E+09	43.08	168.26	
		250	9.86E+09	19.79	187.12	
		375	9.96E+09	21.59	191.66	
		500	1.29E+10	25.19	70.2	

Cu\TiO ₂ @ 900°C (Rutile)	250°C	25	-463.06	3.59	148.69	-88.97
		50	-799	1.79	206.02	
		75	-298.2	1.79	120.04	
		100	-532.37	1.79	171.1	
		250	-564.9	1.79	302.78	
		375	-540.29	1.8	178.27	
		500	-4.2E+14	1.79	426.44	
Ag+Cu\TiO ₂ @ 900°C (Rutile)	250°C	25	4587.04	9.02	115.57	0.00
		50	97.78	1.72	340.39	
		75	97.78	1.79	420.2	
		100	-47.64	1.79	199.77	
		250	95.79	9.86	286.75	
		375	97	9.87	125.42	
		500	2.85E+11	7.17	582.49	
-TiO ₂ @ 900°C (Rutile)	300°C	25	0.51	231.28	278.1	7.73
		50	0.86	142.19	416.64	
		75	0.84	177.28	423.03	
		100	0.81	173.62	467.96	
		250	0.97	116.09	497.66	
		375	1.11	104.42	485.12	
		500	1.4	120.56	689.4	
Ag\TiO ₂ @ 900°C (Rutile)	300°C	25	0.03	564.26	103.57	30.73
		50	0.21	233.88	61.25	
		75	0.28	297.84	294.33	
		100	0.31	299.6	297.89	
		250	0.47	305.97	297.88	
		375	0.52	295.18	310.46	
		500	0.58	291.68	315.78	
Cu\TiO ₂ @ 900°C (Rutile)	300°C	25	0.17	128.11	384.38	6.79
		50	0.2	154.09	379	
		75	0.21	210.48	456.93	
		100	0.22	135.28	507.09	
		250	0.3	76.15	99.45	
		375	0.36	157.72	249.04	
		500	0.49	94.98	527.7	
Ag+Cu\TiO ₂ @ 900°C (Rutile)	300°C	25	0.08	7.17	265.17	11.26
		50	0.09	142.43	298.32	
		75	0.07	218.61	280.43	
		100	0.09	307.29	521.43	
		250	0.18	68.08	120.05	
		375	0.28	52.87	282.22	
		500	0.42	189.03	363.78	
-TiO ₂ @ 900°C (Rutile)	350°C	25	0.79	318.73	291.71	81.24
		50	1.03	301.55	303.39	
		75	0.6	297.08	308.8	
		100	0.42	295.28	314.18	
		250	0.57	286.31	325.89	
		375	0.56	271.88	343.01	
		500	0.58	575.27	#N/A	

Ag\TiO ₂ @ 900°C (Rutile)	350°C	25	0.16	507.77	323.27	106.85
		50	0.42	276.36	316.02	
		75	0.59	277.22	334.9	
		100	0.68	265.57	373.71	
		250	0.95	232.19	372.76	
		375	0.91	235.95	366.31	
		500	0.83	487.03	#N/A	
Cu\TiO ₂ @ 900°C (Rutile)	350°C	25	0.23	112.91	1092.21	254.85
		50	0.37	116.47	215.91	
		75	0.36	222.17	59.12	
		100	1	116.45	309.07	
		250	0.93	100.36	111.11	
		375	3.12	54.65	71.66	
		500	3.28	103.04	66.31	
Ag+Cu\TiO ₂ @ 900°C (Rutile)	350°C	25	0.02	599.58	51.87	-50.56
		50	0.08	188.2	423.88	
		75	0.07	269.73	207	
		100	0.16	89.6	51.97	
		250	0.16	292.15	298.4	
		375	0.14	283.18	297.51	
		500	0.57	290.35	304.67	

6.3.3 Performance of Anatase versus Rutile TiO₂ under NH₃

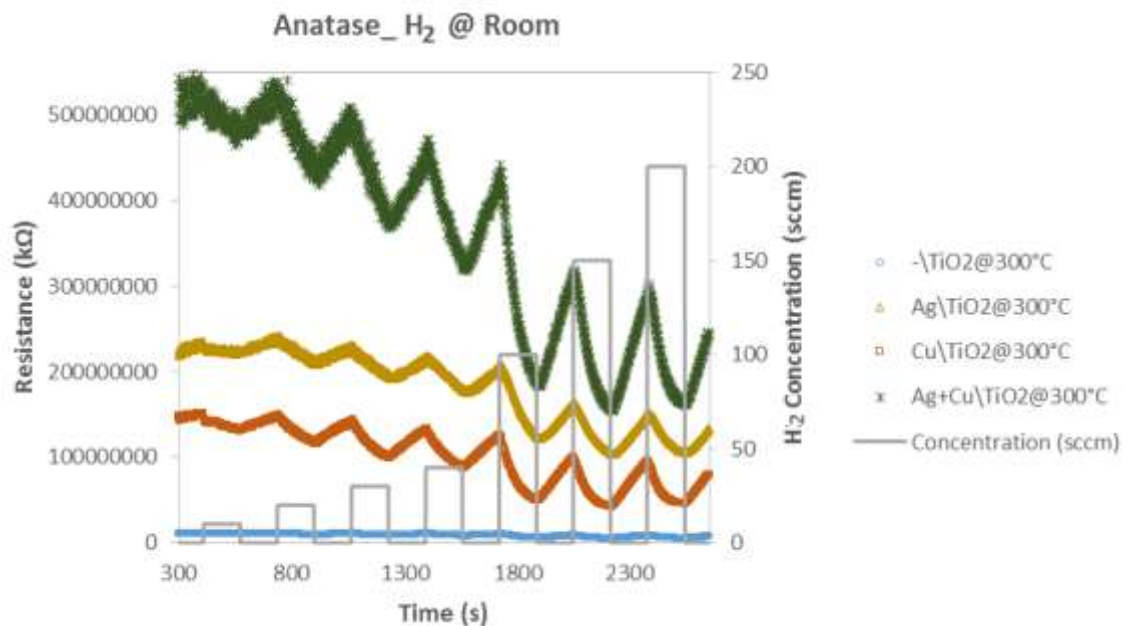
As it was in the case of humidity, the rutile samples registered higher impedances (over the anatase counterpart) but failed to exhibit discernable dynamic response profiles at certain operating temperatures. Notably are, Ag\TiO₂ and Cu\TiO₂ at room temperature and at 250°C, as well as Ag+Cu\TiO₂ at 350°C. In operating environments where temperatures may range between room temperature and 300°C, the anatase powders will be suitable as sensor material for detecting NH₃, the optimal being the Cu\TiO₂. For higher temperatures (at least up to 350°C) the undoped -\TiO₂, in its rutile form, will suffice. The rutile samples not only feature higher impedances over the anatase counterparts, but also higher sensitivities.

6.4 HYDROGEN GAS (H₂)

The “gas-in”/“gas-out” profile for detecting H₂ involved concentrations of 15, 20, 30, 40, 100, 150, and 200 sccm. An investigation of the sensor response to H₂ at four different operating temperatures (“Room”, 250°C, 300°C and 350°C) is revealed in Figure 66 & Figure 67 for anatase powders, as well as Figure 68 & Figure 69 for the rutile powders, in respect of the -TiO_2 , $\text{Ag}\text{-TiO}_2$, $\text{Cu}\text{-TiO}_2$ and $\text{Ag+Cu}\text{-TiO}_2$ species. Their extracted sensor sensitivity dependence on temperature are reported in Table 17 (for anatase) and Table 18 (for rutile) respectively, alongside the response and recovery data.

6.4.1 Response of Anatase TiO₂ to H₂

Large and reproducible responses, which are in step with the changes in H₂ concentration, can be observed in Figure 66 for all the anatase sensor materials. However, when exposed to the gas at room temperature, the impedances tend to decrease as the concentration increases, whereas the baseline remains fairly steady at other operating temperatures. When considering the range of temperatures from “Room” to 300°C, the most reliable performance comes from the undoped -TiO_2 sample. This is closely followed by that of the $\text{Cu}\text{-TiO}_2$.



(a)

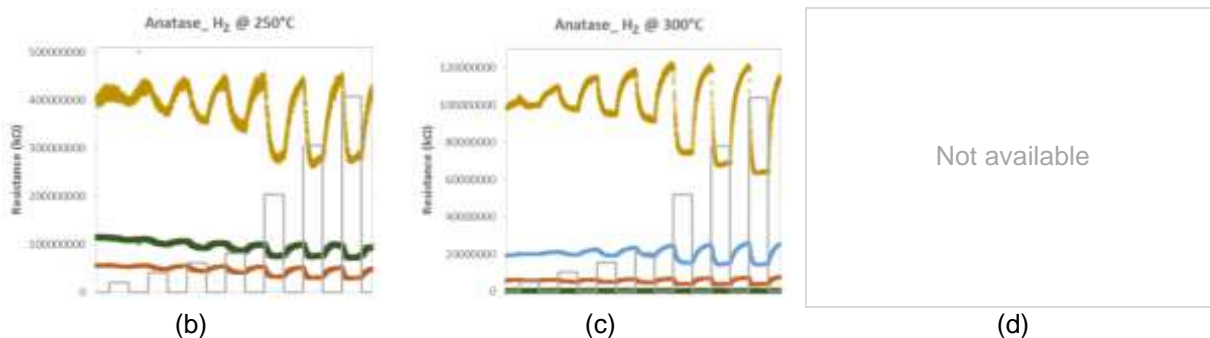
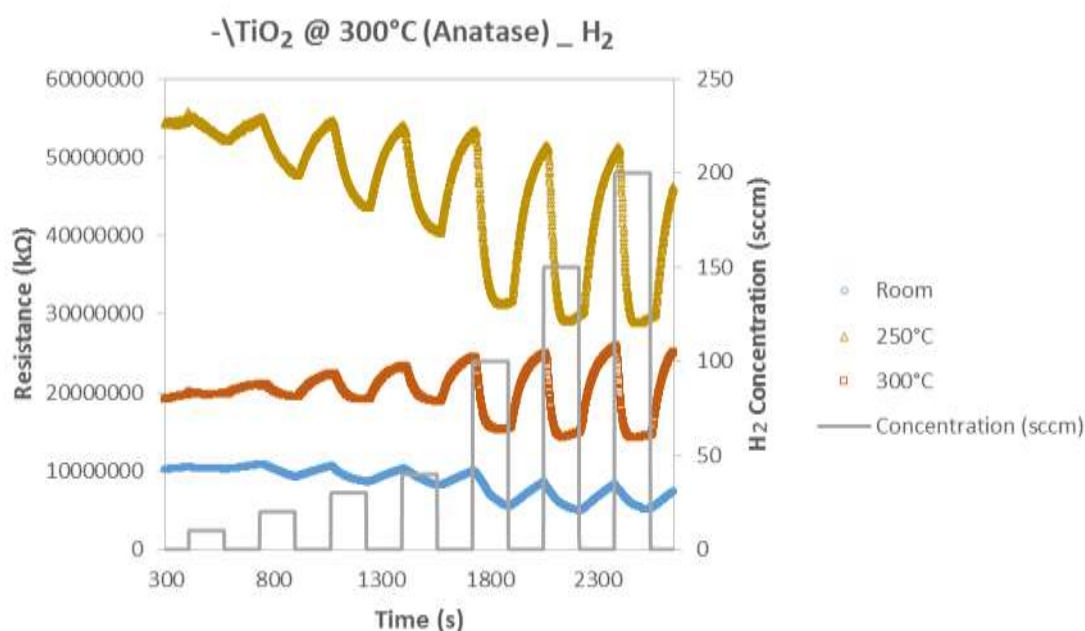
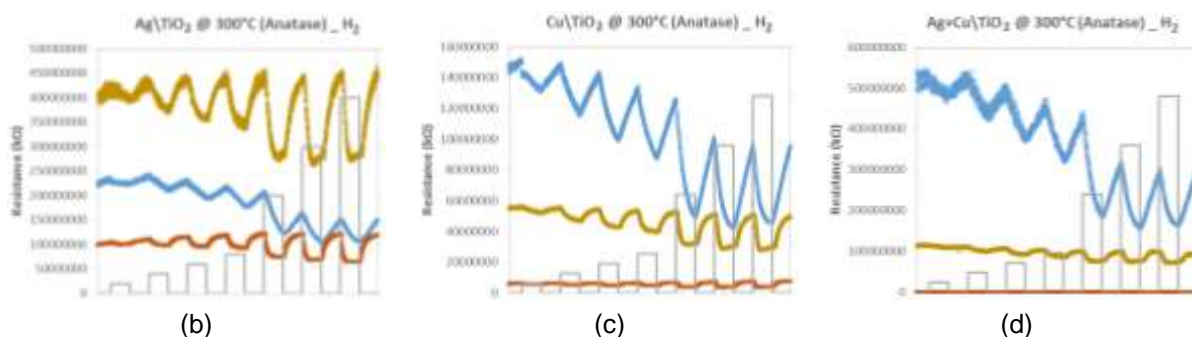


Figure 66: The dynamic responses of prepared gas sensors based on anatase TiO_2 nanopowders (annealed at $300^\circ C$), when exposed to various H_2 concentrations at different operating temperatures. (a) Room temperature, (b) $250^\circ C$, (c) $300^\circ C$ and (d) Not available.



(a)



(b)

(c)

(d)

Figure 67: Dynamic response of prepared gas sensors based on anatase TiO_2 nanopowders (annealed at $300^\circ C$), when exposed to various concentrations of H_2 at room temperature, $250^\circ C$ and $300^\circ C$. (a) Undoped $-TiO_2$, (b) Ag/TiO_2 , (c) Cu/TiO_2 and (d) $Ag+Cu/TiO_2$.

Table 19: Performance data of the anatase TiO₂ samples that were exposed to various concentrations of H₂ at different operating temperatures.

Gas: H ₂ Crystallographic Structure: Anatase						
Sample	Temperature (°C)	Gas Concentration (sccm)	Sensitivity	Response Time (s)	Recovery Time (s)	Fractional Baseline Drift (%)
-TiO ₂ @ 300°C (Anatase)	Room	10	0.06	366.41	301.57	-23.52
		20	0.14	285.31	300.63	
		30	0.18	264.65	338.49	
		40	0.21	288.89	315.96	
		100	0.55	260.14	334.88	
		150	0.68	261.05	337.55	
		200	0.02	234.95	779.54	
Ag\TiO ₂ @ 300°C (Anatase)	Room	10	0.1	329.34	369.93	-37.45
		20	0.11	244.67	327.51	
		30	0.13	278.95	337.43	
		40	0.16	277.16	323.96	
		100	0.32	260.95	311.44	
		150	0.44	286.06	330.24	
		200	0	240.31	339.16	
Cu\TiO ₂ @ 300°C (Anatase)	Room	10	0.14	276.24	352.75	-35.2
		20	0.22	276.26	327.51	
		30	0.33	250.15	336.85	
		40	0.43	277.73	314.94	
		100	1.02	246.59	356.4	
		150	1.23	220.37	381.53	
		200	0	188.08	396.85	
Ag+Cu\TiO ₂ @ 300°C (Anatase)	Room	10	0.16	8.98	254.54	-43.83
		20	0.2	433.55	325.64	
		30	0.26	303.15	320.21	
		40	0.35	257.25	366.08	
		100	0.66	262.71	300.37	
		150	0.86	257.32	355.42	
		200	0.02	234.85	383.33	
-TiO ₂ @ 300°C (Anatase)	250°C	10	0.05	276.29	332.97	-6.87
		20	0.14	249.28	278.98	
		30	0.24	287.09	305.97	
		40	0.32	270.88	316.77	
		100	0.65	209.68	395.98	
		150	0.76	178.17	422.12	
		200	0.78	166.49	430.22	
Ag\TiO ₂ @ 300°C (Anatase)	250°C	10	0.28	174.5	349.04	3.28
		20	0.21	253.65	314.83	
		30	0.29	249.27	379.5	
		40	0.35	216.76	354.41	
		100	0.64	200.59	404.89	
		150	0.74	165.5	438.17	
		200	0.73	153.81	#N/A	

Cu\TiO ₂ @ 300°C (Anatase)	250°C	10	0.06	815.35	333.87	-8.29
		20	0.16	235.78	269.98	
		30	0.25	275.39	315.87	
		40	0.32	243.88	355.47	
		100	0.62	197.97	385.17	
		150	0.75	196.19	405.89	
		200	0.81	184.49	#N/A	
Ag+Cu\TiO ₂ @ 300°C (Anatase)	250°C	10	0.04	1541.59	255.58	-12.83
		20	0.09	306.9	226.78	
		30	0.13	420.26	336.67	
		40	0.18	103.4	466.17	
		100	0.35	122.39	350.08	
		150	0.36	236.68	993.66	
		200	0.35	#N/A	#N/A	
-TiO ₂ @ 300°C (Anatase)	300°C	10	0.07	109.83	471.71	22.83
		20	0.15	237.65	317.77	
		30	0.23	216.05	361.90	
		40	0.30	240.35	363.74	
		100	0.64	187.27	402.43	
		150	0.81	175.56	436.65	
		200	0.88	158.44	408.71	
Ag\TiO ₂ @ 300°C (Anatase)	300°C	10	0.12	100.78	453.56	10.31
		20	0.19	215.97	301.49	
		30	0.26	242.96	415.77	
		40	0.34	193.49	399.61	
		100	0.64	156.62	409.49	
		150	0.80	177.30	417.60	
		200	0.88	177.29	368.07	
Cu\TiO ₂ @ 300°C (Anatase)	300°C	10	0.08	136.82	421.29	20.81
		20	0.22	235.84	274.57	
		30	0.31	237.65	342.05	
		40	0.4	251.14	371.83	
		100	0.8	192.68	375.41	
		150	1.02	216.07	415.93	
		200	1.21	181.04	543.62	
Ag+Cu\TiO ₂ @ 300°C (Anatase)	300°C	10	0.03	379.87	296.19	6.3
		20	0.11	338.49	246.66	
		30	0.19	285.38	314.24	
		40	0.24	217.98	396.01	
		100	0.4	193.57	421.36	
		150	0.46	180.95	368.2	
		200	0.48	625.67	#N/A	

6.4.2 Response of Rutile TiO₂ to H₂

All the sample species, in their rutile form behaved as expected when exposed to H₂ at 300°C, unlike at room temperature in which all the samples failed. In spite of Cu\TiO₂ showing the quickest response and recovery times, if rutile TiO₂ is to be used as a sensor material, the undoped -TiO₂ sample may be selected, even though its performance at room temperature is much weaker when compared to others. It was also noted that none of the doped samples (Ag\TiO₂, Cu\TiO₂ and Ag+Cu\TiO₂) registered any meaningful and repeatable responses to H₂ at 250°C and below.

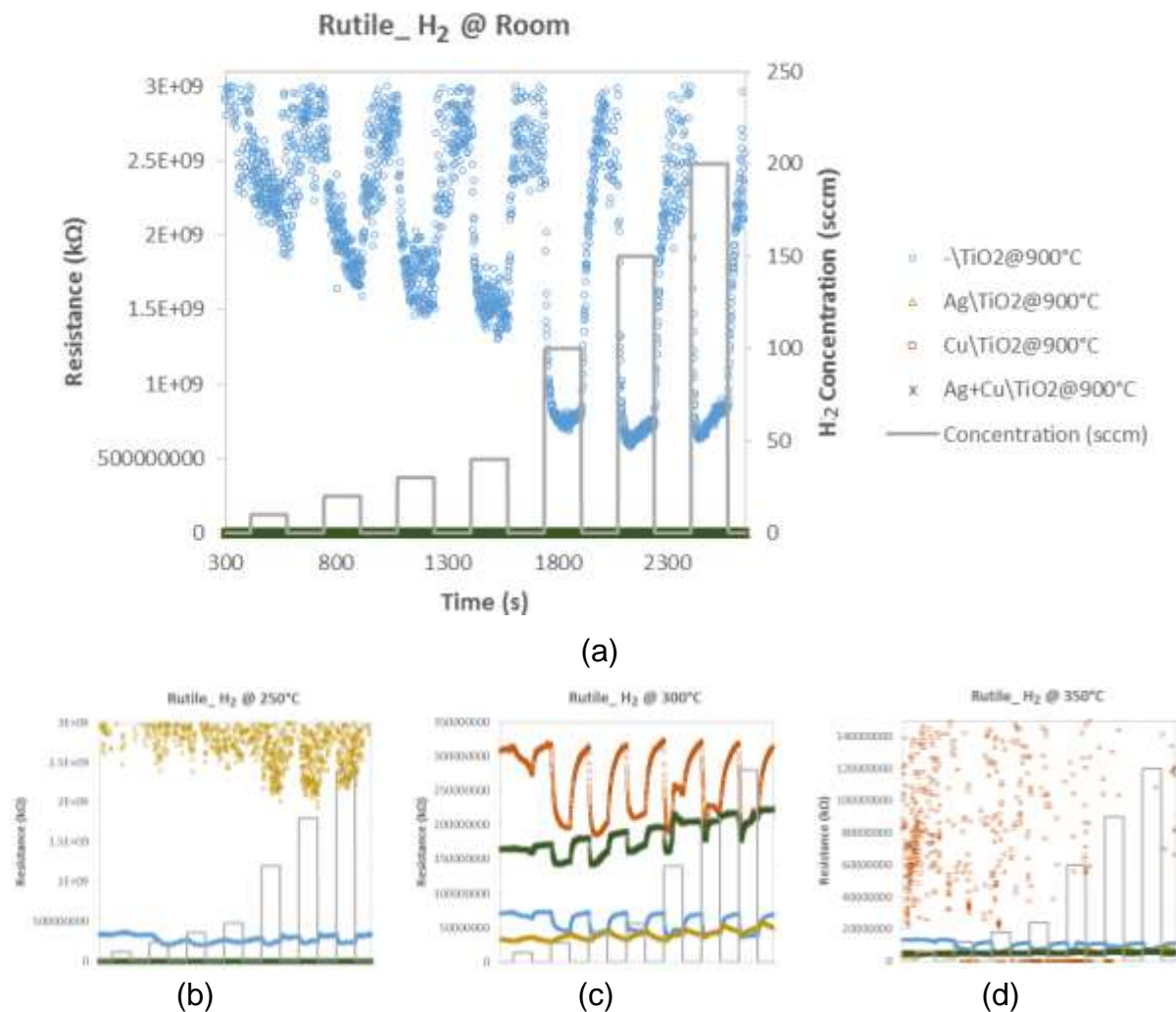
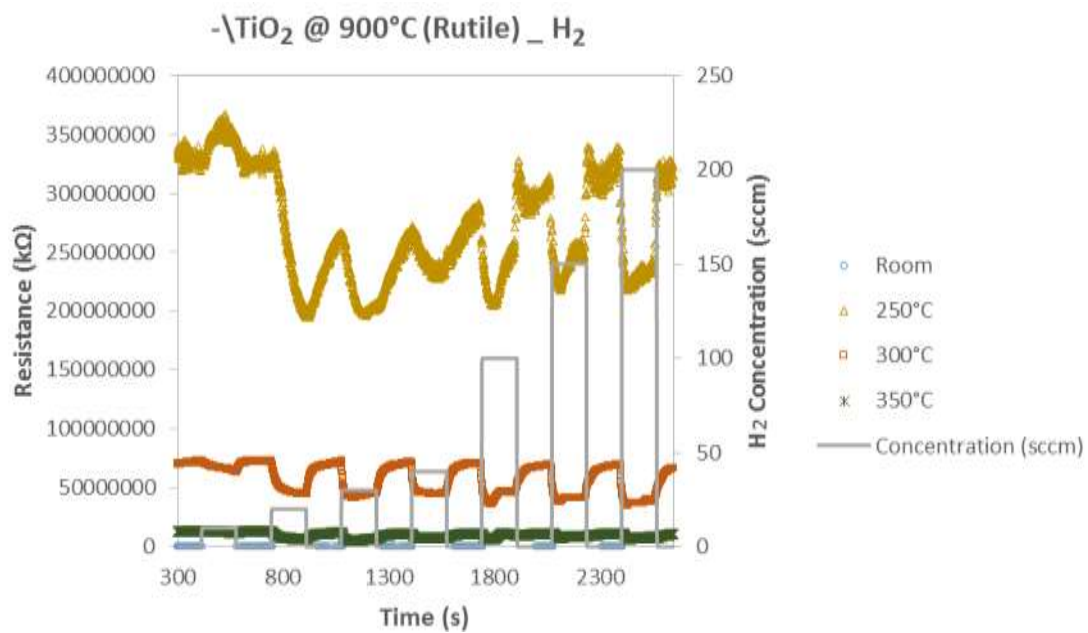
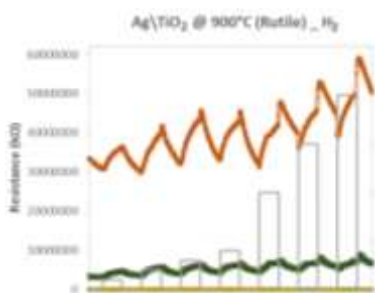


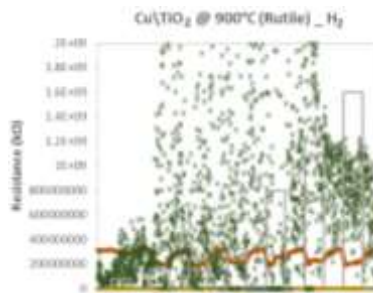
Figure 68: The dynamic responses of prepared gas sensors based on rutile TiO₂ nanopowders (annealed at 900°C), when exposed to various H₂ concentrations at different room temperatures. (a) Room temperature, (b) 250°C, (c) 300°C and (d) 350°C.



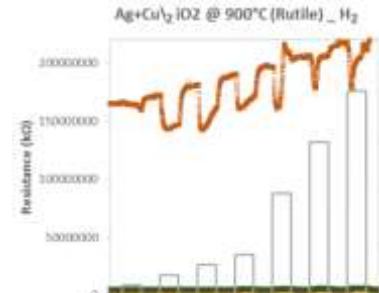
(a)



(b)



(c)



(d)

Figure 69: The dynamic response of prepared gas sensors based on rutile TiO_2 nanopowders (annealed at 900°C), when exposed to various concentrations of H_2 at room temperature, 250°C , 300°C and 350°C . (a) Undoped TiO_2 , (b) AgTiO_2 , (c) CuTiO_2 and (d) $\text{Ag}+\text{Cu}\text{TiO}_2$.

Table 20: Performance data of the rutile TiO₂ samples that were exposed to various concentrations of H₂ at different temperatures.

Gas: H ₂ Crystallographic Structure: Rutile						
Sample	Temperature (°C)	Gas Concentration (sccm)	Sensitivity	Response Time (s)	Recovery Time (s)	Fractional Baseline Drift (%)
-TiO ₂ @ 900°C (Rutile)	Room	10	9.15E+09	59.37	227.68	0.59
		20	9.5E+09	1.8	142.2	
		30	9.91E+09	23.39	111.6	
		40	9.85E+09	7.2	135.01	
		100	9.37E+09	24.3	429.98	
		150	8.06E+09	80.96	607.16	
		200	8.73E+09	5.4	228.47	
Ag\TiO ₂ @ 900°C (Rutile)	Room	10	-438.68	1.8	113.38	227.42
		20	-691.05	1.8	233.98	
		30	-384	1.8	333.94	
		40	-6326.43	1.8	126.01	
		100	-818.35	1.8	325.75	
		150	-1115.57	1.8	153.02	
		200	-4E+10	1.8	215.09	
Cu\TiO ₂ @ 900°C (Rutile)	Room	10	626.2	1.79	393.4	25.46
		20	628.69	1.79	143.47	
		30	-238.97	5.28	127.28	
		40	-1749.5	1.98	330.49	
		100	174.33	1.79	86.03	
		150	-44530.6	1.79	216.85	
		200	926.55	1.79	450.74	
Ag+Cu\TiO ₂ @ 900°C (Rutile)	Room	10	-345.87	1.89	90.42	542.14
		20	4711.79	1.82	218.63	
		30	394.44	1.79	440.04	
		40	-1709.14	2.7	210.59	
		100	15.78	1.8	475.92	
		150	393.13	1.85	139.79	
		200	0.06	1.74	214.17	
-TiO ₂ @ 900°C (Rutile)	250°C	10	0.09	5.49	292.25	0.82
		20	0.35	3.6	125.04	
		30	0.36	3.6	302.25	
		40	0.29	197.91	172.7	
		100	0.61	303.27	345.53	
		150	0.56	165.59	415.79	
		200	0.59	211.45	367.17	
Ag\TiO ₂ @ 900°C (Rutile)	250°C	10	9.96E+09	99.02	98.14	-1.84
		20	9.98E+09	1.79	307	
		30	9.93E+09	1.8	199.89	
		40	9.94E+09	1.78	282.71	
		100	9.97E+09	1.8	162.07	
		150	9.96E+09	19.81	239.45	
		200	9.88E+09	1.86	231.3	

Cu\TiO ₂ @ 900°C (Rutile)	250°C	10	-456.29	21.5	160.44	2142.29
		20	-104.42	1.72	585.9	
		30	-2265.32	1.84	199.72	
		40	-2598.09	1.79	705.05	
		100	-467.98	1.87	402.13	
		150	-292.71	1.89	231.03	
		200	-2.5E+10	5.67	212.92	
Ag+Cu\TiO ₂ @ 900°C (Rutile)	250°C	10	99.63	7.17	162.22	-6.06
		20	97	110.24	93.2	
		30	261.08	3.58	202.5	
		40	96.58	48.39	328.87	
		100	-463.67	3.58	109.32	
		150	96.58	5.37	104.87	
		200	5.07E+12	57.33	236.62	
-TiO ₂ @ 900°C (Rutile)	300°C	10	0.14	770.34	157.49	-4.53
		20	0.61	279.08	349.93	
		30	0.71	153.89	407.65	
		40	0.6	201.6	391.52	
		100	0.91	206.94	368.96	
		150	0.82	227.69	402.27	
		200	0.97	190.78	404.98	
Ag\TiO ₂ @ 900°C (Rutile)	300°C	10	0.2	279.88	344.67	45.15
		20	0.4	251.96	350.06	
		30	0.44	251.09	350.08	
		40	0.38	269.08	340.17	
		100	0.54	291.59	314.08	
		150	0.47	286.16	312.31	
		200	0.51	305.99	#N/A	
Cu\TiO ₂ @ 900°C (Rutile)	300°C	10	0.17	82.38	422.68	0.46
		20	0.62	292.93	254.34	
		30	0.71	184.53	368.29	
		40	0.55	154.85	431.83	
		100	0.7	169.27	434.5	
		150	0.61	152.28	114.67	
		200	0.71	122.86	251.6	
Ag+Cu\TiO ₂ @ 900°C (Rutile)	300°C	10	0.08	1.7	413	26.69
		20	0.29	260.7	221.3	
		30	0.34	143.32	357.47	
		40	0.24	206.06	354.78	
		100	0.3	239.21	346.78	
		150	0.23	267.07	124.56	
		200	0.26	128.4	139.52	
-TiO ₂ @ 900°C (Rutile)	350°C	10	0.1	34.21	378.12	-10.12
		20	0.8	362.8	281	
		30	1.03	185.35	426.74	
		40	0.53	167.45	454.62	
		100	0.68	165.65	106.21	
		150	0.44	137.73	314.2	
		200	232.8	50.4	549.17	

Ag\TiO ₂ @ 900°C (Rutile)	350°C	10	0.47	261.98	375.48	48.18
		20	0.62	232.23	378.09	
		30	0.6	228.66	373.61	
		40	0.56	246.77	190.75	
		100	0.67	464.57	305.17	
		150	0.7	294.38	310.59	
		200	11390.18	282.68	1.89	
Cu\TiO ₂ @ 900°C (Rutile)	350°C	10	20.97	7.17	410.3	48.18
		20	6.96E+09	132.58	297.42	
		30	8.23E+09	17.03	146.02	
		40	8.45E+11	41.21	360.99	
		100	-4.2E+09	7.16	232.98	
		150	4.89E+09	7.07	150.45	
		200	9.7	1.81	177.34	
Ag+Cu\TiO ₂ @ 900°C (Rutile)	350°C	10	0.15	103.06	58.24	285.99
		20	0.05	71.68	303.83	
		30	0.03	95.9	430.15	
		40	0.04	67.21	179.23	
		100	0.11	19.72	241.95	
		150	0.15	153.24	345.9	
		200	2244.59	146.98	143.38	

6.4.3 Performance of Anatase versus Rutile TiO₂ under NH₃

The rutile samples continue to display responses that, collectively, is below par when compared with that of the anatase counterpart. If the temperature limitation of 300°C is not an inhibiting factor, the undoped TiO_2 rutile powder will be suitable as a sensor material for H₂. The single-doped Cu-impregnated sample (Cu\TiO₂) comes in next. To cover the entire range from “Room” to 350°C, the only sample that can be utilised is the undoped TiO_2 .

6.5 DISCUSSION

It is the concern of this chapter to attempt to demonstrate the advantage of single or double doping of TiO₂ nanoparticles with Ag and Cu, if any, in gas sensing applications. Given the high impedances that is normally registered by TiO₂, in the presence of the interacting gases, conductivity improvements are important for proposing the semiconductor as a remarkable candidate base material for gas sensing.

Broadly, (in over 75% of the cases), the gas-sensing results presented here show that the sol-gel fabricated TiO₂ nanoparticles (particularly in anatase form), has excellent fast and stable dynamic responses to humidity, NH₃ and H₂. They feature good sensitivities, even at a low operating temperatures. However, the recovery of the signal was generally not complete when the air flux is restored within 5 minutes following the gas injection.

The more pronounced gas sensing abilities observed for the anatase TiO₂ over the rutile, can be ascribed to the morphological characteristics of the two material categories [305]. As evident from Table 10 of Section 4.4, anatase TiO₂ is characterised by a smaller crystallite sizes relative to the rutile powders. This implies higher surface area to volume ratio for anatase and consequently, a greater surface activity over rutile [305].

For the majority of samples tested, the measured resistances decrease upon interacting with the reducing gases – a typical behaviour for *n*-type semiconductors. This is because, the gases act as a reducing agent for the metal-oxide [306]. The process involves the extraction of electrons from its conduction band by the adsorbed oxygen species at the surface of the semiconductor [306]. In other words, the chemisorbed oxygen species trap free electrons on the surface of the grains which results in a build-up of a negative surface charge [306]. This in turn creates an energetic barrier in the conduction band which electrons must overcome in order to cross to the next grain. When the desired concentration of the target gas is introduced, the gas then reacts with the adsorbed oxygen. This leads to the freeing of previously trapped electrons (i.e. a reduction in the amount of bound surface charge), thereby decreasing the *n*-type carrier content and lowering the barrier potential. Thus, the resistivity decreases in the presence of a reducing gas, owing to electron transfer into the conduction band [306].

However, acceptor behaviour, for which there was a conductivity switch from *n*-type to *p*-type [307], was recorded for the Ag-doped rutile samples (Ag\TiO₂) at operating temperatures of 300°C and 350°C. In these cases, it is believed that the Ag dopant impurities modify the electronic structure of TiO₂ and form localised acceptor levels in the forbidden band gap [308]. This leads to the increase in the electron concentration and the decrease in the electrical resistance over a low-to-medium

temperature range [308]. The discussion here is only qualitative since generally, the energetic barrier is not constant but changes with varying temperature [306], thereby rendering the temperature dependencies more complicated.

It is worth mentioning here, that a metal oxide can adsorb oxygen from the atmosphere both as the O^{2-} and O^- species. The adsorption of O^- is more reactive and thus makes the material more sensitive to the presence of a reducing gas [309]. Now at relatively low temperatures the surface preferentially adsorbs O^{2-} and the sensitivity of the material is consequently low. As the temperature increases the dominant process becomes the adsorption of O^- thereby increasing the sensitivity of the material. As the temperature increase becomes large enough, the desorption of all the previously adsorbed oxygen ionic species occurs, thus decreasing the sensitivity [309].

In a quest to determine the sample with best overall performance for each intervening gas, and at each of the four operating temperatures, the performances indices were combined and ranked in

Table 21. Here, samples that exhibit acceptor (p -type conduction) behaviour are marked “▣”, while those that do not display a stable and reproducible response to all gas concentrations are marked “‡”. According to these estimates, to sense water vapour (at room temperature) the anatase $Cu\backslash TiO_2$ comes out on top. NH_3 and H_2 are best detected using undoped rutile $\backslash TiO_2$, for temperatures ranging from “Room” to $350^\circ C$ and probably beyond. Where specific operating temperatures (except at temperatures exceeding $300^\circ C$) are required in applications, the anatase powders remains generally preferred. Otherwise, the rutile samples may come into play. It is also important to note that only one of the two brookite-bearing samples was available for gas-sensing investigations, that is, the double-doped $Ag+Cu\backslash TiO_2$ sample that was annealed at $300^\circ C$. This sample showed better promise in detecting water-vapour, NH_3 and H_2 at various temperatures over other powders.

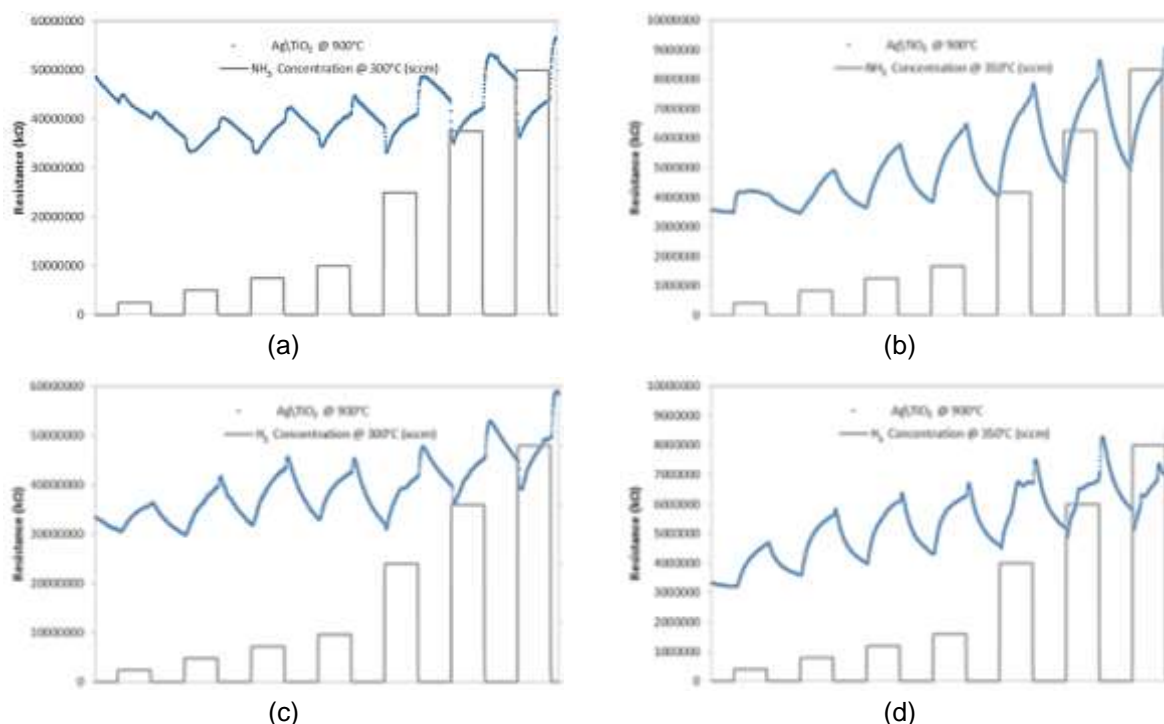


Figure 70: Acceptor behaviour recorded for Ag-doped samples (Ag/TiO₂) when exposed to intervening gases (a) NH₃ at 300°C, (b) NH₃ at 350°C, (c) H₂ at 300°C and (d) H₂ at 350°C

Table 21: A ranking of the overall performances of the TiO₂ sensor materials tested in the presence of humidity, NH₃ and H₂ at various operating temperatures.

Gas	Powder Phase	Operating Temperature	Rank			
			1 st	2 nd	3 rd	4 th
Humidity	Anatase	Room	Cu	Ag+Cu	-	Ag
	Rutile	Room	Ag	-	Cu [‡]	Ag+Cu [‡]
NH ₃	Anatase	Room	Cu	Ag+Cu	Ag	-
		250°C	-	Ag	Cu	Ag+Cu [‡]
		300°C	Cu	-	Ag	Ag+Cu
		350°C	Not available			
	Rutile	Room	-	Ag [‡]	Cu [‡]	Ag+Cu [‡]
		250°C	-	Ag [‡]	Cu [‡]	Ag+Cu [‡]
		300°C	-	Ag+Cu	Cu	Ag [Ⓜ]
		350°C	Ag+Cu	-	Ag [Ⓜ]	Cu [‡]
H ₂	Anatase	Room	Ag+Cu	-	Cu	Ag
		250°C	Ag	-	Cu	Ag+Cu
		300°C	Ag	-	Cu	Ag+Cu
		350°C	Not available			
	Rutile	Room	- [‡]	Ag [‡]	Cu [‡]	Ag+Cu [‡]
		250°C	-	Ag [‡]	Cu [‡]	Ag+Cu [‡]
		300°C	Cu	Ag+Cu	-	Ag [Ⓜ]
		350°C	Ag [Ⓜ]	-	Ag+Cu	Cu [‡]

[‡]No stable repeatable pattern found [Ⓜ]Acceptor behaviour

**SUMMARY,
RECOMMENDATIONS,
CONCLUSION**

7.1 INTRODUCTION

This study started out to investigate how the structural, optical and gas-sensing properties of TiO₂ nanopowders are affected when Ag and Cu are combined as a dopant for the TiO₂ host. These two metal impurities are known to enhance the performance of TiO₂-based devices individually. The objectives include synthesising doped titania nanoparticles so as to employ characterisation techniques that would aid the understanding of the parameters that inhibit or promote phase formation in TiO₂. It was also desired to investigate the performance of nanosized TiO₂ in photocatalysis and gas sensing applications. It was anticipated that the simultaneous introduction of two metal impurities into titania nanostructures will result in improved performance over single-element doping.

7.2 RESEARCH DESIGN AND METHOD

The research paradigm for this study comprised of synthesis (in which doped and undoped samples were prepared), characterisation (which involved subjecting the synthesised samples to a variety of analytical techniques), and application (where the nanopowders are tested for their suitability in gas sensing).

7.3 LIMITATIONS OF THE STUDY

As expected, this research and its scope had limited resources such as equipment, funds and time. Even though other possibilities exist, the scope was restricted to investigating the properties of titania nanoparticles that have been doped with Ag and Cu singly, as well as simultaneously.

Only the sol-gel sample preparation route was used and the purity of precursor materials was limited to what was commercially available. Dopant levels were also restricted to 5 wt%. Further, annealing temperatures were chosen so as to indicate ranges at which the phase transformation of TiO₂ occurred.

7.4 OVERVIEW OF RESEARCH FINDINGS

7.4.1 Structural Properties

In addition to identifying the different phases of TiO_2 , XRD further revealed grain growth inhibition in the anatase structures through doping. Cu impurities were observed to reduce the temperature at which anatase TiO_2 transforms to rutile, while the combination of Ag and Cu as dopants goes even further in lowering this temperature. The double-doped powders also revealed the existence of a brookite phase between the annealing temperatures of 300°C and 600°C . Grain sizes deduced from SEM micrographs confirmed increases with increasing annealing temperature.

7.4.2 Optical Properties

For the double-doped $\text{Ag+Cu}\backslash\text{TiO}_2$ samples that were annealed at 300°C and at 600°C , UV-Vis spectroscopy registered a red-shift towards a lower energy band gap which falls squarely within the visible region of the solar radiation spectrum. This ensures a better light absorption in the visible-light range in comparison with other powders.

On the other hand, photoluminescence investigations favoured the creation of exciton energy levels which subsequently led to higher PL signals.

7.4.3 Electrical Properties

Even though not all synthesised powders could be tested in this work, the double-doped $\text{Ag+Cu}\backslash\text{TiO}_2$ sample (annealed at 300°C) showed good promise in detecting water-vapour and the other two reducing gases, NH_3 and H_2 , at various operating temperatures ranging from “Room” to 350°C .

7.5 CONCLUSIONS

Through XRD, the initial analyses in this study verified that the sol-gel method of synthesis used yielded the desired products. Doping generally reduced the grain size of titania but did not deform the anatase lattice. The rutile cell volume however shrunk by 36%. The crystallite sizes of the double-doped species ($\text{Ag+Cu}\backslash\text{TiO}_2$) were found to be substantially greater than those of the single-doped samples. This difference in sizes may be attributed to dopants being incorporated into the TiO_2 matrix rather than distributed over the surface, as was the case with single-doped samples. It was also found that doping TiO_2 with Ag has little or no effect on the anatase-to-rutile transformation temperature whereas Cu impurities reduce it. Double doping with Ag and Cu further reduces the transition temperature.

The crystallisation of the brookite phase of titania was achieved at lower temperatures (less than 300°C) through the introduction of multiple dopants into the TiO_2 structure. In contrast to single doping, double-doping of TiO_2 favoured two-phase structures (anatase-brookite at 300°C and brookite-rutile at 600°C). The rate of anatase to rutile transformation is also much faster than the brookite to rutile one. The existence of brookite is believed to be responsible for the anatase to rutile transformation enhancement.

In Raman analysis, Cu as an impurity was also able to introduce a blue-shift towards higher energies in the E_g mode as a result of phonon confinement.

$\text{Ag+Cu}\backslash\text{TiO}_2$, double doped powders annealed at 300°C and at 600°C (i. e. the samples that incorporated the brookite phase) also brought about substantial photo-absorption improvements over other samples by reducing the energy band gap (595 and 624 nm respectively) well into the visible region of the electromagnetic spectrum. With this, higher photocatalytic efficiencies, resulting from greater production of electron-hole pairs under visible light illumination, can be achieved.

The brookite-bearing double-doped $\text{Ag+Cu}\backslash\text{TiO}_2$ sample that was annealed at 300°C also showed better promise in detecting water-vapour, NH_3 and H_2 at various temperatures as compared with other powders. However, though the $\text{Ag+Cu}\backslash\text{TiO}_2$ sample that was annealed at 600°C was not available for gas-sensing investigations,

it is expected that it will also reveal exceptional gas-detection properties because of the presence of the brookite phase in its structures.

7.6 RECOMMENDATIONS/FUTURE WORK

Although synthetic methods, other than sol-gel route, are not expected to lead to any substantially different conclusions, it may be worthwhile to investigate the effects of procedures such as hydrothermal and vapour deposition methods on properties of titania.

In this study, dopant levels were also restricted to 5 wt%, except in the case of the double-doped $\frac{1}{2}\text{Ag}+\text{Cu}\backslash\text{TiO}_2$, in which the additional samples with dopant concentrations of 2.5 wt% were prepared in order to have a closer look at the presence of the brookite phase. Since the possibility of a different outcome at other dopant levels may not be ruled out, investigating doped TiO_2 at lower dopant concentration may also be considered in future.

Aside from Ag and Cu, other metal impurities (Fe, Pd, Pt...), have also been found to independently improve the properties of titania. Combining two (or even three) of them as impurities in TiO_2 may be the subject of future investigations.

Quantitative studies, which may attempt to identify the exact phase transformation temperatures of the TiO_2 nanopowders may also be embarked upon. In this case, annealing temperatures will have to be finely chosen.

Finally, the response of the TiO_2 nanomaterials to NH_3 and H_2 presented in this work serves as a case study for reducing gases. Analysing the detection of oxidising gases may also be explored in future. Due to time and funding constraints, not all samples could be tested for gas detection. To confirm the superiority of the double-doped $\text{Ag}+\text{Cu}\backslash\text{TiO}_2$ in responding to gases, more samples would be put to test. This way, the conversion of TiO_2 from its *n*-type behaviour to *p*-type may be further investigated.

7.7 CONTRIBUTIONS OF THE STUDY

An advanced understanding of the parameters that determine phase formation is crucial for the successful technological application of nanomaterials. TiO₂ nanomaterials play an important role in the protection of the environment and in the search for greener energy technologies. The present study serves to illuminate the understanding of the fundamentals and working principles of nanosized TiO₂-based devices. This will facilitate further improvement of current and practical titania nanotechnology. Greater insights will therefore be gained into phase formation mechanisms. This work has also shed some light on the gas-sensing behaviour of doped titania. All-in-all, it will further enhance the understanding of the structural, thermal, electronic, and optical properties of titania nanomaterials and promote on-going interest in TiO₂-based research and technological applications.

REFERENCES

- [1] S. D. Mo and W. Y. Ching, "Electronic structure and optical properties of the three phases of TiO₂: Rutile, anatase and brookite," *Phys. Rev.*, vol. B51, no. 19, p. 13023 – 13032, 1995.
- [2] J. G. Yu, J. C. Yu, B. Cheng, S. Hark and K. lu, "The effect of F--doping and temperature on the structural and textural evolution of mesoporous TiO₂ powders," *J. Solid State Chem.*, vol. 174, p. 372 – 380, 2003.
- [3] A. Beltran, L. Gracia and J. Andres, "Density functional theory study of the brookite surfaces and phase transitions between natural titania polymorphs," *J. Phys. Chem.*, vol. B, no. 110, p. 23417 – 23423, 2006.
- [4] D. A. H. Hanaor and C. C. Sorrell, "Review of the anatase to rutile phase transformation," *J. Mater. Sci.*, vol. 46, p. 855 – 874, 2011.
- [5] H. Shin, H. S. Jung, K. S. Hong and J. K. Lee, "Crystal phase evolution of TiO₂ nanoparticles with reaction time in acidic solutions studied via freeze-drying method," *J. Solid State Chem.*, vol. 178, p. 15 – 21, 2005.
- [6] Q. Sheng, Y. Cong, S. Yua, J. Zhang and M. Anpo, "Synthesis of bi-porous TiO₂ with crystalline framework using a double surfactant system," *Microporous Mesoporous Mater.*, vol. 95, p. 220 – 225, 2006.
- [7] G. Pfaff and P. Reynders, "Angle-Dependent Optical Effects Deriving from Submicron Structures of Films and Pigments," *Chem. Rev.*, vol. 99, p. 1963, 1999.
- [8] A. Salvador, M. C. Pascual-Marti, J. R. Adell, A. Requeni and J. G. March, "Analytical methodologies for atomic spectrometric determination of metallic oxides in UV sunscreen creams," *J. Pharm. Biomed. Anal.*, vol. 22, p. 301, 2000.
- [9] R. Zallen and M. P. Moret, "The optical absorption edge of brookite TiO₂," *Solid State Commun.*, vol. 137, pp. 154-157, 2006.

- [10] J. H. Braun, A. Baidins and R. E. Marganski, "TiO₂ pigment technology: A review," *Prog. Org. Coat.*, vol. 20, p. 105, 1992.
- [11] S. A. Yuan, W. H. Chen and S. S. Hu, "Fabrication of TiO₂ nanoparticles-surfactant polymer complex film on glassy carbon electrode and its application to sensing trace dopamine," *Mater. Sci. Eng. C*, vol. 25, p. 479, 2005.
- [12] X. Chen and S. S. Mao, "Titanium Dioxide Nanomaterials: Synthesis, Properties, Modifications, and Applications," *Chem. Rev.*, vol. 107, no. 7, pp. 2891 - 2959, 2007.
- [13] A. Hagfeldt and M. Grätzel, "Light-induced Redox Reactions in Nanocrystalline Systems," *Chem. Rev.*, vol. 95, p. 49, 1995.
- [14] A. Millis and S. J. Le Hunte, "An Overview of Semiconductor Photocatalysis," *Photochem. Photobiol. A*, vol. 1, p. 108, 1997.
- [15] A. P. Alivisatos, "Perspectives on the physical chemistry of semiconductor nanocrystals," *J. Phys. Chem.*, vol. 100, no. 31, p. 13226–13239, 1996.
- [16] X. Chen, Y. Lou, S. Dayal, X. Qiu, R. Krolicki, C. Burda, C. Zhao and J. Becker, "Doped semiconductor nanomaterials," *Nanosci. Nanotechnol.*, vol. 5, no. 9, pp. 1408-1420, 2005.
- [17] M. Grätzel, "Conversion of sunlight to electric power by nanocrystalline dye-sensitized solar cells," *J. Photochem. Photobiol., A*, vol. 164, pp. 3-14, 2004.
- [18] M. Grätzel, "Dye-Sensitized Solid-State Heterojunction Solar Cells," *MRS Bull.*, vol. 30, pp. 23-27, 2005.
- [19] P. Yang, C. Lu, N. Hua and Y. Du, "Titanium dioxide nanoparticles co-doped with Fe³⁺ and Eu³⁺ ions for photocatalysis," *Mater. Lett.*, vol. 57, p. 794 – 801, 2002.
- [20] J. Colmenares, M. Aramendia, A. Marinas, J. Marinas and F. Urbano, "Synthesis, characterization and photocatalytic activity of different metal-doped

- titania systems,” *Appl. Catal.*, vol. A: General, no. 306, p. 120 – 127, 2006.
- [21] K. Loganathan, P. Bommusamy, P. Muthaiahpillai and M. Velayutham, “The syntheses, characterizations, and photocatalytic activities of silver, platinum, and gold doped TiO₂ nanoparticles,” *Environ. Eng. Res.*, vol. 16, no. 2, p. 81 – 90, 2011.
- [22] M. Grätzel, “Photoelectrochemical cells,” *Nature*, vol. 414, p. 338 –344, 15 Nov 2001.
- [23] R. Asahi, T. Morikawa, T. Ohwaki, K. Aoki and Y. Taga, “Visible-Light Photocatalysis in Nitrogen-Doped Titanium Oxides,” *Science*, vol. 293, p. 269 – 271, 2001.
- [24] W. Choi, A. Termin and M. Hoffmann, “The role of metal ion dopants in quantum-sized TiO₂: Correlation between photoreactivity and charge carrier recombination dynamics,” *J. Phys. Chem.*, vol. 98, p. 13669 – 13679, 1994.
- [25] E. Borgarello, J. Kiwi, M. Grätzel, E. Pelizzetti and M. Visca, “Visible light induced water cleavage in colloidal solutions of chromium-doped titanium dioxide particles,” *J. Am. Chem. Soc.*, vol. 104, p. 2996 – 3002, 1982.
- [26] M. Anpo and M. Takeuchi, “The design and development of highly reactive titanium oxide photocatalysts operating under visible light irradiation,” *J. Catal.*, vol. 216, p. 505 – 516, 2003.
- [27] L. Liu, S. Chen, W. Sun and J. Xin, “Enhancing the visible light absorption via combinational doping of TiO₂ with nitrogen (N) and chromium (Cr),” *J. Mol. Struct.*, vol. 1001, p. 23 – 28, 2011.
- [28] H. Yamashita, Y. Ichihashi, M. Takeuchi, S. Kishiguchi and M. Anpo, “Characterization of metal ion-implanted titanium oxide photocatalysts operating under visible light irradiation,” *Synchrotron Radiat.*, vol. 6, pp. 451-452, 1999.
- [29] M. Takeuchi and M. Anpo, “TiO₂ Nanoparticles - Photocatalytic Oxidation,” *J.*

Photoenergy, vol. 3, pp. 1-6, 2001.

- [30] D. Chen, Z. Jiang, J. Geng, Q. Wang and D. Yang, "Carbon and nitrogen co-doped TiO₂ with enhanced visible-light photocatalytic," *Ind. Eng. Chem. Res.*, vol. 46, p. 2741 – 2746, 2007.
- [31] H. Klug and L. Alexander, "X-ray diffraction procedures for polycrystalline and amorphous materials," *J. Appl. Crystallogr.*, vol. 8, p. 573 – 574, 1975.
- [32] R. Zallen and M. P. Moret, "The optical absorption edge of brookite TiO₂," *Solid State Commun.*, vol. 137, pp. 154-157, 2006.
- [33] K. Siwińska-Stefańska, A. Krysztafkiewicz, F. Ciesielczyk, D. Paukszta, J. Sójka-Ledakowicz and T. Jesionowski, "Physicochemical and Structural Properties of TiO₂ Precipitated in an Emulsion System," *Physicochem. Probl. Miner. Process.*, vol. 44, pp. 231-244, 2010.
- [34] M. Mahalakshmi, B. Arabindoo, M. Palanichamy and V. Murugesan, "Photocatalytic degradation of carbofuran using semiconductor oxides," *J Hazard Mater.*, vol. 143, pp. 240-245, 2007.
- [35] M. Abu Tariq and M. Faisal, "Semiconductor-mediated photocatalysed degradation of two selected azo dye derivatives, amaranth and bismarck brown in aqueous suspension," *J Hazard Mater.*, vol. 127, pp. 172-179, 2005.
- [36] J. C. Yu, Y. Xie, H. Y. Tang, L. Zhang, H. C. Chan and J. Zhao, "Visible light-assisted bactericidal effect of metalphthalocyanine-sensitized titanium dioxide films," *J Photochem Photobiol, A: Chem.*, vol. 156, pp. 235-241, 2003.
- [37] R. L. Penn and J. F. Banfield, "Morphology development and crystal growth in nanocrystalline aggregates under hydrothermal conditions: Insights from titania," *Geochim. Cosmochim. Acta*, vol. 63, no. 10, p. 1549 –1557, 1999.
- [38] G. Oskam, A. Nellore, R. L. Penn and P. C. Searson, "The growth kinetics of TiO₂ nanoparticles from titanium (IV) alkoxide at high water/titanium ratio," *J. Phys. Chem. B*, vol. 107, no. 8, p. 1734 – 1738, 2003.

- [39] D. Reyes-Coronado, G. Rodríguez-Gattorno, M. E. Espinosa-Pesqueira, C. Cab, R. de Coss and G. Oskam, "Phase-pure TiO₂ nanoparticles: Anatase, brookite and rutile," *Nanotechnology*, vol. 19, no. 145605, p. 1 – 10, 2008.
- [40] X. Nie, S. Zhuo, G. Maeng and K. Sohlberg, "Doping of TiO₂ polymorphs for altered optical and photocatalytic properties," *Int. J. Photoenergy*, vol. 2009, no. 294042, p. 1 – 22, 2009.
- [41] H. Zhang and J. F. Banfield, "Understanding polymorphic phase transformation behavior during growth of nanocrystalline aggregates: Insights from TiO₂," *J. Phys. Chem. B*, vol. 104, no. 15, p. 3481 – 3487, 2000.
- [42] Y. Hu, H. L. Tsai and C. L. Huang, "Effect of brookite phase on the anatase-rutile transition in titania nanoparticles," *J. Eur. Ceram. Soc.*, vol. 23, p. 691 – 696, 2003.
- [43] S. Bakardjieva, V. Stengl, L. Szatmary, J. Subrt, J. Lukac, N. Murafa, D. Niznansky, K. Cizek, J. Jirkovsky and N. Petrova, *J. Mater. Chem.*, vol. 16, p. 1709 – 1716, 2006.
- [44] W. Krastchmer, L. D. Lamb, K. Fostiropoulos and D. R. Huffman, "Solid C60: A new form of carbon," *Nature*, vol. 347, pp. 354-358, 1990.
- [45] S. Iijima, "Helical microtubules of graphitic carbon," *Nature*, vol. 354, pp. 56-58, 1991.
- [46] C. T. Kresge, M. E. Leonowicz, W. J. Roth, J. C. Vartulli and J. S. Beck, "Ordered mesoporous molecular sieves synthesized by a liquid-crystal template mechanism," *Nature*, vol. 359, pp. 710-712, 1992.
- [47] A. Z. Sadek, "Investigation of Nanostructured Semiconducting Metal Oxide and Conducting Polymer Thin Films for Gas Sensing Applications," RMIT University, Melbourne, Australia, Ph.D. dissertation, 2008.
- [48] A. Z. Sadek, S. Choopun, W. Wlodarski, S. J. Ippolito and K. Kalantar-zadeh, "Characterization of ZnO nanobelt based gas sensor for H₂, NO₂ and

- hydrocarbon sensing," *IEEE Sensors J.*, vol. 7, no. 6, pp. 919 - 924, 2007.
- [49] S. R. Morrison, "Semiconductor gas sensors," *Sens. Act. B: Chem.*, vol. 2, pp. 329 - 341, 1982.
- [50] Y. Xia, P. Yang, Y. Sun, Y. Wu, B. Mayers, B. Gate, Y. Y. F. Kim and H. Yan, "One dimensional nanostructures: Synthesis, characterization, and applications," *Adv. Mater.*, vol. 15, pp. 353 - 389, 2003.
- [51] A. Zaleska, "Doped-TiO₂: A review," *Recent Pat. Eng.*, vol. 2, no. 3, p. 157 – 164, 2008.
- [52] D. P. Macwan, P. N. Dave and S. Chaturvedi, "A review on nano-TiO₂ sol–gel type syntheses and its applications," *J. Mater. Sci.*, vol. 46, p. 3669 – 3686, 2011.
- [53] Y. L. Hewakuruppu, L. A. Dombrovsky, C. Chen, V. Timchenko, X. Jiang, S. Baek and R. A. Taylor, "Plasmonic "pump–probe" method to study semi-transparent nanofluids," *Appl. Optics*, vol. 52, no. 24, p. 6041 – 6050, 2013.
- [54] R. A. Taylor, T. Robert and G. Rosengarten, "Nanofluid-based optical filter optimization for PV/T systems," *Light: Science & Applications*, vol. e34, no. 10, pp. 1 - 7, 2012.
- [55] R. A. Taylor., P. E. Phelan, T. P. Otanicar., R. Adrian and R. Prasher, "Nanofluid optical property characterization: Towards efficient direct absorption solar collectors," *Nanoscale Res. Lett.*, vol. 6, no. 1, p. 225, 2011.
- [56] "Nanoparticle - Wikipedia, the free encyclopedia," Wikipedia, 2009. [Online]. Available: <http://en.wikipedia.org/wiki/Nanoparticle>. [Accessed 4 December 2014].
- [57] A. I. Gusev and V. V. Ivanov, "Nanopowder," Rusnano, 2011. [Online]. Available: <http://eng.thesaurus.rusnano.com/wiki/article1339>. [Accessed 3 December 2014].

- [58] L. X. Chen, T. Rajh, W. Jager, J. Nedeljkovic and M. C. Thurnauer, "X-ray absorption reveals surface structure of titanium dioxide nanoparticles," *J. Synchrotron Radiat.*, vol. 6, p. 445, 1999.
- [59] X. Qian, D. Qin, Q. Song, Y. Bai, T. Li, X. Tang and E. Wang, "Surface photovoltage spectra and photoelectrochemical properties of semiconductor-sensitized nanostructured TiO₂ electrodes," *Thin Solid Films*, vol. 385, no. 1, pp. 152-161, 2001.
- [60] S. Hamad, C. R. A. Catlow, S. M. Woodley, S. Lago and J. Mejias, "Structure and stability of small TiO₂ nanoparticles," *J. Phys. Chem. B*, vol. 109, no. 33, pp. 15741-15748, 2005.
- [61] V. Swamy, A. Kuznetsov, L. S. Dubrovinsky, R. A. Caruso, D. G. Shchukin and B. C. Muddle, "Finite-Size and Pressure Effects on the Raman Spectrum of Nanocrystalline Anatase TiO₂," *Phys. Rev. B*, vol. 71, p. 184302/1, 2005.
- [62] A. S. Barnard and L. A. Curtiss, "Prediction of TiO₂ Nanoparticle Phase and Shape Transitions Controlled by Surface Chemistry," *Nano Lett.*, vol. 5, p. 1261, 2005.
- [63] A. S. Barnard, P. Zapol and L. A. Curtiss, "Anatase and rutile surfaces with adsorbates representative of acidic and basic conditions," *Surf. Sci.*, vol. 582, p. 173, 2005.
- [64] A. S. Barnard and P. Zapol, "Effects of particle morphology and surface hydrogenation on the phase stability of TiO₂," *Phys. Rev. B*, vol. 70, p. 235403/1, 2004.
- [65] A. S. Barnard, P. Zapol and L. A. Curtiss, "Modeling the morphology and phase stability of TiO₂ nanocrystals in water," *J. Chem. Theory Comput.*, vol. 1, pp. 107-116, 2005.
- [66] A. S. Barnard and P. Zapol, "Predicting the energetics, phase stability, and morphology evolution of faceted and spherical anatase nanocrystals," *J. Phys. Chem. B*, vol. 108, p. 18435, 2004.

- [67] A. N. Enyashin and G. Seifert, "Structure, stability and electronic properties of TiO₂ nanostructures," *Phys. Status Solidi B*, vol. 242, p. 1361, 2005.
- [68] H. Zhang and J. F. Banfield, "Thermodynamic analysis of phase stability of nanocrystalline titania," *J. Mater. Chem.*, vol. 8, p. 2073, 1998.
- [69] Y. Hwu, Y. D. Yao, N. F. Cheng, C. Y. Tung and H. M. Lin, "X-ray Absorption of Nanocrystal TiO₂," *Nanostruct. Mater.*, vol. 9, p. 355, 1997.
- [70] A. A. Gribb and J. F. Banfield, "Particle size effects on transformation kinetics and phase stability in nanocrystalline TiO₂," *Am. Mineral.*, vol. 82, p. 717, 1997.
- [71] X. Ye, J. Sha, Z. Jiao and L. Zhang, "Thermoanalytical characteristic of nanocrystalline brookite-based titanium dioxide," *Nanostruct. Mater.*, vol. 8, pp. 919-927, 1998.
- [72] H. Kominami, M. Kohno and Y. Kera, "Synthesis of brookite-type titanium oxide nano-crystals in organic media," *J. Mater. Chem.*, vol. 10, p. 1151, 2000.
- [73] M. R. Ranade, A. Navrotsky, H. Z. Zhang, J. F. Banfield, S. H. Elder, A. Zaban, P. H. Borse, S. K. Kulkarni, G. S. Doran and H. J. Whitfield, "Energetics of Nanocrystalline TiO₂," *Proc. Natl. Acad. Sci.*, vol. 99, p. 6476, 2002.
- [74] W. Li, C. Ni, H. Lin, C. P. Huang and S. I. Shah, "Size dependence of thermal stability of TiO₂ nanoparticles," *J. Appl. Phys.*, vol. 96, pp. 6663-6668, 2004.
- [75] T. Lindgren, J. M. Mwabora, E. Avendano, J. Jonsson, A. Hoel, C. G. Granqvist and S. E. J. Lindquist, "Photoelectrochemical and optical properties of nitrogen doped titanium dioxide films prepared by reactive DC magnetron sputtering," *Phys. Chem. B*, vol. 107, p. 5709, 2003.
- [76] J. I. Langford and A. J. C. Wilson, "A Survey and Some New Results in the Determination of Crystallite Size," *J. Appl. Cryst.*, vol. 11, pp. 102-113, 1978.
- [77] A. Monshi, M. R. Foroughi and M. R. Monshi, "Modified scherrer equation to estimate more accurately nano-crystallite size using XRD," *World J. Nano Sci.*

- Eng.*, vol. 2, pp. 154-160, 2012.
- [78] M. Niederberger, M. H. Bartl and G. D. Stucky, "Benzyl alcohol and titanium tetrachloride a versatile reaction system for the nonaqueous and low-temperature preparation of crystalline and luminescent titania nanoparticles," *Chem. Mater.*, vol. 14, no. 10, pp. 4364-4370, 2002.
- [79] Z. Zhang, X. Zhong, S. Liu, D. Li and M. Han, "Aminolysis route to monodisperse titania nanorods with tunable aspect ratio," *Angew. Chem., Int. Ed.*, vol. 44, p. 3466, 2005.
- [80] P. D. Cozzoli, A. Kornowski and H. J. Weller, "Low-temperature synthesis of soluble and processable organic-capped anatase TiO₂ nanorods," *Am. Chem. Soc.*, vol. 125, p. 14539, 2003.
- [81] C. S. Kim, B. K. Moon, J. H. Park, B. C. Choi and H. J. Seo, "Solvothermal synthesis of nanocrystalline TiO₂ in toluene with surfactant," *J. Cryst. Growth*, vol. 257, pp. 309-315, 2003.
- [82] L. H. Liang, C. M. Shen, X. P. Chen, W. M. Liu and H. J. Gao, "The size-dependent phonon frequency of semiconductor nanocrystals," *J. Phys.: Condens. Matter*, vol. 16, no. 3, p. 267-272, 2004.
- [83] A. Tanaka, S. Onari and T. Arai, "Low-frequency Raman scattering from CdS microcrystals embedded in a germanium dioxide glass matrix," *Phys. Rev. B*, vol. 47, pp. 1237-1243, 1993.
- [84] Y. Lei, L. D. Zhang and J. C. Fan, "Fabrication, characterization and Raman study of TiO₂ nanowire arrays prepared by anodic oxidative hydrolysis of TiCl₃," *Chem. Phys. Lett.*, vol. 338, no. 4, pp. 231-236, 2001.
- [85] W. F. Zhang, Y. L. He, M. S. Zhang, Z. Yin and Q. Chen, "Raman scattering study on anatase TiO₂ nanocrystals," *J. Phys. D*, Vols. 912-916, p. 33, 2000.
- [86] J. C. Parker and R. W. Siegel, "Raman microprobe study of nano-phase TiO₂ and oxidation-induced spectral changes," *J. Mater. Res.*, vol. 5, p. 1246, 1990.

- [87] J. C. Parker and R. W. Siegel, "Calibration of the raman spectrum to the oxygen stoichiometry of nanophase TiO₂," *Appl. Phys. Lett.*, vol. 57, pp. 943-945, 1990.
- [88] W. Ma, Z. Lu and M. Zhang, "Investigation of structural transformations in nanophase titanium dioxide by Raman spectroscopy," *Appl. Phys. A*, vol. 66, p. 621-627, 1998.
- [89] Z. Wang and S. K. Saxena, "Raman spectroscopic study on pressure-induced amorphization in nanocrystalline anatase (TiO₂)," *Solid State Commun.*, vol. 75-78, p. 118, 2001.
- [90] S. Kelly, F. H. Pollak and M. Tomkiewicz, "Raman Spectroscopy as a Morphological Probe for TiO₂ Aerogels," *J. Phys. Chem. B*, vol. 101, pp. 2730-2734, 1997.
- [91] H. C. Choi, Y. M. Jung and S. B. Kim, "Size effects in the Raman spectra of TiO₂ nanoparticles," *Vib. Spectrosc.*, vol. 37, pp. 33-38, 2005.
- [92] R. Asahi, Y. Taga, W. Mannstadt and A. J. Freeman, "Electronic and optical properties of anatase TiO₂," *Phys. Rev. B*, vol. 61, pp. 7459-7465, 2000.
- [93] P. I. Sorantin and K. Schwarz, "Electronic and optical properties of anatase TiO₂," *Inorg. Chem.*, vol. 31, p. 567, 1992.
- [94] Z. Y. Wu, G. Ouvrard, P. Gressier and C. R. Natoli, "Ti and O K edges for titanium oxides by multiple scattering calculations: Comparison to XAS and EELS spectra," *Phys. Rev. B*, vol. 55, p. 10382, 1997.
- [95] R. Zimmermann, P. Steiner, R. Claessen, F. Reinert and S. Hufner, "Electronic structure systematics of 3d transition metal oxides," *J. Electron. Spectrosc. Relat. Phenom.*, vol. 96, p. 179, 1998.
- [96] V. Luca, S. Djajanti and R. F. Howe, "Structural and Electronic Properties of Sol-Gel Titanium Oxides Studied by X-ray Absorption Spectroscopy," *J. Phys. Chem. B*, vol. 102, no. 52, pp. 10650-10657, 1998.

- [97] H. C. Choi, H. J. Ahn, Y. M. Jung, M. K. Lee, H. J. Shin, S. B. Kim and Y. E. Sung, "Characterization of the structures of size-selected TiO₂ nanoparticles using X-ray absorption spectroscopy," *Appl. Spectrosc.*, vol. 58, p. 598, 2004.
- [98] C. Kormann, D. W. Bahnemann and M. R. Hoffmann, "Preparation and characterization of quantum-size titanium dioxide," *J. Phys. Chem.*, vol. 92, no. 18, pp. 5196-5201, 1988.
- [99] L. Kavan, T. Stoto, M. Grätzel, D. Fitzmaurice and V. Shklover, "Quantum size effects in nanocrystalline semiconducting titania layers prepared by anodic oxidative hydrolysis of titanium trichloride," *J. Phys. Chem.*, vol. 97, pp. 9493-9498, 1993.
- [100] A. Henglein, "Small-particle research: Physicochemical properties of extremely small colloidal metal and semiconductor particles," *Chem. Rev.*, vol. 89, no. 8, pp. 1861-1873, 1989.
- [101] N. Serpone, D. Lawless, R. Khairutdinov and E. Pelizzetti, "Subnanosecond relaxation dynamics in TiO₂ colloidal Sols (particle sizes $R_p = 1.0-13.4$ nm), relevance to heterogeneous photocatalysis," *J. Phys. Chem.*, vol. 99, no. 45, pp. 16655-16661, 1995.
- [102] Y. Li, T. J. White and S. H. Lim, "Low-temperature synthesis and microstructural control of titania nano-particles," *J. Solid State Chem.*, vol. 177, no. 4-5, pp. 1372-1381, 2004.
- [103] K. M. Reddy, C. V. G. Reddy and S. V. Manorama, "Preparation, characterization, and spectral studies on nanocrystalline anatase TiO₂," *J. Solid State Chem.*, vol. 158, no. 2, pp. 180-186, 2001.
- [104] N. Serpone, D. Lawless and R. Khairutdinov, "Size effects on the photophysical properties of colloidal anatase TiO₂ particles: Size quantization versus direct transitions in this indirect semiconductor?," *J. Phys. Chem.*, vol. 99, no. 45, pp. 16646-16661, 1995.
- [105] S. Monticone, R. Tufeu, A. V. Kanaev, E. Scolan and C. Sanchez, "Quantum

- size effect in TiO₂ nanoparticles: Does it exist?," *Appl. Surf. Sci.*, Vols. 162-163, pp. 565-570, 2000.
- [106] L. Braginsky and V. Shklover, "Light absorption in TiO₂ nanoparticles," *Eur. Phys. J. D*, vol. 9, no. 1-4, pp. 627-630, 1999.
- [107] H. Sato, K. Ono, T. Sasaki and A. Yamagishi, "First-principles study of two-dimensional titanium dioxides," *J. Phys. Chem. B*, vol. 107, pp. 9824-9828, 2003.
- [108] T. Sasaki and M. Watanabe, "Semiconductor nanosheet crystallites of quasi-TiO₂ and their optical properties," *J. Phys. Chem. B*, vol. 101, no. 49, p. 10159–10161, 1997.
- [109] D. V. Bavykin, S. N. Gordeev, A. V. Moskalenko, A. A. Lapkin and F. C. Walsh, "Apparent two-dimensional behavior of TiO₂ nanotubes revealed by light absorption and luminescence," *J. Phys. Chem. B*, vol. 109, pp. 8565-8569, 2005.
- [110] S. H. Szczepankiewicz, A. J. Colussi and M. R. Hoffmann, "Infrared spectra of photoinduced species on hydroxylated titania surfaces," *J. Phys. Chem. B*, vol. 104, no. 42, pp. 9842-9850, 2000.
- [111] D. C. Hurum, K. A. Gray, T. Rajh and M. C. Thurnauer, "Recombination pathways in the Degussa P25 formulation of TiO₂: Surface versus lattice mechanisms," *J. Phys. Chem. B*, vol. 109, no. 2, pp. 977-980, 2005.
- [112] T. Berger, M. Sterrer, O. Diwald, E. Knoezinger, D. Panayotov, T. L. Thompson and J. T. Yates Jr, "Light-induced Charge Separation in Anatase TiO₂ Particles," *J. Phys. Chem. B*, vol. 109, pp. 6061-6068, 2005.
- [113] T. Seiyama, A. Kato, K. Fujiishi and M. Nagatani, "A New detector for gaseous components using semiconductive thin films," *Anal. Chem.*, vol. 34, pp. 1502 - 1503, 1962.
- [114] P. Esser and W. Gopel, "Physical adsorption on single crystal zinc oxide," *Surf.*

- Sci.*, vol. 97, pp. 309 - 318, 1980.
- [115] D. M. Wilson, S. Hoyt, J. Janata, K. Booksh and L. Obando, "Chemical sensors for portable, handheld field instruments," *IEEE Sensors J.*, vol. 1, no. 4, pp. 256 - 274, 2001.
- [116] E. Comini, G. Faglia, G. Sberveglieri, Z. W. Pan and Z. L. Wang, "Stable and highly sensitive gas sensors based on semiconducting oxide nanobelts," *Appl. Phys. Lett.*, vol. 81, p. 1869–1871, 2002.
- [117] X. Liu, S. Cheng, H. Liu, S. Hu, D. Zhang and H. Ning, "A Survey on Gas Sensing Technology," *Sensors*, vol. 12, pp. 9635-9665, 2012.
- [118] D. K. Aswal and S. K. Gupta, *Science and Technology of Chemiresistor Gas Sensors*, New York: Nova Science Publishers, Inc., 2007.
- [119] G. Cerrato, L. Marchese and C. Morterra, "Structural and morphological modifications of sintering microcrystalline TiO₂: An XRD, HRTEM and FTIR study," *Appl. Surf. Sci.*, vol. 70/71, pp. 200-205, 1993.
- [120] A. Turkoviæ, M. Ivanda, S. Popoviæ, A. Tonejc, M. Gotiæ, P. Dubèek and M. S, "Comparative Raman, XRD, HREM and SAXS studies of grain sizes in nanophase TiO₂," *J. Mol. Struct.*, Vols. 410-411, pp. 271-273, 1997.
- [121] N. Barsan, D. Koziej and U. Weimar, "Metal oxide-based gas sensor research: How to?," *Sens. Act. B*, vol. 121, p. 18–35, 2007.
- [122] L. E. Depero, L. Sangaletti, B. Allieri, E. Bontempi, R. Salari, M. Zocchi, C. Casale and M. Notaro, "Niobium-titanium oxide powders obtained by laser-laser induced synthesis: Microstructure and structure evolution from diffraction data," *J. Mater. Res.*, vol. 13, no. 6, pp. 1644-1649, 1998.
- [123] C. Wang, L. Yin, L. Zhang, D. Xiang and R. Gao, "Metal Oxide Gas Sensors: Sensitivity and Influencing Factors," *Sensors*, vol. 10, p. 2088–2106, 2010.
- [124] K. Arshak, E. Moore, G. M. Lyons, J. Harris and S. Clifford, "A review of gas sensors employed in electronic nose applications," *Sens. Rev.*, vol. 24, no. 2,

p. 181–198, 2004.

- [125] P. T. Moseley and B. C. Tofield, *Solid state gas sensor*, Bristol and Philadelphia: Adam Hilger, 1987.
- [126] M. Takata, D. Tsubone and H. Yanagida, “Dependance of electrical conductivity of ZnO on degree of sensing,” *J. Am. Ceram. Soc.*, vol. 59, pp. 4 - 8, 1976.
- [127] M. J. Madou and S. R. Morrison, *Chemical sensing with solid state devices*, London: Academic Press Inc., 1989.
- [128] N. Barsan and U. Weimar, “Conduction model of metal oxide gas sensors,” *J. of Electroceramics*, vol. 7, pp. 143 - 167, 2001.
- [129] Y. Shimizu and M. Egashira, “Basic aspects and challenges of semiconductor gas,” *MRS Bulletin*, vol. 6, pp. 18 - 24, 1999.
- [130] A. C. Pierre and G. M. Pajonk, “Chemistry of Aerogels and Their Applications,” *Chem. Rev.*, vol. 102, p. 4243, 2002.
- [131] L. L. Hench and J. K. West, “The sol-gel process,” *Chem. Rev.*, vol. 90, pp. 33-72, 1990.
- [132] Y. Bessekhoud, D. Robert and J. V. Weber, “Synthesis of photocatalytic TiO₂ nanoparticles: Optimization of the preparation conditions,” *J. Photochem. Photobiol. A*, vol. 157, pp. 47-53, 2003.
- [133] L. Znaidi, R. Seraphimova, J. F. Bocquet, C. Colbeau-Justin and C. Pommier, “A Semi-Continuous Process for the Synthesis of Nanosize TiO₂ Powders and Their Use as Photocatalysts,” *Mater. Res. Bull.*, vol. 36, pp. 811-825, 2001.
- [134] T. Sugimoto, “Preparation of Monodispersed Colloidal Particles,” *Adv. Colloid Interface Sci.*, vol. 28, pp. 65-108, 1987.
- [135] M. A. Anderson, M. J. Gieselmann and Q. Xu, “Titania and alumina ceramic membranes,” *J. Membr. Sci.*, vol. 39, p. 243–258, 1988.

- [136] A. Chemseddine and T. Moritz, "Nanostructuring Titania: Control over Nanocrystal Structure, Size, Shape, and Organization," *Eur. J. Inorg. Chem.*, vol. 2, pp. 235-245, 1999.
- [137] T. Moritz, J. Reiss, K. Diesner, D. Su and A. Chemseddine, "Nanostructured crystalline TiO₂ through growth control and stabilization of intermediate structural building units," *J. Phys. Chem. B*, vol. 101, p. 8052, 1997.
- [138] T. Sugimoto, K. Okada and H. Itoh, "Synthesis of Uniform Spindle-Type Titania Particles by the Gel-Sol Method," *J. Colloid Interface Sci.*, vol. 193, p. 140, 1997.
- [139] T. Sugimoto, X. Zhou and A. Muramatsu, "Synthesis of Uniform Anatase TiO₂ Nanoparticles by Gel-Sol Method: 4. Shape Control," *J. Colloid Interface Sci.*, vol. 259, pp. 53-61, 2003.
- [140] T. Sugimoto, X. Zhou and A. Muramatsu, "Synthesis of uniform anatase TiO₂ nanoparticles by gel-sol method: 3. Formation process and size control," *J. Colloid Interface Sci.*, vol. 259, pp. 43-52, 2003.
- [141] N. Uekawa, J. Kajiwara, K. Kakegawa and Y. Sasaki, "Low temperature synthesis and characterization of porous Anatase TiO₂ nanoparticles," *J. Colloid Interface Sci.*, vol. 250, pp. 285-290, 2002.
- [142] K. D. Kim and H. T. Kim, "Synthesis of TiO₂ nanoparticles by hydrolysis of TEOT and decrease of particle size using a two-stage mixed method," *Powder Technol.*, vol. 119, pp. 164-172, 2001.
- [143] K. D. Kim and H. T. Kim, "Synthesis of Titanium Dioxide Nanoparticles Using a Continuous Reaction Method," *Colloids Surf., A*, vol. 207, pp. 263-269, 2002.
- [144] L. Miao, S. Tanemura, S. Toh, K. Kaneko and M. Tanemura, "Fabrication, characterization and Raman study of anatase-TiO₂ nanorods by a heating-sol-gel template process," *J. Cryst. Growth*, vol. 264, no. 1, pp. 246-252, 2004.
- [145] L. Miao, S. Tanemura, S. Toh, K. Kaneko and M. Tanemura, "Heating-sol-gel

- template process for the growth of TiO₂ nanorods with rutile and anatase structure,” *Appl. Surf. Sci.*, vol. 238, no. 1, pp. 175-179, 2004.
- [146] Y. Lin, G. S. Wu, X. Y. Yuan, T. Xie and L. D. Zhang, “Fabrication and optical properties of TiO₂ nanowire arrays made by sol–gel electrophoresis deposition into anodic alumina membranes,” *J. Phys.: Condens. Matter*, vol. 15, p. 2917, 2003.
- [147] S. Lee, C. Jeon and Y. Park, “Fabrication of TiO₂ tubules by template synthesis and hydrolysis with water vapor,” *Chem. Mater.*, vol. 16, no. 22, p. 4292–4295, 2004.
- [148] S. M. Liu, L. M. Gan, L. H. Liu, W. D. Zhang and H. C. Zeng, “Synthesis of single-crystalline TiO₂ nanotubes,” *Chem. Mater.*, vol. 14, no. 3, pp. 1391-1397, 2002.
- [149] J. H. Jung, H. Kobayashi, K. J. C. van Bommel, S. Shinkai and T. Shimizu, “Creation of novel helical ribbon and double-layered nanotube TiO₂ structures using an organogel template,” *Chem. Mater.*, vol. 14, no. 4, pp. 1445-1447, 2002.
- [150] J. H. Jung, T. Shimizu and S. Shinkai, “Self-assembling structures of steroidal derivatives in organic solvents and their sol–gel transcription into double-walled transition-metal oxide nanotubes,” *J. Mater. Chem.*, vol. 15, no. 35-36, pp. 3979-3986, 2005.
- [151] J. J. Qiu, W. D. Yu, X. D. Gao and X. M. Li, “Sol-gel assisted ZnO nanorod array template to synthesize TiO₂ nanotube arrays,” *Nanotechnology*, vol. 17, p. 46954698, 2006.
- [152] T. J. Trentler, T. E. Denler, J. F. Bertone, A. Agrawal and V. L. Colvin, “Synthesis of TiO₂ Nanocrystals by Nonhydrolytic Solution-Based Reactions,” *J. Am. Chem. Soc.*, vol. 121, p. 1613, 1999.
- [153] E. Scolan and C. Sanchez, “Synthesis and characterization of surface-protected nanocrystalline titania particles,” *Chem. Mater.*, vol. 10, p. 3217–

3223, 1998.

- [154] P. D. Cozzoli, E. Fanizza, M. L. Curri, D. Laub and A. Agostiano, "Low-Dimensional Chainlike Assemblies of TiO₂ Nanorod-Stabilized Au Nanoparticles," *Chem. Commun.*, p. 942, 2005.
- [155] J. Joo, S. G. Kwon, T. Yu, M. Cho, J. Lee, J. Yoon and T. J. Hyeon, "Large-Scale Synthesis of TiO₂ Nanorods via Nonhydrolytic Sol-Gel Ester Elimination Reaction and Their Application to Photocatalytic Inactivation of *E. coli*," *Phys. Chem. B*, vol. 109, no. 32, pp. 15297-15302, 2005.
- [156] Y. W. Jun, M. F. Casula, J. H. Sim, S. Y. Kim, J. Cheon and A. P. Alivisatos, "Surfactant-assisted elimination of a high energy facet as a means of Controlling the Shapes of TiO₂ Nanocrystals," *J. Am. Chem. Soc.*, vol. 125, p. 15981, 2003.
- [157] K. D. Kim, S. H. Kim and H. T. Kim, "Applying the Taguchi method to the optimization for the synthesis of TiO₂ nanoparticles by hydrolysis of TEOT in micelles," *Colloids Surf., A*, vol. 254, pp. 99-105, 2005.
- [158] D. Zhang, L. Qi, J. Ma and H. Cheng, "Formation of crystalline nanosized titania in reverse micelles at room temperature," *J. Mater. Chem.*, vol. 12, p. 3677, 2002.
- [159] G. L. Li and G. H. Wang, "Synthesis of nanometer-sized TiO₂ particles by a microemulsion method," *Nanostruct. Mater.*, vol. 11, no. 5, pp. 663-668, 1999.
- [160] K. T. Lim, H. S. Hwang, W. Ryoo and K. P. Johnston, "Synthesis of TiO₂ nanoparticles utilizing hydrated reverse micelles in CO₂," *Langmuir*, vol. 20, no. 6, pp. 2466-2471, 2004.
- [161] J. Lin, Y. Lin, P. Liu, M. J. Meziani, L. F. Allard and Y. P. Sun, "Hot-fluid annealing for crystalline titanium dioxide nanoparticles in stable suspension," *J. Am. Chem. Soc.*, vol. 124, no. 38, pp. 11514-11518, 2002.
- [162] X. Feng, J. Zhai and L. Jiang, "The fabrication and switchable

- superhydrophobicity of TiO₂ nanorod films,” *Angew. Chem., Int. Ed.*, vol. 44, no. 32, pp. 5115-5118, 2005.
- [163] Q. Zhang and L. Gao, “Preparation of oxide nanocrystals with tunable morphologies by the moderate hydrothermal method: Insights from rutile TiO₂,” *Langmuir*, vol. 19, pp. 967-971, 2003.
- [164] M. Wei, Y. Konishi, H. Zhou, H. Sugihara and H. Arakawa, “A simple method to synthesize nanowires titanium dioxide layered titanate particles,” *Chem. Phys. Lett.*, vol. 400, p. 231, 2004.
- [165] T. Kasuga, M. Hiramatsu, A. Hoson, T. Sekino and K. Niihara, “Formation of titanium oxide nanotube,” *Langmuir*, vol. 14, pp. 3160-3163, 1998.
- [166] G. H. Du, Q. Chen, R. C. Che, Z. Y. Yuan and L. M. Peng, “Preparation and structure analysis of titanium oxide nanotubes,” *Appl. Phys. Lett.*, vol. 79, p. 3702–3704, 2001.
- [167] Y. Q. Wang, G. Q. Hu, X. F. Duan, H. L. Sun and Q. K. Xue, “Microstructure and formation mechanism of titanium dioxide nanotubes,” *Chem. Phys. Lett.*, vol. 365, no. 5-6, p. 427–431, 2002.
- [168] B. D. Yao, Y. F. Chan, X. Y. Zhang, W. F. Zhang, Z. Y. Yang and N. Wang, “Formation mechanism of TiO₂TiO₂ nanotubes,” *Appl. Phys. Lett.*, vol. 82, pp. 281-283, 2003.
- [169] D. V. Bavykin, V. N. Parmon, A. A. Lapkin and F. C. Walsh, “The effect of hydrothermal conditions on the mesoporous structure of TiO₂ nanotubes,” *J. Mater. Chem.*, vol. 14, no. 22, pp. 3370-3377, 2004.
- [170] W. Wang, O. K. Varghese, M. Paulose, C. A. Grimes, Q. Wang and E. C. Dickey, “A study on the growth and structure of titania nanotubes,” *J. Mater. Res.*, vol. 19, no. 02, pp. 417-422, 2004.
- [171] X. L. Li, Q. Peng, J. X. Yi, X. Wang and Y. Li, “Near monodisperse TiO₂ nanoparticles and nanorods,” *Chem.sEur. J.*, vol. 12, no. 8, pp. 2383-2391,

2006.

- [172] B. Wen, C. Liu and Y. Liu, "Bamboo-Shaped Ag-Doped TiO₂ Nanowires with Heterojunctions," *Inorg. Chem.*, vol. 44, no. 19, p. 6503–6505, 2005.
- [173] B. Wen, C. Liu and Y. Liu, "Solvothermal synthesis of ultralong single-crystalline TiO₂ nanowires," *New J. Chem.*, vol. 29, p. 969–971, 2005.
- [174] J. M. Wu, S. Hayakawa, K. Tsuru and A. Osaka, "Porous titania films prepared from interactions of titanium with hydrogen peroxide solution," *Scripta Mater.*, vol. 46, no. 1, p. 101, 2002.
- [175] X. Peng and A. Chen, "Aligned TiO₂ nanorod arrays synthesized by oxidizing titanium with acetone," *J. Mater. Chem.*, vol. 14, p. 2542–2548, 2004.
- [176] G. K. Mor, M. A. Carvalho, O. K. Varghese, M. V. Pishko and C. A. Grimes, "A room temperature TiO₂-nanotube hydrogen sensor able to self-clean photoactively from environmental contamination," *J. Mater. Res.*, vol. 19, p. 628–634, 2004.
- [177] O. K. Varghese, D. Gong, M. Paulose, C. A. Grimes and E. C. Dickey, "Crystallization and high-temperature structural stability of titanium oxide nanotube arrays," *J. Mater. Res.*, vol. 18, no. 1, pp. 156-165, 2003.
- [178] X. H. Wang, J. G. Li, H. Kamiyama, M. Katada, N. Ohashi, Y. Moriyoshi and T. Ishigaki, "Pyrogenic iron (III)-doped TiO₂ nanopowders synthesized in RF thermal plasma: Phase formation, defect structure, band gap, and magnetic properties," *J. Am. Chem. Soc.*, vol. 127, no. 31, pp. 10982-10990, 2005.
- [179] J. M. Wu, H. C. Shih and W. T. Wu, "Electron field emission from single crystalline TiO₂ nanowires prepared by thermal evaporation," *Chem. Phys. Lett.*, vol. 413, no. 4, pp. 490-494, 2005.
- [180] B. Xiang, Y. Zhang, Z. Wang, X. H. Luo, Y. W. Zhu, H. Z. Zhang and D. P. Yu, "Field-emission properties of TiO₂ nanowire arrays," *J. Phys. D*, vol. 38, p. 1152–1155, 2005.

- [181] J. C. Yu, J. Yu, W. Ho and L. Zhang, "Preparation of highly photocatalytic active nano-sized TiO₂ particles via ultrasonic irradiation," *Chem. Commun.*, vol. 19, pp. 1942-1943, 2001.
- [182] W. Huang, X. Tang, Y. Wang, Y. Koltypin and A. Gedanken, "Selective synthesis of anatase and rutile via ultra-sound irradiation," *Chem. Commun.*, pp. 1415-1416, 2000.
- [183] Y. Zhu, H. Li, Y. Koltypin, Y. R. Hacoheh and A. Gedanken, "Synthesis of Titania Whiskers and Nanotubes," *Chem. Commun.*, pp. 2616-2617, 2001.
- [184] A. B. Corradi, F. Bondioli, B. Focher, A. M. Ferrari, C. Grippio, E. Mariani and C. Villa, "Conventional and Microwave-Hydrothermal Synthesis of TiO₂ Nanopowders," *J. Am. Ceram. Soc.*, vol. 88, no. 9, pp. 2639-2641, 2005.
- [185] G. Ma, X. Zhao and J. Zhu, "Microwave hydrothermal synthesis of rutile TiO₂," *Int. J. Mod. Phys. B*, vol. 19, pp. 2763-2768, 2005.
- [186] X. Wu, Q. Z. Jiang, Z. F. Ma, M. Fu and W. F. Shangguan, "Synthesis of titania nanotubes by microwave irradiation," *Solid State Commun.*, vol. 136, no. 9, pp. 513-517, 2005.
- [187] C. J. Barbe, F. Arendse, P. Comte, M. Jirousek, F. Lenzmann, V. Shklover and M. Grätzel, "Nanocrystalline titanium oxide electrodes for photovoltaic applications," *J. Am. Ceram. Soc.*, vol. 80, no. 12, pp. 3157-3171, 1997.
- [188] C. Liu, L. Fu and J. Economy, "A simple, template-free route for the synthesis of mesoporous titanium dioxide materials," *J. Mater. Chem.*, vol. 14, pp. 1187-1189, 2004.
- [189] Y. Zhang, G. Li, Y. Wu, Y. Luo and L. Zhang, "The Formation of Mesoporous TiO₂ Spheres via a Facile," *J. Phys. Chem. B*, vol. 109, p. 5478-5481, 2005.
- [190] J. C. Yu, L. Zhang and J. Yu, "Rapid synthesis of mesoporous TiO₂ with high photocatalytic activity by ultrasound-induced agglomeration," *New J. Chem.*, vol. 26, no. 4, pp. 416-420, 2002.

- [191] K. L. Frindell, M. H. Bartl, A. Popitsch and G. D. Stucky, "Sensitized Luminescence of Trivalent Europium by Three-Dimensionally Arranged Anatase Nanocrystals in Mesostructured Titania Thin Films," *Angew. Chem., Int. Ed.*, vol. 114, no. 6, pp. 1001-1004, 2002.
- [192] E. L. Crepaldi, G. J. D. A. Soler-Illia, D. Grosso, F. Cagnol, F. Ribot and C. Sanchez, "Controlled formation of highly organized mesoporous titania thin films: From mesostructured hybrids to mesoporous nanoanatase TiO₂," *J. Am. Chem. Soc.*, vol. 125, no. 32, pp. 9770-9786, 2003.
- [193] L. K. Campbell, B. K. Na and E. I. Ko, "Synthesis and characterization of titania aerogels," *Chem. Mater.*, vol. 4, pp. 1329-1333, 1992.
- [194] G. Dagan and M. Tomkiewicz, "TiO₂ aerogels for photocatalytic decontamination of aquatic environments," *J. Phys. Chem.*, vol. 97, p. 12651-12655, 1993.
- [195] W. Dong, H. J. Bongard and F. Marlow, "New type of inverse opals: Titania with skeleton structure," *Chem. Mater.*, vol. 15, no. 2, pp. 568-574, 2003.
- [196] X. Wang, C. Neff, E. Graugnard, Y. Ding, J. S. King, L. A. Pranger, R. Tannenbaum, Z. L. Wang and C. J. Summers, "Photonic Crystals Fabricated Using Patterned Nanorods," *Adv. Mater.*, vol. 17, p. 2103-2106, 2005.
- [197] B. T. Holland, C. F. Blanford, T. Do and A. Stein, "Synthesis of highly ordered, three-dimensional, macroporous structures of amorphous or crystalline inorganic oxides, phosphates, and hybrid composites," *Chem. Mater.*, vol. 11, no. 3, pp. 795-805, 1999.
- [198] L. Ji, J. Rong and Z. Yang, "Opal gel templated synthesis of oblate titania opal materials," *Chem. Commun.*, vol. 9, pp. 1080-1081, 2003.
- [199] A. L. Linsebigler, G. Lu and J. T. Yates, "Photocatalysis on TiO₂ Surfaces: Principles, Mechanisms, and Selected Results," *Jr. Chem. Rev.*, vol. 95, p. 735, 1995.

- [200] C. Burda, Y. Lou, X. Chen, A. C. S. Samia, J. Stout and J. L. Gole, "Enhanced nitrogen doping in TiO₂ nanoparticles," *Nano Lett.*, vol. 3, p. 1049–1051, 2003.
- [201] F. B. Li, X. Z. Li and M. F. Hou, "Photocatalytic degradation of 2-mercaptobenzothiazole in aqueous. La³⁺-TiO₂ suspension for odor control," *Appl. Catal. B*, vol. 48, pp. 185-194, 2004.
- [202] K. Nagaveni, M. S. Hegde and G. Madras, "Structure and Photocatalytic Activity of Ti_{1-x} MxO_{2±δ} (M= W, V, Ce, Zr, Fe, and Cu) Synthesized by Solution Combustion Method," *J. Phys. Chem. B*, vol. 108, no. 52, pp. 20204-20212, 2004.
- [203] Y. Wang, H. Cheng, Y. Hao, J. Ma, W. Li and S. Cai, "Characterization and photo-electric behaviors of Fe(III) doped TiO₂ nanoparticles," *J. Mater. Sci.*, vol. 34, no. 15, pp. 3721-3729, 1999.
- [204] Y. Bessekhoud, D. Robert, J. V. Weber and N. Chaoui, "Effect of alkaline-doped TiO₂ on photocatalytic efficiency," *J. Photochem. Photobiol. A*, vol. 167, no. 1, pp. 49-57, 2004.
- [205] Y. Cao, W. Yang, W. Zhang, G. Liu and P. Yue, "Improved photocatalytic activity of Sn⁴⁺ doped TiO₂ nanoparticulate films prepared by plasma-enhanced chemical vapor deposition," *New J. Chem.*, vol. 28, p. 218–222, 2004.
- [206] F. Gracia, J. P. Holgado, A. Caballero and A. R. Gonzalez-Elipe, "Structural, optical, and photoelectrochemical properties of Mn⁺-TiO₂ model thin film photocatalysts," *J. Phys. Chem. B*, vol. 108, no. 45, pp. 17466-17476, 2004.
- [207] J. H. Park, S. Kim and A. J. Bard, "Novel carbon-doped TiO₂ nanotube arrays with high aspect ratios for efficient solar water splitting," *Nano Lett.*, vol. 6, no. 1, pp. 24-28, 2006.
- [208] T. Umebayashi, T. Yamaki, H. Itoh and K. Asai, "Analysis of electronic structures of 3d transition metals-doped TiO₂ based on band calculations," *J. Phys. Chem. Solids*, vol. 63, pp. 1909-1920, 2002.

- [209] M. Anpo and M. Takeuchi, "Design and development of second-generation titanium oxide photocatalysts to better our environment—approaches in realizing the use of visible light," *Int. J. Photoenergy*, vol. 3, p. 89 – 94, 2001.
- [210] D. Li, H. Haneda, S. Hishita and N. Ohashi, "Visible-light-driven N–F–codoped TiO₂ photocatalyst. 2. Optical characterization, photocatalysis, and potential application to air purification," *Chem. Mater.*, vol. 17, p. 2596–2602, 2005.
- [211] T. Ohno, M. Akiyoshi, T. Umebayashi, K. Asai, T. Mitsui and M. Matsumura, "Preparation of S-doped TiO₂ photocatalysts and their photocatalytic activities under visible light," *Appl. Catal. A*, vol. 265, pp. 115-121, 2004.
- [212] Y. Choi, T. Umebayashi and M. Yoshikawa, "Fabrication and Characterization of C-doped Anatase TiO₂ Photocatalysts," *J. Mater. Sci.*, vol. 39, no. 5, pp. 1837-1839, 2004.
- [213] H. Luo, T. Takata, Y. Lee, J. Zhao, K. Domen and Y. Yan, "Photocatalytic activity enhancing for titanium dioxide by co-doping with bromine and chlorine," *Chem. Mater.*, vol. 16, no. 5, pp. 846-849, 2004.
- [214] Z. Lin, A. Orlov, R. M. Lambert and M. C. Payne, "New insights into the origin of visible light photocatalytic activity of nitrogen-doped and oxygen-deficient anatase TiO₂," *J. Phys. Chem. B*, vol. 109, p. 20948, 2005.
- [215] S. Livraghi, M. C. Paganini, E. Giamello, A. Selloni, C. Di Valentin and G. Pacchioni, "Origin of Photoactivity of Nitrogen-Doped Titanium Dioxide under Visible Light," *J. Am. Chem. Soc.*, vol. 128, p. 15666, 2006.
- [216] N. Serpone, "Is the band gap of pristine TiO₂ narrowed by anion- and cation-doping of titanium dioxide in second-generation photocatalysts?," *J. Phys. Chem. B*, vol. 110, no. 48, p. 24287–24293, 2006.
- [217] R. Vogel, P. Hoyer and H. Weller, "Quantum-Sized PbS, CdS, Ag₂S, Sb₂S₃, and Bi₂S₃ Particles as Sensitizers for Various Nanoporous Wide-Bandgap Semiconductors," *J. Phys. Chem.*, vol. 98, pp. 3183-3188, 1994.

- [218] Y. Ohko, Y. Tatsuma, T. Fujii, K. Naoi, C. Niwa, Y. Kubota and A. Fujishima, "Multicolour photochromism of TiO₂ films loaded with silver nanoparticles," *Nat. Mater.*, vol. 2, no. 1, pp. 29-31, 2003.
- [219] K. Kawahara, K. Suzuki, Y. Ohko and T. Tatsuma, "Electron Transport in Silver-Semiconductor Nanocomposite Films Exhibiting Multicolor Photochromism," *Phys. Chem. Chem. Phys.*, vol. 7, p. 3851, 2005.
- [220] D. M. Adams, L. Brus, C. E. D. Chidsey, S. Creager, C. Creutz, C. R. Kagan, P. V. Kamat, M. Lieberman, S. Lindsay, R. A. Marcus, R. M. Metzger, M. E. Michel-Beyerle, J. R. Miller, M. D. Newton, D. R. Rolison, O. Sankey, K. S. Schanze, J. Yardley and X. Zhu, "Charge Transfer on the Nanoscale: Current Status," *J. Phys. Chem. B*, vol. 107, p. 6668, 2003.
- [221] M. Zúkalová, A. Zúkal, L. Kavan, M. K. Nazeeruddin, P. Liska and M. Grätzel, "Organized mesoporous TiO₂ films exhibiting greatly enhanced performance in dye-sensitized solar cells," *Nano. Lett.*, vol. 5, pp. 1789-1792, 2005.
- [222] M. Adachi, Y. Murata, I. Okada and S. Yoshikawa, "Formation of titania nanotubes and applications for dye-sensitized solar cells," *J. Electrochem. Soc.*, vol. 150, no. 8, pp. G488-G493, 2003.
- [223] L. Sirghi, T. Aoki and Y. Hatanaka, "Friction Force Microscopy Study of the Hydrophilicity of TiO₂ Thin Films Deposited by Radio Frequency Magnetron Sputtering," *Surf. Rev. Lett.*, vol. 10, p. 345, 2003.
- [224] Z. Z. Gu, A. Fujishima and O. Sato, "Patterning of a Colloidal Crystal Film on a Modified Hydrophilic and Hydrophobic," *Angew. Chem., Int. Ed.*, vol. 41, pp. 2067-2070, 2002.
- [225] M. Anpo, T. Shima, S. Kodama and Y. Kubokawa, "Photocatalytic hydrogenation of CH₃CCH with H₂O on small-particle TiO₂: Size quantization effects and reaction intermediates," *J. Phys. Chem.*, vol. 91, pp. 4305-4310, 1987.
- [226] D. Beydoun, R. Amal, G. Low and S. McEvoy, "Role of nanoparticles in

- photocatalysis," *J. Nanopart. Res.*, vol. 1, p. 439–458, 1999.
- [227] S. Peng, Y. Li, F. Jiang, G. Lu and S. Li, "Effect of Be²⁺ doping TiO₂ on its photocatalytic activity," *Chem. Phys. Lett.*, vol. 398, no. 1-3, p. 235–239, 2004.
- [228] D. Cahen, G. Hodes, M. Grätzel, J. F. Guillemoles and I. Riess, "Nature of photovoltaic action in dye-sensitized solar cells," *J. Phys. Chem. B*, vol. 104, no. 9, pp. 2053-2059, 2000.
- [229] P. R. Somani, C. Dionigi, M. Murgia, D. Palles, P. Nozar and G. Ruani, "Solid-state dye PV cells using inverse opal TiO₂ films," *Sol. Energy Mater. Sol. Cells*, vol. 87, no. 1, pp. 513-519, 2005.
- [230] H. Han, L. Zan, J. Zhong and X. Zhao, "A novel hybrid nanocrystalline TiO₂ electrode for the dye-sensitized nanocrystalline solar cells," *J. Mater. Sci.*, vol. 40, no. 18, pp. 4921-4923, 2005.
- [231] T. S. Kang, S. H. Moon and K. J. Kim, "Enhanced photocurrent-voltage characteristics of Ru(II)-dye sensitized TiO₂ solar cells with TiO₂–WO₃ buffer layers prepared," *J. Electrochem. Soc.*, vol. 149, p. E155–E158, 2002.
- [232] E. W. McFarland and J. Tang, "A photovoltaic device structure based on internal electron emission," *Nature*, vol. 421, p. 616–618, 2003.
- [233] M. Ni, M. K. H. Leung, D. Y. C. Leung and K. Sumathy, "A review and recent developments in photocatalytic water-splitting using TiO₂ for hydrogen," *Renewable Sustainable Energy Rev.*, vol. 11, no. 3, p. 401–425, 2007.
- [234] R. Abe, K. Sayama and H. Arakawa, "Significant effect of iodide addition on water splitting into H₂ and O₂ over Pt-loaded TiO₂ photocatalyst: Suppression of backward reaction," *Chem. Phys. Lett.*, vol. 371, pp. 360-364, 2003.
- [235] A. Galinska and J. Walendziewski, "Photocatalytic water splitting over Pt-TiO₂ in the presence of sacrificial reagents," *Energy Fuels*, vol. 19, no. 3, p. 1143–1147, 2005.

- [236] G. K. Mor, K. Shankar, M. Paulose, O. K. Varghese and C. A. Grimes, "Enhanced Photocleavage of Water Using Titania Nanotube," *Nano Lett.*, vol. 5, pp. 191-195, 2005.
- [237] M. Matsuoka, M. Kitano, M. Takeuchi, M. Anpo and J. M. Thomas, "Preparation and characterization of the visible light responsive TiO₂ thin film photocatalysts prepared by magnetron sputtering method and their photocatalytic activities for the water splitting reactions," *Mater. Sci. Forum*, vol. 81, pp. 486-487, 2005.
- [238] J. H. Park and A. J. Bard, "Unassisted Water Splitting from Bipolar Pt/Dye-Sensitized TiO₂ Photoelectrode Arrays," *Electrochem. Solid-State Lett.*, vol. 8, no. 12, pp. G371-G375, 2005.
- [239] J. Akikusa and S. U. M. Khan, "Photoelectrolysis of water to hydrogen in p-SiC/Pt and p-SiC/n-TiO₂ cells," *Int. J. Hydrogen Energy*, vol. 27, no. 9, pp. 863-870, 2002.
- [240] F. Pichot, S. Ferrere, R. J. Pitts and B. A. Gregg, "Flexible Solid-State Photoelectrochromic Windows," *J. Electrochem. Soc.*, vol. 146, no. 11, pp. 4324-4326, 1999.
- [241] P. Bonhote, E. Gogniat, F. Campus, L. Walder and M. Grätzel, "Nanocrystalline electrochromic displays," *Displays*, vol. 20, no. 3, p. 137-144, 1999.
- [242] U. Bach, D. Corr, D. Lupo, F. Pichot and M. Ryan, "Nanomaterials-based electrochromics for paper-quality displays," *Adv. Mater.*, vol. 14, no. 11, p. 845-848, 2002.
- [243] M. Moeller, S. Asaftei, D. Corr, M. Ryan and L. Walder, "Switchable Electrochromic Images Based on a Combined Top-Down Bottom-Up Approach," *Adv. Mater.*, vol. 16, p. 1558-1562, 2004.
- [244] D. V. Bavykin, A. A. Lapkin, P. K. Plucinski, J. M. Friedrich and F. C. Walsh, "Reversible storage of molecular hydrogen by sorption into multilayered TiO₂ nanotubes," *J. Phys. Chem. B*, vol. 109, no. 41, pp. 19422-19427, 2005.

- [245] N. Taguchi, "A Metal-Oxide Sensor," *Japanese Patent*, Vols. S47-38840, 1962.
- [246] Figaro, "Gas Sensor Catalogue and Technical Information," Figaro and Figaro USA, Inc., 2000. [Online]. Available: <http://www.figarosensor.com>.
- [247] L. D. Birkefeld, A. M. Azad and S. A. Akbar, "Carbon monoxide and hydrogen detection by anatase modification of titanium dioxide," *J. Am. Ceram. Soc.*, vol. 75, no. 11, pp. 2964-2968, 1992.
- [248] Y. Shimizu, "Micro-macro structure control the performance of semiconductor gas sensor," *Chem. Sens.*, vol. 18, no. 2, pp. 42-54, 2002.
- [249] H. Kobayashi, K. Kishimoto and Y. Nakato, "Reactions of hydrogen at the interface of palladium-titanium dioxide Schottky diodes as hydrogen sensors, studied by workfunction and electrical," *Surf. Sci.*, vol. 306, pp. 393-405, 1994.
- [250] C. M. Carney, S. Yoo and S. A. Akbar, "TiO₂-SnO₂ nanostructures and their H₂ sensing behavior," *Sens. Act. B*, vol. 108, no. 1, pp. 29-33, 2005.
- [251] G. S. Devi, T. Hyodo, Y. Shimizu and M. Egashira, "Synthesis of mesoporous TiO₂-based powders and their gas-sensing properties," *Sens. Act. B*, vol. 87, p. 122, 2002.
- [252] L. Gao, Q. Li, Z. Song and J. Wang, "Preparation of nano-scale titania thick film and its oxygen sensitivity," *Sens. Act. B*, vol. 71, no. 3, pp. 179-183, 2000.
- [253] C. Garzella, E. Bontempi, L. E. Depero, A. Vomiero, G. la Mea and G. Sberveglieri, "Novel selective ethanol sensors: W/TiO₂ thin films by sol-gel spin-coating," *Sens. Act. B*, vol. 39, no. 1-3, pp. 495-502, 2003.
- [254] K. D. Benkstein and S. Semancik, "Mesoporous nanoparticle TiO₂ thin films for conductometric gas sensing on microhotplate platforms," *Sens. Act. B*, vol. 113, no. 1, pp. 445-453, 2006.
- [255] G. Montesperelli, A. Pumo, E. Traversa, G. Gusmano, A. Bearzotti, A. Montenero and G. Gnappi, "Sol-gel processed TiO₂-based thin films as

- innovative humidity sensors,” *Sens. Act. B*, vol. 25, no. 1-3, pp. 705-709, 1995.
- [256] B. C. Yadav, R. K. Shukla and L. M. Bali, “Sol-gel processed TiO₂ films on U-shaped glass-rods as optical humidity sensor,” *Indian J. Pure Appl. Phys.*, vol. 43, p. 51, 2005.
- [257] Z. L. Wang, “Functional oxide nanobelts: Materials, properties and potential applications in nanosystems and biotechnology,” *Annu. Rev. Phys. Chem.*, vol. 55, pp. 159 - 196, 2004.
- [258] C. Brinker and G. Scherer, *Sol-gel science: The physics and chemistry of sol-gel processing*, San Diego, CA: Academic Press, 1990.
- [259] C. C. Wang and J. Y. Ying, “Sol-gel synthesis and hydrothermal processing of anatase and rutile titania nanocrystals,” *Chem. Mater.*, vol. 11, p. 3113 – 3120, 1999.
- [260] Sigma-Aldrich, “South Africa | Sigma-Aldrich,” Sigma-Aldrich, 2014. [Online]. Available: <http://www.sigmaaldrich.com/south-africa.html>. [Accessed 2014].
- [261] Wikipedia, “X-ray spectroscopy - Wikipedia, the free encyclopedia,” Wikipedia, 28 December 2015. [Online]. Available: https://en.wikipedia.org/wiki/X-ray_spectroscopy. [Accessed 13 February 2016].
- [262] Wikipedia, “X-ray crystallography,” Wikipedia, 2014. [Online]. Available: https://en.wikipedia.org/wiki/X-ray_crystallography. [Accessed 2014].
- [263] V. Chaudhary, A. K. Srivastava and J. Kumar, “On the sol-gel synthesis and characterization of titanium dioxide nanoparticles,” *Mater. Res. Soc. Symp. Proc.*, vol. 1352, pp. 10-24, 2011.
- [264] ICDD, “The International Centre for Diffraction Data - ICDD - a non-profit scientific organization dedicated to collecting, editing, publishing, and distributing powder diffraction data,” The International Centre for Diffraction Data, 2014. [Online]. Available: www.icdd.com. [Accessed 2014].

- [265] S. Gražulis, "Crystallography Open Database," Vilnius University, 29 October 2014. [Online]. Available: <http://www.crystallography.net/>. [Accessed 23 January 2015].
- [266] R. T. Downs and M. Hall-Wallace, "The American Mineralogist Crystal Structure Database," *American Mineralogist*, vol. 88, pp. 247 - 250, 09 May 2003.
- [267] A. Ueda, T. Nakao, M. Azuma and T. Kobayashi, "Two conversion maxima at 373 and 573 K in the reduction of nitrogen monoxide with hydrogen over Pd/TiO₂ catalyst," *Catal. Today*, vol. 45, pp. 135-138, 1998.
- [268] K. Brandenburg and H. Putz, "Match! - Phase Identification from Powder Diffraction," Crystal Impact, 23 September 2014. [Online]. Available: <http://www.crystalimpact.com/match/Default.htm>. [Accessed 23 January 2015].
- [269] D. J. Gardiner, Practical Raman spectroscopy, Springer-Verlag, 1989.
- [270] Wikipedia, "Raman spectroscopy - Wikipedia," Wikipedia, 2014. [Online]. Available: https://en.wikipedia.org/wiki/Raman_spectroscopy. [Accessed 2014].
- [271] G. A. Tompsett, G. A. Bowmaker, R. P. Cooney, J. B. Metson, K. A. Rodgers and J. M. Seakins, "The Raman Spectrum of Brookite, TiO₂ (Pbca, Z = 8)," *J. Raman Spectrosc.*, vol. 26, pp. 57-62, 1996.
- [272] W. Zhang, C. Wang and L. H., "Treatment of chlorinated organic contaminants with nanoscale bimetallic particles," *Catal. Today*, vol. 40, no. 4, p. 387 – 395, 1998.
- [273] Wikipedia, "Scanning electron microscope - Wikipedia, the free encyclopedia," Wikipedia, 2014. [Online]. Available: https://en.wikipedia.org/wiki/Scanning_electron_microscope. [Accessed 2014].
- [274] Wikipedia, "Energy-dispersive X-ray spectroscopy - Wikipedia, the free encyclopedia," Wikipedia, 2014. [Online]. Available: https://en.wikipedia.org/wiki/Energy-dispersive_X-ray_spectroscopy. [Accessed 2014].

2014].

- [275] Wikipedia, "Ultraviolet–visible spectroscopy - Wikipedia, the free encyclopedia," Wikipedia, 2014. [Online]. Available: https://en.wikipedia.org/wiki/Ultraviolet%E2%80%93visible_spectroscopy. [Accessed 2014].
- [276] P. Kubelka and F. Munk, "Ein Beitrag zur Optik der Farbanstriche," *Z. Tech. Phys.*, vol. 12, p. 593 – 601, 1931.
- [277] A. E. Morales, E. Sanchez Mora and U. Pal, "Use of diffuse reflectance spectroscopy for optical characterization of unsupported nanostructures," *Revista Mexicana de Fisica S*, vol. 53, no. 5, p. 18 – 22, 2007.
- [278] A. B. Murphy, "Band-gap determination from diffuse reflectance measurements of semiconductor films, and application to photoelectrochemical water-splitting," *Sol. Energ. Mat. Sol. Cells*, vol. 91, no. 14, p. 1326–1337, 2007.
- [279] J. Tauc, "Absorption edge and internal electric fields in amorphous semiconductors," *Mater Res Bull.*, vol. 5, p. 721 – 730, 1970.
- [280] N. Ghobadi, "Band gap determination using absorption spectrum fitting procedure," *Int. Nano Lett.*, vol. 3, no. 1, p. 2, 2013.
- [281] Z. Jing, C. Wang, G. Wang, W. Li and D. Lu, "Preparation and antibacterial activities of undoped and palladium doped titania nanoparticles," *J. of Sol-Gel Sci. Techn.*, vol. 56, no. 2, pp. 121-127, 2010.
- [282] C. R. Aita, Y. -L. Liu, M. L. Kao and S. D. Hansen, "Optical behavior of sputter-deposited vanadium pentoxide," *J. Appl. Phys.*, vol. 60, p. 749–753, 1986.
- [283] A. Slav, "Optical characterization of TiO₂-Ge nanocomposite films obtained by reactive magnetron sputtering," *Dig. J. Nanomater. Bios.*, vol. 6, no. 3, pp. 915 - 920, 2011.
- [284] M. A. Debeila, M. C. Raphulu, M. Mokoena, M. Avalos, V. Petranovskii, N. J. Coville and M. S. Scurrill, "The influence of gold on the optical properties of

- sol-gel derived titania," *Mat. Sci. Eng. A*, vol. 396, p. 70 – 76, 2005.
- [285] D. B. Hamal and K. J. Klabunde, "Synthesis, characterization, and visible light activity of new nanoparticle photocatalysts based on silver, carbon, and sulfur-doped TiO₂," *J. Colloid Interf. Sci.*, vol. 311, p. 514 – 522, 2007.
- [286] T. H. Gfroerer, "Photoluminescence in Analysis of Surfaces and Interfaces," in *Encyclopedia of Analytical Chemistry*, Chichester, John Wiley & Sons Ltd., 2000, p. 9209 – 9231.
- [287] Wikipedia, "Photoluminescence - Wikipedia, the free encyclopedia," Wikipedia, 2014. [Online]. Available: <https://en.wikipedia.org/wiki/Photoluminescence>. [Accessed 2914].
- [288] G. R. Hayes and B. Deveaud, "Is Luminescence from Quantum Wells Due to Excitons?," *physica status solidi (a)*, vol. 190, no. 3, p. 637–640, 2002.
- [289] U. o. W. Department of Physics, "Photoluminescence," University of Warwick, 4 January 2011. [Online]. Available: <https://www2.warwick.ac.uk/fac/sci/physics/current/postgraduate/regs/mpags/ex5/techniques/optical/pl/>. [Accessed 2014].
- [290] J. Liqiang, S. Xiaojun, X. Baifu, W. Baiqi, C. Weimin and F. Honggang, "The preparation and characterization of La doped TiO₂ nanoparticles and their photocatalytic activity," *J. Solid State Chem.*, vol. 177, p. 3375 – 3382, 2004.
- [291] "Gas Sensor Testing System," Kenosistec, [Online]. Available: http://www.kenosistec.com/en/product_card.php?id=9.
- [292] M. Hema, A. Y. Arasi, P. Tamilselvi and R. Anbarasan, "Titania Nanoparticles Synthesized by Sol-Gel Technique," *Chem. Sci. Trans.*, vol. 2, no. 1, pp. 239 - 245, 2013.
- [293] S. Mozia, "Effect of calcination temperature on photocatalytic activity of TiO₂. Photodecomposition of mono- and polyazo dyes in water," *Pol. J. Chem. Tech.*, vol. 10, no. 3, pp. 42-49, 2008.

- [294] M. H. Mangrola, B. H. Parmar, A. S. Pillai and C. G. Joshi, "Structural, Optical and Electrical Properties of Titanium Dioxide Nanoparticles," *Multi. Disci. Edu. Glob. Que.*, vol. 1, no. 1, pp. 24-32, 2011.
- [295] Z. Zhang, C. C. Wang, R. Zakaria and J. Y. Ying, "Role of particle size in nanocrystalline TiO₂-based photocatalysts," *J. Phys. Chem. B*, vol. 102, no. 52, p. 10871 – 10878, 1998.
- [296] F. D. Hardcastle, "Raman spectroscopy of Titania (TiO₂) nanotubular water-splitting catalysts," *J. Ark. Acad.Sci.*, vol. 65, pp. 43-48, 2011.
- [297] R. S. Katiyars, P. Dawsons, M. M. Hargreaves and G. R. Wilkinson, "Dynamics of the rutile structure. III. Lattice dynamics, infrared and Raman spectra of SnO₂," *J. Phys. C: Solid St. Phys.*, vol. 4, pp. 2421 - 2431, 1971.
- [298] O. Manuel, J. V. Garcia-Ramos and C. J. Serna, "Low-Temperature Nucleation of Rutile Observed by Raman Spectroscopy during Crystallization of TiO₂," *J. Am. Ceram. Soc.*, vol. 75, p. 2010, 1992.
- [299] J. Kim, K. C. Song, S. Foncillas and S. E. Pratsinis, " , 21 ()," *J. Eur. Ceram. Soc.*, vol. 21, p. 2863–2872, 2001.
- [300] B. Akbari, M. P. Tavandashti and M. Zandrahimi, "PARTICLE SIZE CHARACTERIZATION OF NANOPARTICLES – A PRACTICAL APPROACH," *Iranian Journal of Materials Science & Engineering*, vol. 8, no. 2, pp. 48-56, 2011.
- [301] G. V. Khade, M. B. Suwarnkar, N. L. Gavade and K. M. Garadkar, "Green synthesis of TiO₂ and its photocatalytic activity," *J Mater Sci: Mater Electron*, vol. 26, no. 5, pp. 3309-3315, 2015.
- [302] P. Anandgaonker, G. Kulkarni, S. Gaikwad and A. Rajbhoj, "Synthesis of TiO₂ nanoparticles by electrochemical method and their antibacterial application," *Arabian J. Chem.*, vol. <http://dx.doi.org/10.1016/j.arabjc.2014.12.015>, 2015.
- [303] M. M. Khan, S. A. Ansari, D. Pradhan, M. O. Ansari, D. H. Han, J. Lee and M.

- H. Cho, "Band gap engineered TiO₂ nanoparticles for visible light induced photoelectrochemical and photocatalytic studies," *J. Mater. Chem. A*, vol. 2, p. 637–644, 2014.
- [304] G. F. Fine, L. M. Cavanagh, A. Afonja and R. Binions, "Metal Oxide Semiconductor Gas Sensors in Environmental Monitoring," *Sensors*, vol. 10, pp. 5469-5502, 2010.
- [305] C. Garzella, E. Comini, E. Tempesti, C. Frigeri and G. Sberveglieri, "TiO₂ thin films by a novel sol–gel processing for gas sensor applications," *Sens. Act. B*, vol. 68, no. 1, p. 189–196, 2000.
- [306] A. A. Haidry, P. Schlosser, P. Durina, M. Mikula, M. Tomasek, T. Plecenik, T. Roch, A. Pidik, M. Stefecka, J. Noskovic, M. Zahoran, P. Kus and A. Plecenik, "Hydrogen gas sensors based on nanocrystalline TiO₂," *Cent. Eur. J. Phys.*, vol. 9, no. 5, pp. 1351-1356, 2011.
- [307] K. Zakrzewska, M. Radecka and M. Rekas, "Effect of Nb, Cr, Sn additions on gas sensing properties of TiO₂ thin films," *Thin Solid Films*, vol. 310, no. 1, pp. 161-166, 1997.
- [308] M. Radecka, M. Jasiński, J. Klich-Kafel, M. Rękas, B. Łysoń, A. Czapla, M. Lubecka, M. Sokołowski, K. Zakrzewska, A. Heel and T. J. Graule, "TiO₂-based Nanopowders for Gas Sensor," *Ceram. Mater.*, vol. 62, no. 4, pp. 545-549, 2010.
- [309] B. Karunagaran, P. Uthirakumar, S. J. Chung, S. Velumani and E.-K. Suh, "TiO₂ thin film gas sensor for monitoring ammonia," *Mater. Charact.*, vol. 58, no. 8, p. 680–684, 2007.
- [310] M. A. Henderson, J. M. White, H. Uetsuka and H. J. Onishi, "Photochemical charge transfer and trapping at the interface between an organic adlayer and an oxide semiconductor," *Am. Chem. Soc.*, vol. 125, p. 14974 – 14975, 2003.
- [311] A. Zaban, S. T. Aruna, S. Tirosh, B. A. Gregg and Y. Mastai, "The effect of the preparation condition of TiO₂ colloids on their surface structures," *J. Phys.*

- Chem. B*, vol. 104, no. 17, p. 4130 – 4133, 2000.
- [312] L. D. Finkelstein, E. Z. Kurmaev, M. A. Korotin, A. Moewes, B. Schneider, S. M. Butorin, J. H. Guo, J. Nordgren, D. Hartmann, M. Neumann and D. L. Ederer, *Phys. Rev. B*, vol. 60, p. 2212, 1999.
- [313] R. A. Taylor., T. P. Otanicar., Y. Herukerrupu, F. Bremond, G. Rosengarten, E. R. Hawkes, X. Jiang and S. Coulombe, “Feasibility of nanofluid-based optical filters,” *Appl. Optics*, vol. 53, no. 7, p. 1413–22, 2013.
- [314] E. Barborini, I. N. Kholmanov, P. Piseri, C. Ducati, C. E. Bottani and P. Milani, “Hierarchically organized nanostructured TiO₂ for photocatalysis applications,” *Appl. Phys. Lett.*, vol. 81, no. 16, pp. 3052-3054, 2002.
- [315] D. Bersani, P. P. Lottici and X. Z. Ding, “Phonon confinement effects in the Raman scattering by TiO₂ nanocrystals,” *Appl. Phys. Lett.*, vol. 72, p. 73, 1998.
- [316] R. Brydson, B. G. Williams, W. Engel, H. Sauer, E. Zeitler and J. M. Thomas, “Electron energy-loss spectroscopy (EELS) and the electronic structure of titanium dioxide,” *Solid State Commun.*, vol. 64, p. 609, 1987.
- [317] R. Brydson, H. Sauer, W. Engel, J. M. Thomas, E. Zeitler, N. Kosugi and H. Kuroda, “Electron-energy-loss and X-ray absorption spectroscopy of rutile and anatase,” *J. Phys.: Condens. Matter*, vol. 1, p. 797, 1989.
- [318] R. Sanjines, H. Tang, H. Berger, F. Gozzo, G. Margaritondo and F. Levy, “Electronic structure of anatase TiO₂ oxide,” *J. Appl. Phys.*, vol. 75, pp. 2945-2951, 1994.
- [319] Z. L. Lu, E. Lindner and H. A. Mayer, “Applications of sol-gel-processed interphase Catalysts,” *Chem. Rev.*, vol. 102, p. 3543–3578, 2002.
- [320] A. P. Wight and M. E. Davis, “Design and Preparation of Organic-Inorganic Hybrid Catalysts,” *Chem. Rev.*, vol. 102, p. 3589, 2002.
- [321] J. A. Schwarz, C. Contescu and A. Contescu, “Methods of Preparation of

Catalytic Materials,” *Chem. Rev.*, vol. 95, pp. 477-510, 1995.

[322] R. Chauhan, A. Kumar and R. P. Chaudhary, “Structural and photocatalytic studies of Mn doped TiO₂ nanoparticles,” *Spectrochim. Acta A*, vol. 98, p. 256–264, 2012.

[323] R. López and R. Gómez, “Band gap energy estimation from diffuse reflectance measurements on sol-gel and commercial TiO₂: A comparative study,” *J. Sol-Gel Sci. Technol.*, vol. 61, p. 1–7, 2012.

[324] J. M. Wu, “Low-temperature preparation of titania nanorods through direct oxidation of titanium with hydrogen peroxide,” *J. Cryst. Growth*, vol. 269, no. 2-4, pp. 347-352, 2004.

Appendix A: List of Publications & Presentations

Below are publications and conference presentations linked to this study:

Publications:

1. O. O. Nubi, K. E. Rammutla and T. E. Mosuang, "Synthesis and Characterisation of Ag- Cu-Doped Nano TiO₂," Proceedings of the 57th annual conference of the South African Institute of Physics Hosted by the University of Pretoria, Pretoria, South Africa, 9th – 13th July 2012.
2. O. O. Nubi, K. E. Rammutla and T.E. Mosuang, "Effects of Ag/Cu Metal Co-doping on the Structural Properties of NanocrystallineTiO₂," Proceedings of the "International Conference on Advanced Nanomaterials & Emerging Engineering Technologies" (ICANMEET-2013) organized by Sathyabama University, Chennai, India in association with DRDO, New Delhi, India, 24th - 26th, July 2013.
3. O. O. Nubi, K. E. Rammutla and T. E. Mosuang, "Structural and optical characterisation of double-doped TiO₂ nanoparticles," Proceedings of the 59th annual conference of the South African Institute of Physics hosted by the University of Johannesburg, Johannesburg, South Africa, 7th – 11th July 2014.
4. O. O. Nubi, K. E. Rammutla and T. E. Mosuang, "Single versus Double Doping of Sol-Gel Derived Nanotitania with Ag and Cu," *Adv. Sci. Lett.*, vol. 22, p. 889-895, 2016.

Presentations:

5. O. O. Nubi, K. E. Rammutla and T. E. Mosuang, "Synthesis and Characterisation of Ag- Cu-Doped Nano TiO₂," 57th annual conference of the South African Institute of Physics Hosted by the University of Pretoria, Pretoria, South Africa, 9th – 13th July 2012.
6. O. O. Nubi, K. E. Rammutla and T. E. Mosuang, "Effects of Ag/Cu Combinational Doping on Phase Transformation of TiO₂ Nanopowders," 2013 Faculty of Science & Agriculture Research Day Hosted by the University of Limpopo, Limpopo, South Africa, 9th – 13th Oct 2013.

7. O. O. Nubi, K. E. Rammutla and T. E. Mosuang, "Effects of Ag/Cu Double-Doping on the Structural Properties of Nanostructured Titanium Dioxide (TiO₂)TiO₂," 2013 IBSA Workshop on Advanced Materials (Sensors), St George Hotel & Convention Centre, Gauteng Province, South Africa, 17th – 20th March 2013.
8. O. O. Nubi, K. E. Rammutla and T. E. Mosuang, "Combinational Doping & Phase Transformation of Nano TiO₂," 2013 India-Brazil-South Africa (IBSA) Nanotechnology Workshop, St George's Hotel & Convention Centre, Centurion, South Africa, 29th – 31st May 2013.
9. O. O. Nubi, K. E. Rammutla and T. E. Mosuang, "Effects of Metal Combinational Doping on Phase Transformation of Nanostructured Titanium Dioxide," 58th annual conference of the South African Institute of Physics Hosted by the University of Zululand, Richards Bay, South Africa, 8th – 12th July 2013.
10. O. O. Nubi, K. E. Rammutla and T.E. Mosuang, "Effects of Ag/Cu Metal Co-doping on the Structural Properties of NanocrystallineTiO₂," International Conference on Advanced Nanomaterials & Emerging Engineering Technologies" (ICANMEET-2013) organized by Sathyabama University, Chennai, India in association with DRDO, New Delhi, India, 24th -26th, July 2013.
11. O. O. Nubi, K. E. Rammutla and T. E. Mosuang, "Phases & Transformation of Double-Doped TiO₂ Nanopowders," IBSA Meeting on Nanotechnology, Curitiba, Brazil, 27th – 29th November 2013.
12. O. O. Nubi, K. E. Rammutla and T. E. Mosuang, "Structural and optical characterisation of double-doped TiO₂ nanoparticles," 59th annual conference of the South African Institute of Physics University of Johannesburg, Johannesburg, South Africa, 7th – 11th July 2014.
13. O. O. Nubi, K. E. Rammutla and T.E. Mosuang, "Single versus Double Doping of Sol-Gel Derived NanoTitania with Ag and Cu," International Conference on Nanotechnology" (NANOCON 014) organised by Bharati Vidyapeeth University, Pune, India, 14th – 15th Oct, 2014.

Appendix B: List of Abbreviations

Below are some of the abbreviations used in this thesis:

-TiO_2 : Undoped TiO_2

$\text{Ag}\backslash\text{TiO}_2$: Ag-doped TiO_2

$\text{Cu}\backslash\text{TiO}_2$: Cu-doped TiO_2

$\text{Ag+Cu}\backslash\text{TiO}_2$: Ag and Cu co-doped TiO_2

AMCSD: American Mineralogist Crystal Structure Database

COD: Crystallography Open Database

CVD: Chemical Vapour Deposition

DRS: Diffuse reflectance spectroscopy

DSC: Differential scanning calorimetry

DSSC: Dye-sensitised nanocrystalline solar cell

EDS, EDX: Energy dispersive X-ray spectroscopy

ESR: Electron-spin resonance spectroscopy

FTIR: Fourier-transform infrared spectroscopy

FWHM: Full-width at half-maximum

JCPDS: Joint Committee on Powder Diffraction Standards

MOS: Metal-Oxide Semiconductor

PL: Photoluminescence

SEM: Scanning electron microscopy

SGS: Semiconductor Gas Sensors

TEM: Transmission electron microscopy

TGA: Thermogravimetric analysis

TTIP: Titanium Isopropoxide

UV-Vis: Ultraviolet visible spectroscopy

XANES: X-ray-absorption near-edge structure

XPS: X-ray photoelectron spectroscopy

XRD: X-ray diffraction

Appendix C: Specification Sheets

Crystallography Open Database (COD) entries for phase identification in XRD data analyses:

C1: Anatase TiO₂ – Entry # 96-901-5930 [268]

Phase classification

Name	
Mineral Name	Anatase
Formula	O ₂ Ti
I/ICor	5.320000
Sample Name	9015929
Quality	C (calculated)

References

Publication

Bibliography Howard C. J., Sabine T. M., Dickson F., "Structural and thermal parameters for rutile and anatase", Acta Crystallographica, Section B 47, 462-468 (1991)

Origin of data

Source of entry COD (Crystallography Open Database)
Link to orig. entry <http://www.crystallography.net/cif/9/01/59/9015929.cif>

Crystal structure

Crystallographic data

Space group I 41/a m d (141)
Crystal system tetragonal
Cell parameters a= 3.7845 Å c= 9.5143 Å

Atom coordinates	Element	Oxide	x	y	z	Bi	Focc	U11	U22	U33	U12	U13	U23
	Ti		0.00	0.00	0.00	1.00	1.00	0.00	0.00	0.00	0.00	0.00	0.007
			0	0	0	0000	0000	5100	0000	0000	5100	0000	000
	O		0.00	0.00	0.20	1.00	1.00	0.01	0.00	0.00	0.00	0.00	0.007
			0	0	8	0000	0000	1700	0000	0000	2700	0000	100

Diffraction data

Diffraction lines

d [Å]	Int.	h	k	l	Mult.
3.5165	1000.0	0	1	1	8
2.4308	59.9	0	1	3	8
2.3786	197.0	0	0	4	2
2.3323	67.0	1	1	2	8
1.8922	267.1	0	2	0	4
1.7001	167.4	0	1	5	8
1.6663	162.0	1	2	1	16
1.4932	25.5	1	2	3	16
1.4808	123.1	0	2	4	8
1.3642	52.5	1	1	6	8
1.3380	58.7	2	2	0	4
1.2792	4.2	0	1	7	8
1.2646	88.7	1	2	5	16
1.2506	23.4	0	3	1	8
1.1893	3.8	0	0	8	2
1.1722	5.2	0	3	3	8
1.1662	43.1	2	2	4	8
1.1606	15.1	1	3	2	16
1.0598	4.7	1	2	7	16
1.0514	21.1	0	3	5	8
1.0433	23.5	2	3	1	16
1.0182	15.7	0	1	9	8

1.0069 9.0 0 2 8 8

Experimental

Physical Properties

Calc. density 3.89400 g/cm³

Remarks

Remarks

Comments - Space group has been derived from given symmetry operations.
 - Diffraction pattern calculated by Match!.
 - I/lcor calculated by Match!.

C2: Brookite TiO₂ – Entry # 96-900-4140 [268]

Phase classification

Name	
Mineral Name	Brookite
Formula	O ₂ Ti
I/lcor	1.790000
Sample Name	9004139
Quality	C (calculated)

References

Publication

Bibliography Meagher E. P., Lager G. A., "Polyhedral thermal expansion in the TiO₂ polymorphs: Refinement of the crystal structures of rutile and brookite at high temperature Sample at 425 degrees C", The Canadian Mineralogist **17**, 77-85 (1979)

Origin of data

Source of entry COD (Crystallography Open Database)
 Link to orig. entry <http://www.crystallography.net/cif/9/00/41/9004139.cif>

Crystal structure

Crystallographic data

Space group P b c a (61)
 Crystal system orthorhombic
 Cell parameters a= 9.1910 Å b= 5.4630 Å c= 5.1570 Å

Atom coordinates	Element	Oxid.	x	y	z	Bi	Focc	U11	U22	U33	U12	U13	U23
	Ti		0.12 9	0.09 9	0.86 3	1.00 000	1.000 000	0.01 540	0.01 220	0.008 000	- 0.000	0.000 800	0.0001 00
	O		0.01 0	0.14 9	0.18 4	1.00 000	1.000 000	0.01 450	0.01 600	0.010 600	- 0.003	0.002 500	- 0.0022
	O		0.23 1	0.11 2	0.53 6	1.00 000	1.000 000	0.01 540	0.01 770	0.009 400	0.003 700	0.002 200	0.0020 00

Diffraction data

Diffraction lines

d [Å]	Int.	h	k	l	Mult.
4.5955	3.8	2	0	0	2
3.5167	1000.0	2	1	0	4
3.4722	747.8	1	1	1	8
2.9055	933.9	2	1	1	8
2.7315	39.1	0	2	0	2

2.5785	2.4	0	0	2	2
2.4827	234.4	1	0	2	4
2.4138	174.0	0	2	1	4
2.3726	71.0	3	1	1	8
2.3480	19.7	2	2	0	4
2.3346	20.4	1	2	1	8
2.2977	38.6	4	0	0	2
2.2602	38.6	1	1	2	8
2.2487	152.3	2	0	2	4
2.1370	151.9	2	2	1	8
2.1180	3.7	4	1	0	4
2.0794	3.8	2	1	2	8
1.9728	193.8	3	0	2	4
1.9592	11.7	4	1	1	8
1.8960	318.5	3	2	1	8
1.8750	1.2	0	2	2	4
1.8555	200.6	3	1	2	8
1.8372	23.9	1	2	2	8
1.7584	30.2	4	2	0	4
1.7361	0.2	2	2	2	8
1.7155	8.2	4	0	2	4
1.6929	211.5	2	3	0	4
1.6879	21.3	1	3	1	8
1.6643	313.3	4	2	1	8
1.6506	52.8	5	1	1	8
1.6367	4.5	4	1	2	8
1.6142	147.3	1	1	3	8
1.6085	12.9	2	3	1	8
1.5993	18.1	3	2	2	8
1.5444	60.2	2	1	3	8
1.5318	2.6	6	0	0	2
1.4979	0.1	3	3	1	8
1.4968	109.4	5	0	2	4
1.4749	15.2	6	1	0	4
1.4684	71.2	1	3	2	8
1.4624	102.8	5	2	1	8
1.4549	63.5	0	2	3	4
1.4527	4.4	4	2	2	8
1.4457	36.7	3	1	3	8
1.4436	66.4	5	1	2	8
1.4370	136.5	1	2	3	8
1.4272	3.3	4	3	0	4
1.4181	76.8	6	1	1	8
1.4152	1.9	2	3	2	8
1.3870	2.2	2	2	3	8
1.3755	1.6	4	3	1	8
1.3657	69.0	0	4	0	2
1.3381	82.6	3	3	2	8
1.3361	0.3	6	2	0	4
1.3347	1.2	4	1	3	8
1.3202	27.5	0	4	1	4
1.3170	10.7	6	0	2	4
1.3142	18.9	3	2	3	8
1.3126	8.3	5	2	2	8
1.3092	0.3	2	4	0	4
1.3068	4.9	1	4	1	8
1.2934	3.7	6	2	1	8
1.2893	20.7	0	0	4	2
1.2803	2.4	6	1	2	8
1.2768	10.7	1	0	4	4
1.2689	1.2	2	4	1	8
1.2548	1.0	5	3	1	8
1.2487	1.1	4	3	2	8
1.2432	0.8	1	1	4	8
1.2413	1.1	2	0	4	4
1.2392	44.4	7	1	1	8
1.2386	20.0	1	3	3	8
1.2292	7.2	4	2	3	8
1.2236	3.5	5	1	3	8
1.2124	10.5	3	4	1	8

1.2105	27.6	2	1	4	8
1.2069	0.1	0	4	2	4
1.2062	3.3	2	3	3	8
1.1966	18.6	1	4	2	8
1.1883	0.1	3	0	4	4
1.1863	0.0	6	2	2	8
1.1740	5.3	4	4	0	4
1.1722	24.8	6	3	0	4
1.1700	13.9	7	0	2	4
1.1673	11.2	2	4	2	8
1.1659	3.0	0	2	4	4
1.1612	12.7	3	1	4	8
1.1574	0.0	3	3	3	8
1.1566	1.0	1	2	4	8
1.1563	39.6	5	3	2	8
1.1534	1.5	7	2	1	8
1.1489	37.3	8	0	0	2
1.1447	7.2	4	4	1	8
1.1441	11.4	7	1	2	8
1.1431	6.3	6	3	1	8
1.1408	11.8	5	2	3	8
1.1301	0.0	2	2	4	8
1.1244	41.7	4	0	4	4
1.1243	0.2	8	1	0	4
1.1229	25.1	3	4	2	8
1.1194	7.4	6	1	3	8
1.1013	0.0	4	1	4	8
1.0985	0.0	8	1	1	8
1.0980	0.1	4	3	3	8
1.0897	0.1	3	2	4	8
1.0755	1.3	7	2	2	8
1.0723	9.8	5	4	1	8
1.0693	3.2	0	4	3	4
1.0685	1.9	4	4	2	8
1.0671	4.0	6	3	2	8
1.0630	0.0	2	5	0	4
1.0622	11.0	1	4	3	8
1.0617	10.8	1	5	1	8
1.0590	2.2	8	2	0	4
1.0555	0.6	5	0	4	4
1.0549	0.0	6	2	3	8
1.0494	0.8	8	0	2	4
1.0454	1.0	1	3	4	8
1.0430	6.6	7	3	1	8
1.0415	0.7	2	4	3	8
1.0411	33.5	2	5	1	8
1.0397	6.2	4	2	4	8
1.0374	16.3	8	2	1	8
1.0364	3.0	5	1	4	8
1.0337	0.8	5	3	3	8
1.0306	2.3	8	1	2	8
1.0257	41.9	2	3	4	8
1.0249	18.4	7	1	3	8
1.0194	0.5	6	4	0	4
1.0096	3.2	3	4	3	8
1.0092	8.7	3	5	1	8
1.0089	29.7	5	4	2	8
1.0074	0.5	1	1	5	8

Experimental

Physical Properties

Calc. density 4.09700 g/cm³

Remarks

Remarks

Comments - Diffraction pattern calculated by Match!.
- I/I_{cor} calculated by Match!.

C3: Rutile TiO₂ – Entry # 96-900-7532 [268]

Phase classification

Name	
Mineral Name	Rutile
Formula	O ₂ Ti
I/Icor	3.860000
Sample Name	9007531
Quality	C (calculated)

References

Publication

Bibliography Baur W. H., Khan A. A., "Rutile-type compounds. VI. SiO₂, GeO₂ and a comparison with other rutile-type structures", Acta Crystallographica, Section B 27, 2133-2139 (1971)

Origin of data

Source of entry COD (Crystallography Open Database)

Link to orig. entry <http://www.crystallography.net/cif/9/00/75/9007531.cif>

Crystal structure

Crystallographic data

Space group P 4₂/m n m (136)

Crystal system tetragonal

Cell parameters a= 4.5941 Å c= 2.9589 Å

Atom coordinates	Element	Oxid.	x	y	z	Bi	Focc	U11	U22	U33	U12	U13	U23
	Ti		0.00	0.00	0.00	1.00	1.000	0.007	0.007	0.007	-	0.00	0.0000
			0	0	0	000	000	100	100	700	0.000	000	00
						0					100	0	
	O		0.30	0.30	0.00	1.00	1.000	0.008	0.008	0.007	-	0.00	0.0000
			6	6	0	000	000	000	000	700	0.000	000	00
						0					100	0	

Diffraction data

Diffraction lines

d [Å]	Int.	h	k	l	Mult.
3.2485	1000.0	1	1	0	4
2.4876	439.3	1	0	1	8
2.2970	66.1	2	0	0	4
2.1875	177.8	1	1	1	8
2.0545	64.8	1	2	0	8
1.6876	514.4	2	1	1	16
1.6243	150.4	2	2	0	4
1.4794	70.0	0	0	2	2
1.4528	69.6	1	3	0	8
1.4238	5.5	2	2	1	8
1.3600	172.5	3	0	1	8
1.3464	83.9	1	1	2	8
1.3041	8.9	3	1	1	16
1.2742	1.9	2	3	0	8
1.2438	17.5	2	0	2	8
1.2006	9.9	2	1	2	16
1.1703	33.7	3	2	1	16
1.1485	22.7	4	0	0	4
1.1142	8.2	1	4	0	8
1.0937	54.5	2	2	2	8
1.0828	29.9	3	3	0	4
1.0427	51.5	4	1	1	16
1.0366	38.5	3	1	2	16
1.0273	22.9	2	4	0	8
1.0169	0.4	3	3	1	8

Experimental

Physical Properties

Calc. density 4.24800 g/cm³

Remarks

Remarks

Comments - Diffraction pattern calculated by Match!.
- I/Icor calculated by Match!.

C4: Silver (Ag) – Entry # 96-900-8460 [268]

Phase classification

Name	
Mineral Name	Silver
Formula	Ag
I/Icor	19.120001
Sample Name	9008459
Quality	C (calculated)

References

Publication

Bibliography Wyckoff R. W. G., "Second edition. Interscience Publishers, New York, New York Cubic closest packed, ccp, structure", Crystal Structures 1, 7-83 (1963)

Origin of data

Source of entry COD (Crystallography Open Database)
Link to orig. entry <http://www.crystallography.net/cif/9/00/84/9008459.cif>

Crystal structure

Crystallographic data

Space group	F m -3 m (225)														
Crystal system	cubic														
Cell parameters	a= 4.0862 Å														
Atom coordinates	<table border="1"> <thead> <tr><th>Element</th><th>Oxid.</th><th>x</th><th>y</th><th>z</th><th>Bi</th><th>Focc</th></tr> </thead> <tbody> <tr><td>Ag</td><td></td><td>0.000</td><td>0.000</td><td>0.000</td><td>1.000000</td><td>1.000000</td></tr> </tbody> </table>	Element	Oxid.	x	y	z	Bi	Focc	Ag		0.000	0.000	0.000	1.000000	1.000000
Element	Oxid.	x	y	z	Bi	Focc									
Ag		0.000	0.000	0.000	1.000000	1.000000									

Diffraction data

Diffraction lines

d [Å]	Int.	h	k	l	Mult.
2.3592	1000.0	1	1	1	8
2.0431	467.8	2	0	0	6
1.4447	256.2	2	0	2	12
1.2320	271.7	3	1	1	24
1.1796	76.9	2	2	2	8
1.0216	36.9	4	0	0	6
0.9374	129.9	3	1	3	24
0.9137	128.9	4	0	2	24
0.8341	151.9	4	2	2	24
0.7864	359.5	3	3	3	8

Experimental

Physical Properties

Calc. density 10.50000 g/cm³

Remarks

Remarks

Comments - Diffraction pattern calculated by Match!.
- I/Icor calculated by Match!.

C5: Tenorite (CuO) – Entry # 96-901-6327 [268]

Phase classification

Name	
Mineral Name	Tenorite
Formula	CuO
I/Icor	4.900000
Sample Name	9016326
Quality	C (calculated)

References

Publication

Bibliography Asbrink S., Waskowska A., "CuO: x-ray single-crystal structure determination at 196 K and room temperature Note: T = room temperature", Journal of Physics: Condensed Matter 3, 8173-8180 (1991)

Origin of data

Source of entry COD (Crystallography Open Database)
Link to orig. entry <http://www.crystallography.net/cif/9/01/63/9016326.cif>

Crystal structure

Crystallographic data

Space group	C 1 c 1 (9)												
Crystal system	monoclinic												
Cell parameters	a= 4.6927 Å b= 3.4283 Å c= 5.1370 Å β= 99.546 °												
Atom coordinates	Element	Oxid.	x	y	z	Bi	Focc	U11	U22	U33	U12	U13	U23
	Cu		0.25	0.24	0.00	1.000	1.0000	0.0064	0.0086	0.0057	0.0016	0.0022	0.0000
			0	7	0	00	00	00	00	00	00	00	00
	O		-	0.41	0.26	1.0000	1.0000	0.0061	0.0119	0.0054	-	0.0030	-
			0.01	8	0	00	00	00	00	00	0.0020	00	0.0005
			0								00		00

Diffraction data

Diffraction lines

d [Å]	Int.	h	k	l	Mult.
2.7547	62.4	1	1	0	4
2.5329	304.7	0	0	2	2
2.5270	809.9	1	1	-1	4
2.3256	1000.0	1	1	1	4
2.3139	234.0	2	0	0	2
1.9636	16.2	-1	1	2	4
1.8697	280.6	2	0	-2	2
1.7791	11.1	1	1	2	4
1.7141	110.4	0	2	0	2
1.6237	7.4	0	2	1	4
1.5826	146.1	2	0	2	2
1.5075	198.9	-1	1	3	4
1.4196	155.4	0	2	2	4
1.4116	150.3	3	1	-1	4
1.4067	3.3	3	1	0	4
1.3802	94.3	1	1	3	4
1.3774	136.4	2	2	0	4
1.3636	2.8	2	2	-1	4
1.3173	2.7	3	1	-2	4
1.3055	74.7	3	1	1	4
1.2971	2.4	2	2	1	4
1.2665	55.1	0	0	4	2
1.2635	65.0	2	2	-2	4
1.2030	1.5	0	2	3	4
1.1977	22.0	-2	0	4	2
1.1964	1.7	-1	1	4	4
1.1715	48.5	3	1	-3	4
1.1628	46.0	2	2	2	4

1.1577	1.3	3	1	2	4
1.1569	37.5	4	0	0	2
1.1252	17.3	4	0	-2	2
1.1230	1.4	-2	2	3	4
1.1099	1.0	1	1	4	4
1.1094	0.2	1	3	0	4
1.0929	60.3	1	3	-1	4
1.0749	28.2	1	3	1	4
1.0406	12.9	2	0	4	2
1.0314	0.1	-1	3	2	4
1.0211	0.7	-3	1	4	4
1.0192	0.8	2	2	3	4
1.0186	29.4	0	2	4	4
1.0084	40.2	3	1	3	4

Experimental

Physical Properties

Calc. density 6.48200 g/cm³

Remarks

Remarks

Comments - Synthetic
- Diffraction pattern calculated by Match!.
- I/I_{cor} calculated by Match!.

C6: AgCl (Chlorargyrite) – Entry # 96-901-6327 [268]

Phase classification

Name	
Mineral Name	Chlorargyrite
Formula	AgCl
I/I _{cor}	9.500000
Sample Name	9011666
Quality	C (calculated)

References

Publication

Bibliography Hull S., Keen D. A., "Pressure-induced phase transitions in AgCl, AgBr, and AgI Locality: synthetic Sample: P = 0.0 GPa, Phase I", Physical Review B 59, 750-761 (1999)

Origin of data

Source of entry COD (Crystallography Open Database)
Link to orig. entry <http://www.crystallography.net/cif/9/01/16/9011666.cif>

Crystal structure

Crystallographic data

Space group	F m -3 m (225)																					
Crystal system	cubic																					
Cell parameters	a= 5.5463 Å																					
Atom coordinates	<table border="1"> <thead> <tr><th>Element</th><th>Oxid.</th><th>x</th><th>y</th><th>z</th><th>Bi</th><th>Focc</th></tr> </thead> <tbody> <tr><td>Ag</td><td></td><td>0.500</td><td>0.500</td><td>0.500</td><td>5.500000</td><td>1.000000</td></tr> <tr><td>Cl</td><td></td><td>0.000</td><td>0.000</td><td>0.000</td><td>3.200000</td><td>1.000000</td></tr> </tbody> </table>	Element	Oxid.	x	y	z	Bi	Focc	Ag		0.500	0.500	0.500	5.500000	1.000000	Cl		0.000	0.000	0.000	3.200000	1.000000
Element	Oxid.	x	y	z	Bi	Focc																
Ag		0.500	0.500	0.500	5.500000	1.000000																
Cl		0.000	0.000	0.000	3.200000	1.000000																

Diffraction data

Diffraction lines

d [Å]	Int.	h	k	l	Mult.
-------	------	---	---	---	-------

3.2022	506.1	1	1	1	8
2.7731	1000.0	2	0	0	6
1.9609	498.9	2	0	2	12
1.6723	99.8	3	1	1	24
1.6011	120.8	2	2	2	8
1.3866	39.8	4	0	0	6
1.2724	15.6	3	1	3	24
1.2402	79.8	4	0	2	24
1.1321	44.9	4	2	2	24
1.0674	4.7	3	3	3	8
0.9805	9.6	4	0	4	12
0.9375	2.1	5	3	1	48
0.9244	17.9	4	2	4	24
0.8769	11.7	6	0	2	24
0.8458	0.4	5	3	3	24
0.8361	10.5	6	2	2	24
0.8005	3.7	4	4	4	8

Experimental

Physical Properties

Calc. density 5.58000 g/cm³

Remarks

Remarks

Comments - Diffraction pattern calculated by Match!.
- I/I_{cor} calculated by Match!.

Appendix D: Sigma-Aldrich Data Specification Sheets

Sigma-Aldrich [260] data specification sheets of precursors used for synthesising samples – as supplied by the manufacturer:

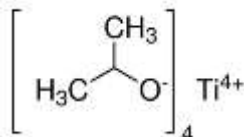
D1: Titanium(IV) Isopropoxide [260]

687502 ALDRICH – Packaged for use in deposition systems

Synonym: TTIP, Tetraisopropyl orthotitanate

CAS Number 546-68-9

- Linear Formula $\text{Ti}[\text{OCH}(\text{CH}_3)_2]_4$
- Molecular Weight 284.22
- Beilstein Registry Number 3679474
- EC Number 208-909-6
- MDL number MFCD00008871



Properties

Form	liquid
Refractive Index	$n_{20/D}$ 1.464(lit.)
Bp	232 °C(lit.)
Mp	14-17 °C(lit.)
Density	0.96 g/mL at 20 °C(lit.)

D2: Silver Nitrate [260]

31630 SIGMA-ALDRICH – Puriss. p.a., ACS reagent, reagent ISO, reagent Ph. Eur., ≥99.8%

Synonym: Nitric acid silver(I) salt

- CAS Number [7761-88-8](#)
- Linear Formula AgNO_3
- Molecular Weight 169.87
- EC Number [231-853-9](#)
- MDL number [MFCD00003414](#)
- PubChem Substance ID [24859006](#)



Properties

Grade	ACS reagent, reagent ISO, reagent Ph. Eur.
Vapor Density	5.8 (vs air)
Grade	puriss. p.a.
Assay	≥99.8%
Form	solid
Impurities	≤0.01% subst. not precipitated by HCl (as SO_4)
Mp	212 °C (dec.)(lit.)
Anion Traces	chloride (Cl^-): ≤1 mg/kg
	nitrite (NO_2^-): ≤500 mg/kg
	sulfate (SO_4^{2-}): ≤20 mg/kg
Cation Traces	Cd: ≤1 mg/kg
	Cu: ≤2 mg/kg
	Fe: ≤2 mg/kg
	Mn: ≤5 mg/kg
	Pb: ≤10 mg/kg
	Zn: ≤1 mg/kg

D3: Copper(II) Chloride [260]

451665 ALDRICH – Anhydrous, powder, ≥99.995% trace metals basis

Synonym: Cupric chloride

- CAS Number [7447-39-4](#)
- Linear Formula CuCl_2

- Molecular Weight 134.45
- EC Number [231-210-2](#)
- MDL number [MFCD00010972](#)
- PubChem Substance ID [24868644](#)



Properties

Grade	anhydrous
Assay	≥99.995% trace metals basis
Form	powder
Mp	620 °C(lit.)
Density	3.386 g/mL at 25 °C(lit.)

Appendix E: Dopant Quantity Calculator

Description:

The Microsoft Excel® Program for calculating the quantity of precursor needed for the desired mass of the final sample, based on the wt % of dopant impurities. The filename of the workbook is “Dopant Levels.xlsx”. There is an option to carry out calculations for dopant concentration based on the number of moles (%*n*) as opposed to the mass percent (wt %). The program is designed to handle the adding of a maximum of two different dopants to the TiO₂ material, using a variety of mixing-order options, including:

- a. Add Dopant 1 first, then add Dopant 2
- b. Add Dopant 2 first, then add Dopant 1
- c. Add both Dopant 1 with Dopant 2 simultaneously.

Theory:

The %*n* and wt % calculations are based on the formulae:

$$\%n_D = \frac{n_D}{n_D + n_H} \times 100\%$$

$$w\% = \frac{m_D}{m_D + m_H} \times 100\%$$

Here *n* stands for number of moles and *m* represents the mass. The subscript D is for the dopant, while H is for the TiO₂ host.

Usage:

(Enter values in blue cells only. Other cells are calculated.)

- Enter chemical symbols for the constituent elements for matrix and dopants
- Enter corresponding number of atoms for each element
- Enter the concentrations (purities) and densities
- Enter the wt. % (or %*n*) for each of the dopants
- Enter the amount of the final product (in grams or mL) required.

Interface:

Dopant Level Calculator					
This program determines the amount or concentration of dopant (impurities) for a given matrix compound.					
Host					
		Initial		Final	
Constituents		Ti[OCH(CH3)2]4	MM	TiO2	
1	Symbol	ti	Titanium	47.9	
	Atoms	1			1
	Molar mass	47.9			47.9
2	Symbol	O	Oxygen	16	
	Atoms	4			2
	Molar mass	64			32
3	Symbol	C	Carbon	12	
	Atoms	12			
	Molar mass	144			0
4	Symbol	H	Hydrogen	1.01	
	Atoms	28			
	Molar mass	28.28			0
5	Symbol				
	Atoms				
	Molar mass				
	MolarMass	284.18			79.9
	No of moles:	1.251564			1.25156
	Concentration (%)	97			100
	Density (g/cm ³)	0.96			0.8
	Mass (g)	366.6697	TiO2 needed:	100	
	Volume (cm ³)	381.9476			Solid

Dopant 1				Dopant 2				
		Initial		Final		Initial		Final
Constituents		AgNO3	MM	Ag		CuCl3	MM	Cu
1	Symbol	Ag	Silver	107.9		Cu	Copper	63.6
	Atoms	1				1		1
	Molar mass	107.9				63.6		63.6
2	Symbol	N	Nitrogen	14		Cl	Chlorine	35.5
	Atoms	1				7		
	Molar mass	14				248.5		0
3	Symbol	O	Oxygen	16				
	Atoms	3						
	Molar mass	48						
4	Symbol							
	Atoms							
	Molar mass							
5	Symbol							
	Atoms							
	Molar mass							
	MolarMass	169.9		107.9		312.1		63.6
	Moles required:	0.00659		0.006587181		0.00659		0.006587181
	Concentration	99.8				99		
	Density (g/cm ³)	1	%n	2.5		0.9	%n	2.5
	Required Mass (g):	1.1214		0.71075687		2.07663		0.41894473
	Required Volume (cm ³)	1.1214				2.30736		

Calculation Method: %n (dopant concentration)

Doping Method: Add both Dopant 1 with Dopant 2 simultaneously

Total Dopant Conc. (%): 5

Total no of moles required: 0.013174

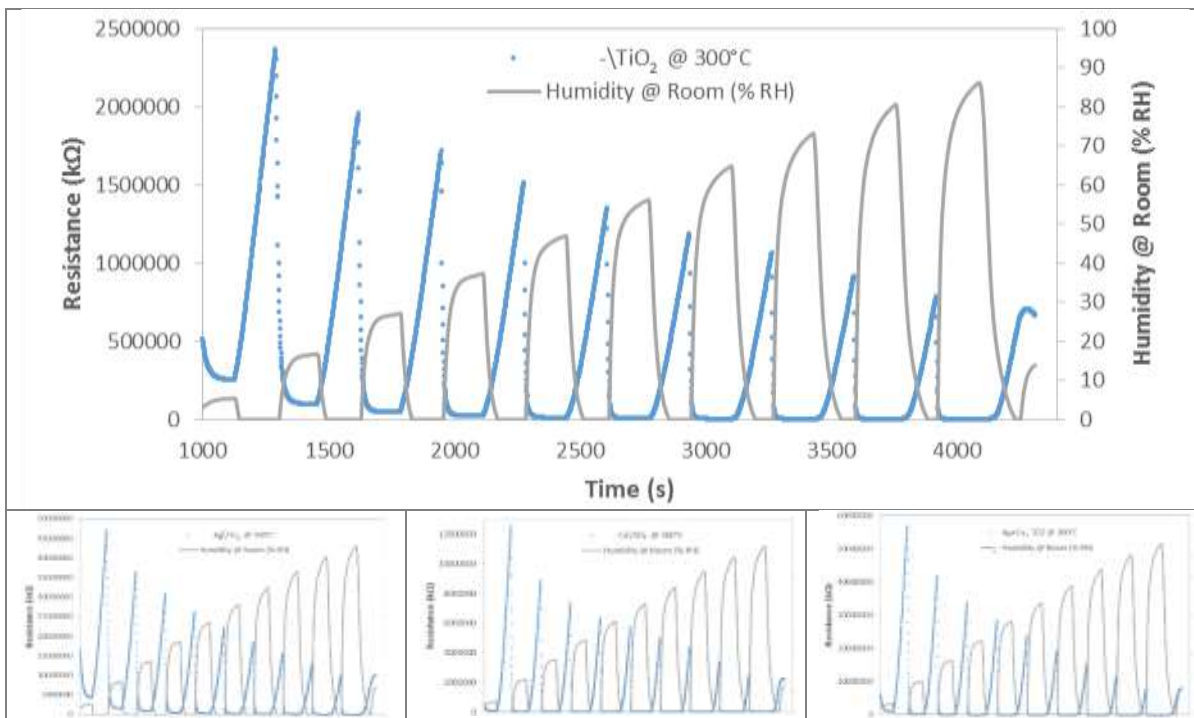
Total mass (g) required: 3.19803/1.1297

Total dopant volume (cm³) required: 3.428767

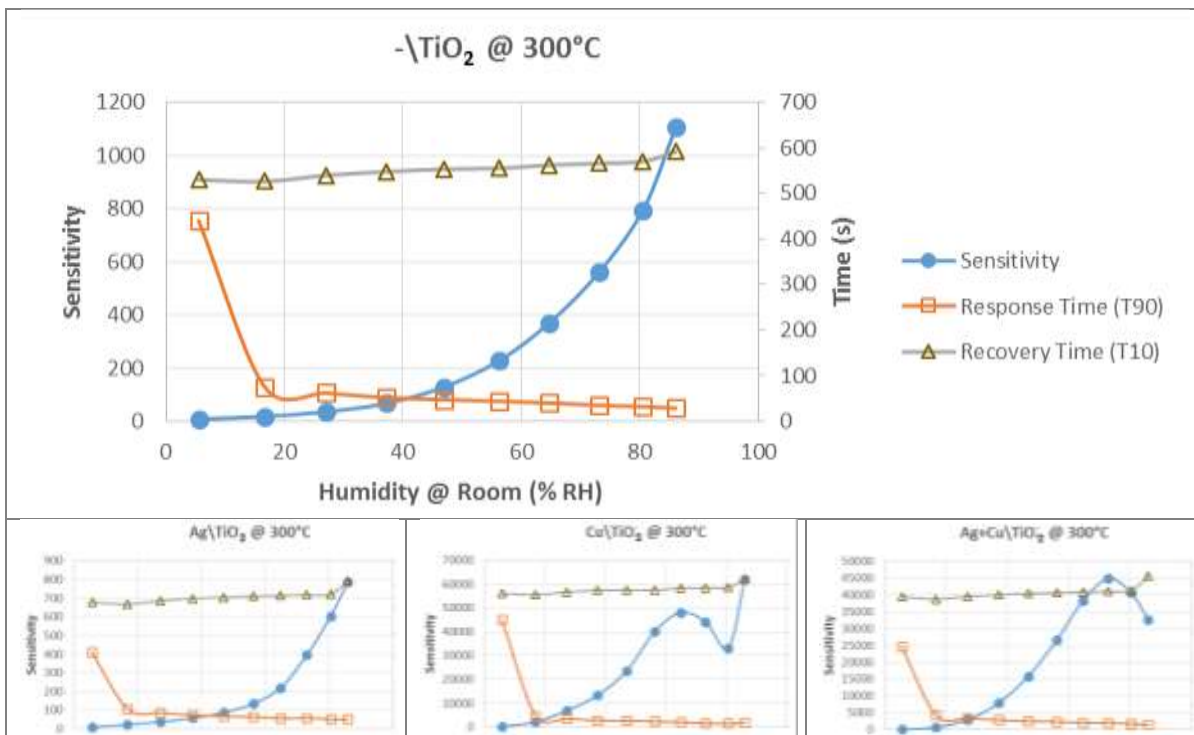
Appendix F: Gas-Sensing Data Sheets

Anatase Nanopowders Exposed to Humidity at Room Temperature

Dynamic Response

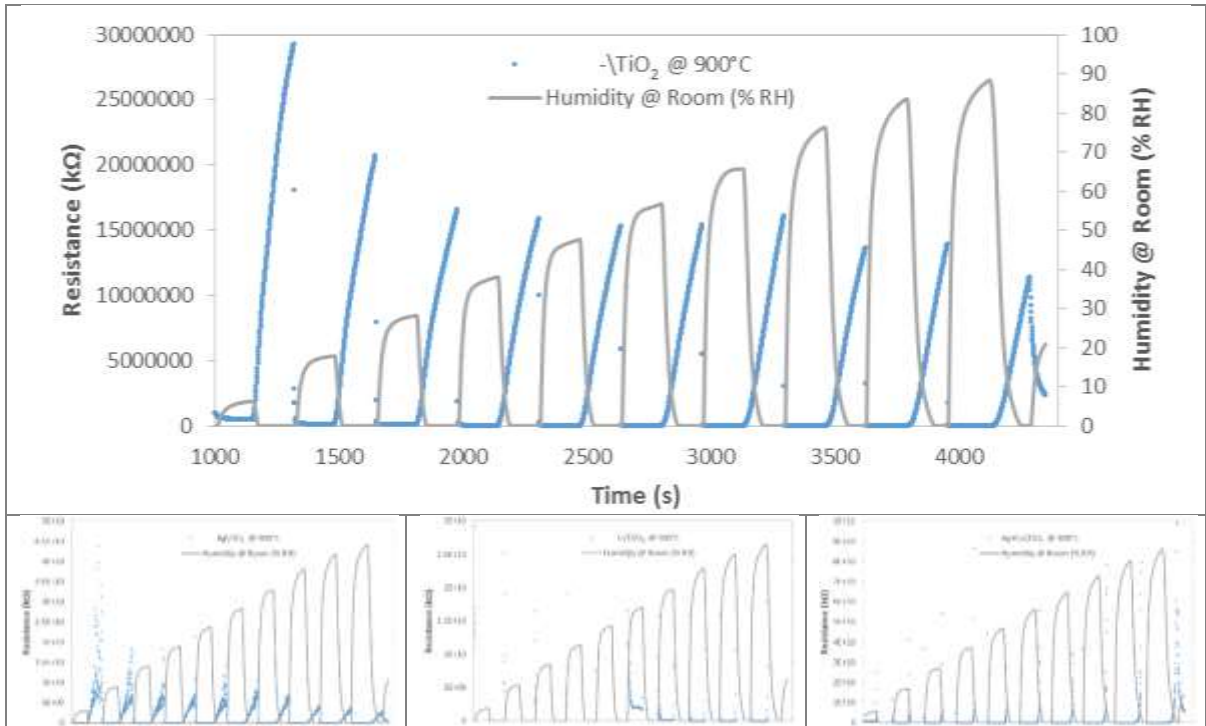


Performance Indices

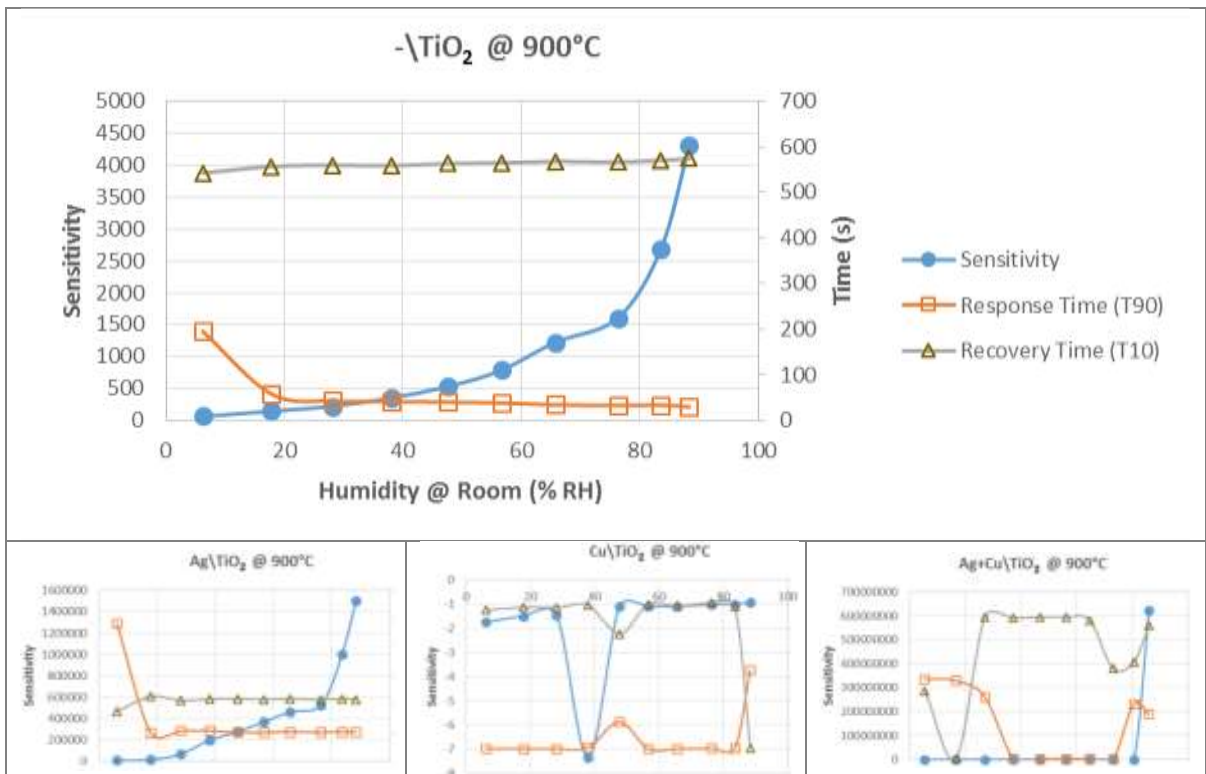


Rutile Nanopowders Exposed to Humidity at Room Temperature

Dynamic Response

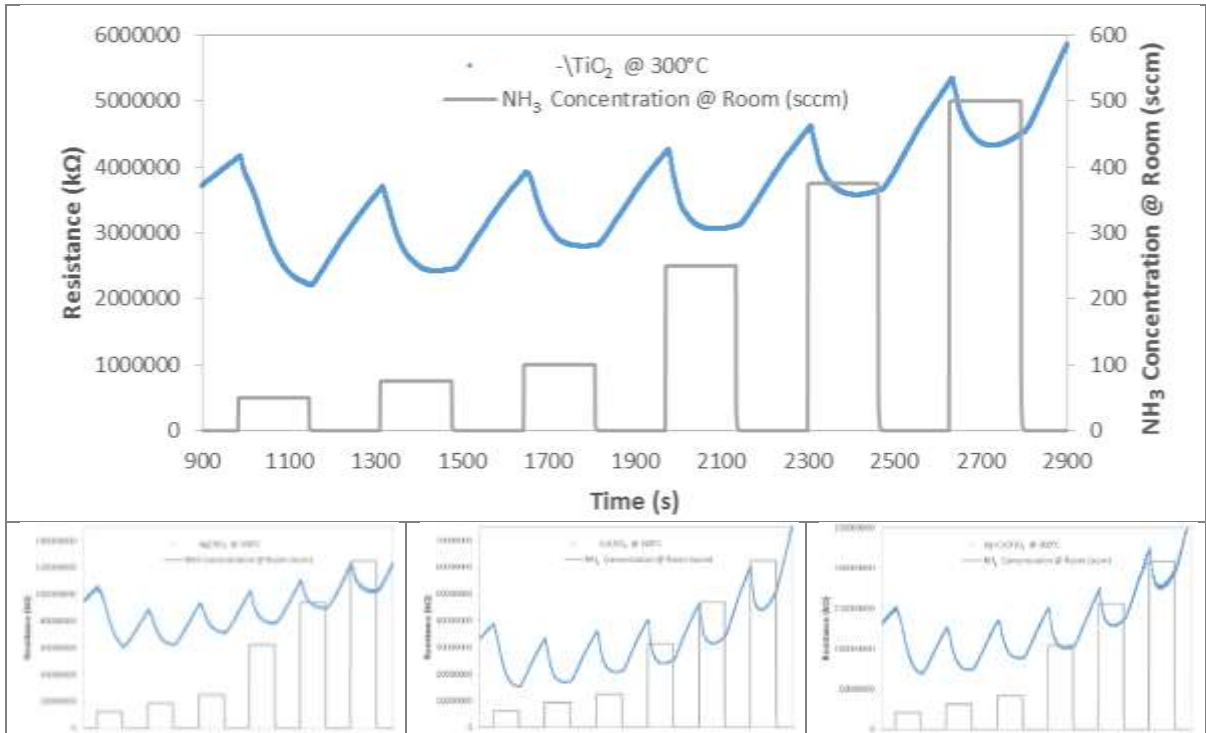


Performance Indices

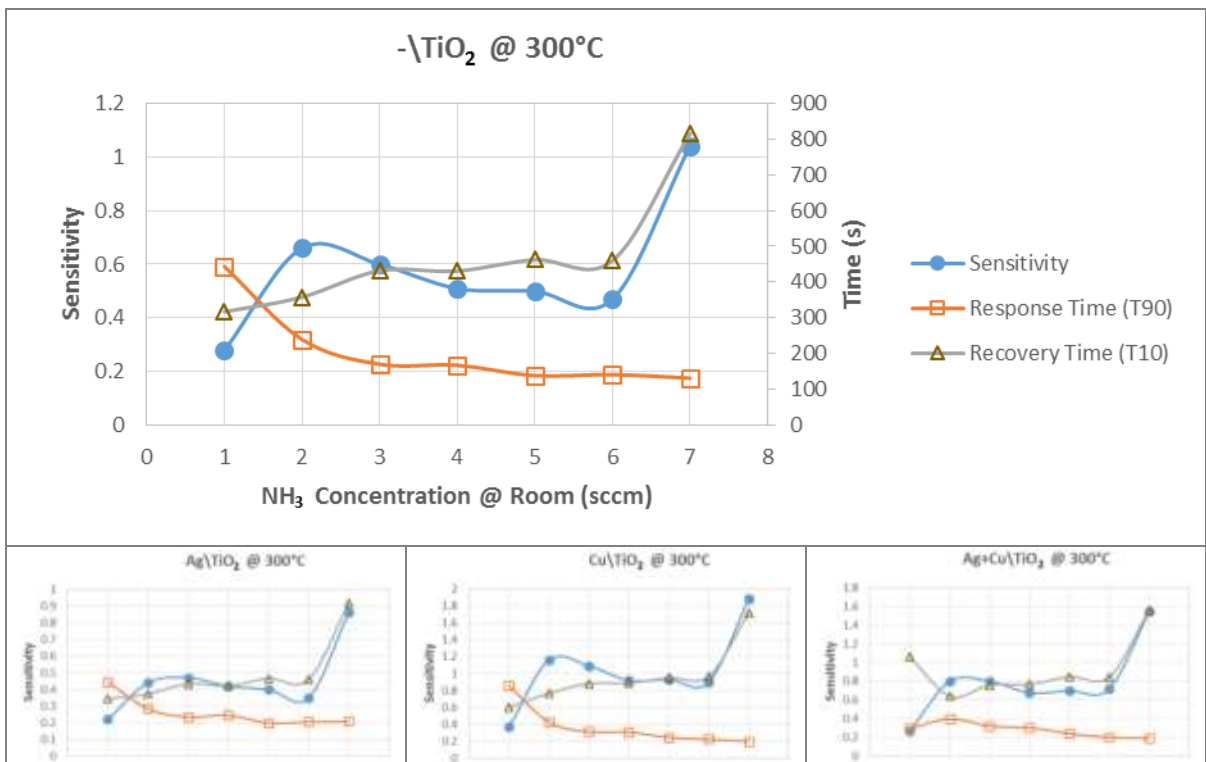


Anatase Nanopowders Exposed to NH₃ at Room Temperature

Dynamic Response

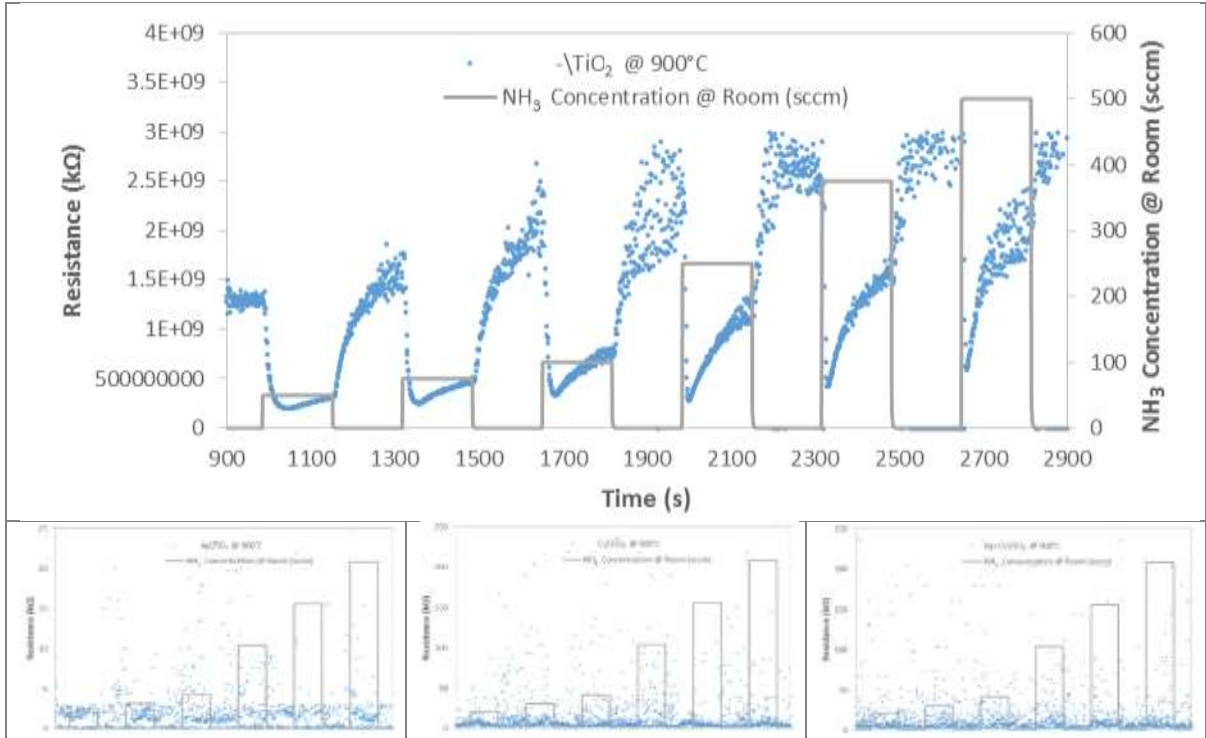


Performance Indices

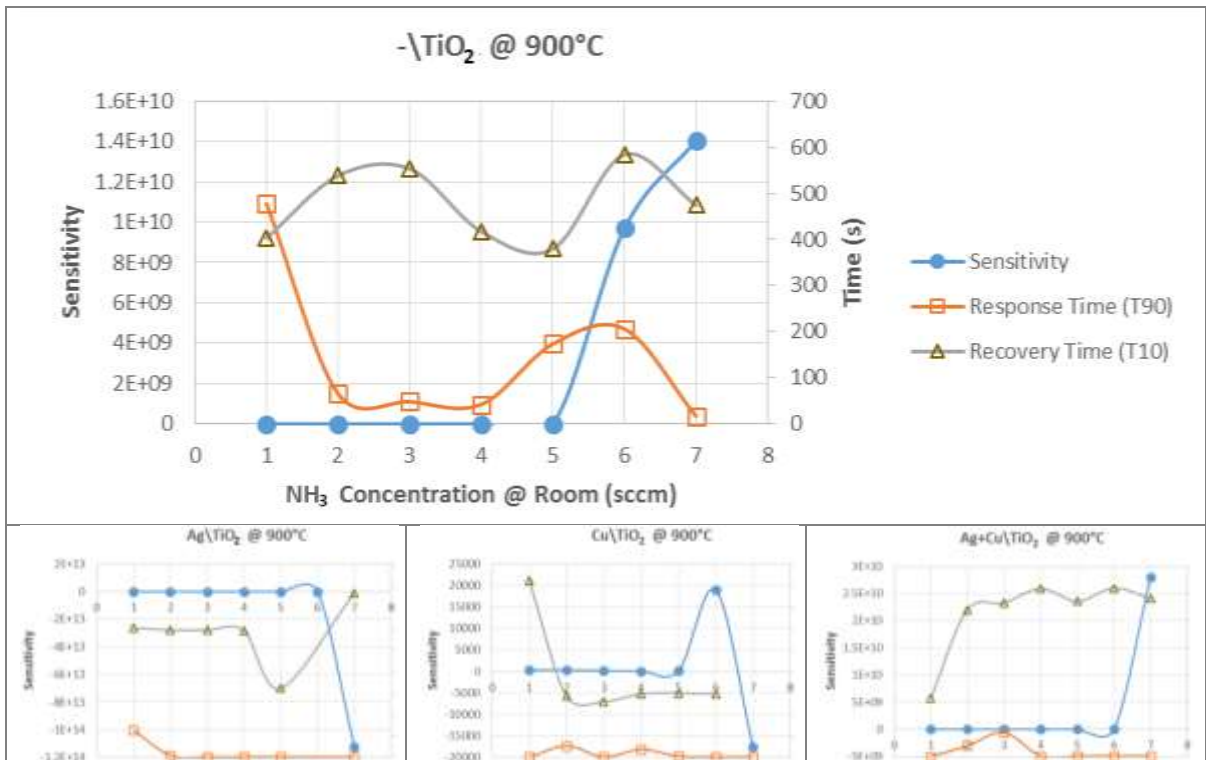


Rutile Nanopowders Exposed to NH₃ at Room Temperature

Dynamic Response

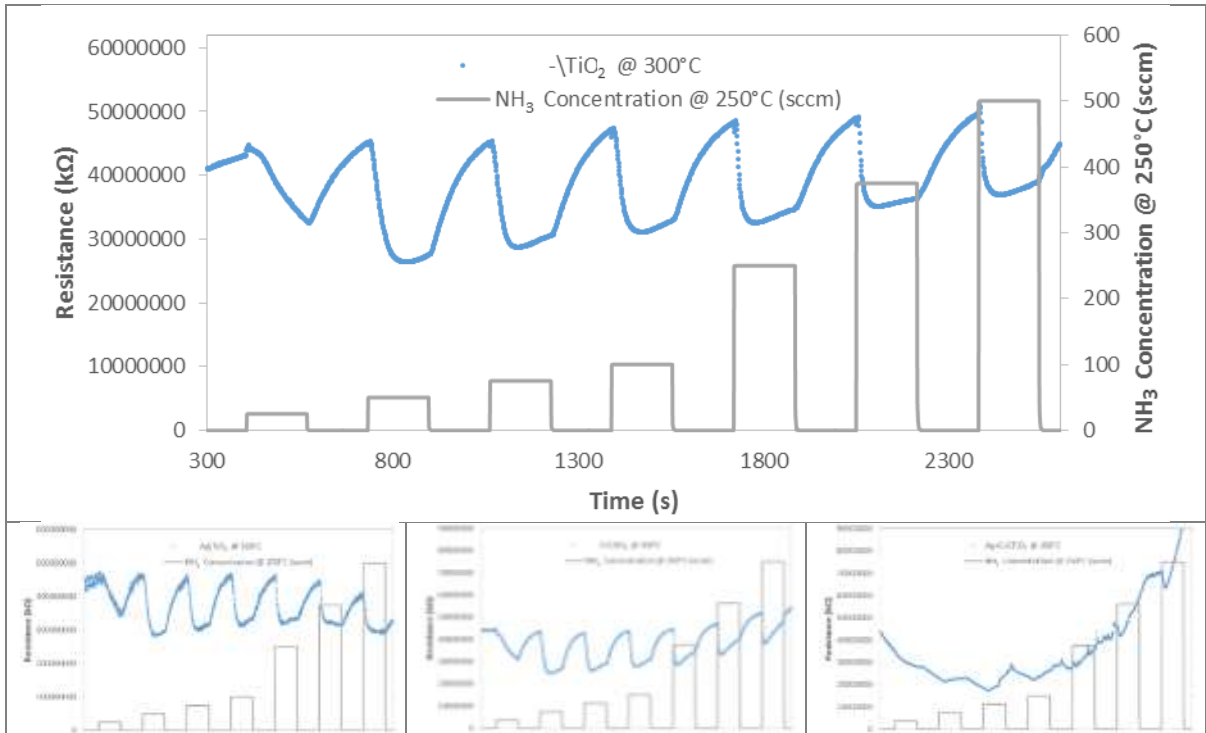


Performance Indices

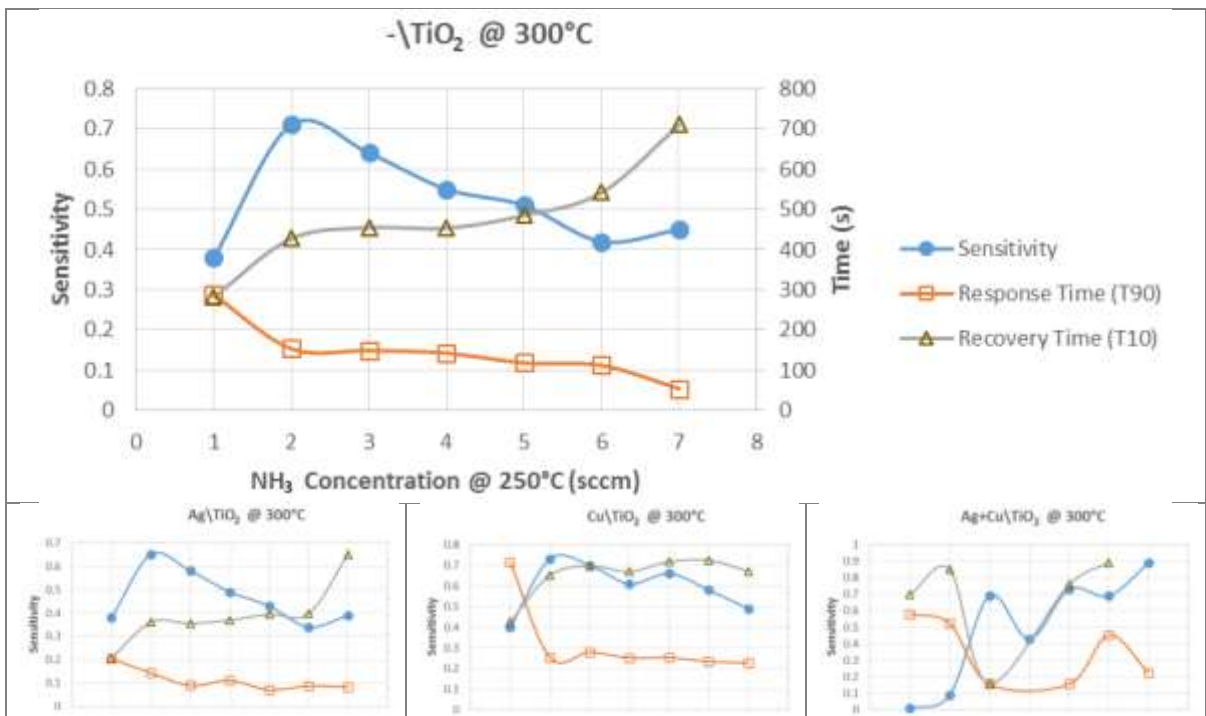


Anatase Nanopowders Exposed to NH₃ at 250°C

Dynamic Response

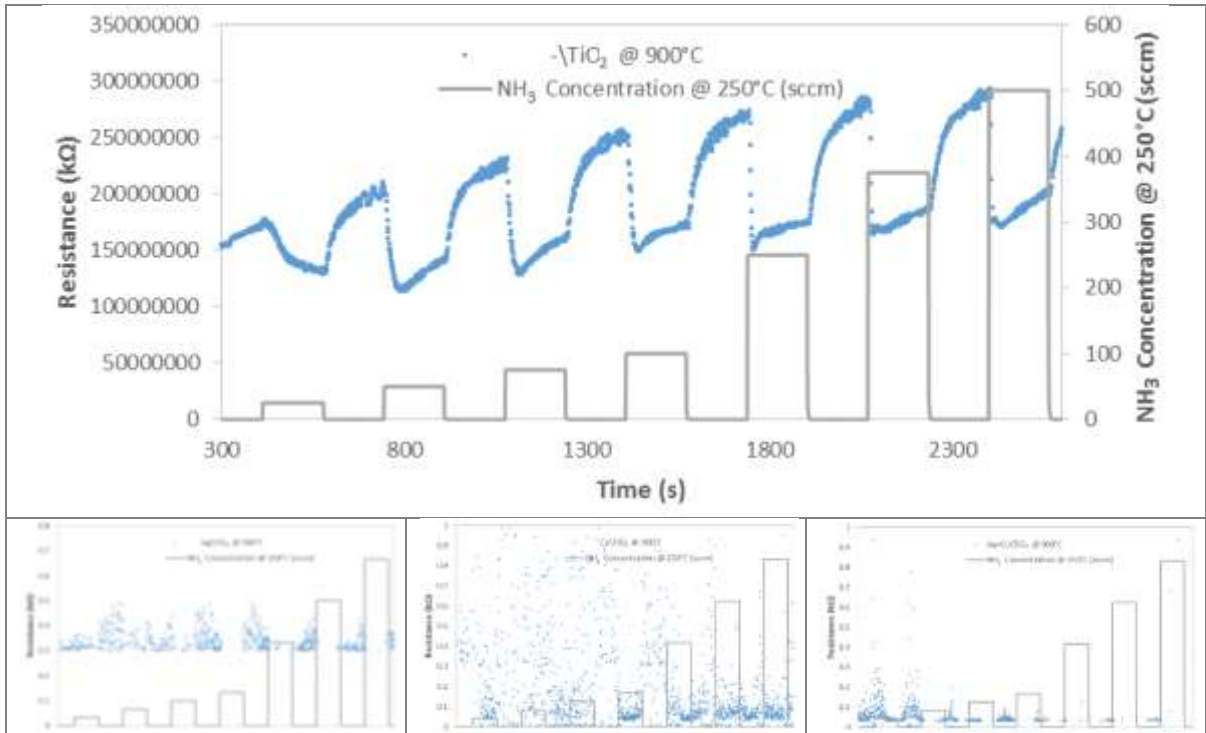


Performance Indices

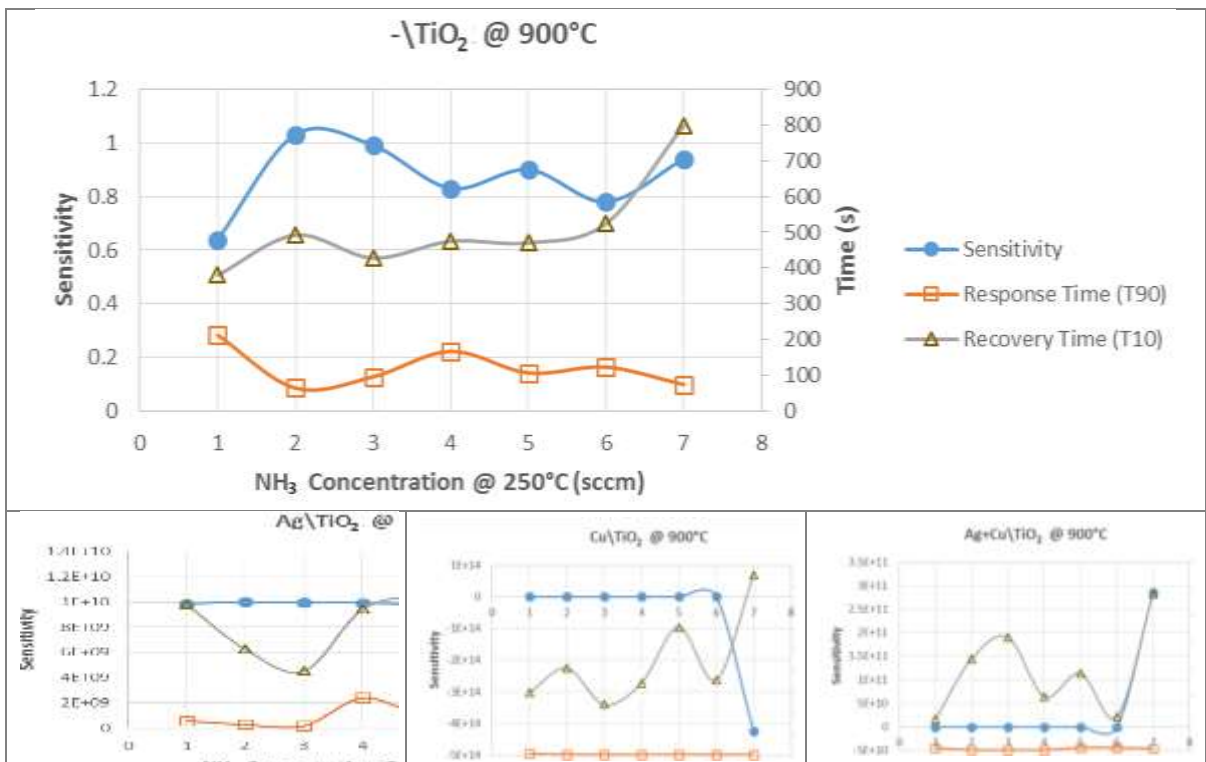


Rutile Nanopowders Exposed to NH₃ at 250°C

Dynamic Response

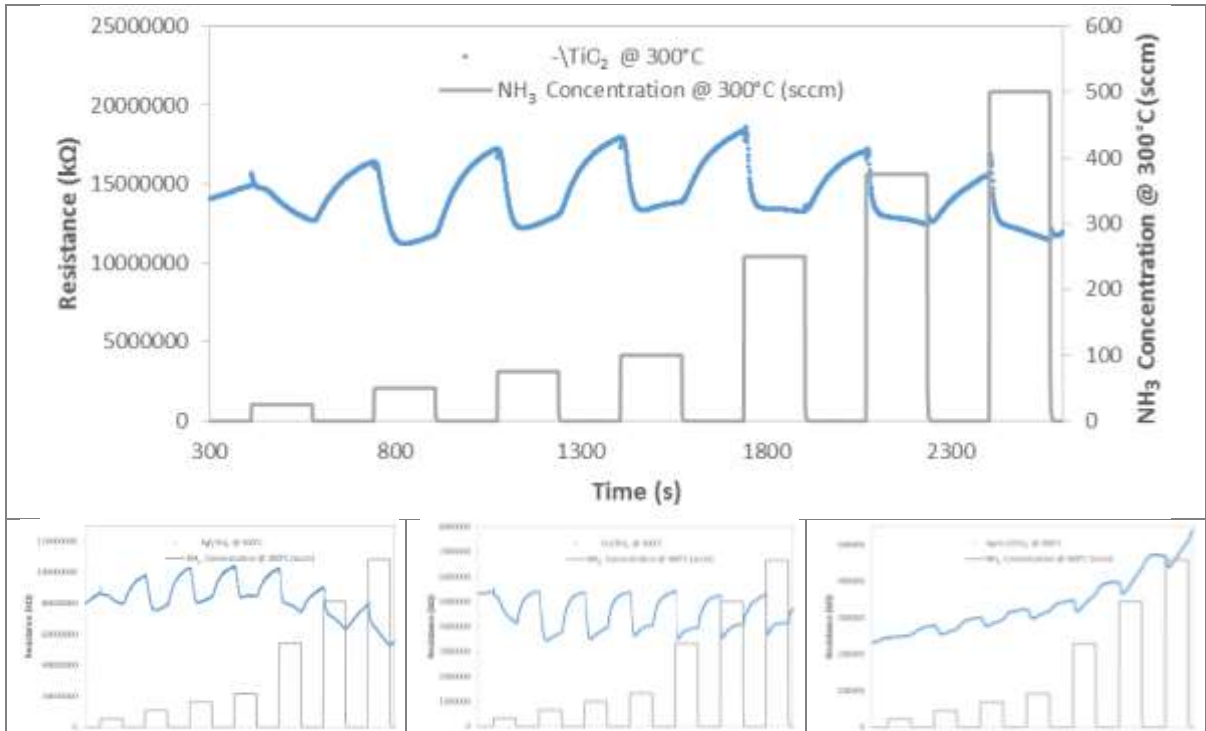


Performance Indices

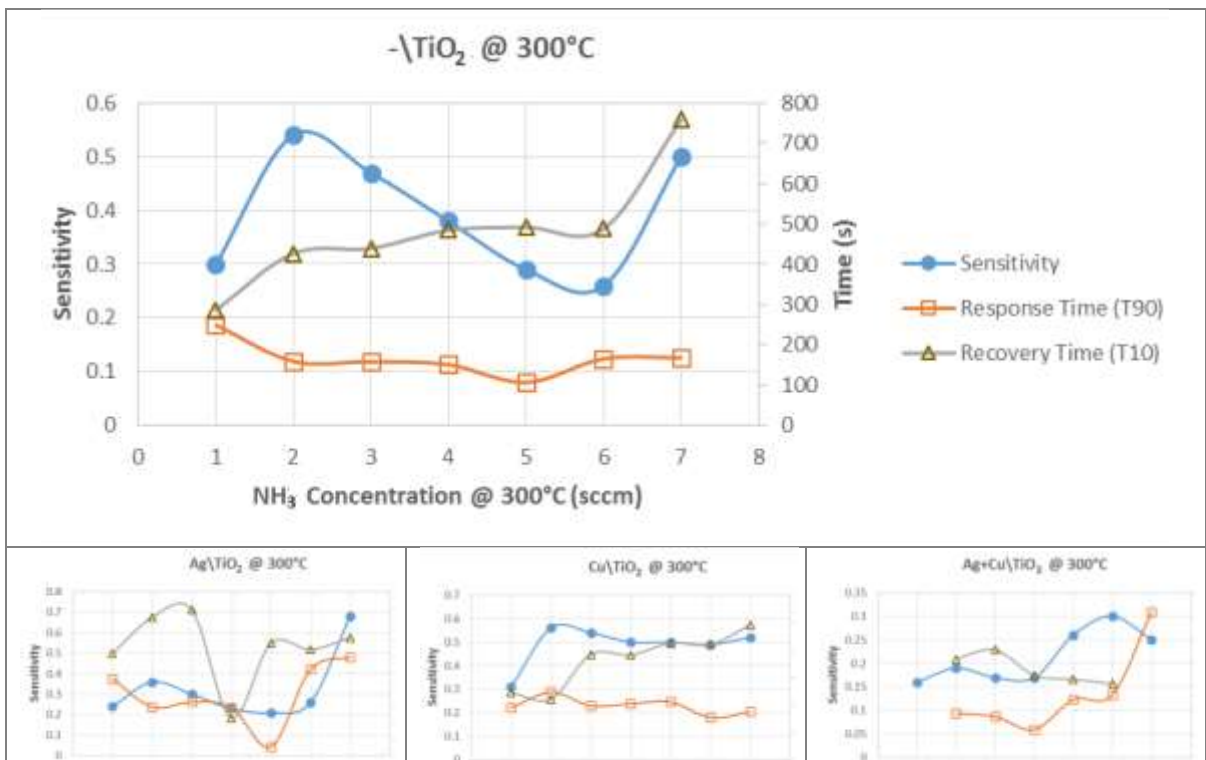


Anatase Nanopowders Exposed to NH₃ at 300°C

Dynamic Response

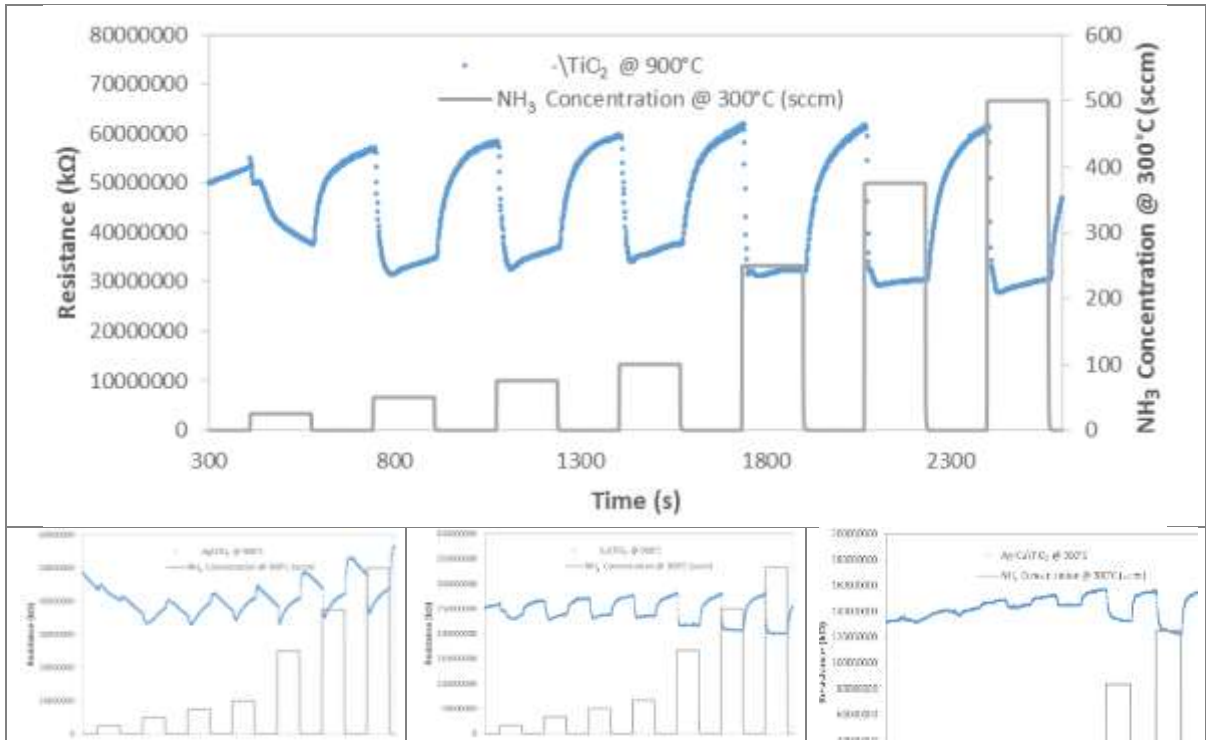


Performance Indices

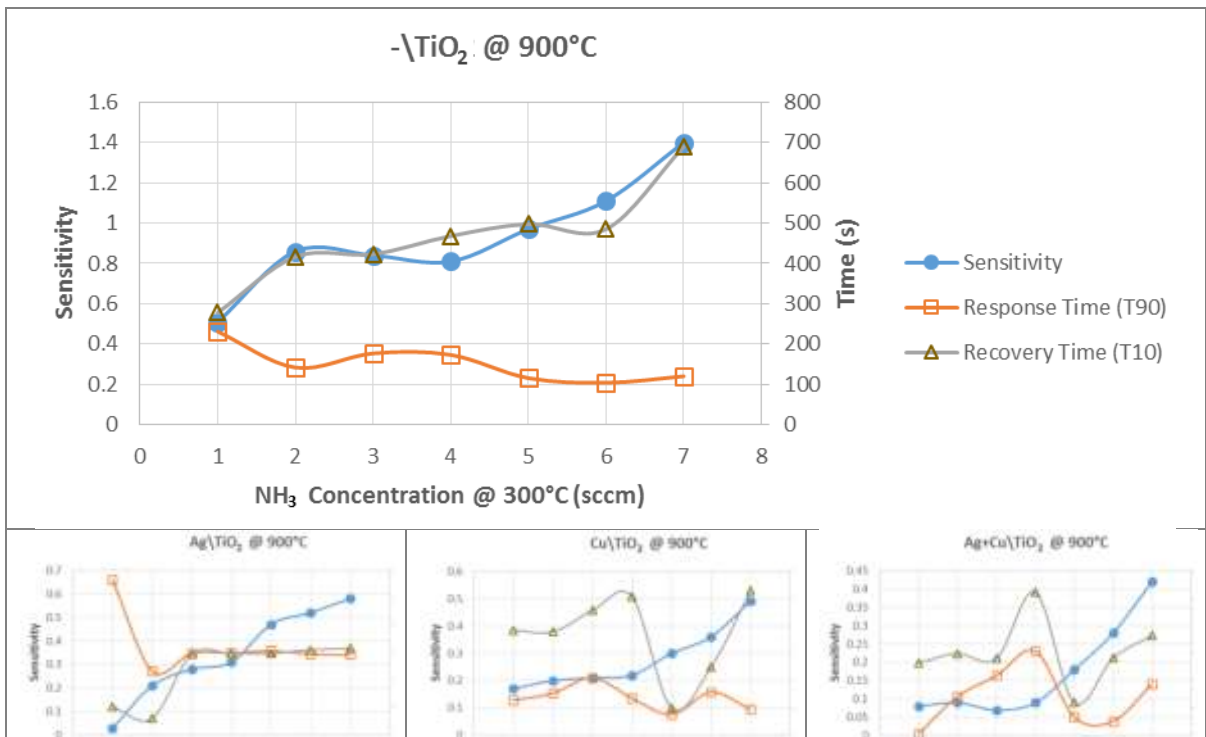


Rutile Nanopowders Exposed to NH₃ at 300°C

Dynamic Response



Performance Indices



Anatase Nanopowders Exposed to NH₃ at 350°C

Dynamic Response

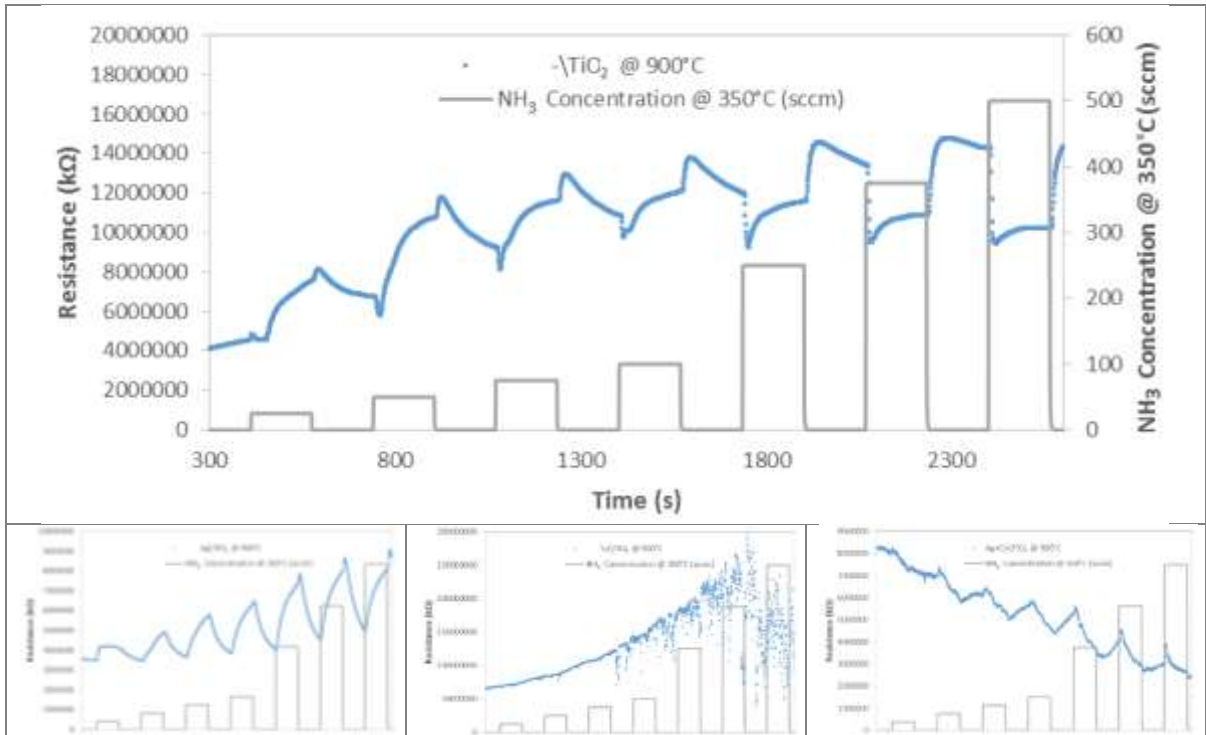
Not available

Performance Indices

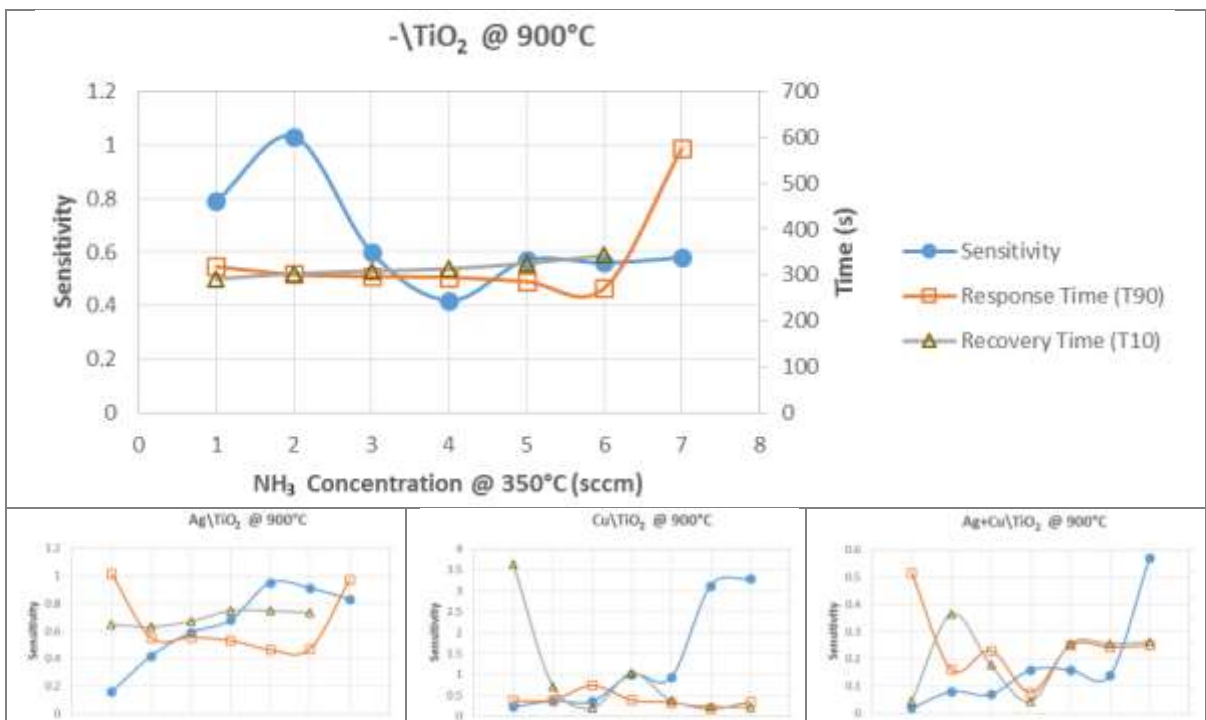
Not available

Rutile Nanopowders Exposed to NH₃ at 350°C

Dynamic Response

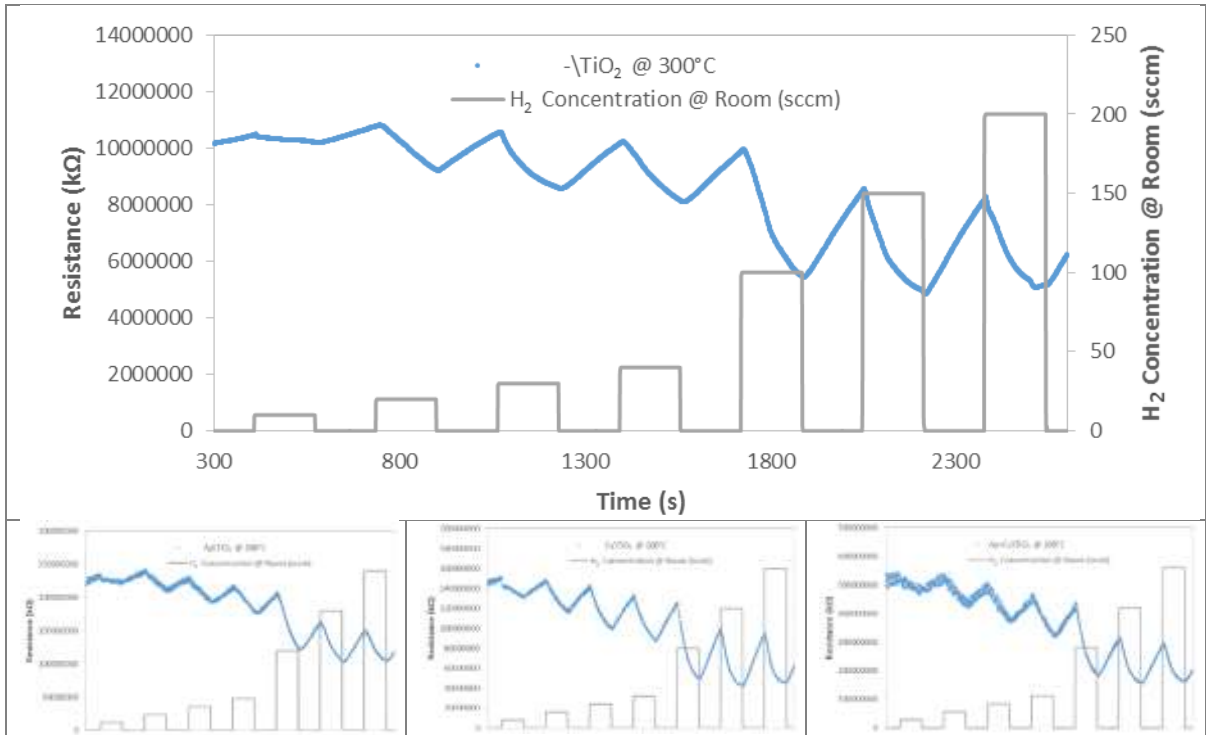


Performance Indices

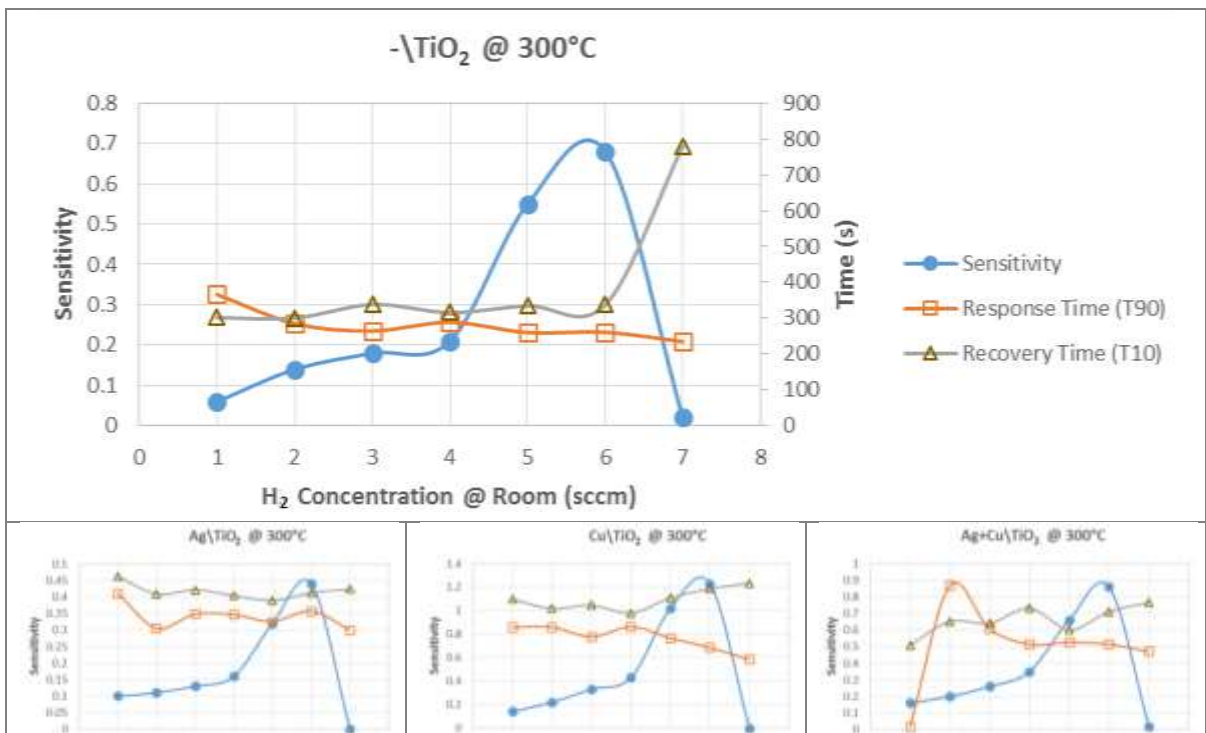


Anatase Nanopowders Exposed to H₂ at Room Temperature

Dynamic Response

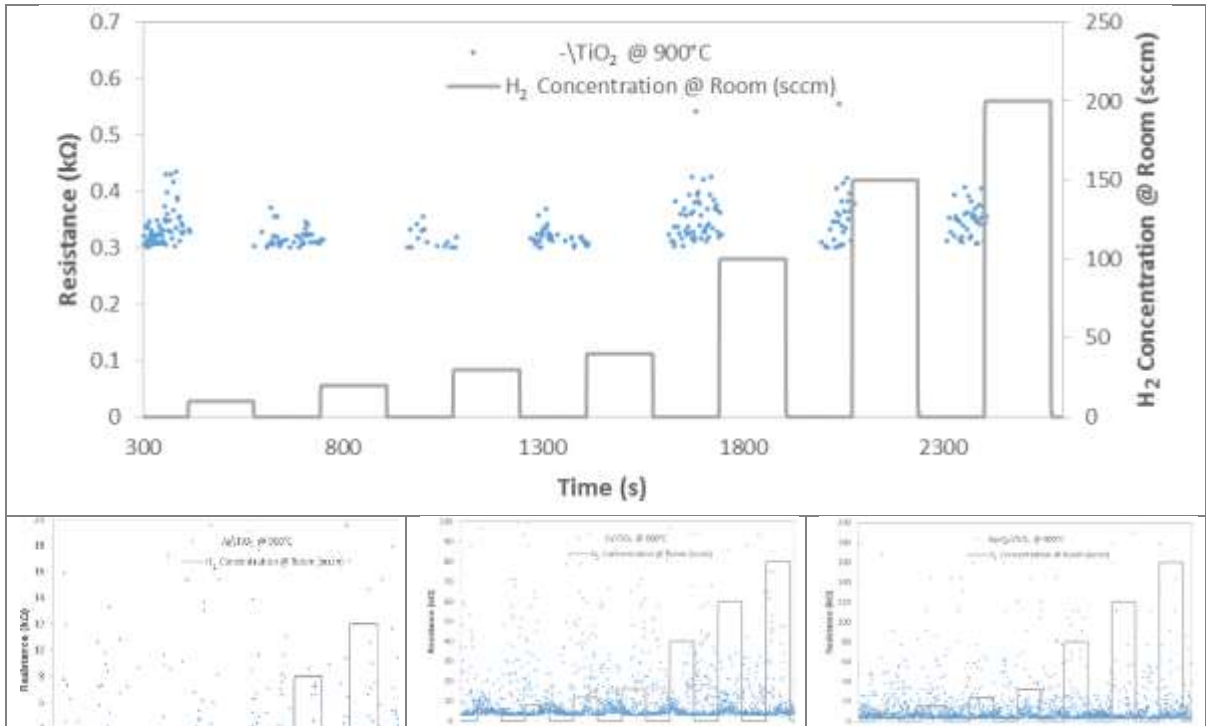


Performance Indices

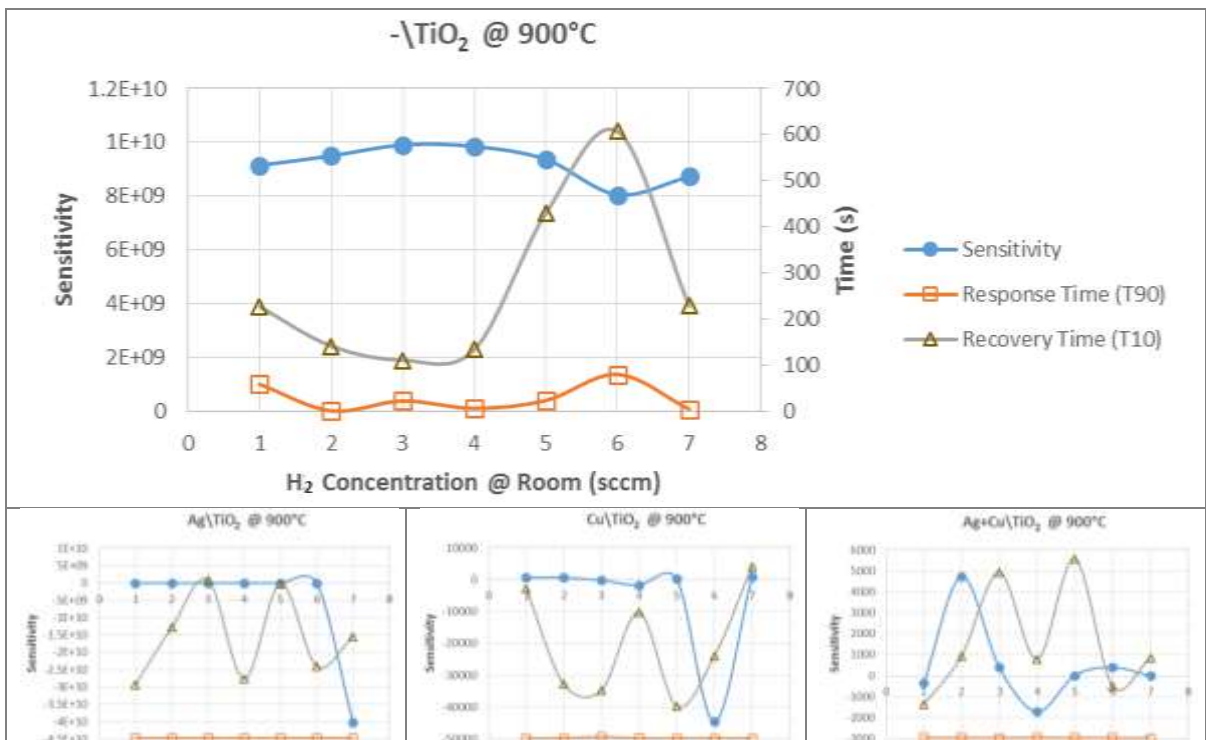


Rutile Nanopowders Exposed to H₂ at Room Temperature

Dynamic Response

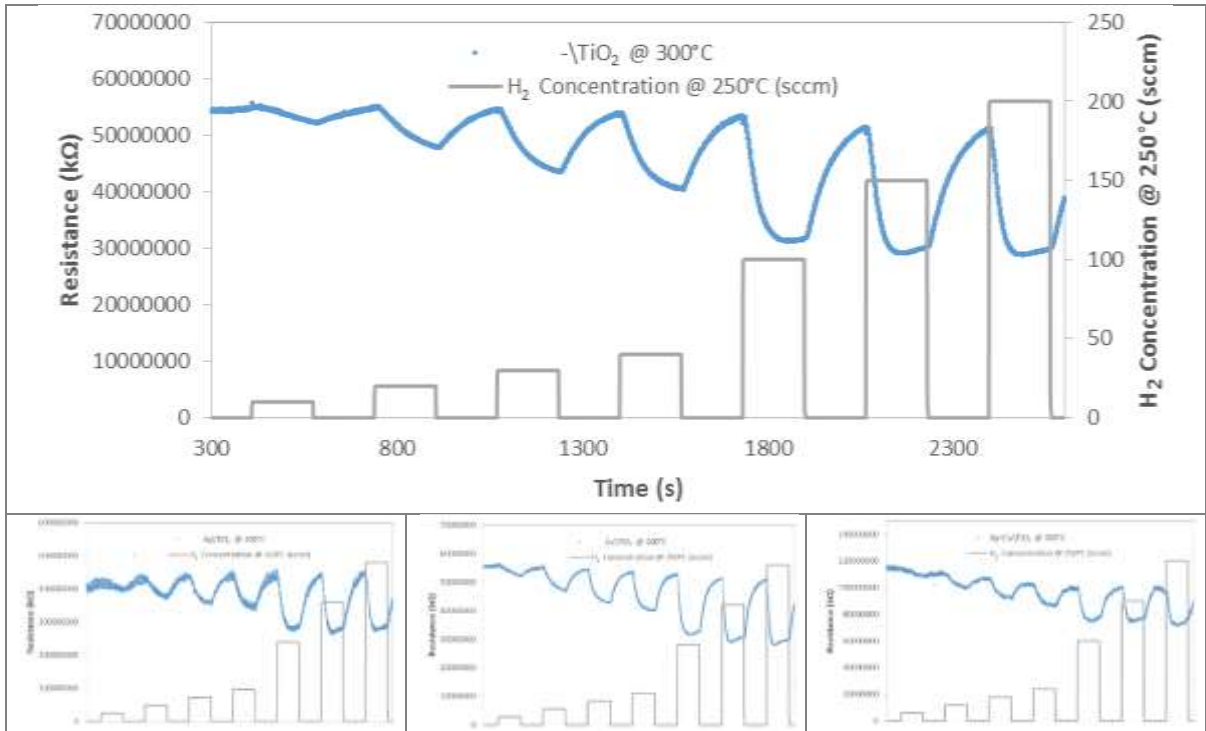


Performance Indices

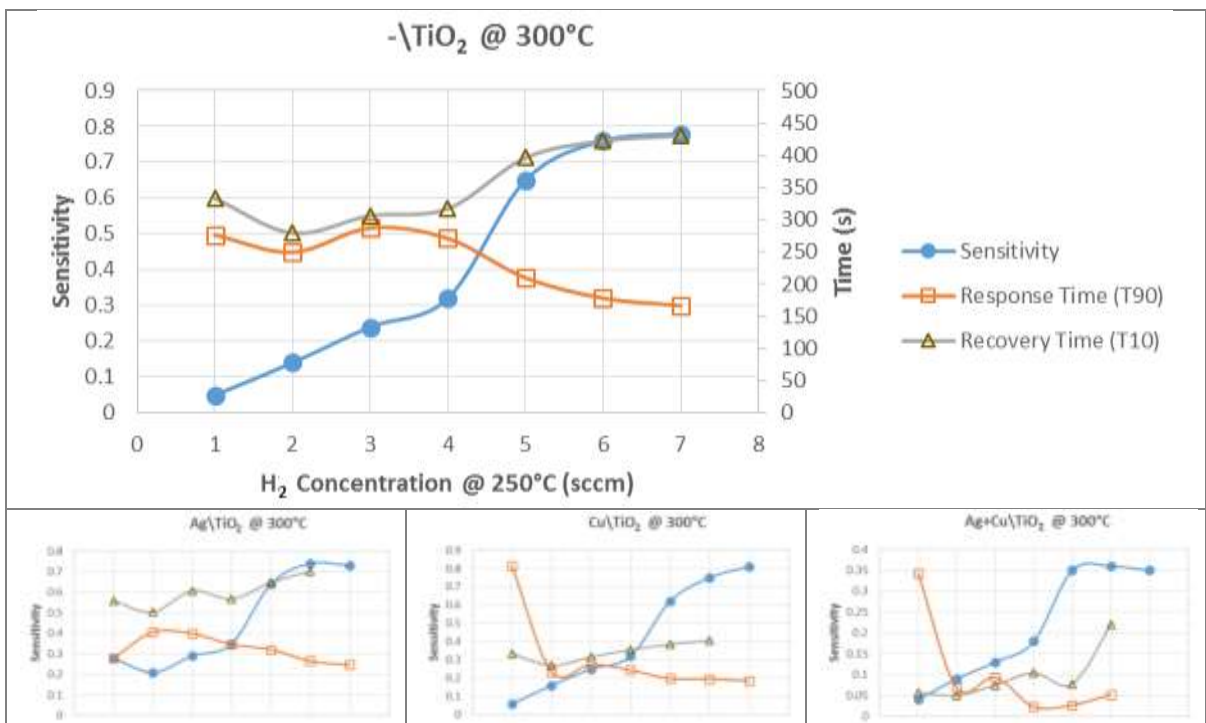


Anatase Nanopowders Exposed to H₂ at 250°C

Dynamic Response

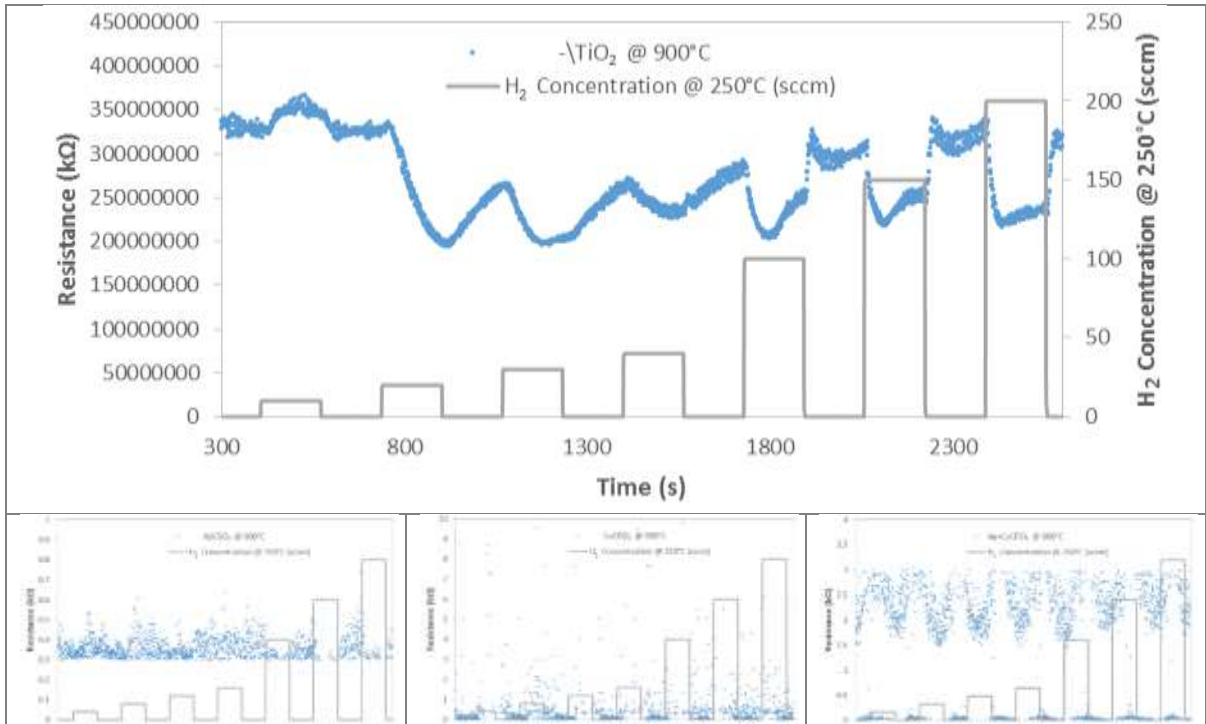


Performance Indices

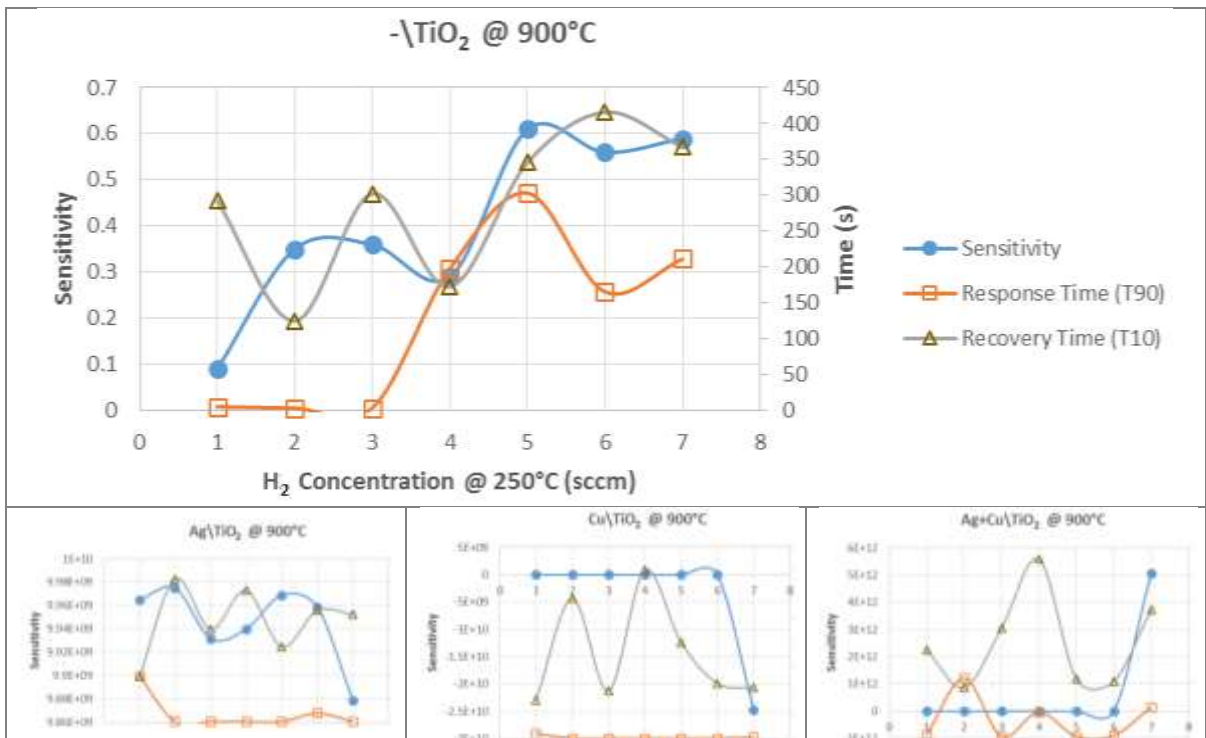


Rutile Nanopowders Exposed to H₂ at 250°C

Dynamic Response

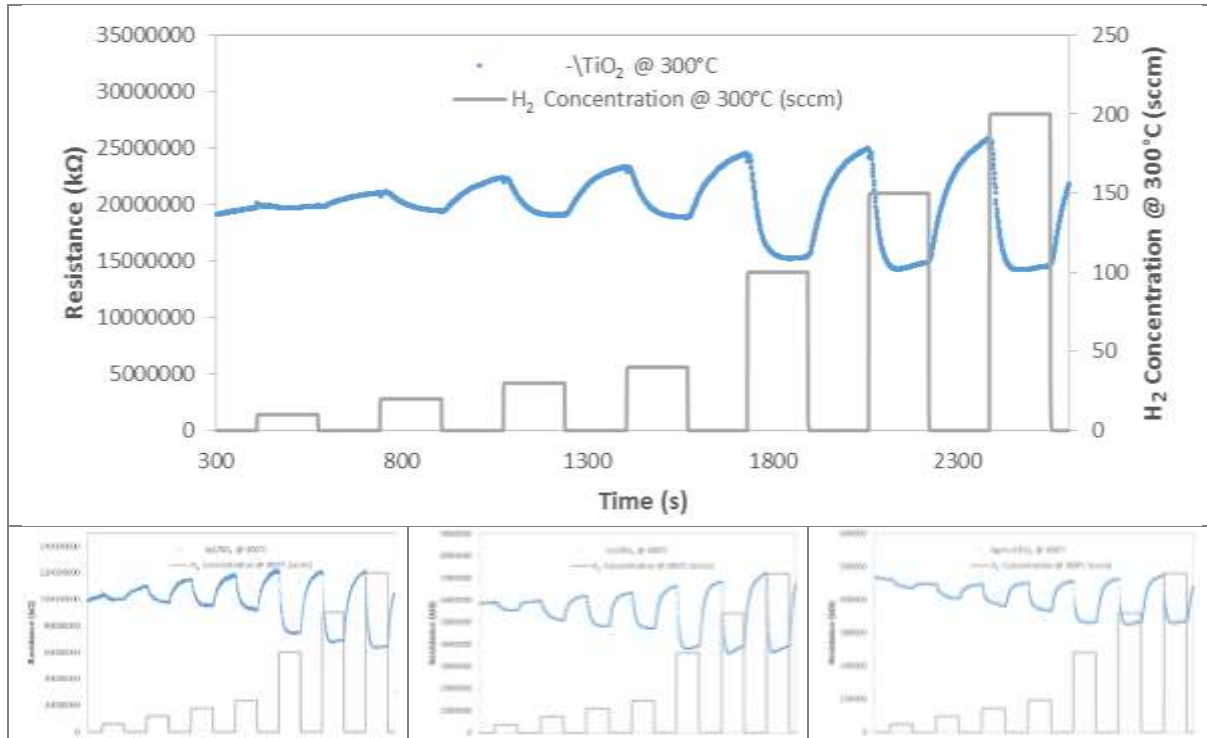


Performance Indices



Anatase Nanopowders Exposed to H₂ at 300°C

Dynamic Response



Performance Indices

**Single and Double Doping of Nanostructured Titanium Dioxide with Silver and
Copper: Structural, Optical and Gas-Sensing Properties**

by

NUBI OLATUNBOSUN OWOLABI

THESIS

Submitted in fulfilment of the requirements for the degree of

DOCTOR OF PHILOSOPHY

in

PHYSICS

in the

FACULTY OF SCIENCE & AGRICULTURE

(School of Physical and Mineral Sciences)

at the

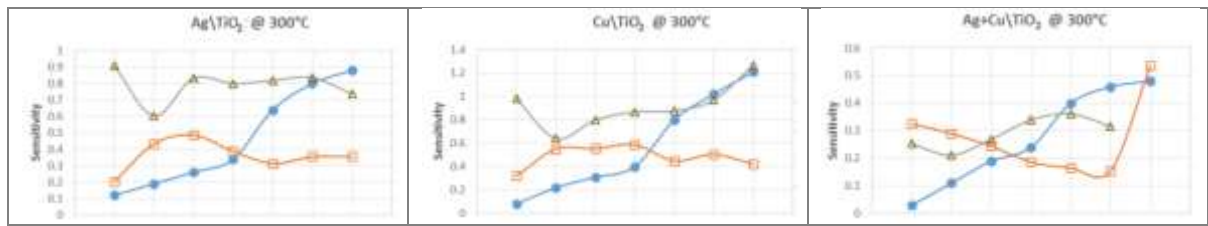
UNIVERSITY OF LIMPOPO

PROMOTER: Prof. K.E. Rammutla

CO-PROMOTER: Dr. T.E. Mosuang

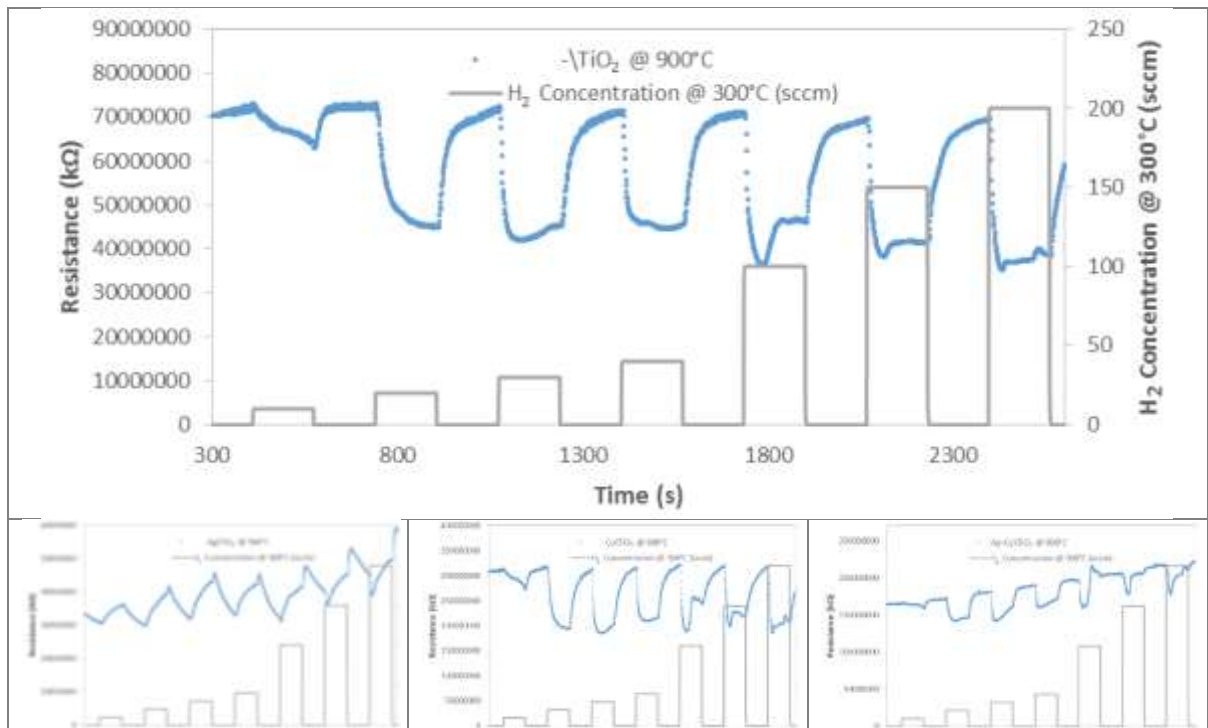
2016



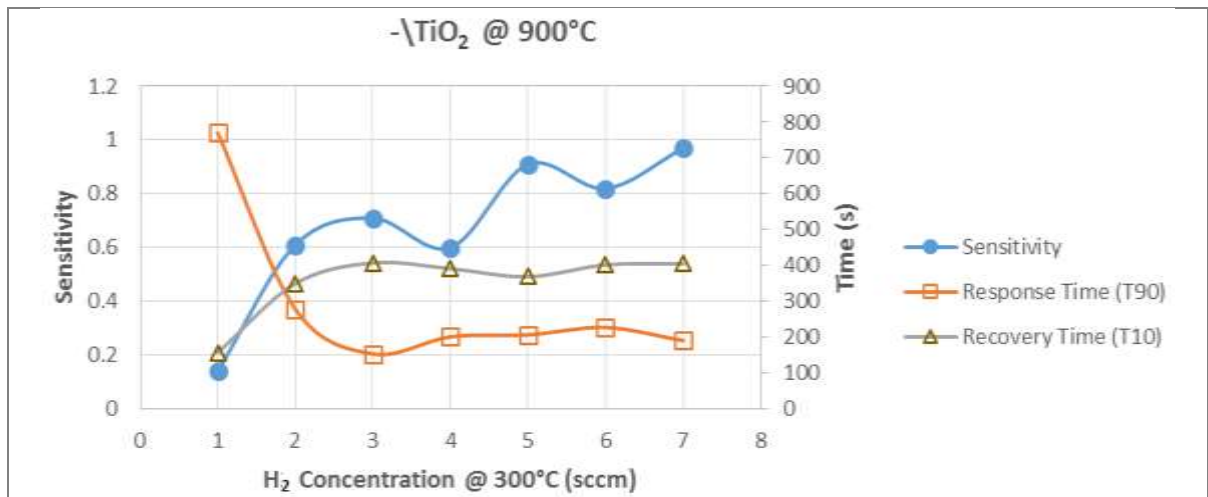


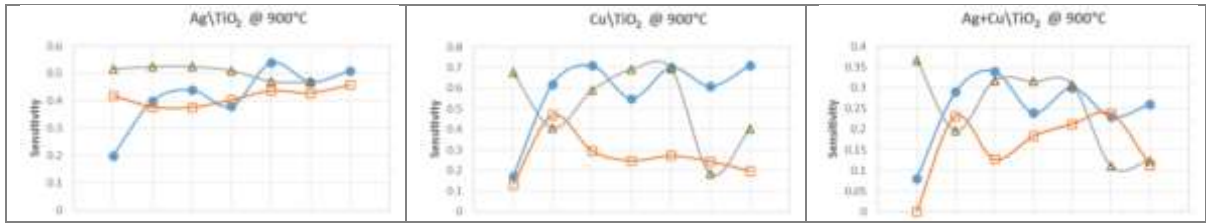
Rutile Nanopowders Exposed to H₂ at 300°C

Dynamic Response



Performance Indices



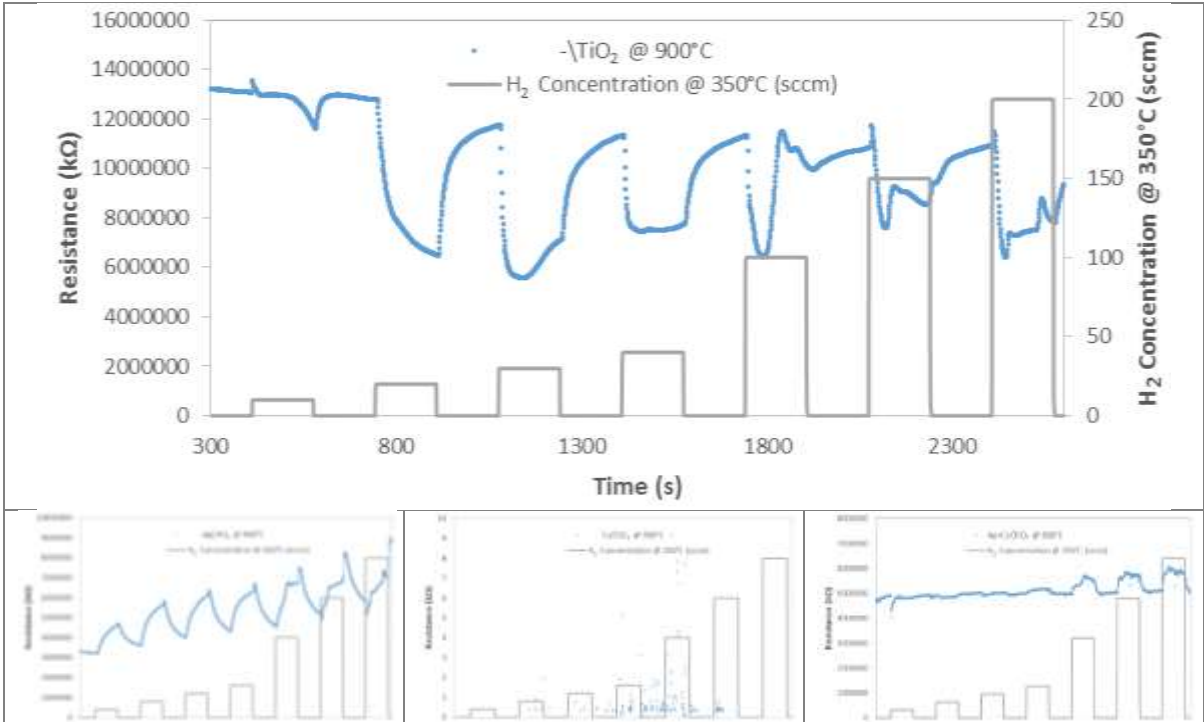


Anatase Nanopowders Exposed to H ₂ at 350°C	
Dynamic Response	
Not available	
Performance Indices	
Not available	

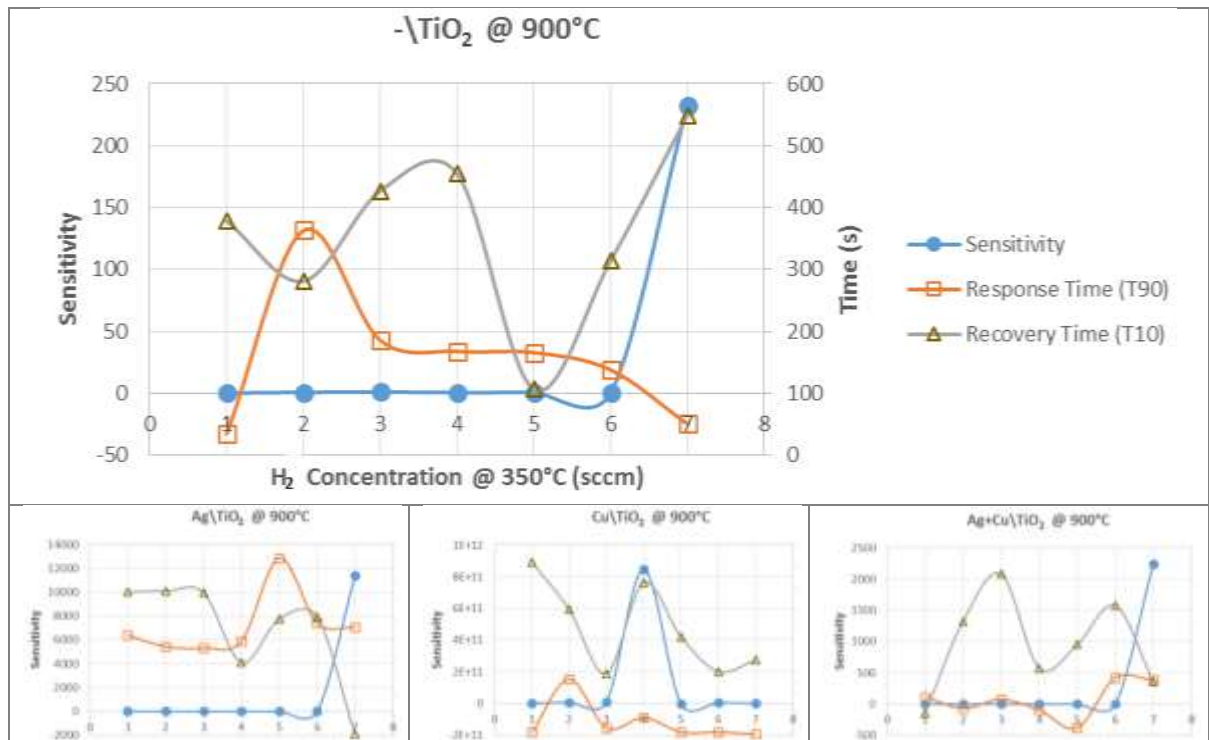
--	--	--

Rutile Nanopowders Exposed to H₂ at 350°C

Dynamic Response



Performance Indices



Ni Ipari, "O ti bushe".